Identification of seedling-specific effectors in the *Ustilago maydis* – maize interaction: From organ to cell type specificity

Dissertation

zur
Erlangung des Doktorgrades
der Naturwissenschaften
(Dr. rer. nat.)

Dem Fachbereich Biologie
der Philipps-Universität Marburg
vorgelegt von

Alexandra Matei
aus Temeschburg

Marburg/Lahn, 2016

Identification of seedling-specific effectors in the *Ustilago maydis* – maize interaction: From organ to cell type specificity

Dissertation

zur
Erlangung des Doktorgrades
der Naturwissenschaften
(Dr. rer. nat.)

Dem Fachbereich Biologie
der Philipps-Universität Marburg
vorgelegt von

Alexandra Matei
aus Temeschburg

Marburg/Lahn, 2016

Die Untersuchungen zur vorliegenden Arbeit wurden von Juni 2012 bis November 2014 am Max-Planck-Institut für terrestrische Mikrobiologie in der Abteilung Organismische Interaktionen in Marburg und von Dezember 2014 bis Oktober 2016 am Lehrstuhl für Terrestrische Mikrobiologie an der Universität zu Köln unter der Betreuung von Herrn Prof. Dr. Gunther Döhlemann durchgeführt.

Vom Fachbereich Biologie
der Philipps-Universität Marburg als Dissertation
angenommen am: 13.12.2016

Erstgutachter: Herr Prof. Dr. Gunther Döhlemann
Zweitgutachter: Frau Prof. Dr. Regine Kahmann

Tag der mündlichen Prüfung: 23.01.2017

Teile dieser Arbeit wurden in folgenden Artikeln veröffentlicht oder zur Veröffentlichung eingereicht:

Matei, A., Ernst, C., Günl, M., Thiele, B., Altmüller, J., Doehlemann, G. (2016). Cell type specific dissection of *Ustilago maydis*-induced tumor development in maize leaves. In preparation.

Schilling, L.*, Matei, A.*, Redkar, A., Walbot, V. and Doehlemann, G. (2014). Virulence of the maize smut *Ustilago maydis* is shaped by organ-specific effectors. Mol. Plant. Pathol. 15(8): 780-9. *contributed equally

Weitere Veröffentlichungen:

Redkar, A., Matei, A., Doehlemann, G. (2016). Insights into the host cell modulation and induction of new cells by corn smut *Ustilago maydis*. Front Plant Sci, submitted.

Matei, A. and Doehlemann, G. (2016). Cell Biology of Corn Smut Disease – *Ustilago maydis* as a Model for Biotrophic Interactions. Curr Opin Microbiol. 34:60-66.

Hemetsberger, C., Mueller, A.N., Matei, A., Herrberger, C., Hensel, G., Kumlehn, J., Mishra, B., Sharma, R., Thines, M., Hueckelhoven, R. and Doehlemann, G. (2015). The fungal core effector Pep1 is conserved across smuts of dicots and monocots. New Phytol. 206(3): 1116-26.

Erklärung

Ich versichere, dass ich meine Dissertation mit dem Titel „Identification of seedling-specific effectors in the *Ustilago maydis* – maize interaction: From organ to cell type specificity“, selbstständig und ohne unerlaubte Hilfe angefertigt und mich dabei keiner anderen als der von mir ausdrücklich bezeichneten Quellen und Hilfsmittel bedient habe.

Diese Dissertation wurde in der jetzigen oder einer ähnlichen Form noch bei keiner anderen Hochschule eingereicht und hat noch keinen sonstigen Prüfungszwecken gedient.

(Ort/Datum) (Alexandra Matei)

Es ist wichtiger, dass jemand sich über eine Rosenblüte freut, als dass er ihre Wurzel unter das Mikroskop bringt.

Oscar Wilde (1854-1900)

Zusammenfassung

Der Basidiomyzet *Ustilago maydis* ist der Erreger des Maisbeulenbrands in *Zea mays* (Mais). Nach Etablierung der biotrophen Interaktion induziert *Ustilago maydis* Tumore in allen oberirdischen pflanzlichen Organen. Zur Unterdrückung des pflanzlichen Immunsystems sowie zur Etablierung der biotrophen Interaktion und Tumorinduktion sekretiert der Pilz mehr als 500 sogenannter Effektorproteine. Neben allgemeiner Effektoren sekretiert der Pilz auch organspezifische Effektoren, die eine Anpassung an die physiologisch unterschiedlichen Gewebe der pflanzlichen Organe gewährleisten (Skibbe et al., 2010; Schilling et al., 2014)

Um die organspezifische Etablierung der *U. maydis* – Mais Interaktion aufzuklären, wurde in dieser Studie eine Gruppe an Effektorproteinen untersucht und charakterisiert, die spezifisch an der Virulenz im Blatt oder der männlichen Blüte beteiligt sind (Schilling et al., 2014). Der hierbei identifizierte blattspezifische Effektor Um01690 (Small tumors in seedling 1, Sts1) wurde mit Hilfe des Hefe-Zwei-Hybrid-Systems auf seine Interaktion mit potentiellen Maisproteinen untersucht. Es wurde eine Mais Carboxypeptidase als potentieller Interaktor identifiziert, welche möglicherweise eine Rolle in der Regulation der pflanzlichen meristematischen Gewebe und des Wachstums spielt.

In einem zweiten Teil dieser Arbeit wurde die gewebe- und zelltypspezifische Interaktion von *U. maydis* und dem Mais Blattgewebe untersucht. Histologische Untersuchungen der Zellanatomie während der Tumorinduktion haben hierbei zum Verständnis der Entwicklung von Blatttumoren beigetragen und den Einfluss von *U. maydis* auf Mesophyll und Bündelscheidezellen identifiziert. Die Interaktion von Pilz und Pflanze wurde hierbei auf die physiologischen bis hin zu subzellulären Veränderungen während des Tumorwachstums untersucht. DNA Syntheseuntersuchungen in Wirtszellen haben hierbei zur genauen Charakterisierung des Ursprungs und der Entwicklung von hyperplastischen (aus den Bündelscheidezellen resultierenden) und hypertrophen (aus dem Mesophyll resultierenden) Tumorzellen beigetragen. Zusätzlich wurde der vorher beschriebene Effektor See1 (Redkar et al., 2014) als erster zelltypspezifischer Effektor in der Blatttumorinduktion in der *U. maydis* – Mais Interaktion identifiziert. Mit Hilfe einer zelltypspezifischen Genexpressionsanalyse (laser capture microdissection) wurden individuell exprimierte pilzliche Effektorproteine in beiden Tumorzelltypen identifiziert.

Summary

Ustilago maydis is a basidiomycete fungus that causes smut disease on maize. As tumor formation occurs on all aerial parts of the plant, the fungus has to adapt to different types of host tissues which differ in structure and physiology. *U. maydis* therefore deploys an organ-specific set of adaptable virulence-related proteins (effectors) to circumvent host immunity and induce tumor-formation (Skibbe et al., 2010). Individual effector genes that are required for virulence in an organ-specific manner were identified in this study (Schilling et al., 2014).

To understand, how organ-specific effectors contribute to fungal virulence, the seedling-specific effector Um01690 (Sts1) was analyzed for its host interactor by yeast-2-hybrid analysis. This identified a maize carboxypeptidase as a putative interactor of Sts1 which is described to be involved in growth and developmental control.

In the second approach, tissue- and cell type-specific activity of *U. maydis* was investigated. A cell type-specific gene expression analysis as well as a microscopic cell size measurement was performed to analyze leaf tumor formation on the cellular level. Tracking of cell development, together with *in-vivo* visualization of plant DNA synthesis identified bundle sheath cells as the origin of hyperplasic cell division, while mesophyll cells turn into hypertrophic tumor cells showing endoreduplication. In parallel to that, cell wall component analyses in tumors have elucidated *U. maydis*-induced cell wall reformations. Histological stainings have visualized interactions of fungal and host factors in a cell type-specific and temporal context and shown physiological changes of seedling leaf tissue during tumor development. Furthermore, the *U. maydis* effector See1 (Redkar et al., 2015a) was identified in this study as the first effector that acts in a cell type-specific context upon leaf tumor induction.

RNAseq analysis of micro-dissected tumor cells showed that the fungus deploys cell type-specific effector gene expression in leaves upon tumor induction in addition to generally transcribed core effector genes. In summary this study elucidated cell type-specific processes leading to *U. maydis*-induced tumor formation in maize leaves.

Abbreviations

°C	Degree Celsius
aa	Amino acid
ABA	Abscisic acid
AC	Axenic culture
Ade	Adenine hemisulfate
AIR	Alcohol insoluble residue
Amp	Ampicillin
AMP1	Altered meristem program 1
ATP	Adenosine triphosphate
AX	Arabinoxylan
BiFC	Bimolecular fluorescence complementation
bm2	Brown midrip 2
bp	Base pairs
BSA	Bovine serum albumin
Carb	Carbenicillin
Cbx	Carboxin
cc domain	Coiled-coil domain
cDNA	Complementary DNA
CDS	Coding sequence
CERK1	Chitin elicitor receptor kinase 1
CFP	Cyan fluorescent protein
Chla	Chlorophyll a
Chlb	Chlorophyll b
Clm	Chloramphenicol
Cmu1	Chorismate mutase 1
Co-IP	Co-immunoprecipitation
CWI	Cell wall integrity
DAMP	Damage-associated molecular pattern
DMSO	Dimethylsulfoxid
DNA	Deoxyribonucleic acid
dai	Days after infiltration
dpi	Days post infection
DTT	Dithiothreitol
EDTA	Ethylenediaminetetraacetic acid
EdU	5-ethynyl-2-deoxyuridine
EF-Tu	Elongation factor Tu
EFR	EF-Tu Receptor
EGB	Early golden bantam
ER	Endoplasmic reticulum
ETI	Effector-triggered immunity
EtOH	Ethanol
ETS	Effector-triggered susceptibility
f.c.	Final concentration
FLS2	Flagellin-sensing 2

GAX	Glucoarabinoxylan
Gent	Gentamycin
$H_2O_{bid.}$	Double distilled water
HGA	Homogalacturonan
His	Histidine
HPAEC-PAD	High-performance anion-exchange chromatography with pulsed amperometric detection
hpi	Hours post infection
HR	Hypersensitive response
IPTG	Isopropyl-B-D-thiogalactopyranoside
JA	Jasmonic acid
Kan	Kanamycin
kb	Kilobases
kDA	Kilodalton
KNOX	Knotted1-like homeobox
LCM	Laser capture microdissection
Leu	Leucine
LRR	Leucine rich repeat
M phase	Mitosis phase
m/z	Mass-to-charge ratio
mA	Milliampere
MAMP	Microbe-associated molecular pattern
MAPK	Mitogen-activated protein kinase
min	Minute(s)
mL	Millilitre
MoClo	Modular cloning
NLR	Nucleotide-binding/leucine-rich-repeat
nm	Nanometer(s)
OD	Optical density
PAGE	Polyacrylamide gel electrophoresis
p	Statistical probability value
PA domain	Protease-associated domain
PAMP	Pathogen-associated molecular pattern
PBS	Phosphate buffered saline
Pep1	Protein essential during penetration 1
PI	Propidium iodide
Pit2	Protein involved in tumors 2
PRR	Pattern recognition receptor
PSI/II	Photosystem I/II
PTI	Pattern-triggered immunity
qRT PCR	Quantitative real-time polymerase chain reaction
R protein	Resistance protein
Rif	Rifampicin
RNA	Ribonucleic acid
RNAseq	Ribonucleic acid sequencing
ROS	Reactive oxygen species

rpm	Rounds per minute
S phase	Synthesis phase
SA	Salicylic acid
SAM	Shoot apical meristem
SAR	Systemic acquired resistance
SDS	Sodium dodecyl sulfate
See1	Seedling efficient effector 1
SGT1	Suppressor of G2 allele of skp 1
Spec	Spectinomycin
Sts1	Small tumors in seedling 1
SWEET	Sugar will eventually be exported transporter
TE-buffer	Tris-EDTA buffer solution
TEM	Transmission electron microscopy
TEMED	Tetramethylethylenediamine
Tet	Tetracyclin
TFR	Transferrin receptor-like dimerization domain
Tin2	Tumor inducing 2
TIR domain	Toll-interleukin 1 receptor domain
TM domain	Transmembrane domain
TOR	Target of Rapamycin
Trp	Tryptophane
TTSS	Type III secretion system
U	Unit (Enzyme activity)
V	Volt
v/v	Volume/volume
VP8	Viviparous 8
w/v	Weight/volume
WAK1	Wall-associated kinase 1
WGA	Wheat germ agglutinin
X-Gal	5-bromo-4chloro-3indolyl-ß-D-galactopyranoside
xg	Times gravity
YFP	Yellow fluorescent protein
µg	Microgram
µL	Microliter
µM	Micromolar
µm	Micrometer

Table of contents

1 Introduction

1.1 The study of organismic interactions

Plants are constantly exposed to a plethora of abiotic and biotic environmental stress conditions. These include climatic changes, nutrient availability and soil composition as well as a constant exposure to diverse microbial communities. The plant's interaction with its microbial surrounding can lead to either beneficial, disease causing or mutual interactions, depending on the microbial agent and the individual setup of the plant's innate immune system. Symbiotic interactions benefit the plant and are characterized by a close interaction between both partners for the acquisition of nutrients in order to sustain growth. Plant disease can lead to a devastating effect on the yield in crop plants. For example the annual yield of corn is diminished by about 10% due to pathogen attack (Oerke, 2006). The world population is estimated to rise towards 9 billion people by the year 2050 which will demand a strong increase in food production (Alexandratos and Bruinsma, 2012). Understanding organismic interactions is therefore the key towards fighting threats in order to secure food production. This is reinforced by the notion that climate change will lead to a decrease in arable land. Due to their implications on crop yield, understanding the changes in plant physiology caused by biotic and abiotic threats is a very contemporary issue.

1.2 Plant-microbe interactions

Plants as carbon fixing organisms serve as nutrient source for a diversity of microbes. In order to obtain nutrients from plants, microorganisms can establish various forms of interactions with their feeding source. Primarily, those interactions can be divided into necrotrophic, hemibiotrophic and biotrophic based on their lifestyle. Necrotrophic pathogens actively kill the invaded tissue and feed on dead plant material while biotrophs depend on the survival of the host and use its metabolism as nutritional source (Glazebrook, 2005; Horbach et al., 2011). Hemibiotrophic pathogens initially develop a biotrophic interaction with their host before switching to a necrotrophic lifestyle (Horbach et al., 2011).

Biotrophic pathogens develop a close interaction with their source of energy, the living plant. They have developed diverse forms of colonization structures In order to avoid recognition by the plant and to manipulate their host's metabolism towards their needs (Lo Presti et al., 2015).

1.2.1 *Ustilago maydis* – the causative agent of corn smut disease

U. maydis is a soil borne, basidiomycetious fungus that causes smut disease on maize (*Zea mays*) and teosinte (*Euchlaena mexicana*) by induction of tumors on all aerial plant organs (Figure 1; Martinez-Espinoza et al., 2002). The haploid, non-pathogenic form of the fungus is described as a yeast-like stage in which the fungus proliferates by budding (Banuett and Herskowitz, 1996; Christensen, 1963). *U. maydis* is a well-studied biotroph that serves since long as a model organism in fungal cell biology and plant-microbe interactions as it fulfills the requirements of easy genetic accessibility and availability of several reporter genes (Brefort et al., 2009; Matei and Doehlemann, 2016).

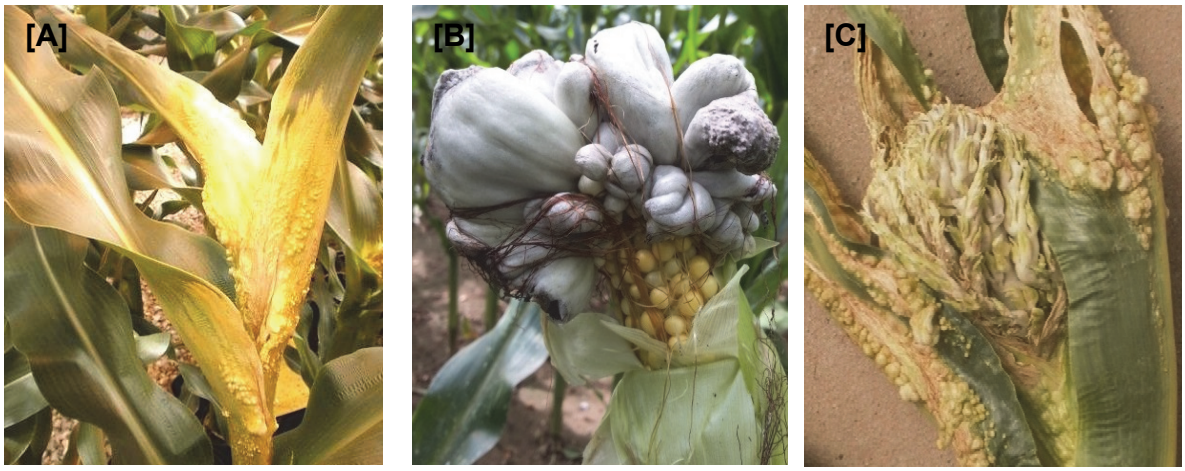

Figure 1: Smut disease symptoms caused by *U. maydis* on different organs. [A] Maize leaves infected with *U. maydis* form chlorotic regions in which tumors are formed. **[B]** *U. maydis* infected ears form large tumors in which spores develop (black regions). Picture kindly provided by A. Müller. **[C]** Male floral organ (tassel) infected by *U. maydis* and forming tumors in anther tissue instead of pollen.

Many cytological studies have added contribution towards the understanding of the *U. maydis* infection and tumor formation process in leaves (Banuett and Herskowitz, 1996; Snetselaar and Mims, 1992, 1993). On the plant's surface, haploid *U. maydis* sporidia of two different mating types fuse and form the invading dikaryotic filament which is able to penetrate the leaf surface and thereby initiate pathogenesis (Figure 2A; Kahmann et al.,

1995). The hyphae gradually enter the leaf surface most likely via secretion of cell wall degrading enzymes that are also involved in cell wall hydrolysis for cell enlargement during tumor formation (Doehlemann et al., 2008b; Schirawski et al., 2005). Penetration of the leaf surface leads to invagination of the plasma membrane of the infected cell (Snetselaar and Mims, 1993, 1994). While growing inside the plant, fungal hyphae are always surrounded by the plant plasma membrane and upon disease progression the fungal hyphae grow intra- and intercellularly (Banuett and Herskowitz, 1996; Doehlemann et al., 2008b).

First symptoms of *U. maydis* leaf infection become visible already 24 hours post infection (hpi) when some epidermal cells undergo cell death (Doehlemann et al., 2008b). Two days post infection (dpi), the fungal hyphae begin to proliferate, branch intracellularly and move towards the bundle sheath cells (Figure 2B). At this time point, most of the infected plant cells still appear normal except that their chloroplasts start to over-accumulate starch granules (Snetselaar and Mims, 1994). The symptom development in maize leaves infected by *U. maydis* is accompanied by a downregulation of the photosynthetic apparatus and a loss in chlorophyll content (Doehlemann et al., 2008a; Horst et al., 2008). The photosynthesis pigment chlorophyll as well as its accessory pigments, the carotenoids are localized inside chloroplasts (Randolph, 1922). Chloroplasts are double-membrane-enclosed organelles that contain a third membrane system, the thylakoids (Menke, 1962). Photosynthesis pigments are embedded inside thylakoid membranes. Inside the mesophyll of mature C_4 plants, thylakoids are furthermore organized in grana by forming stacks of several thylakoid membranes (Kirchanski, 1975).

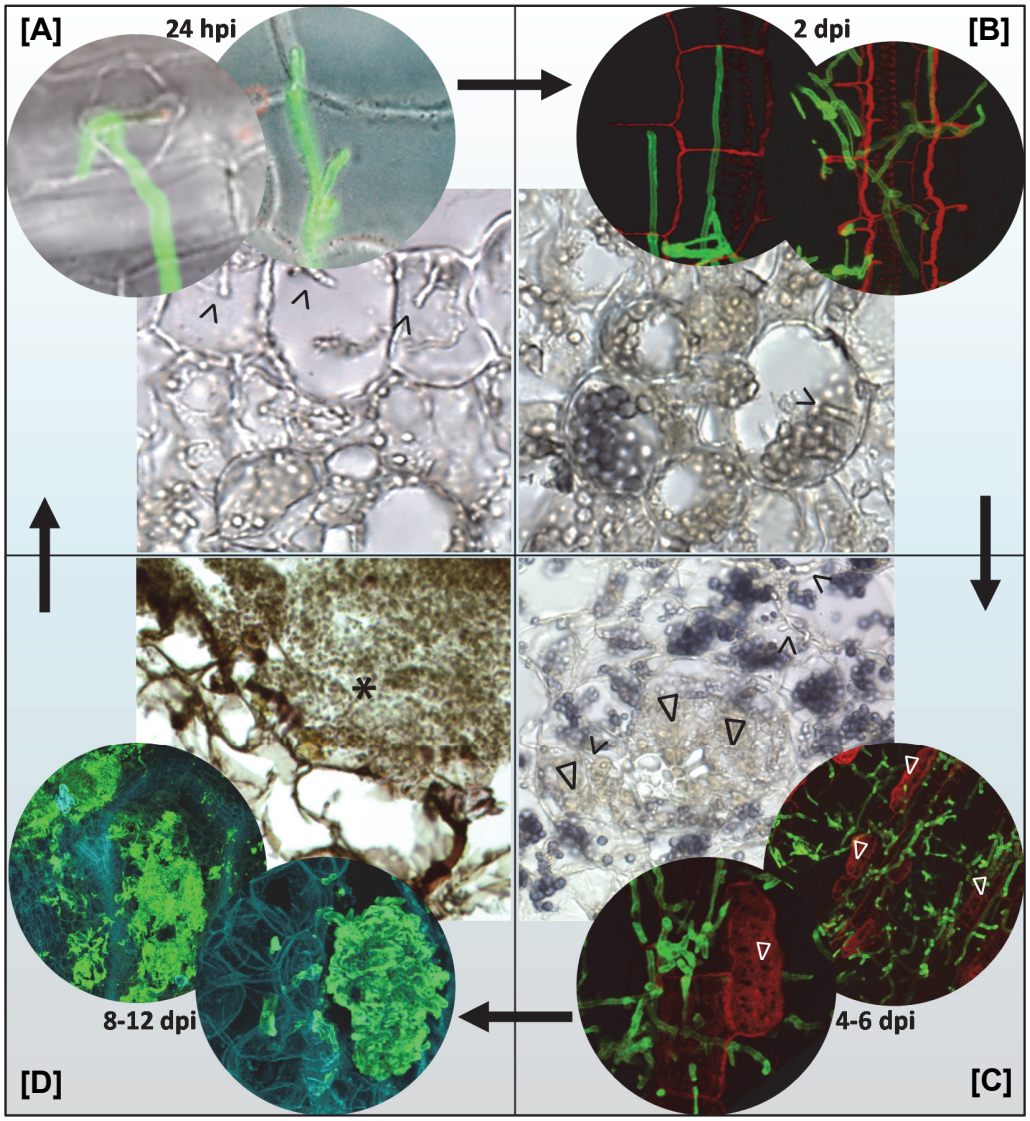

Figure 2: Overview of the *U. maydis* disease progression on the cellular level in maize seedling leaves. Transversal sections and confocal projections show the main stages of infection in which **[A]** *U. maydis* hyphae penetrate the plant surface (24 hpi), **[B]** the invasive hyphae branch and grow towards the bundle sheath cells (2 dpi), **[C]** tumor cells are produced after 4 dpi and hyphae show strong proliferation **[D]**. Fungal aggregates are formed inside the maturing tumor at 8–13 dpi.
> indicate fungal hyphae, Δ indicate tumor cells, * indicates spore aggregate; green staining: hyphae in confocal projections stained by WGA-AF488; red staining: Plant cell walls in confocal projections stained by propidium iodide. Figure from Matei and Doehlemann (2016).

Tumor formation is initiated on the cellular level as early as 4 dpi but cannot be seen macroscopically at this time point (Figure 2C; Doehlemann et al., 2008a). The first tumors are macroscopically visible 5 dpi which is followed by the production of anthocyanins (Banuett and Herskowitz, 1996; Hanna, 1929). Furthermore, fungal hyphae are associated to the site of tumor development indicating a connection between fungal

proliferation and tumor induction (Banuett and Herskowitz, 1996; Doehlemann et al., 2008b). The leaf tumor development involves both, cell enlargement as well as cell division but has not yet been related to any specific cell types (Banuett and Herskowitz, 1996; Callow and Ling, 1973). Upon maturation of a tumor, the plant cells have increased in size 8 dpi and fungal hyphae have undergone substantial branching at the tip which has been described as the beginning of teliospore formation (Figure 2D; Banuett and Herskowitz, 1996). Inside the matured tumor, fungal cells can proliferate intracellularly. However, in most of the cases they form large aggregates inside the apoplast which are surrounded by a mucilageous layer and heavily exceed the size of a plant cell (Doehlemann et al., 2008b; Snetselaar, 1994; Tollot et al., 2016). The shape of the fungal cells changes towards a fragmented, rounded morphology, followed by spore wall maturation leading to an echinulated, yellow-brown and later dark brown appearance of the spores which mainly perform dispersal of the pathogen inoculum (Figure 2D; Banuett and Herskowitz, 1996; Begerow et al., 2006).

The study of tumor formation in anthers revealed that the fungus is present in the epidermal cell layer within the first two days of colonization (Gao et al., 2013). After penetration of anthers the fungus spreads sub-epidermally and perturbs the cell fate of distinct cell layers in order to change anther lobe structure and induce tumor formation by changing cell fate (Gao et al., 2013). In contrast to leaves where the fungus needs to reinitiate cell cycle activity, *U. maydis* alters ongoing cell division patterns in the sub epidermal anther cells and does therefore not act as an oncogenic agent that induces cell division but forms passive tumors utilizing ongoing cell division processes (Gao et al., 2013).

The transcriptional adaptations and responses of both, maize plant and fungus during establishment of this biotrophic interaction have been extensively studied in the past (Basse, 2005; Doehlemann et al., 2008a; Skibbe et al., 2010). This research revealed strong changes in gene expression of both organisms which are primarily related to pathogenicity and immune reactions. Overall, independent of the organ in which tumors are induced, the fungus proliferates in aggregates leading to the formation of teliospores which is orchestrated by the transcriptional masterregulator ROS1 (Tollot et al., 2016).

1.3 The plant innate immune system

To fend off herbivores and invading pathogens plants bear preformed surface characteristics such as thorns or hairs, wax layers, secondary metabolites, anti-microbial enzymes and rigid cell walls (Heath, 2000; Muthamilarasan and Prasad, 2013). Beyond these preformed barriers, effective immune responses are essential for the defense against pathogens and therefore crucial for plant survival after pathogen attack. Plants have developed a sophisticated signaling system in order to mediate adequate immune responses depending on the lifestyle of the invader. This system is in part linked to two main signaling routes depending on the defense hormones, salicylic acid (SA) and jasmonic acid (JA) (Dong, 1998). These two hormonal immune response pathways antagonize each other with SA signaling being induced upon biotrophic pathogen attack and JA being induced during necrotrophic attack (Glazebrook, 2005). While SA signaling induction leads to activation of reactive oxygen species (ROS) and programed cell death around the infected area (hypersensitive response, HR), JA signaling does not induce cell death but leads to the secretion of antimicrobial metabolites that fend off the invading pathogen (Morel and Dangl, 1997; Turner et al., 2002).

Due to the various modes of pathogen contact, every plant cell needs to be able to effectively recognize potential pathogens in order to initiate immune responses. In contrast to vertebrates which bear an adaptive immune system consisting of mobile systemic immune cells and antigens that together form an immunological memory, plants possess a local, multilayered innate immune system (Jones and Dangl, 2006; Nuernberger et al., 2004). The first layer consists of cell surface-localized transmembrane proteins, the pattern/pathogen recognition receptors (PRRs), which recognize evolutionary conserved microbial molecules, the pathogen- or microbe-associated molecular patterns (PAMPs/MAMPs), and initiate the so-called pattern triggered immunity (PTI) (Figure 3; Boller, 1995; Boller and Felix, 2009; Felix et al., 1999; Monaghan and Zipfel, 2012). In the model plant *Arabidopsis thaliana*, the best studied MAMPs are the bacterial flagellin epitope flg22, that is recognized by the MAMP-receptor FLAGELLIN SENSING2 (FLS2) (Gomez-Gomez and Boller, 2000), the bacterial elongation factor thermo unstable (EF-Tu) and its corresponding receptor EF-Tu RECEPTOR (EFR) (Zipfel

et al., 2006) as well as the fungal and oomycete cell wall component chitin and its cognate receptor CHITIN ELICITOR RECEPTOR KINASE1 (CERK1) (Miya et al., 2007). The perception of MAMPs leads to activation of their cognate PRRs and potential co-receptors such as BAK1 for FLS2 and EFR (Figure 3; Couto and Zipfel, 2016; Jones and Dangl, 2006; Monaghan and Zipfel, 2012).

Other receptors can perceive damage-associated molecular patterns (DAMPs) (Figure 3; Boller and Felix, 2009; Boller and He, 2009; Chisholm et al., 2006). DAMPs are plant-derived signals which are released during pathogen attack (Boller and Felix, 2009; Brutus et al., 2010). The DAMP receptor WALL-ASSOCIATED KINASE 1 (WAK1) is a receptor like kinase (RLK) that perceives oligogalacturonides which are cell wall fragments that are released during wounding or pathogen attack (Brutus et al., 2010). A second group of well-studied DAMP receptors are the *Arabidopsis* PLANT ELICITOR RECEPTOR PROTEIN1 and 2 (PEPR1 and PEPR2) RLKs that recognize the AtPeps which are defined to be peptide DAMPS that amplify PTI signaling (Krol et al., 2010; Yamaguchi and Huffaker, 2011; Yamaguchi et al., 2006).

PTI can be divided into two types of responses, early and late defense responses. One of the first PTI responses is a change in ion-flux at the plasma membrane leading to a rapid influx of Ca^{2+} that results in the generation ROS (Boller and Felix, 2009). The Ca^{2+} influx also leads to the activation of downstream mitogen-activated protein kinase (MAPK) cascades which further on activate defense-gene expression and transcriptional reprograming to manifest PTI (Boller and Felix, 2009; Couto and Zipfel, 2016; Lee et al., 2015). The late defense responses include the synthesis of defense hormones like SA or JA, which amplify disease resistance signaling and also induce the production of antimicrobial compounds as well as the accumulation of reinforcing cell wall components (Couto and Zipfel, 2016; Lee et al., 2015).

Together with the above-mentioned preformed surface barriers and the PTI signaling system prevents plants from destruction by non-adapted microbial pathogens, leading to the fact that plant disease is rather an exception than the rule in nature (Lipka et al., 2008; Thordal-Christensen, 2003).

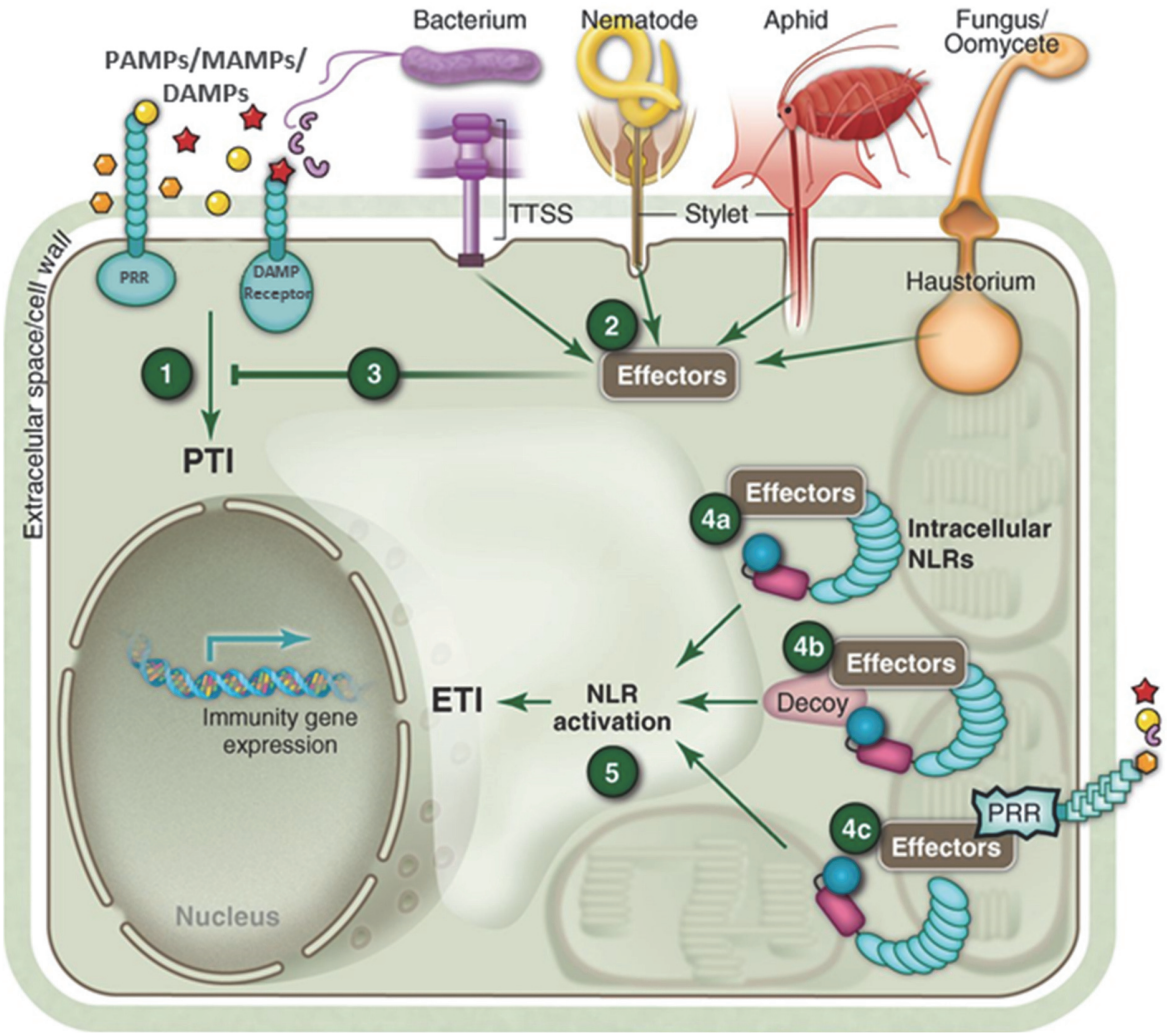

Figure 3: Model of the plant's innate immune system. Pattern/Pathogen recognition receptors (PRRs) or damage-associated molecular pattern (DAMPs) receptors recognize pathogen-/ microbe associated molecular patterns (P-/ MAMPs) or DAMPs the extracellular space of plants which can lead to pattern-triggered immunity, PTI (1). Suppression of this immune level is mediated by pathogens via secretion of effectors into the plant cell (2) that suppress PTI (3). Effectors are either secreted into the extracellular space or into the host cell via a type three secretion system (TTSS) in the case of bacterial attack, via a stylet in the case of nematode or aphid attack or via haustoria/hyphae that are built by most fungal pathogens. Effectors can be recognized by plant intracellular nucleotide-binding/leucine-rich-repeat (NLR) receptors (4) that recognize effectors either directly (4a, guard model), indirectly via a decoy protein (4b, decoy model) or monitor the status of a common effector target (4c, integrated decoy model). NLR activation leads to effector triggered immunity (ETI). Figure modified from Dangl et al. (2013).

In contrast to non-adapted pathogens, adapted pathogens can avoid the early defense responses by injecting effector molecules/ virulence (vir) factors into the host cell which lead to the suppression of PTI and render the plant susceptible again (Jones and Dangl, 2006). In turn, plants have evolved resistance (R) proteins that can mediate effector-

triggered immunity (ETI) through either recognizing the effector molecules or surveying the alterations caused by effectors during pathogen attack (Jones and Dangl, 2006).

The R gene activation following recognition of effectors is induced by the family of intracellular nucleotide-binding/leucine-rich-repeat (NLR) receptors (Cui et al., 2015; Dangl and Jones, 2001). These receptors are grouped into two different classes, depending on their N-terminal domain (Dangl and Jones, 2001; Gay and Gangloff, 2007). The first group is restricted to dicots and consists of NLR proteins that bear a Toll-interleukin 1 receptor (TIR) domain, the so-called TNLs while the second group is present in both, monocots and dicots and bears a coiled-coil (CC) domain, called CNLs (Cui et al., 2015; Jacob et al., 2013).

NLR receptors can recognize effectors either directly or indirectly through the surveillance of their activities (Cui et al., 2015). The process of indirect recognition is currently described by three different models, the guard model, the decoy model and the integrated decoy model (Figure 3; Cesari et al., 2014; Wu et al., 2015). In the guard and decoy recognition model NLR receptors either guard a protein that is an actual effector target or they guard a protein that mimics an effector target (decoy). The interaction of the effector with the guarded protein or the protein mimic is then sensed by the NLR receptor and defense responses are activated (Dodds and Rathjen, 2010; Hann et al., 2010; Mackey et al., 2003). In the integrated decoy model the decoy effector target is integrated into the structure of the NLR receptor and therefore a direct part of it (Cesari et al., 2014; Jones et al., 2016).

ETI amplifies the PTI-triggered antimicrobial defense responses and very often leads to localized plant cell death (HR) together with systemic immunity (systemic acquired resistance, SAR; Fu and Dong, 2013). HR restricts the growth and spread of biotrophic pathogens (Dangl and Jones, 2001; Fu and Dong, 2013). This can lead to priming of whole tissues for following microbial attacks (Conrath et al., 2015).

The first (PTI) and second (ETI) layers of the plant's immune system together with their matching partners (MAMPs/DAMPs and effectors) on the other side, reflect the evolutionary arms race between plants and pathogens which is described as the Zig-zag

model (Jones and Dangl, 2006). This model defines a constantly ongoing evolution of new effectors. This process avoids recognition by the plant and thereby maintains effector-triggered susceptibility (ETS).

1.3.1 Effectors in plant-pathogenic interactions

Effectors are defined to be either proteins or toxic secondary metabolites that aim to manipulate the host plant depending on the nature of the plant-microbial interaction (Lo Presti et al., 2015; Selin et al., 2016). They bear a high variety in structure and function that often goes along with a lack of defined functional domains and their expression is restricted to the stage of pathogenic infection (Okmen and Doehlemann, 2014; Stergiopoulos and de Wit, 2009). The delivery of effectors to their scenes of action, either the apoplast or the plant cell, can as well be very diverse and again depends on the plant-microbe interaction (de Wit et al., 2009; Lo Presti et al., 2015). Effector proteins can bear a signal peptide for secretion via the endoplasmic reticulum (Lo Presti et al., 2015). Some effector proteins such as the *P. infestans* effector proteins lack a secretion signal but contain a defined N-terminal RxLR motif which is required for their translocation into the host cytoplasm (Whisson et al., 2007). Different hypotheses for effector translocation via host endocytosis are under strong debate and the process of cellular effector uptake is to date lacking strong datasets (Wawra et al., 2013).

Biotrophic fungi develop a close interaction with their host in which the fungal hyphae is in close contact with the invaginating plant plasma membrane and in some cases specialized fungal feeding sites, so-called haustoria, are formed that serve as the place of dense effector secretion (Figure 3; de Wit et al., 2009; Panstruga and Dodds, 2009; Selin et al., 2016). Plant infectious bacteria like *Pseudomonas syringae* on the other hand deliver effector molecules into host cells through puncturing them via their type III secretion system (TTSS) (Figure 3; Dangl et al., 2013; Navarro et al., 2008).

To promote disease susceptibility, common effector targets include plant signaling and defense components in the first row (Lo Presti et al., 2015). Herein, plant defense components like proteases can be inhibited by effectors as it is done by Pit2 (protein involved in tumors 2) in the *U. maydis* – maize interaction (Mueller et al., 2013). Plant

immune receptors can be inactivated in order to prevent defense immune signaling upon microbial recognition which was shown for several bacterial effectors (Göhre and Robatzek, 2008). *P. syringae* for example was found to inject effectors such as AvrPto which functions as a general kinase inhibitor for FLS2 and EFR to inhibit PTI signaling (Xiang et al., 2008). The *Cladosporium fulvum* fungal effector protein Ecp6 prevents MAMP recognition by sequestration of chitin to prevent activation of the chitin receptor CERK1 (Sanchez-Vallet et al., 2013). Plant hormone defense signaling pathways like SA and JA signaling are also targeted by effectors such as *P. syringae* HopX1 (Hrp outer protein X1) or HopM1 showing that effectors influence phytohormonal pathways (Gimenez-Ibanez et al., 2014; Hann et al., 2014; Kazan and Lyons, 2014). The presence of effectors can furthermore be sensed by the second layer of plant defense signaling, the resistance (R) proteins (Dangl and Jones, 2001).

1.3.2 Effector proteins in the *U. maydis* – maize interaction

In the *U. maydis* – maize interaction, the establishment of pathogenesis and tumor formation is dependent on the secretion of effector proteins which are crucial for the overcome of the plant's innate immune system (Kämper et al., 2006). During plant invasion an interaction zone between plant and fungus is built; the so-called biotrophic interface. At the very early infection time point of 12 hpi plant defense gene expression is initiated which is most likely due to recognition of the fungus via the plant's MAMP receptors (Doehlemann et al., 2008a). These defense responses are repressed at 24 hpi allowing for establishment of fungal biotrophy and virulence which is mediated by the secretion of effector proteins (Doehlemann et al., 2008a; Kämper et al., 2006).

Analysis of the *U. maydis* genome sequence identified more than 500 genes encoding for effector proteins which were predicted to be secreted out of which 168 were predicted to be putative enzymes (Kämper et al., 2006; Mueller et al., 2008a; Mueller et al., 2008b). Including potential effector proteins that are presumed to be unconventionally secreted, *U. maydis* bears in total more than 700 candidate effector proteins out of which 546 bear a secretion signal (Dutheil et al., 2016). The enzymes are involved in modification of either the plant or fungal cell wall, in degradation of other plant components or they might serve as extracellular metabolic enzymes which interfere in plant metabolic pathways (Mueller

et al., 2008b). Seventy percent of all proteins which were predicted to be secreted by *U. maydis* are not ascribed to any discrete function, yet. Twenty percent of these proteins are arranged in 22 gene clusters of different sizes, most of which were found to be upregulated during tumor development while five of these gene clusters are functionally involved in tumor formation (Dutheil et al., 2016; Kämper et al., 2006). Nevertheless, it is still a major undertaking in the field to elucidate the exact functions of most of the *U. maydis* effector proteins. These proteins might be involved in suppression of plant defense or in reprogramming the plant's metabolism for tumor induction and feeding of the fungus. Some of the *U. maydis* effector genes have been studied in great detail due to its good amenability towards genetic modification (Kämper, 2004; Selin et al., 2016).

To date, five effector proteins, Pep1, Pit2, Cmu1, Tin2 and See1 have been characterized and pinned down to their scene of action. Pep1 (protein essential for penetration 1) was identified to be a secreted effector protein acting in the apoplast during the very early stage of infection (Doehlemann et al., 2009). It was furthermore identified to interact with the maize peroxidase POX12 in order to prevent ROS generation and following plant defense initiation (Hemetsberger et al., 2012). Pit2 (protein involved in tumors 2) was identified to function in the early stages of infection through the inhibition of cysteine proteases to prevent SA signaling (Doehlemann et al., 2011; Mueller et al., 2013). The *U. maydis* effector Cmu1 (chorismate mutase 1) is translocated into host cells and was shown to act as a chorismate mutase leading to the reduction of SA biosynthesis (Djamei et al., 2011). Further changes of the host's physiology are promoted by the Tin2 (tumor inducing 2) effector which induces anthocyanin accumulation during *U. maydis* infection and thereby promotes virulence through suppression of defense lignin biosynthesis (Brefort et al., 2009; Tanaka et al., 2014). Recently, See1 (seedling efficient effector 1) was the first organ-specific *U. maydis* effector that was characterized (Redkar et al., 2015a; Schilling et al., 2014). See1 was found to be required for tumor formation in vegetative plant tissue via its interaction with maize SGT1 (suppressor of G2 allele of *skp1*) (Redkar et al., 2015a). SGT1 was shown to be a cell cycle progression factor and essential part of the plant's innate immune system (Dubacq et al., 2002; Shirasu, 2009).

U. maydis effector proteins can be classified into core effectors that are required for full virulence on the one hand and organ/tissue-specific effectors on the other hand. The core effector Pep1 for example is defined to be conserved among biotrophic smut fungi and hereby playing a crucial role for virulence (Hemetsberger et al., 2015). In contrast, See1 as a highly diversified effector among smuts has an organ-specific function in *U. maydis*-infected maize leaves but is not required for full virulence (Redkar et al., 2015b).

1.4 Organ and cell type specificity in the *U. maydis* – maize interaction

The plant infection process goes along with transcriptional changes related to the attenuation of defense responses, suppression of cell death and physiological changes in primary and secondary metabolism of the plant (Doehlemann et al., 2008a). In comparison to other members of the Ustilaginales, *U. maydis* is the only smut fungus that can induce tumors in all aerial parts of the plant, including leaves. The closely related smut fungi *Sporisorium reilianum* and *Ustilago hordei* exclusively cause disease symptoms in the inflorescences (Laurie et al., 2012; Schirawski et al., 2010). Interestingly the genomes of these three fungi show high synteny but differ significantly concerning the sequences of their effector genes which may cause the different pathogenesis patterns exhibited by these fungi (Laurie et al., 2012; Schirawski et al., 2010).

Transcriptome analysis of three different *U. maydis*-infected maize organs (seedling leaf, adult leaf and tassel; Figure 4) at different time points during infection revealed the gene expression profiles leading to tumor formation (Skibbe et al., 2010). In maize seedling leaves, two thirds of all regulated genes were downregulated whereas contrarily, in adult leaves more genes were upregulated than downregulated (Skibbe et al., 2010). Surprisingly, in tassels only 7 % of the maize transcripts were altered during *U. maydis* infection which indicates that plant organs show defined transcriptional responses to *U. maydis* infection and that most of the transcriptional reprogramming in maize organs occurs in the plant leaves (Figure 4; Skibbe et al., 2010). Interestingly, only 21 % of the *U. maydis* effector show similar expression patterns in seedling leaves, adult leaves and tassels whereas 45 % of the effectors are organ-specifically expressed (Skibbe et al., 2010). These findings strongly indicate an organ-specific orchestration of *U. maydis* effectors (Figure 4; Skibbe et al., 2010).

The finding of organ-specific effectors points to a defined and tailored adjustment of the fungus to the respective tissues that it colonizes (Schilling et al., 2014). The fungus seems to respond to individual types of plant tissue with a specific effector combination in order to reprogram it for its needs (Djamei and Kahmann, 2012; Schilling et al., 2014; Skibbe et al., 2010).

As tumor formation occurs in all aerial parts of the plant, including leaves, tassel and ear, the fungus has to cope with a diversity in tissue structure and physiology while overcoming the maize's immune system and reprogramming its metabolism (Doehlemann et al., 2008a; Skibbe et al., 2010). Therefore, the fungus needs a distinct and adaptable set of infection weapons that enables it to induce tumors in the different plant organs. Interestingly, the fungus deploys less tassel-specific effector genes than leaf-specific effector genes which might be due to the fact that the flower tissue is actively proliferating tissue in contrast to leaf tissue and thereby easy to modulate for tumor development (Schilling et al., 2014; Skibbe et al., 2010). In a screen for organ-specific effector genes performed in this study, candidate genes have been identified that contribute to virulence in an organ-specific manner (Schilling et al., 2014).

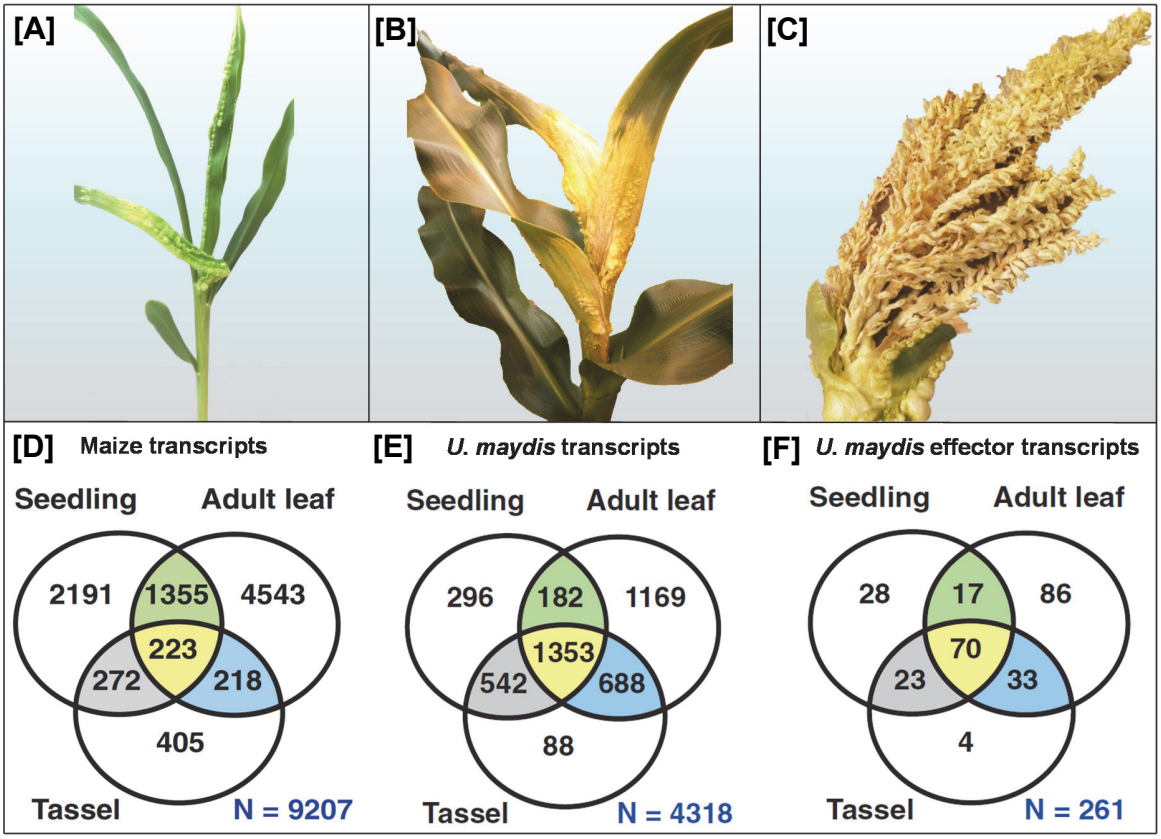

Figure 4: Analysis of differentially expressed maize and *U. maydis* genes in infected versus mock-infected tissue (**[A]** seedling, **[B]** adult leaf and **[C]** tassel) at 3 dpi. Venn diagrams display transcript sets of analyzed genes. **[D-F]** Venn diagrams showing organ-specific gene expression (white), transcripts common to all organs (yellow), and shared between organs (green, seedling leaf and adult leaf; blue, adult leaf and tassel; gray, seedling leaf and tassel). **[D]** Maize transcripts detected at 3 dpi and, **[E]** *U. maydis* transcripts found at 3 dpi and **[F]** *U. maydis* genes encoding secretome proteins at 3 dpi. Figure modified from Skibbe et al. (2010).

1.5 Physiological changes during *U. maydis*-induced leaf tumor formation

Successful colonization and tumor induction in leaves is restricted to young meristematic sink tissue and does not occur in differentiated source leaves (Wenzler and Meins, 1987). Inside young, emerging maize leaves cell specification has taken place but cells have not matured yet (Facette et al., 2013; Li et al., 2010; Nelissen et al., 2016). The basal leaf region of a maturing maize leaf is a photosynthetic sink tissue consisting of very young tissue that shows transcriptomic activity that is mainly linked to DNA synthesis, cell wall synthesis and hormone signaling (Li et al., 2010).

During tumor formation, infected areas remain in their sink stage (Doehlemann et al., 2008a; Horst et al., 2008). Photosynthetic development and productivity is at this timepoint not established and therefore also plastids have not yet matured into chloroplasts (Kirchanski, 1975; Leech et al., 1973). Processes that are usually transcriptionally induced upon leaf maturation such as the light reaction, the Calvin cycle, photorespiration and sugar synthesis lack induction in infected leaves of the same age indicating that the juvenile sink stage is maintained (Doehlemann et al., 2008a). One further hint for the maintenance of the juvenile stage is the lack of C_4 photosynthesis establishment in infected leaves which continue C_3 photosynthesis (Horst et al., 2008). An additional characteristic of juvenile sink tissue is enhanced content of free hexose compared to adult leaves that correlates with the increase in free hexose in tumorous tissue (Doehlemann et al., 2008a). This might be due to the active proliferation inside this tissue but also serve as a nutritional source for the fungus. It is however not understood if *U. maydis* has an influence on development or reprogramming of cellular organelles and energy storage processes.

To form tumors in leaves *U. maydis* needs to reinitiate the proliferative capacity of the leaf tissue. This reinitiation is restricted to the region of immature leaf tissue, in which cells still undergo longitudinal expansion (Wenzler and Meins, 1987) and gives a physiological explanation why tumors can only be formed on emerging leaves. In the *U. maydis* – maize interaction, leaf tumors consist of enlarging (hypertrophic) as well as proliferating cells (Callow, 1975; Callow and Ling, 1973). Plant tissue can increase in size via two different strategies, cell expansion or cell division (Kalve et al., 2014; Sablowski and Carnier Dornelas, 2014). Those two processes are generally described to antagonize each other (Green, 1976; Kalve et al., 2014). The process of endoreduplication was found to occur inside expanded, neoplastic maize cells in *U. maydis*-induced tumors (Callow, 1975). Endoreduplication is an alternative form of the cell cycle in which the mitosis step is omitted and thereby cells do not divide but cell ploidy is doubled during each cycle (Nagl, 1976; Wildermuth, 2010). In plants, endoreduplication very often occurs in hypertrophic cells with nurturing functions like the endosperm (Sabelli et al., 2013) and is also commonly described to occur in fruits (Chevalier, 2007) as well as trichomes (Hülskamp

et al., 1994). Endoreduplication has also been described to occur in several biotrophic plant-pathogen interactions including symbiotic as well as parasitic interactions such as arbuscular mycorrhizal fungi, nematodes and powdery mildews (Wildermuth, 2010).

The cell cycle which terminates in mitotic cell division is regulated by a complex, conserved molecular mechanism. It can principally be divided into a DNA synthesis phase (S phase) in which nuclear DNA is duplicated followed by an equal division during the mitosis phase (M phase) leading to two daughter cells (Inzé et al., 1999; Kalve et al., 2014). Cell cycle and the transition throughout its different stages is tightly controlled via a plethora of protein complexes, signaling cascades, transcription factors as well as the hormonal status of the cells (Kalve et al., 2014).

The *U. maydis* effector See1 was found to contribute to tumor formation in vegetative tissue by promoting the reactivation of cell division in vegetative tissue (Redkar et al., 2015a). Interestingly, the maize SGT1 protein was found to be the target of this effector (Redkar et al., 2015a). SGT1 is described to have a diverse spectrum of action in plants among which it is mainly active in vegetative tissue and described to play a major role in disease-resistance pathways (Noel et al., 2007; Shirasu and Schulze-Lefert, 2003). Interestingly, the human SGT1 homolog was found to also act during the cell cycle by assisting the kinetochore formation rendering it thereby essential for the assembly of the mitotic spindle during mitosis phase (Steensgard et al., 2004). However, it was not clarified whether See1 is acting in a cell type-specific manner by reinitiating the cell division of a specific tissue type and whether the re-initiation of cell division in vegetative tissue by See1 is dependent on its interaction with SGT1.

1.6 Cell wall composition and its role in plant immunity

The plant cell wall provides structure and rigidity to shape and strengthen the plant tissue and together with the plant cuticle it forms the first barrier that pathogens encounter during plant infection (Hematy et al., 2009). In order to gain access to the plant tissue pathogens need to break down cell walls. The containing polysaccharides could thereby serve as first carbons sources. Nevertheless, due to their complex structure, those carbon sources might be difficult to access and the invaders simultaneously need to avoid the plant's cell

wall integrity (CWI) sensing system (Nuhse, 2012). The extent of cell wall break-down during pathogenicity mainly depends on the lifestyle of the respective pathogen. While necrotrophic pathogens such as *Botrytis cinerea* bear a broad weaponry of cell wall degrading enzymes leading to an overall cell wall degradation, most of the biotrophic pathogens digest and rearrange cell walls very often only in the area of infection, avoiding the activation of CWI sensing (Nuhse, 2012; Walton, 1994). A search for predictable functional domains in the organ-specific *U. maydis* effectors revealed a strong implication in degradation of cell walls for seedling-specific effector genes (Schilling et al., 2014).

Overall, plant cell walls consist of cellulose microfibrils that are embedded in a matrix of hemicelluloses, pectins, proteins and, in the case of secondary cell walls, additional phenolics/lignins (Figure 5; Carpita and Gibeaut, 1993; Somerville et al., 2004). Cell wall fortification in primary and secondary cell walls can be achieved by the interconnection of cellulose microfibrils with hemicelluloses via hydrogen bonds and by the further interconnection of hemicelluloses with lignin and some pectic polysaccharides (Pauly et al., 2013; Somerville et al., 2004). Cell walls differ in their fine structure depending on the age and type of cell as well as species and accession of the plant (Hazen et al., 2003). In grass species like *Z. mays* the typical primary cell wall contains 25 % cellulose, 55 % hemicellulose and 10 % pectin (Cosgrove, 1997).

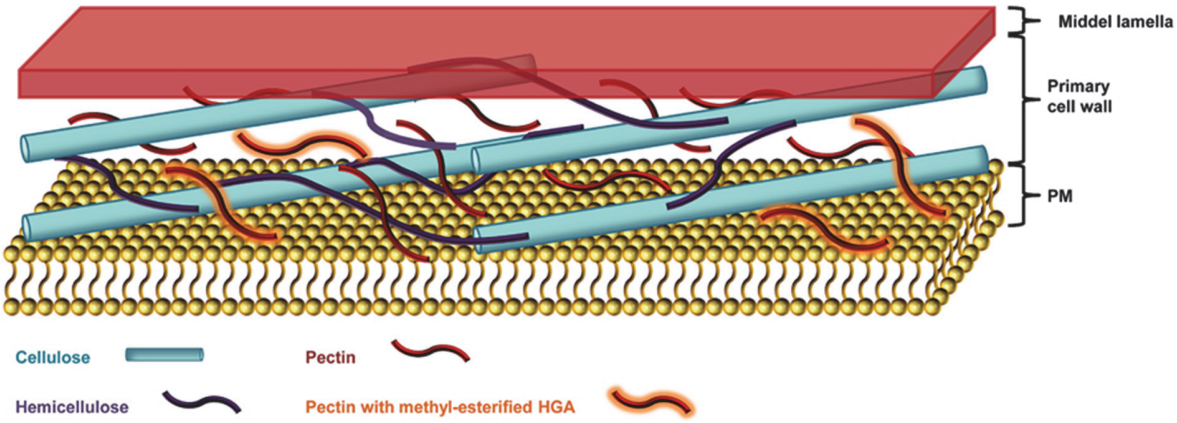

Figure 5: Plant primary cell wall composition. The primary cell wall is located between the plasma membrane and the middle lamella. Primary cell walls generally consist of a network of cellulose micro-fibrils that is interconnected by hemicellulose polysaccharides and pectins. Figure modified from Malinovsky et al. (2014).

Cellulose is the most abundant polymer in nature. It consists of condensed, cristalline ß-(1→4) linked D-glucose units that bear a high recalcitrance and thereby contribute to disease resistance by making cell walls resistant to degradation (Malinovsky et al., 2014).

Hemicelluloses comprise a diverse class of polysaccharides that generally consist of ß-(1→4)-linked glycans with various glycosyl substituents (Scheller and Ulvskov, 2010). They can be classified into four subgroups: (1) Mannan as the most abundant hemicellulose group in the secondary cell wall of gymnosperms, (2) Xyloglucan as the main hemicellulose in dicot primary cell walls, (3) Xylan as the major hemicellulose of dicot secondary walls and of all types of cell walls of the poaceae and (4) Mixed-linkage glucan (MLG) as a homopolymer in poaceae cell walls (Pauly et al., 2013; Pauly and Keegstra, 2010; Scheller and Ulvskov, 2010). The most common form of hemicellulose in dicot and monocot secondary cell walls are xylans which constitute of a ß-(1→4)-linked D-Xyl*p* backbone (Malinovsky et al., 2014). This backbone can be substituted with arabinose or glucuronic acid side chains, called arabinoxylan or glucoronoarabinoxylan (Scheller and Ulvskov, 2010). Further substitution of these arabinoxylans with phenolic acid residues, like ferulic-, p-coumaric or 4-O-methylglucuronic acid permits cross-linking with lignin giving arabinoxylans a structural role in enhancement of cell wall strength (Hartley, 1972). Xylan of maize is strongly substituted with α-L-arabinofuranosyl (Aspinall, 1959; Scheller and Ulvskov, 2010). Cell wall fortifications of hemicelluloses can be broken by the secretion of xylanases during pathogen attack which degrade the xylan backbone into xylose units (Belien et al., 2006). A notable example for degradation of hemicelluloses is the *U. maydis* organ-specific effector gene *um01829* that encodes an α-L-arabinofuranosidase which seems to have a leaf-specific role in cell wall reorganization during tumor formation (Schilling et al., 2014).

Pectins constitute the major cell wall matrix components in primary cell walls and their backbones consist of either homogalacturonan (HGA) or rhamnogalacturonan with a strong implication of HGA in defense response (Malinovsky et al., 2014). During pathogen attack, some fungi secrete endo-polygalacturonases that cleave HGA and thereby disturb cell wall integrity for pathogenic progression (Annis and Goodwin, 1997). The hereby

released oligogalacturonide fragments can simultaneously be sensed by one of the plant cell wall integrity sensors (WAKs) and induce defense responses (Ferrari et al., 2013).

Lignin is a phenolic polymer that bears high recalcitrance due to complex heteropolymer formation. It is produced from the three primary monolignols *p*-coumaryl alcohol, coniferyl alcohol and sinapyl alcohol that lead to the formation of the three phenylpropanoid polymer units, p-hydroxyphenyl (H), guaiacyl (G), and syringyl (S) (Zhao, 2016). The deposition of these three lignin types is individually and temporally regulated depending on the tissue (Santiago et al., 2013). Lignin is furthermore involved in plant defense. Deposition of lignin in response to biotic or abiotic stresses leads to a strengthening of previously unfortified cell walls to limit pathogenic growth (Barros et al., 2015; Sattler and Funnell-Harris, 2013).

There is diverse evidence for cell wall composition changes upon pathogen attack (Bellincampi et al., 2014; Chowdhury et al., 2014; Douchkov et al., 2016; Lionetti et al., 2015). The *U. maydis* effector Tin2 was found to alter the lignin biosynthesis pathway towards an accumulation of anthocyanin thereby avoiding increased lignification of vascular tissue (Tanaka et al., 2014). Tissue-specific cell wall changes play an important role during tumor development in the *U. maydis*-maize interaction. New primary cell walls are synthesized in dividing, hyperplasic tissue whereas older cell walls inside the mesophyll need to be loosened and expand during hypertrophic tumor cell development. Nevertheless, the exact cell wall changes during tumor formation have not yet been resolved on the cellular level.

1.7 Aims of the Study

(1) One major aim of the following study was the identification and characterization of organ-specific, in particular tassel- and leaf-specific *U. maydis* effector proteins based on a previous transcriptome analysis that was done by Skibbe et al. (2010). To understand how tissue-specific effectors contribute to fungal virulence this work aimed at the identification of the *in planta* target of the seedling-specific effector protein, Um01690 (Small tumors in seedling 1, Sts1).

(2) To understand the functional basis of organ-specific effectors, detailed understanding of cellular processes in tumorigenesis is required. Since most organ-specific effectors are associated to leaf tumors, the second major part of this study aimed at the elucidation of tumor cell origin by tracking the cell type-specific *U. maydis*-induced changes in leaf tissue. In line with that, histological methods together with biochemical tissue analyses were used to investigate physiological and cell morphological changes upon leaf tumor development. A further aim of this part of the study was the identification of cell type-specific effector genes which was addressed by use of the leaf-specific *U. maydis* SG200Δsee1 strain (Redkar et al., 2015a) in histological tissue sections.

(3) To study *U. maydis*-induced cell type-specific processes on the molecular level, a cell type-specific laser capture microdissection approach and subsequent RNAseq analysis was performed. This study aimed at the identification of fungal effectors that are expressed in a cell type-specific context.

2 Results

2.1 Identification of organ-specific effectors in the *U. maydis* – maize interaction

One goal of this thesis was the identification organ-specific effector genes. In collaboration with Lena Schilling, twenty *U. maydis* effector candidate genes were selected based on the organ-specific transcriptome data published by Skibbe et al. (2010). This candidate gene selection approach aimed at identifying fungal effectors that contribute to virulence depending on the colonized host organ. The group of candidate effector genes was selected based on their significantly higher transcriptional regulation in either seedling leaves or tassel. To verify organ-specific expression of effector genes observed by Skibbe et al. (2010) the set of candidate genes was retested via qRT-PCR for significant expression differences in either seedling leaf or tassel (Figure 6; Schilling et al., 2014). The expression of the candidate effector genes was tested in the stationary phase of axenic culture, 3 dpi (reflecting an early stage of infection before the onset of fungal proliferation) as well as 9 dpi (when tumor formation is established) in infected seedling leave tissue as well as tassel (Figure 6). This screening resulted in a group of twenty effector candidate genes that were chosen for further analysis. Seventeen of these candidate genes were leaf-induced effector candidates and thereby putatively leaf-specific and three effector candidate genes were tassel-induced (Figure 6).

The set of twenty candidate genes was further assessed using the PEDANT software tool (MIPS; http://pedant.gsf.de/; Walter et al., 2009) in order to search for predictable functional domains. This analysis revealed putative functional domains in six of the twenty candidate effector proteins including a xylanase, an endoglucanase, a beta-1,6-glucanase and an alpha-L-arabinofuranosidase (Table 1; Schilling et al., 2014).

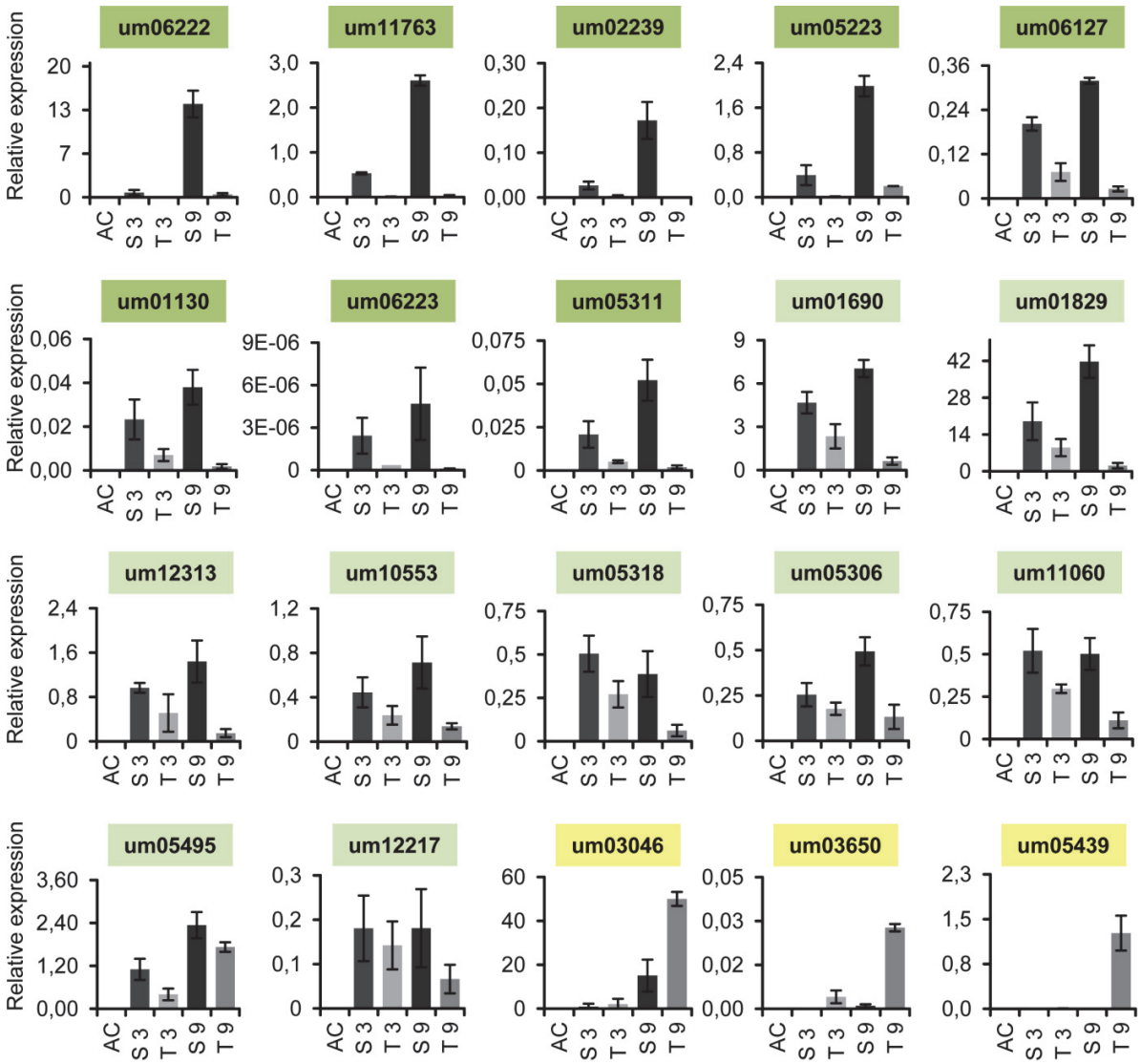

Figure 6: Expression profile of the organ-specific *U. maydis* effector candidate genes selected for further analysis

Gene expression of the candidate genes was assessed relative to the housekeeping gene *ppi* in axenic culture (AC), in seedlings at 3 dpi (S 3), in tassel at 3 dpi (T 3), in seedlings at 9 dpi (S 9) and in tassel at 9 dpi (T 9). Three independent biological replicates of infection experiments and subsequent cDNA synthesis were performed. Candidate genes marked in dark green are seedling-specifically expressed at both time points, candidate genes marked in light green are seedling-specifically expressed at one time point and candidate genes marked in yellow are tassel-specifically expressed. Figure from Schilling et al. (2014).

A basic local alignment search tool (BLAST; https://blast.ncbi.nlm.nih.gov/Blast.cgi; Altschul et al., 1997) analysis was made for each of the twenty effector candidate genes in order to find the homologues in the closely related species *S. reilianum* and *U. hordei* (Table 1; Schilling et al., 2014). This was followed by a sequence similarity analysis using the ClustalW2 sequence alignment program (ClustalW;

http://www.genome.jp/tools/clustalw/; Larkin et al., 2007). This analysis aimed for the identification of high sequence divergences due to newly evolved effector functions that would enable *U. maydis* to cause tumors in leaves. Thirteen of the analyzed effector candidate genes had a sequence similarity of less than 50 % in comparison to their orthologues (Table 1; Schilling et al., 2014). Furthermore, for the tassel-induced *U. maydis* effector candidate gene *um03046* no homologous genes were found in *S. reilianum* or *U. hordei* while the effector candidate gene *um03650* lacked a homologous gene in *S. reilianum* (Table 1).

Table 1: Organ-specific *U. maydis* effector candidate genes, their putative function and sequence similarity towards orthologous species
Leaf-induced (green) as well as tassel-induced (yellow) effector candidate genes are listed with their putative protein function predicted by the PEDANT software, their sequence similarity towards the orthologous species *S. reilianum* and *U. hordei.* Table modified from Schilling et al. (2014).

	Gene	Putative function	Similarity *S. reilianum* (%)	Similarity *U. hordei* (%)
Leaf induced	*um01130*	metal ion binding	62	58
	um06222	uncharacterized protein	14	19
	um12217	**uncharacterized protein**	**19**	**20**
	um06223	**uncharacterized protein**	**13**	**15**
	um12313	uncharacterized protein	40	38
	um11763	esterase (xylanase)	54	54
	um10553	uncharacterized protein	34	15
	um05306	**uncharacterized protein**	**32**	**31**
	um06127	uncharacterized protein	14	26
	um05311	**uncharacterized protein**	**22**	**23**
	um05318	**uncharacterized protein**	**31**	**19**
	um11060	**uncharacterized protein**	**16**	**16**
	um05495	endoglucanase	47	44
	um02239 (Δsee1)	**uncharacterized protein**	**40**	**34**
	um01690 (Δsts1)	**uncharacterized protein**	**45**	**46**
	um01829	**alpha-L-arabinofuranosidase**	**81**	**72**

	um05223	beta-1,6-glucanase	67	64
Tassel	*um03046*	uncharacterized protein	-	-
	um03650	**uncharacterized protein**	**-**	**26**
	um05439	**chitin-binding protein**	**63**	**63**

2.2 Characterization of organ-specific effector candidate mutants

In collaboration with Lena Schilling, deletion mutants for each of the candidate effector genes were generated in the solopathogenic *U. maydis* SG200 background (Kämper et al., 2006). To assess the organ-specific contribution to virulence, each effector gene deletion mutant was tested for virulence on both, seedling leaves and tassel in comparison to SG200 (Figure 7; Table 2; Schilling et al., 2014). Seedling leaf infection symptoms were scored 12 dpi and tassel disease symptoms were scored 14 dpi as described in Redkar and Doehlemann (2016b). Disease ratings for all knockout strains that had defect in virulence in either leaf or tassel, or both, are shown in Figure 7. The virulence defects that were observed for the organ-specific effector knockout mutants were reduced none of them was apathogenic (Figure 7). For statistical classification of the virulence defects, a disease index for the effector knockout mutants was calculated using an unpaired *t*-test (Table 2). The strongest reduction in virulence was observed for the tassel-specific effector knockout mutant *um03650* with a disease index of 0.64 ± 0.06 and the leaf-specific effector knockout mutant *um02239* with a disease index of 0.65 ± 0.05 (Table 2). The deletion of *um06223* and *um12217* led to a virulence reduction in both, seedling as well as tassel (Figure 7; Table 2). Those two effectors are therefore required for full virulence in both organs and not considered as organ-specific effector genes any more. In order to proof that the observed virulence defects were due to the respective gene for which the effector knockout strain was generated, complementation strains were generated and assessed for restoration of virulence to wild type levels in the respective organ infection (Figure 7).

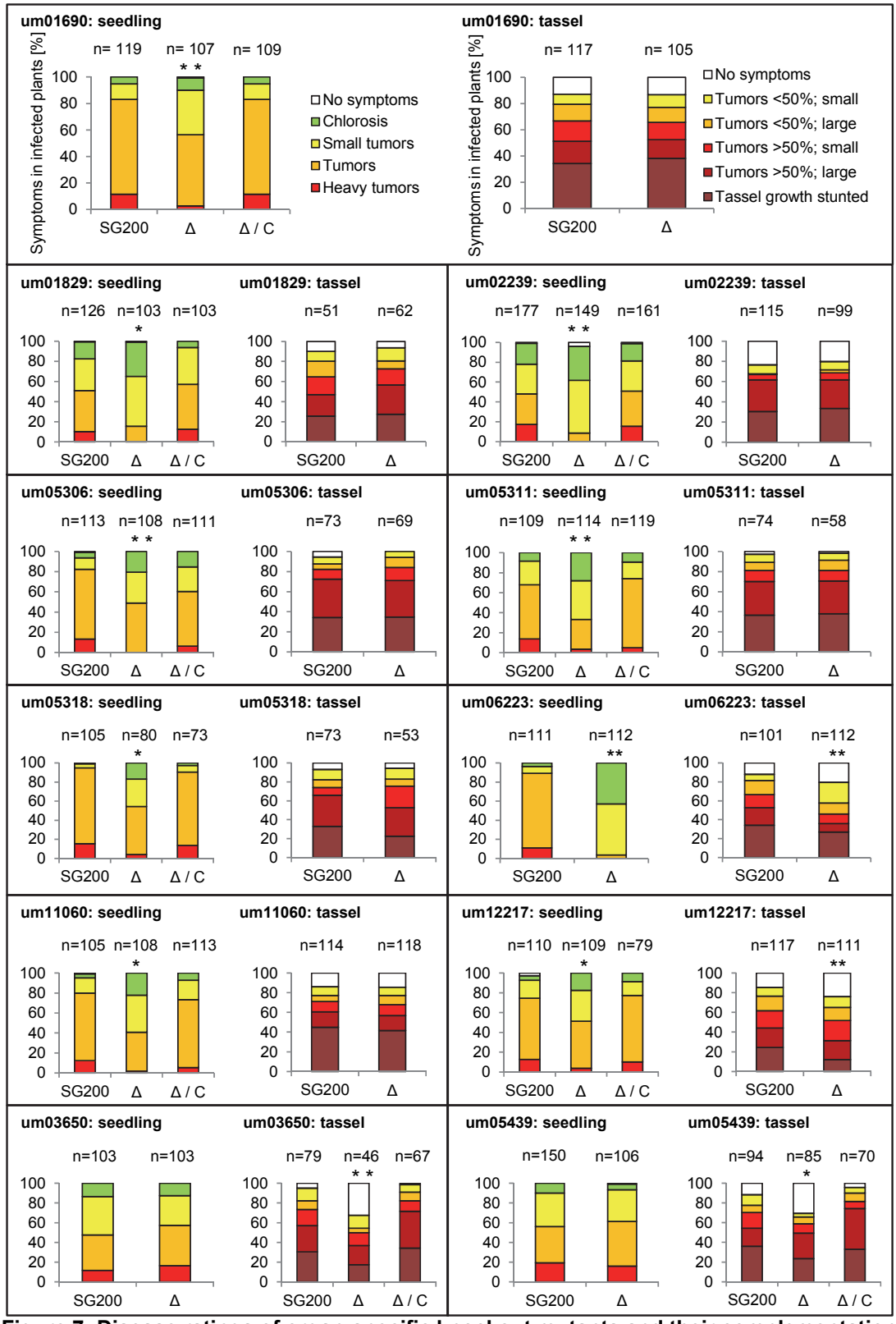

Figure 7: Disease ratings of organ-specific knockout mutants and their complementation strains in seedling and tassel infections

Disease symptom classification was done 12 dpi for seedling infections and 14 dpi for tassel infections, respectively. SG200: solopathogenic *U. maydis* progenitor strain; Δ: deletion mutant for the respective candidate gene; Δ/C: strain bearing genetic complementation of the respective deletion mutant; n: number of infected plants; P-values were calculated using the unpaired student's t-test; *p ≤ 0.01; **p ≤ 0.001. Three independent biological replicates of infection experiments were performed with the same results. Figure from Schilling et al. (2014).

Table 2: Disease indices for effector knockout mutants with virulence reduction
List of leaf- and tassel-specific effector knockout mutants and their corresponding disease indices. Effector candidate genes investigated in this study are marked in bold. Disease indices reflect severity of symptoms caused by the knock out strains in relation to disease severity caused by SG200. SG200 symptoms were set to 1; WT = wild type virulence pattern; reduced = reduced virulence pattern. Table modified from Schilling et al. (2014).

Gene	Virulence leaf	Disease index leaf	Virulence tassel	Disease index tassel
***um01690* (sts1)**	Reduced	0.86 ± 0.02	WT	1.01 ± 0.04
um01829	Reduced	0.69 ± 0.13	WT	1.03 ± 0.22
***um02239* (see1)**	Reduced	0.65 ± 0.05	WT	1.03 ± 0.04
um05306	Reduced	0.76 ± 0.06	WT	1.04 ± 0.11
um05311	Reduced	0.72 ± 0.15	WT	1.00 ± 0.05
um05318	Reduced	0.75 ± 0.12	WT	0.98 ± 0.02
um06223	Reduced	0.45 ± 0.11	Reduced	0.77 ± 0.04
um11060	Reduced	0.72 ± 0.07	WT	0.98 ± 0.03
um12217	Reduced	0.83 ± 0.1	Reduced	0.80 ± 0.04
um03650	WT	1.08 ± 0.26	Reduced	0.64 ± 0.06
um05439	WT	1.03 ± 0.09	Reduced	0.84 ± 0.09

In order to exclude that deletion of the respective candidate gene has any influence on saprophytic growth and might therefore influence disease progression *in planta*, vegetative growth of the *U. maydis* effector knockout strains with a reduction in virulence was assessed on various stress media (Figure 8; Schilling et al., 2014). Strains were plated in a serial dilution on CM plates and CM plates containing several stress factors and incubated for 2 days at 28 °C. Cell wall stress was induced by addition of calcofluor or congo red, oxidative stress was induced by addition of H_2O_2 and osmotic stress was induced by addition of sorbitol or NaCl to the CM media. Growth of deletion mutants on stress media was compared to the growth of SG200 and to the growth of the knockout strains on normal CM growth media. This analysis revealed that all deletion strains except

Δum06223 showed growth patterns similar to SG200 on stress-inducing media, suggesting that they were not compromised in their overall fitness (Figure 8). However, deletion of *um06223* led to a general growth defect. This deletion strain was defective in its overall growth on all stress media, especially on the call wall stress causing congo red and calcofluor containing media (Figure 8). *Δum06223* also showed reduced filamentation when grown on charcoal containing media (Figure 8). The filament formation of all other knockout strains was similar to that of SG200 indicating that their ability to form infection structures was not impaired (Figure 8).

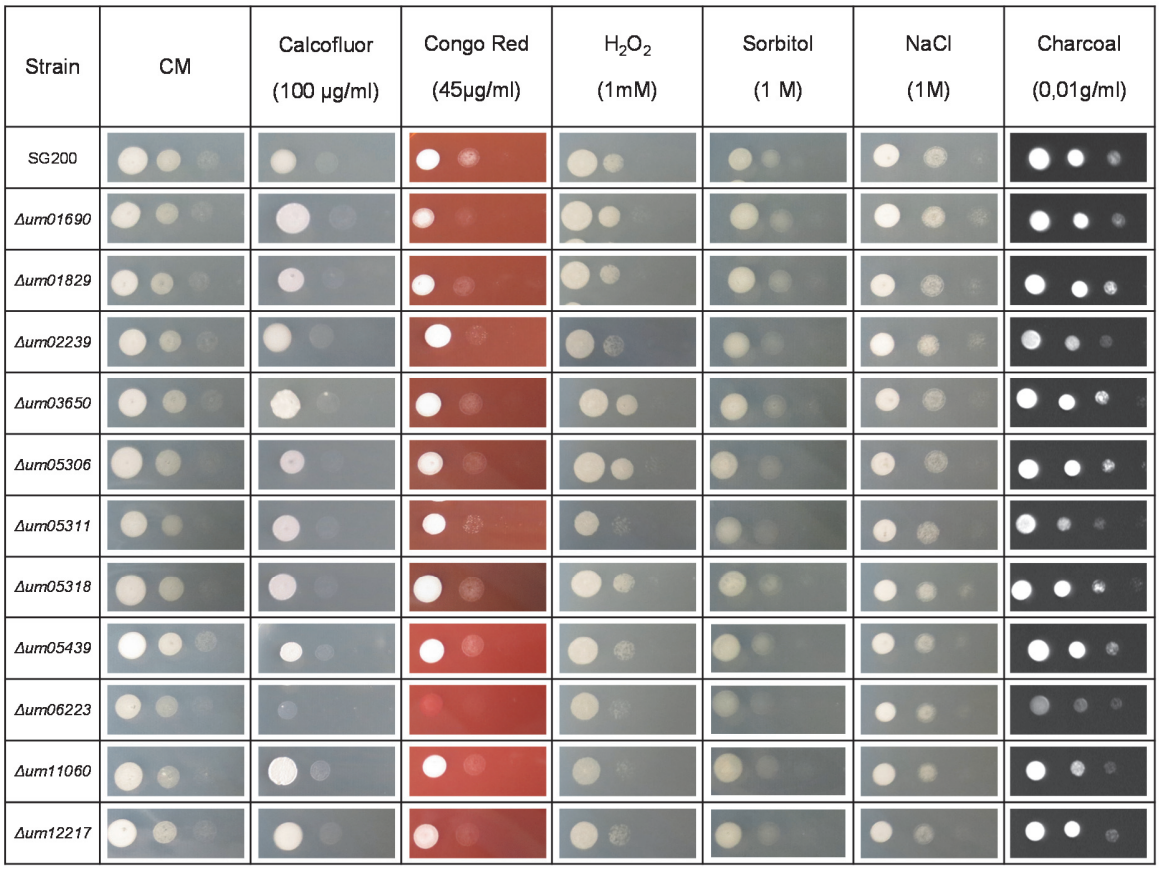

Figure 8: Growth of the organ-specific *U. maydis* effector knockouts bearing a reduction in virulence on different stress media
Serial dilutions were spotted on CM plates and CM plates containing stress factors for cell wall stress (calcofluor and congo red) oxidative stress (H_2O_2) and osmotic stress (sorbitol and NaCl). Filamentous growth was assessed on charcoal containing plates. The experiment was repeated three times. Images show representative examples. Figure from Schilling et al. (2014).

2.3 The leaf-specific effector Sts1 was screened for its host interactors in *Zea mays*

Out of the seven leaf-specific effectors identified in this project, Sts1 (Um01690) was chosen for functional characterization. As a first step Sts1 was screened for host targets in maize via yeast two hybrid (Y2H) screening. Therefore, *Sts1*$_{aa20\text{-}aa198}$ coding sequence was cloned into the binding domain vector (pGBKT7) and transformed into yeast together with the cDNA library of *U. maydis* infected maize tissue in an activation domain vector (pGADT7). Expression of the MYC-tagged Sts1 bait fusion protein (39.8 kDa) in the *S. cerevisiae* strain AH 109 was tested by western blot (Figure 9 A).

After transformation of AH 109 with cDNA library from infected maize tissue and *U. maydis* Sts1, the transformation efficiency for the screen was estimated and reached $1.6*10^{-6}$. The transformed yeast colonies were washed off the low stringency transformation plates and plated on high stringency selection plates for interaction screen. 200 clones were picked from high stringency selection medium and afterwards transferred to fresh high stringency plates, in order to check for regrowth. 35 clones with different digestion patterns of inserts were sequenced. The Y2H screening revealed several potential interaction partners for Sts1 in maize, most of them corresponding to the maize glutamate carboxypeptidase II (CBPII) (Figure 9 B).

CBPII transcripts are described to be present in two different splicing variants in maize, *CBPII T01* (GRMZM2G159171_T01) and *T02* (GRMZM2G159171_T02), (MaizeCyc; http://www.maizegdb.org; Monaco et al., 2013; Figure 9 C). *CBPII T01* shows high expression of up to 700 RMA (linearized expression values) in seedlings as well as in immature leaves and at the base of leaves that are in the second stage of leaf growth before their onset of differentiation (Maize eFP Browser; http://bar.utoronto.ca/efp_maize; Winter et al., 2007). However, *CBPII T02* is not transcribed in any maize organ or tissue during normal maize development (Maize eFP Browser; http://bar.utoronto.ca/efp_maize; Winter et al., 2007). A Pfam database scan (Pfam; http://www.ebi.ac.uk/Tools/pfa/pfamscan/help/; Mistry et al., 2007) predicted that the maize CBPII T01 protein consists of four major domains, a transmembrane (TM) domain, a protease associated domain (PA), a peptidase domain belonging to the MEROPS

peptidase family M28 (Peptidase M28) and a transferrin receptor-like dimerization domain (TFR dimer) (Figure 9 C). The shorter splicing variant CBPII T02 is lacking TM and PA domain (Figure 9 C). Glutamate carboxypeptidases were found to be involved in the regulation of growth and development in plants (Chaudhury et al., 1993; Helliwell et al., 2001; Hongkun et al., 2014). However, the maize glutamate carboxypeptidase II has not been functionally characterized yet.

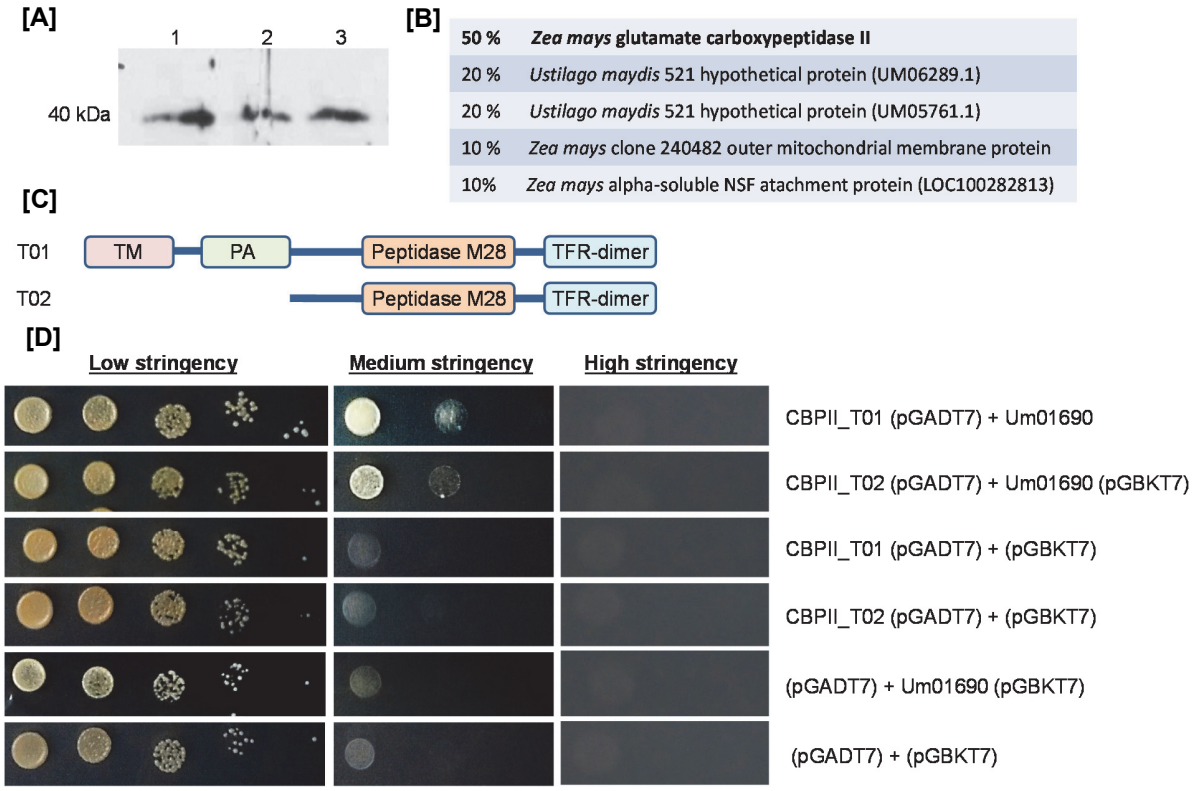

Figure 9: Sts1 expression control experiment and yeast II hybrid analysis
[A] Western blot analysis as expression control for transformed yeast colonies (1-3) expressing Myc-Sts1$_{aa20\text{-}aa198}$ (39.8 kDa). **[B]** Potential interaction partners for Sts1 found in the Y2H screening and their relative abundance among the screened clones. **[C]** Protein structure of maize carboxypeptidase II (CBPII) T01 and T02 bearing a protease associated domain (PA), a peptidase domain belonging to the MEROPS peptidase family M28 (Peptidase M28) and a transferrin receptor-like dimerization domain (TFR dimer). **[D]** Y2H experiment to re-test for interaction of Sts1 with the full length CBP II T01 and T02 on selection media. The drop dilution experiment was repeated at least three times. Images show representative growth patterns.

In order to verify the Sts1 interaction with maize CBPII, the full length sequences for both *CBPII* splicing variants were amplified from maize *cv.* Early Golden Bantam (EGB) cDNA. The variants were re-cloned into the Y2H activation domain vectors (pGADT7) for co-transformation with Sts1 in the Y2H binding domain vector (pGBKT7). Yeast

transformants were afterwards plated on selection medium of low, medium and high stringency plates. Growth of yeast transformants with either CBPII T01 or CBPII T02 with the Sts1 effector was observed under on medium stringency conditions indicating a weak interaction of both proteins (Figure 9 D). Plating of the yeast transformants on high stringency selection medium revealed no growth of both full length splicing variants of the carboxypeptidase II with Sts1 (Figure 9 D).

To obtain proof if Sts1 is interacting with CBPII T01/T02 splicing variants, the interaction was assessed via an *in planta* co-immunoprecipitation (Co-IP) experiment. The proteins of interest were expressed in *Nicotiana benthamiana* using the modular cloning system for assembly of multigene constructs (MoClo) (Engler et al., 2014; Weber et al., 2011). This golden gate modular cloning toolbox allowed for cloning of multigene overexpression constructs bearing CBPII T01-HA or CBPII T02-HA respectively together with Sts1-cMyc. Leaf tissue for Co-IP experiments was harvested 3 days after infiltration (dai). From this tissue, Co-IP experiments using an anti-HA affinity matrix were performed with subsequent immunoblot analysis for the detection of CBPII T01-HA (88 kDa) / CBPII T02-HA (54 kDa) and Sts1-cMyc (25 kDa) (Figure 10). In order to check for protein expression, input fractions were used. This revealed a robust expression of CBPII T01-HA and low expression of CBPII T02-HA (Figure 10). However, by use of HA beads, CBPII T02-HA enriched which led to a visible immunoblot signal (Figure 10). An unspecific binding of antibodies was tested via loading of empty anti-HA affinity matrix (Figure 10). The α-cMyc western blot was done using a HRP-linked α-cMyc antibody in order to avoid unspecific binding of a secondary antibody to the heavy chain of the HA antibody on the HA matrix. Affinity of CBPII T02 for Sts1 seemed stronger as the IP signal for α-cMyc was much stronger than in the CBPII T01 pulldown although input of CBPII T02 showed a much weaker signal than CBPII T01 input (Figure 10).

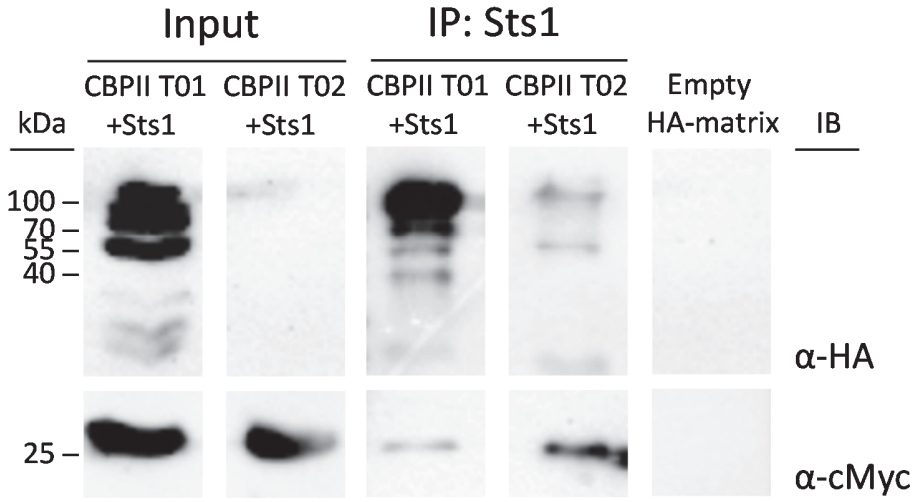

Figure 10: Co-immunoprecipitation experiment of transiently expressed Sts1 with CBPII T01 and CBPII T02 in *N. benthamiana*
Immunoblot showing co-expression of Sts1-cMyc (25 kDa) and CBPII T01-HA (88 kDa) / CBPII T02-HA (54 kDa) 3 dai. Input: fusion proteins detected in crude extract; IP:Sts1: HA-tag purification experiment with HA matrix; empty HA-matrix used as negative control for unspecific band detection. Experiment was repeated twice with similar results.

For investigating the interaction of Sts1 and CBPII T01/T02 *in vivo*, bimolecular fluorescence complementation (BiFC) experiments were done via transient overexpression in *N. benthamiana* leaves. The coding sequence used for the generation of BiFC analysis constructs (Hemetsberger et al., 2012) was cloned into the MoClo vector system plant toolkit for *Agrobacterium* mediated transformation (Engler et al., 2014; Weber et al., 2011). The BiFC constructs were tested for interaction 3 dpi via confocal microscopy. Sts1 was fused to CFP linked to the c-terminal part of the HA-tagged split YFP coding sequence (pSPYCE_Sts1). CBPII T01/T02 were fused to mCherry which is linked to the cMyc-tagged N-terminal part of the split YFP coding sequence (pSPYNE_CBPII T01/T02). The constructs pSPYCE-*p35S::*Sts1-CFP-C_YFP-HA and pSPYNE-*p35S::*CBPII T01-mCherry-N_YFP-cMyc or pSPYNE-*p35S::*CBPII T02-mCherry-N_YFP-cMyc, respectively were transiently co-expressed in *N. benthamiana* leaves under the control of the 35S promoter (Figure 11 A, B). While Sts1-mCherry was strongly expressed and localized in the cytoplasm (Figure 11 A, B, F) both CBPII constructs (T01 and T02) were hardly expressed in tobacco and detection of their mCherry fluorescence tag not possible (Figure 11 A, B, D, E). Co-expression of pSPYCE_Sts1 with pSPYNE_CBPII T01 or T02 did furthermore not result in a detectable

YFP signal (Figure 11 A, B). As a control for autoactivation, empty pSPYNE_N and empty pSPYCE_C were co-expressed (Figure 11 C) as well as pSPYNE_CBPII T01/ T02 with pSPYCE_C (Figure 11 D, E) and pSPYCE_Sts1 with pSPYNE_N respectively (Figure 11 F). As the co-expression of pSPYCE_Sts1 with pSPYNE_N resulted in a very strong autoactivation of the split YFP parts leading to a very strong fluorescence signal, this method cannot be used for reliable analyses of *in vivo* interaction studies for the Sts1 protein (Figure 11 F).

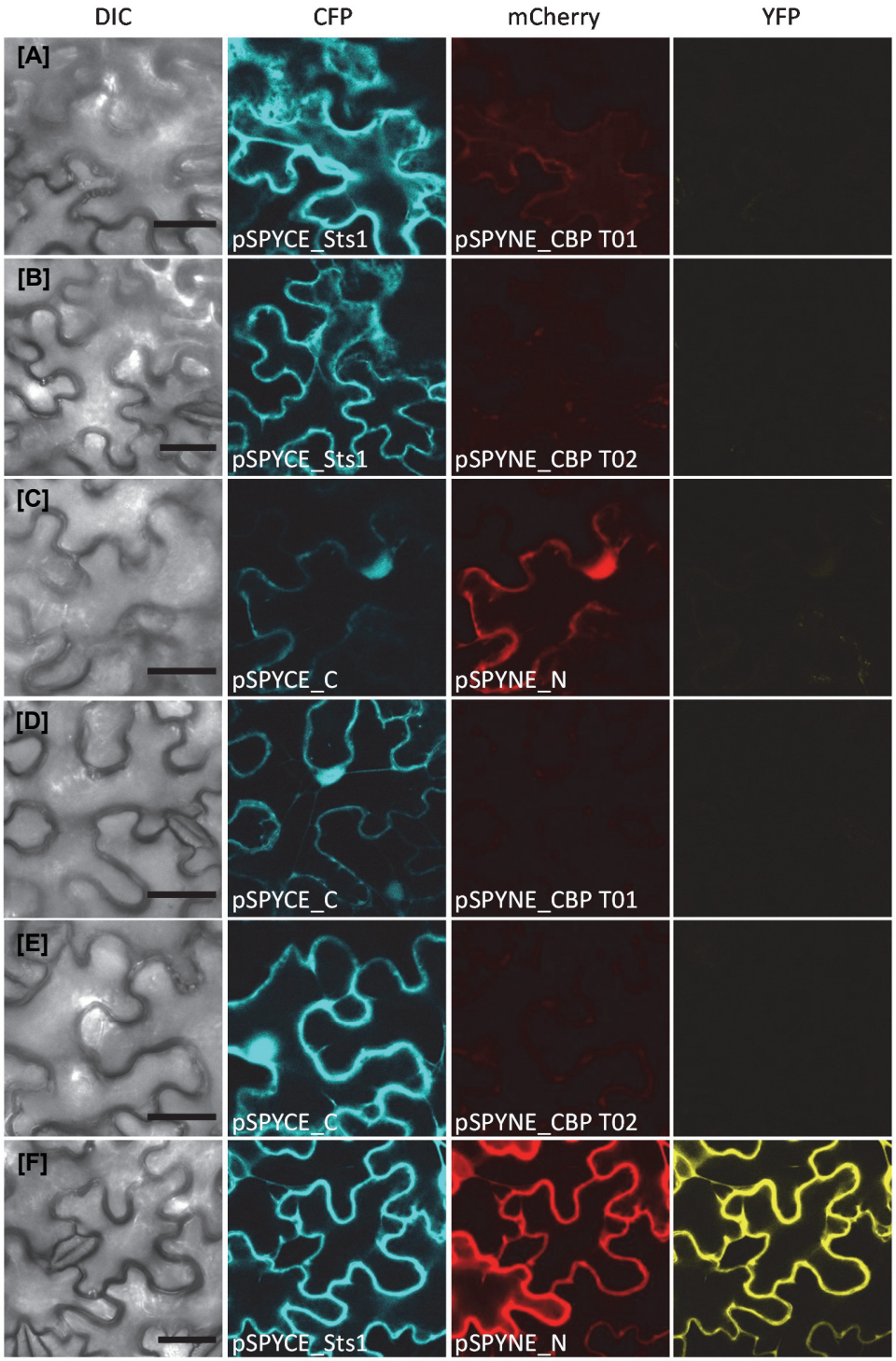

Figure 11: Bimolecular fluorescence complementation (BiFC) analysis 3 dai for Sts1-CFP and CBPII T01/T02-mCherry interaction in transiently expressing *N. benthamiana* cells
[A] Co-expression of pSPYCE_Sts1-CFP and pSPYNE_CBPIIT01-mCherry; **[B]** Co-expression of pSPYCE_Sts1-CFP and pSPYNE_CBPIIT02-mCherry; **[C]** Co-expression of pSPYCE-CFP and pSPYNE-mCherry; **[D]** pSPYCE-CFP and pSPYNE_CBPIIT01-mCherry; **[E]** pSPYCE_CFP and

pSPYNE_CBPIIT02-mCherry; **[F]** pSPYCE_Sts1-CFP and pSPYNE-mCherry. Experiment was repeated twice with similar results. Figure shows representative images. Scale bar = 25 µm.

2.4 Dissection of tumor development and physiological changes in maize leaves

Previous histological studies have shown that *U. maydis*-induced tumor formation involves hyperplasia and hypertrophy (Banuett and Herskowitz, 1996; Callow and Ling, 1973; De Bary, 1853). However, the exact cellular origin and morphological distribution of hyperplasia and hypertrophy during tumor formation has not been elucidated until now. The first governing question concerning tumor development is about the cellular origin of tumor cells. To address this question, the tumor development was followed over time by a series of paraplast embedded *U. maydis* infected leaf tissue sections. The major goal was to identify leaf tissue changes induced by *U. maydis* SG200 on the cellular and physiological level. The fungal disease progression was followed in the maize variety *c.v.* Early Golden Bantam (EGB) over the time of tumor formation from 36 hpi to 13 dpi and compared to sections of mock treated plants of the same age (Figure 12 A-H, see Annexure Figure 27). Microscopy pictures of infected and mock treated maize leaf tissue sections were hereby taken with a filter for cell wall autofluorescence (425-250 nm).

The first changes in cell morphology were observed to occur inside bundle sheath cells around 4 dpi by the induction of internal cell division as new cell walls emerged inside the cells (Figure 12 C, D). The first stages of tumor development were macroscopically visible at 5-6 dpi when infected tissue parts started to swell and enlarge (Figure 12 E). At this time point, the thickening of tumorous tissue was mainly due to newly synthesized hyperplasic tissue around the vasculature (Figure 12 F). *U. maydis*-induced tumor maturation up to spore formation took an overall developing time of about 13 days and at later stages, tumor cells mainly grew by hypertrophic cell enlargement (Figure 12 G-H).

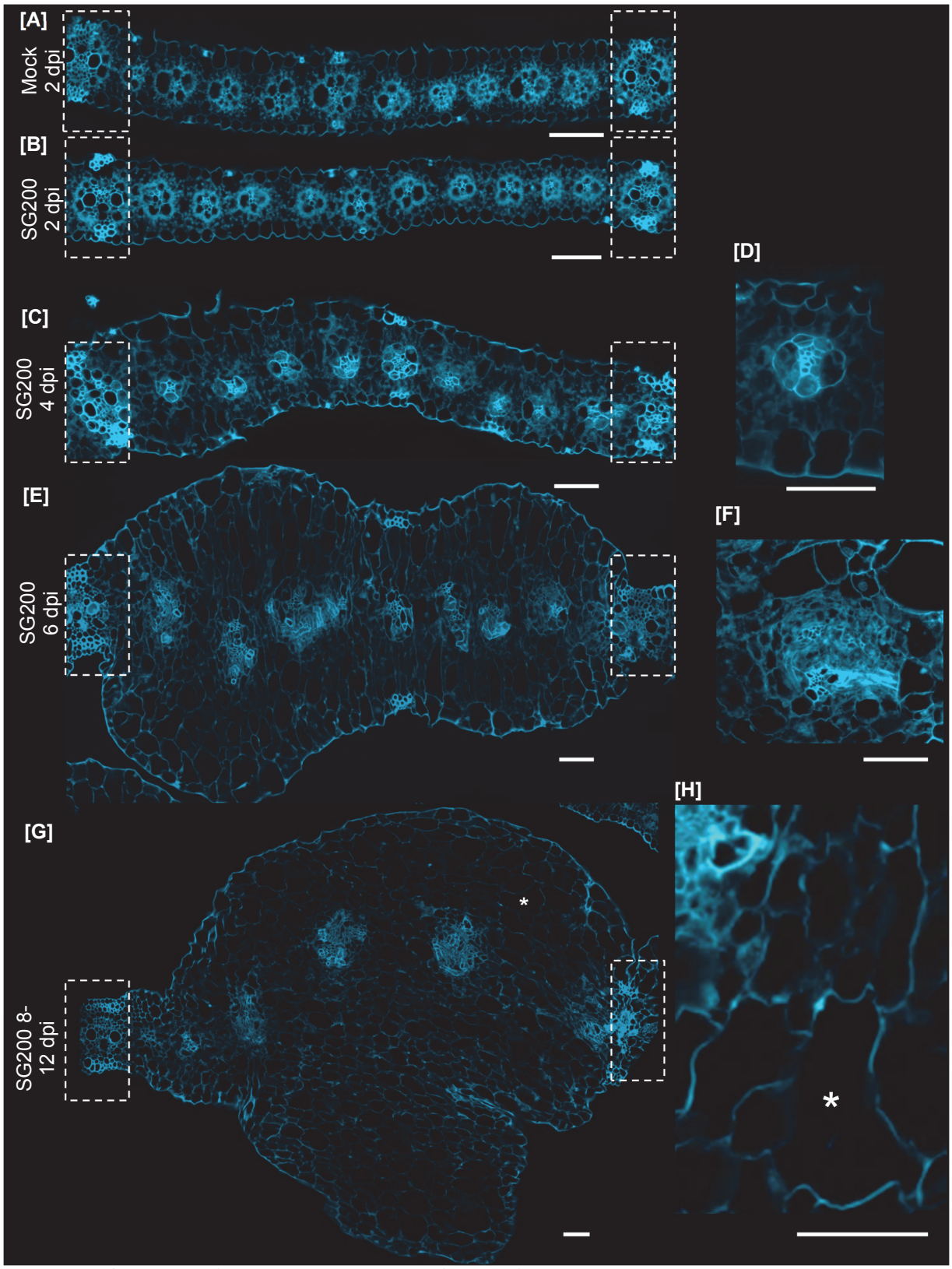

Figure 12: Overview of *U. maydis*-induced leaf tumor formation on the cellular level

Pictures show leaf tissue sections taken with a filter for cell wall autofluorescence (425-450 nm). Primary veins in all sections are highlighted by dash-lined boxes. **[A]** Representative picture of a mock treated leaf section; here 2 dpi; (see annexure Figure 27 for later time points of mock treated sections) **[B]** *U. maydis* infected leaf section 2 dpi; **[C]** *U. maydis* infected leaf section 4 dpi showing first changes in cell morphology that involve **[D]** internal cell division of bundle sheath cells; **[E]** *U. maydis* infected leaf section 6 dpi showing swelling tumorous tissue which involves **[F]** massive hyperplasic cell division; **[G]** *U. maydis* infected leaf section 8-12 dpi showing a typical shape of a fully developed, maturing tumor with **[H]** hypertrophic tumor cell growth. Tissue from four independent biological replicates of infection experiments was embedded and sectioned. Images show representative stages of tumor development. * = hypertrophic tumor cell; Scale bars = 50 µm.

Overall, one of the first major conspicuities of tumor formation was that the primary veins built out a rigid border for tumor depletion. During the development and maturation of tumors, primary veins hereby limit tumor development and restrict the areas of cell enlargement (highlighted by dashed lines, Figure 12). An increase in cell wall autofluorescence is a common histological indicator for assessing lignin deposition and it is furthermore known to occur as a defense response in plants (Sattler and Funnell-Harris, 2013). While primary veins that built out tumor borders did not lose autofluorescence intensity, (Figure 12 A-C, E, G, highlighted by dashed lines) cell wall autofluorescence of tumorous tissue between primary veins was changed compared to mock treated tissue. Interestingly, tumorous tissue showed decreased cell wall autofluorescence which can be clearly seen in pictures taken with the same acquisition settings (Figure 13 A, B). Cell wall autofluorescence intensity was quantified along cross sections using the Nikon NIS Elements software (Figure 13 C). Quantification of autofluorescence intensities revealed an average decrease of 43 % in infected tissue sections compared to mock treated tissue at 6 dpi when tumors are established and start to mature (Figure 13 C).

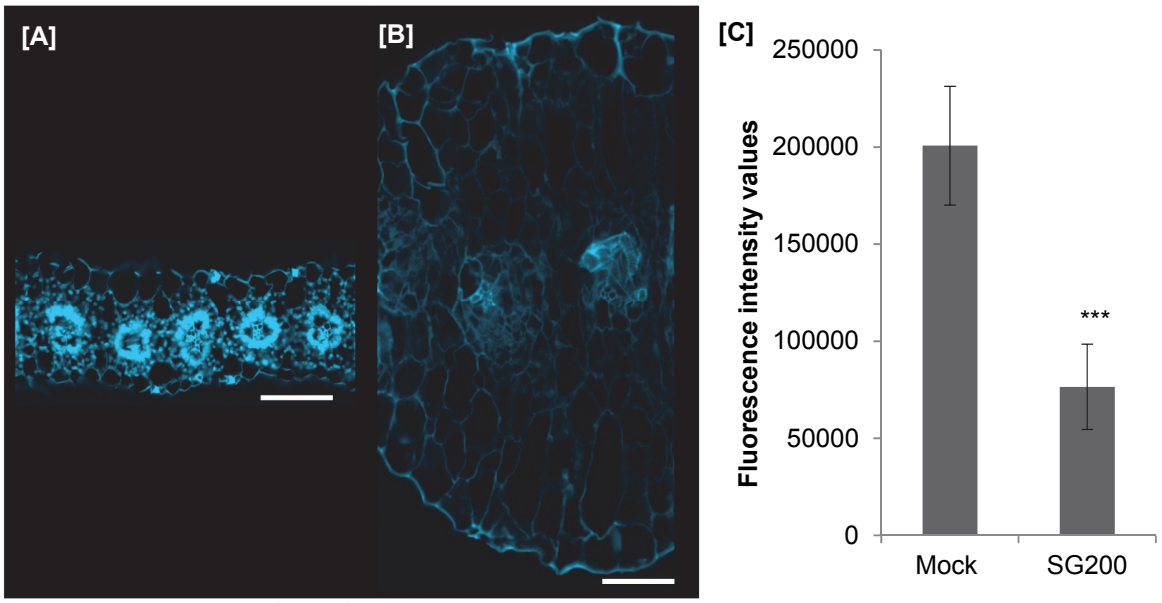

Figure 13: Decrease of autofluorescence intensity in tumorous tissue
Pictures show leaf tissue sections taken with a filter for cell wall autofluorescence (425-450 nm). **[A]** Mock treated tissue sections in mature tissue (6 dpi) showed stronger autofluorescence than **[B]** SG200 infected leaf tissue sections; scale bar = 100 µm. **[C]** Average fluorescence intensity values in tumorous tissue sections (6 dpi). Fluorescence intensity was measured in 4 tissue sections from independent biological replicates of infection experiments. Results represent the mean ± SD, asterisks indicate statistical significance of fluorescence intensity in SG200 infected sections compared to mock treated sections. P-values were calculated using the unpaired student's t-test; ***: p≤ 0.001.

2.4.1 Lignification in tumorous tissue

In order to clarify whether the restriction of tumor growth by primary veins was due to a natural preformed barrier caused by stronger lignification of primary veins compared to secondary veins, tumorous and mock treated leaf sections were stained with Safranin-O. Safranin-O is a common lignin staining as described in Srebotnik and Messner (1994). The time point of 10 dpi was chosen for this analysis as the tumors are completely established at this stage (Figure 12). The lignin overexpressing maize line M541J as well as its cognate control line M142V together with the lignin deficient maize line *brown midrip2* (*bm2*) were assessed concerning their lignification of primary veins surrounding tumors. For this, mature tumorous tissue was embedded in paraplast and sectioned 10 dpi to assess lignin distribution on the cellular level. Safranin-O staining of primary veins in mock treated maize leave sections showed no obvious difference between the control line M142V (Figure 14 A) and the lignin overexpressing line M541J (14 B) as well as the deficient line *bm2* (14 C).

U. maydis infection of the control line M142V led to normal tumor development (Figure 14 D) as it was previously found for infected EGB plants (Figure 12). Primary veins of mature tumors were observed to stain dark red by Safranin-O which is indicative for a stronger lignification (Figure 14 D) compared to uninfected primary veins (Figure 14 A). However, the primary veins around tumors of the control line M142V developed a flattened and compressed morphology (Figure 14 D). Furthermore, the xylem tracheary elements of *U. maydis* infected primary veins got partially clogged by yellow staining components (arrowhead Figure 14 D, G) while no clogging was observed in primary veins of uninfected leaves independent of their endogenous lignin amount (Figure 14 A-C, I). This clogging was also observed in primary veins that surround tumors developing in the lignin overexpressing line M541J (Figure 14 E, arrowhead). Tumors that developed in this maize line were generally smaller than tumors developing in the control line M142V and showed an overall darker Safranin-O staining than the control line M142V (Figure 14 D, E). In contrast to the control line, the morphology of primary veins around tumors in the lignin overexpressing line M541J was retained and these veins were not compressed (Figure 14 E).

Sclerenchyma is a tissue type of primary veins that is located below the epidermis providing structural support due to lignification of secondary cell walls (Figure 14 A-C, arrows). It is important to note that the sclerenchyma in the *U. maydis* infected control line M142V (Figure 14 D, arrows) as well as in the lignin overexpressing line M541J (Figure 14 E, arrows) was much more prominent than in primary veins of uninfected leaves 10 dpi (Figure 14 A, B arrows). It became furthermore apparent that the sclerenchyma in the *U. maydis* infected lignin overexpressing line M541J (Figure 14 E, arrows) was enhanced compared to the infected control line M142V (Figure 14 D, arrows) which was reflected in a prominent Safranin-O staining.

To further investigate whether lignin contributes to the restriction of tumor formation, the lignin deficient maize line *bm2* was included and assessed for its lignification in *U. maydis*-induced tumors (Figure 14 F). While primary veins built out a defined barrier for tumor formation in the control line M142V as well as in the lignin overexpressing line M541J, the lignin deficient *bm2* line did not show the same restriction of tumor formation by primary

veins (Figure 14 D-F). In this line, tumorous tissue exceeded the defined barrier that was built out by primary veins (Figure 14 F). During tumor formation, both, the observed induction of sclerenchyma (Figure 14 D, arrows) as well as clogging of xylem tracheary elements was lacking in the *bm2* lignin deficient line (Figure 14 D, arrowheads).

Inside tumorous areas, secondary veins underwent a strong morphological restructuration compared to mock treated tissue (highlighted by dash-lined boxes Figure 14 D-F, I). The secondary veins developed a prominent metaxylem (Figure 14 H, asterisks) which was not observed in secondary veins of mock treated M142 leaf tissue sections (highlighted by dash-lined box Figure 14 I).

All in all, Safranin-O stainings point towards a *U. maydis*-induced lignification of primary veins that goes along with clogging of primary tracheary elements and an induction of sclerenchyma formation below the epidermis of primary veins (Figure 14 A, D, I). While this effect was more prominent in the lignin overexpressing line M541J compared to the control line M142V, the lignin deficient line *bm2* was heavily impaired in restriction of tumors by primary veins.

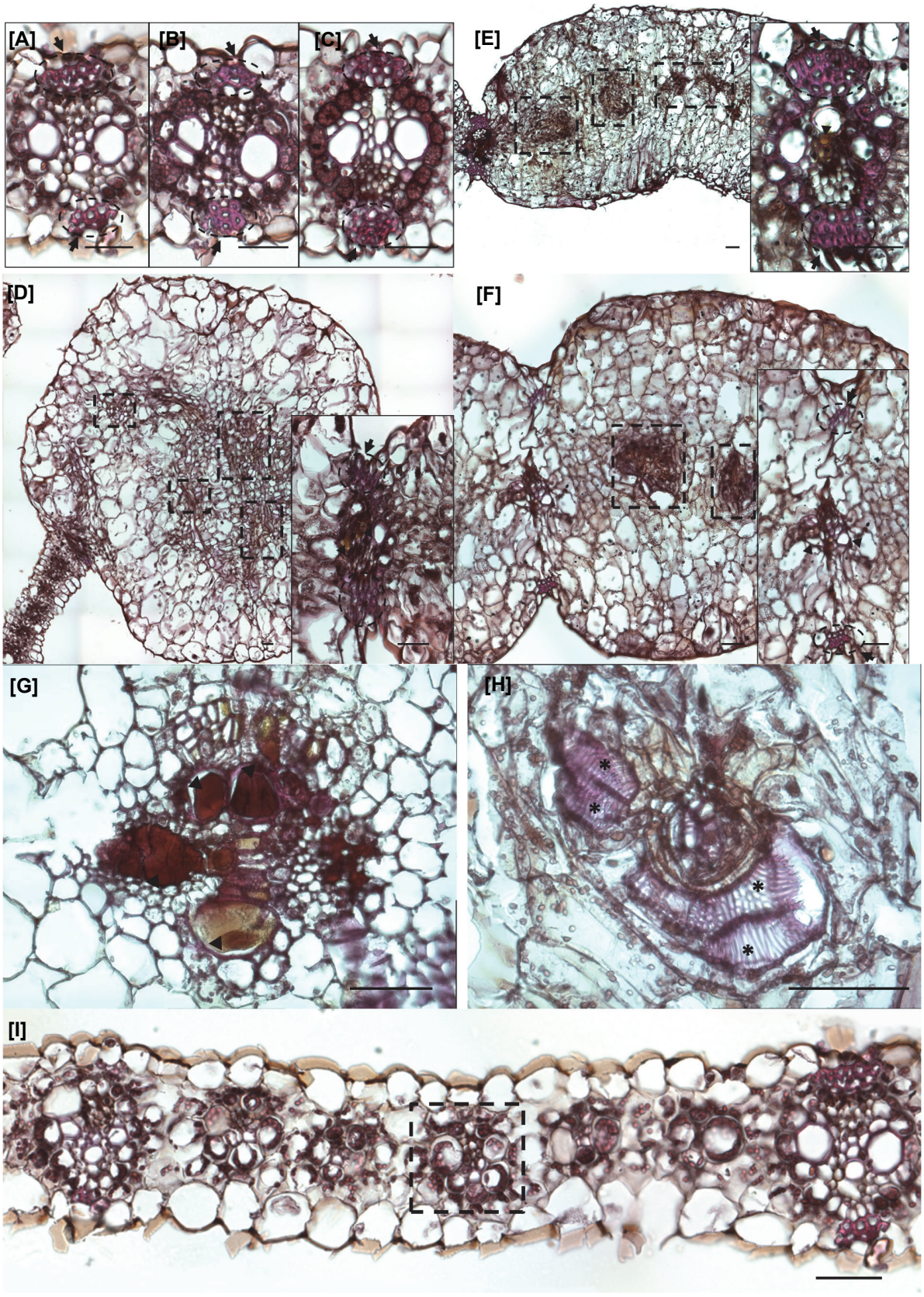
[A]
[B]
[C]
[E]
[D]
[F]
[G]
[H]
[I]

Figure 14: Safranin-O staining of mock treated and SG200 infected leaf tissue sections in control lines and lignin mutant lines 10 dpi.
[A] Tissue section of primary vein in the mock treated control line M142V; **[B]** Tissue section of primary vein in the mock treated lignin overexpressing line M541J; **[C]** Tissue section of primary vein in the mock treated lignin deficient line *bm2*; **[D]** Tissue section of leaf tumor and close-up of primary vein in the SG200 infected control line M142V; **[E]** Tissue section of leaf tumor and close-up of primary vein in the SG200 infected lignin overexpressing line M541J; **[F]** Tissue section of leaf tumor and close-up of primary vein in the SG200 infected lignin deficient line *bm2*; **[G]** Close-up view of clogging in a primary vein of SG200 infected control line M142V; **[H]** Close-up view of tissue restructuration into metaxylem in secondary veins around hyperplasic tumor cell areas; **[I]** Representative picture of a mock treated leaf tissue section 13 dpi of the M142V control line.
Arrows indicate sclerenchyma tissue; dash-lined boxes indicate secondary veins; arrowheads indicate clogging of xylem; asterisks indicate metaxylem; scale bars = 50 µm.

Lignin comprises about 20 % of the maize cell wall and it is composed of three monolignol compound groups, guaiacyl (G), syringyl (S) and p-hydroxyphenyl (H) phenylpropanoid (Vanholme et al., 2010). Genes encoding proteins involved in the secondary metabolism, including genes of the phenolic secondary metabolite and phenylpropanoid pathway for lignin and lignin biosynthesis were found to be upregulated from 0.5 – 8 dpi in *U. maydis* infected tissue (Doehlemann et al., 2008a). In order to investigate the quantitative increase in lignification upon *U. maydis* infection and attribute it towards a specific form of monolignol, lignin composition was analyzed in the maize variety EGB. Monolignol profiling was done in collaboration with the Laboratory of Prof. Dr. Björn Usadel (Forschungzentrum Jülich, Germany). Mock treated leaf tissue, *U. maydis* tumors as well as infected chlorotic (but not tumorous) tissue at the time point of 6 dpi was cut out and assessed for its lignin composition (Figure 15). This analysis revealed no significant changes in the three different tissue types for guaiacyl (G) monolignol composition whereas the p hydroxyphenyl (H) monolignol was significantly reduced in chlorotic tissue compared to mock treated as well as tumorous tissue (Table 3). Furthermore, syringyl (S) monolignol content was doubled in chlorotic tissue compared to mock treated tissue and also in tumorous tissue, the S monolignol content was significantly increased compared to mock treated tissue (Table 3). These results show that lignification in maize leaf tissue is induced by *U. maydis* infection. However, this effect is not specific to tumorous tissue as it is a general modification that is observed also in tumor surrounding, chlorotic tissue.

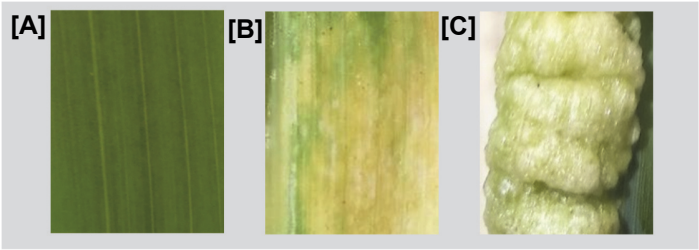

Figure 15: Dissected leaf tissue for cell wall component analysis (6 dpi)
[A] Mock treated leaf tissue, **[B]** chlorotic leaf tissue and **[C]** tumorous leaf tissue used for cell wall composition analysis.

Table 3: Monolignol composition in cell walls of mock treated, chlorotic and tumorous maize tissue (6 dpi)
Monolignol composition analysis data (mean ± SD) is shown from three independent biological replicates of infection experiments with SG200. G (%): relative abundance of cell wall guaiacyl monolignol in percent; H (%): relative abundance of cell wall p hydroxyphenyl monolignol in percent; S (%): relative abundance of cell wall syringyl monolignol in percent. Asterisks indicate statistical significance of monolignol abundance compared to mock treated tissue. P-values were calculated using the unpaired student's t-test; *: p≤ 0.05; **: p≤ 0.01.

	Mock	Chlorotic	Tumor
G (%)	55.15 ± 0.78	57.76 ± 1.90	51.81 ± 2.54
H (%)	36.39 ± 0.85	21.69 ± 3.53 (**)	33.76 ± 4.22
S (%)	8.46 ± 1.21	20.55 ± 2.25 (**)	14.42 ± 2.18 (*)

2.4.2 Modification of hemicellulose composition in tumorous tissue

Hemicelluloses comprise 55 % of the cell wall in grasses (*Poaceae*) and were found to contribute to resistance against plant pathogens (Cosgrove, 1997; Lionetti et al., 2015). To test if *U. maydis* exerts an influence on hemicellulose composition in addition to lignin composition, the hemicellulose content in infected chlorotic and tumorous maize tissue was analyzed and compared to mock treated tissue at 6 dpi (Figure 15 and Figure 16). Hemicellulose content was profiled by Dr. Markus Günl (Forschungszentrum Jülich, Germany; Figure 16). To profile the most prominent changes in cell wall composition during *U. maydis* infection, cell wall matrix polysaccharide composition was quantified after starch digest by high-performance anion-exchange chromatography with pulsed amperometric detection (HPAEC-PAD).

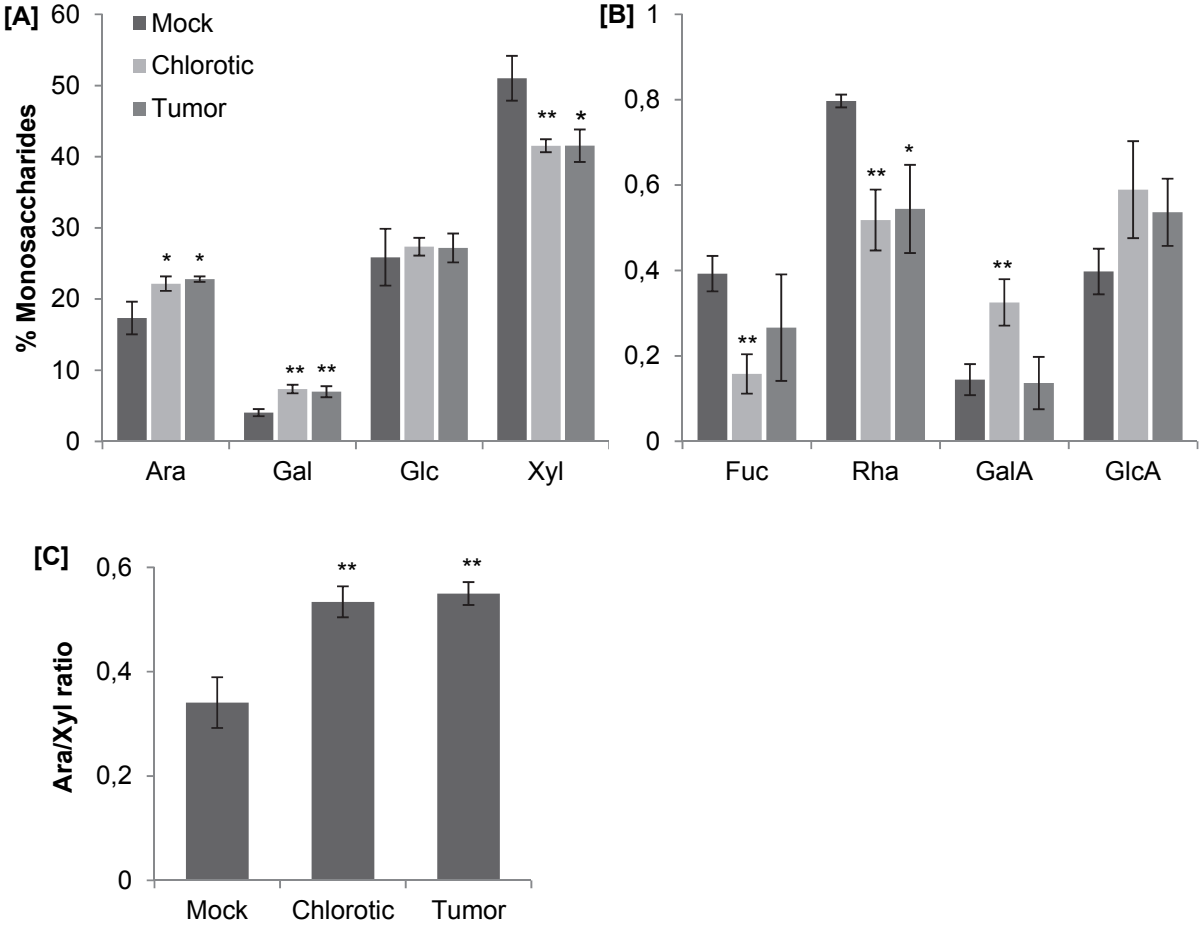

Figure 16: Tissue-specific hemicellulose composition in cell walls of mock treated, chlorotic and tumorous maize tissue (6 dpi)

Tissue-specific hemicellulose composition analysis obtained by HPAEC-PAD. Results represent the mean ± SD of three independent biological replicates. Mock treated, SG200 infected chlorotic and SG200 infected tumorous tissue was analyzed for overall content of **[A]** arabinose (Ara), galactose (Gal), glucose (Glc), xylose (Xyl), **[B]** fucose (Fuc), rhamnose (Rha), galacturonic acid (GalA) and glucuronic acid (GlcA). **[C]** Arabinose/Xylose ratio in mock treated, SG200 infected chlorotic and tumorous tissue. Asterisks indicate data sets significantly different between mock and chlorotic or mock and tumorous tissue. P-values were calculated using the unpaired student's t-test; *: p≤ 0.05, **: p≤ 0.01.

This analysis revealed significant differences for arabinose, galactose, xylose, fucose, rhamnose and galacturonic acid in cell walls of infected tissue (Figure 16 A, B). The main differences were observed in the xylose content for both, chlorotic as well as tumorous tissue compared to mock treated control tissue. Here, a 10 % lower xylose content than in *U. maydis* infected tissue was measured (Figure 16 A). At the same time, arabinose (5 %) and galactose (3 %) contents were increased in infected tissue (Figure 16 A). Together, these changes resulted in a 22% increase in Ara/Xyl ratio (Figure 16 C). Furthermore, some of the less abundant hemicellulose monosaccharides showed

significant changes upon *U. maydis* infection (Figure 16 B). The fucose content was significantly lower in chlorotic but not in tumorous tissue while rhamnose content was lowered by half in both chlorotic as well as tumorous tissue when compared to mock treated tissue (Fig 16 B). Galacturonic acid was increased upon *U. maydis* infection in chlorotic tissue compared to mock treated tissue but not significantly changed in tumorous tissue (Figure 16 B).

In summary, analysis of hemicellulose content revealed an influence of *U. maydis* infection on monosaccharide composition of hemicelluloses in leaves. This influence was most prominent for the ratio of xylose and arabinose in both, chlorotic as well as tumorous tissue.

2.4.3 Change in chloroplast function and loss of C_4 dimorphism in tumorous tissue

U. maydis infection and disease symptom development in maize leaves is accompanied by chlorosis. This was shown to correlate with a transcriptional downregulation of photosynthesis and an increase in hexose content while keeping the infected leaf areas in a sink tissue stage (Banuett and Herskowitz, 1996; Doehlemann et al., 2008a). The crucial photosynthesis pigments that enable plants to gather light energy for carbon fixation are chlorophyll a, chlorophyll b and carotenoids (Blinks, 1954). The loss of photosynthetic capacity therefore goes along with a decrease in photosynthesis pigments. This can be observed as formation of chlorosis in *U. maydis* infected chlorotic and tumorous leaf regions when compared to mock treated tissue (Figure 15). To determine the amount of photosynthetic pigments upon *U. maydis* infection the absorption rate of pigments in chlorotic, tumorous and mock treated seedling leaf tissue over the time of disease progression was measured (Figure 17). This revealed an early (2 dpi) decrease of photosynthesis pigments in chlorotic tissue (1.0 $mg*g^{-1}$ pigment concentration) compared to mock treated tissue (1.8 $mg*g^{-1}$; Figure 17). Over the time of disease progression (4 dpi and 6 dpi) the absorption rate of chlorophyll a was significantly further decreased in chlorotic tissue compared to 2 dpi up to 0.219 $mg*g^{-1}$ (Figure 17). In contrast, absorption rates of chlorophyll b and carotenoids in infected tissue stayed mostly unchanged during disease progression from 2 to 6 dpi showing that these pigments did

not further decrease during disease progression (Figure 17). In addition, tumorous tissue contained less photosynthetic pigments (0.3 mg*g^{-1} chlorophyll a, 0.1 mg*g^{-1} chlorophyll b, 0.2 mg*g^{-1} carotenoids) than chlorotic tissue (1.3 mg*g^{-1} chlorophyll a, 0.6 mg*g^{-1} chlorophyll b, 0.6 mg*g^{-1} carotenoids, Figure 17). All in all, measurement of absorption of photosynthesis pigments revealed that *U. maydis* infection led to a significant decrease of photosynthesis pigments in infected leaf areas which started at the very early time point of 2 dpi when leaves appear symptomless (Figure 17).

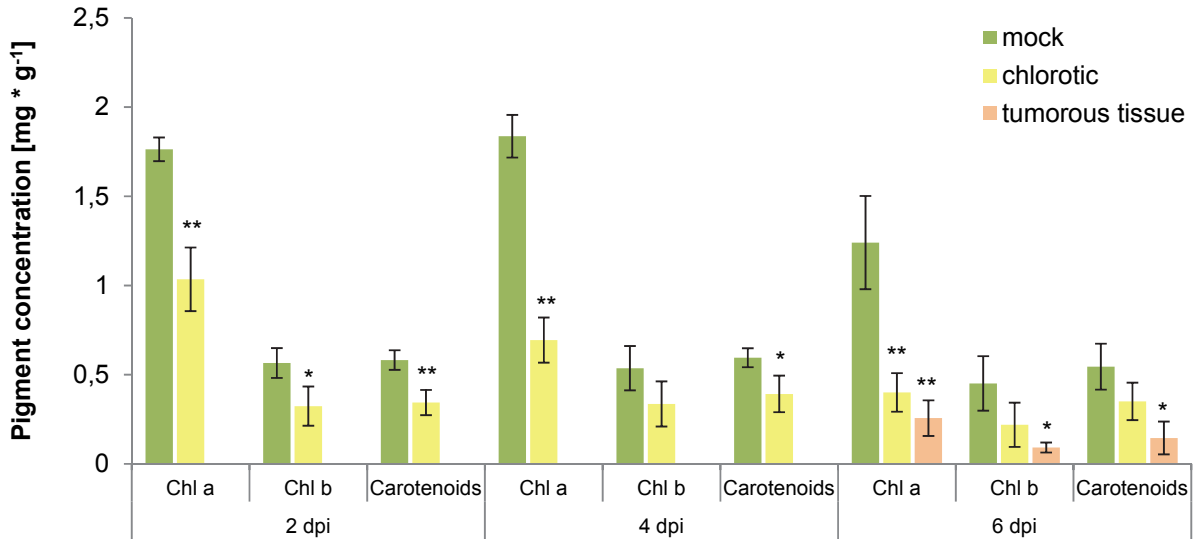

Figure 17: Measurement of photosynthetic pigment contents in mock treated and SG 200 infected seedling leaf tissue upon disease progression
Pigment content [mg*g^{-1}] was assessed via absorption rate measurements for chlorophyll a (Chl a), chlorophyll b (Chl b) and carotenoids in mock treated, chlorotic and tumorous tissue during disease progression (2 to 6 dpi). Tumorous tissue is only apparent 6 dpi. Results represent the mean ± SD from three independent biological replicates of infection experiments with SG200. Asterisks indicate data sets significantly different between mock and chlorotic tissue or mock and tumorous tissue. P-values were calculated using the unpaired student's t-test; *: p≤ 0.05, **: p≤ 0.01.

U. maydis-induced loss of chlorophyll was also evident in paraplast embedded tissue sections by a decrease in chlorophyll autofluorescence. Microscopic pictures of infected and mock treated maize leaf tissue sections were taken with a filter for chlorophyll autofluorescence (540-580 nm). In pictures taken with normalized exposition time, autofluorescence strongly decreased in tumorous tissue from 6 - 8 dpi compared to mock treated tissue (Figure 18 A-C).

In order to assess whether the loss of photosynthesis pigments has an influence on chloroplast morphology or chloroplast abundance, transmission electron microscopic (TEM) analysis of infected leaf sections was carried out. TEM analysis allowed for the investigation of the anatomical structure of chloroplasts in infected areas compared to mock-infected areas (Figure 18 D-E). Comparison of infected and mock treated leaf sections revealed a strong over-accumulation of starch between the thylakoids of bundle sheath chloroplasts in infected tissue at 4 dpi when tumor formation is initiated (Figure 18 D-E, Figure 12). This accumulation led to a deformation of the organelles from the longitudinal shape in mock treated tissue towards a big, round shape in *U. maydis* infected tissue (Figure 18 D-E). The chloroplasts of mock treated leaf tissue in bundle sheath cells accumulated starch granules to a much lesser extent than bundle sheath chloroplasts of infected leaf tissue, maintaining their typical oval shape (Figure 18 D). In a next step tissue-specific starch measurement from tumorous tissue and mock treated tissue was performed 6 dpi by Dr. Markus Günl (Forschungszentrum Jülich, Germany). This measurement did not show a significant increase of starch in tumorous tissue although a trend towards higher starch content in tumors compared to mock treated tissue was observed (Figure 18 F).

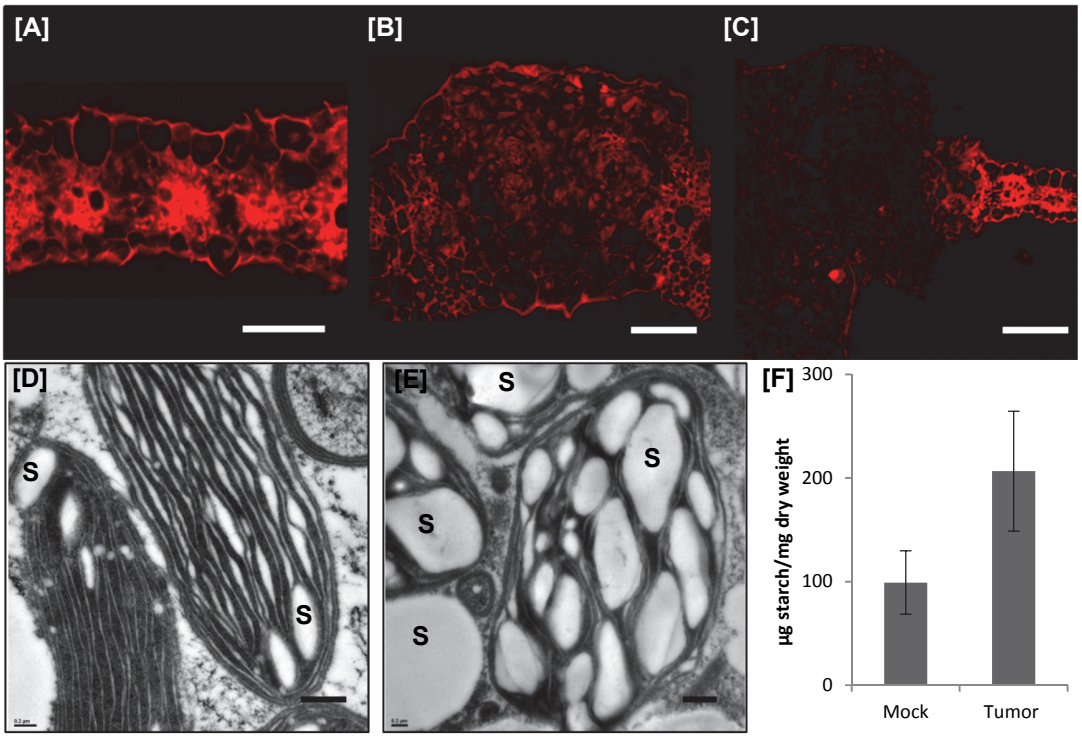

Figure 18: *U. maydis*-induced chlorophyll autofluorescence decrease and starch distribution changes
[A-C] Pictures show leaf tissue sections taken with a filter for chlorophyll autofluorescence (600-690 nm); scale bars = 50 µm. **[A]** Representative picture of chlorophyll autofluorescence in a mock treated leaf section 6 dpi; SG200 infected leaf section **[B]** 6 dpi and **[C]** 8 dpi shows continuous decrease of autofluorescence; **[D]** TEM image showing a mock treated bundle sheath chloroplast 4 dpi; scale bar = 0.4 µm; S indicates starch granule **[E]** TEM image showing a SG200 infected bundle sheath chloroplast 4 dpi; scale bar = 0.4 µm; S indicates starch granule **[F]** Measurement of starch levels in mock treated and tumorous tissue, 6 dpi, data is shown from two independent biological replicates of infection experiments with SG200.

To further visualize the starch distribution in leaf sections during disease progression iodine staining for starch detection was used (Figure 19). Application of this staining solution leads to the production of an intense blue, almost purple color in the presence of amylose that is part of the polymeric carbohydrate starch. Leaf sections of mock treated and SG200 infected EGB tissue harvested at 2 dpi, 4 dpi and 6 dpi were stained with Lugol's iodine staining solution (Figure 19). At 2 dpi, only a slight starch staining was observed in mock treated tissue around the collar of chloroplasts inside bundle sheath cells (Figure 19 A). Chloroplasts of SG200-infected leaf tissue showed a disturbance of the collar-like distribution in most bundle sheath cells and did not show any blue staining (Figure 19 B). At 4 dpi, the mock treated leaf sections showed a strong blue to purple amylose staining in bundle sheath cells reflecting the presence of starch in this maturing

tissue. Chloroplasts were still organized in a collar-like distribution inside the bundle sheath cells (Figure 19 C). In contrast, the SG200 infected leaf sections did not show the same staining pattern of bundle sheath cells at 4 dpi (Figure 19 D). Purple staining was prominent only in some bundle sheath cells while other bundle sheath cells in infected leaf areas did not show any presence of amylose (Figure 19 D). Pronounced changes in amylose distribution were observed in infected tissue at 6 dpi when tumors were established. At this time point the typical chloroplast dimorphism of C_4 plants was seen in mock treated tissue sections which was reflected in strong amylose staining inside carbon fixing bundle sheath cells but not in mesophyll cells (Figure 19 E). This chloroplast dimorphism was turned around in SG200 infected tumor sections (Figure 19 F-G). Mesophyll chloroplasts of infected leaf tissue showed strong accumulation of starch while the bundle sheath cells had disappeared (Figure 19 F-G). Furthermore, the newly synthesized hyperplasic tumor cells around the vasculature (see 2.4.4 for further explanation) did not show purple starch staining indicating that they lack organelles for accumulation of starch (asterisks Figure 19 F-G). A representative picture of a typical tumor developed at 6 dpi shows that the change in chloroplast dimorphism was a local effect as chloroplasts next to the tumor showed a typical starch distribution similar to mock treated tissue (Figure 19 G, indicated by dashed line).

Taken together, chlorophyll measurements, TEM analysis and histological staining revealed a strong influence of *U. maydis* infection on chloroplast function and abundance in infected leaves (Figure 17-19). The overall function of chloroplasts in infected areas is changed. This is reflected by a loss of chlorophyll upon disease progression that was induced as early as 2 dpi (Figure 17). Furthermore, an accumulation of starch between thylakoid membranes of bundle sheath chloroplasts was observed after 4 dpi in infected areas (Figure 18 D-E). The typical C_4 dimorphism of chloroplasts was reversed and an accumulation of starch in chloroplasts of mesophyll cells was observed in tumorous mesophyll tissue upon *U. maydis* infection (Figure 19).

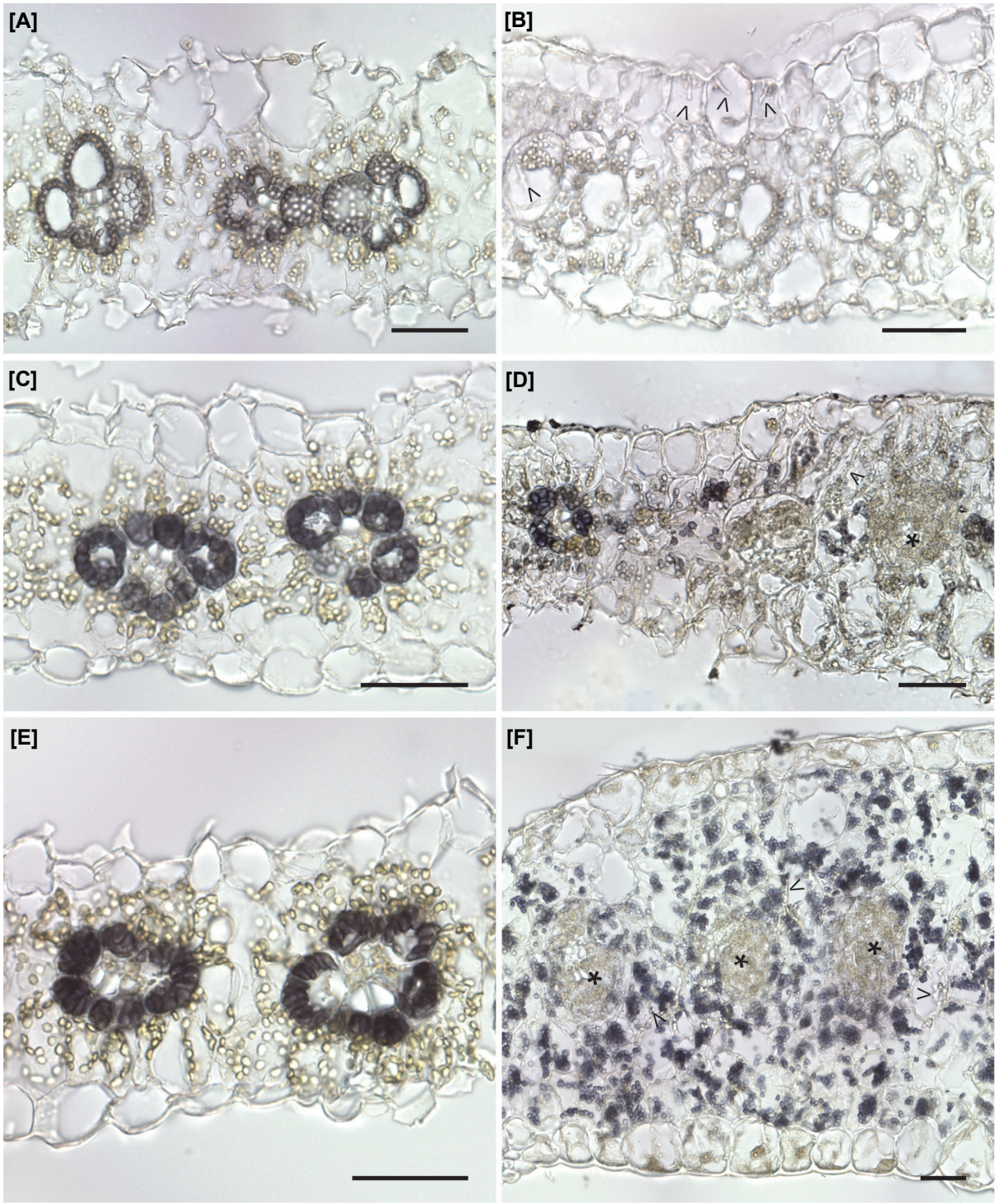
[A]
[B]
[C]
[D]
[E]
[F]

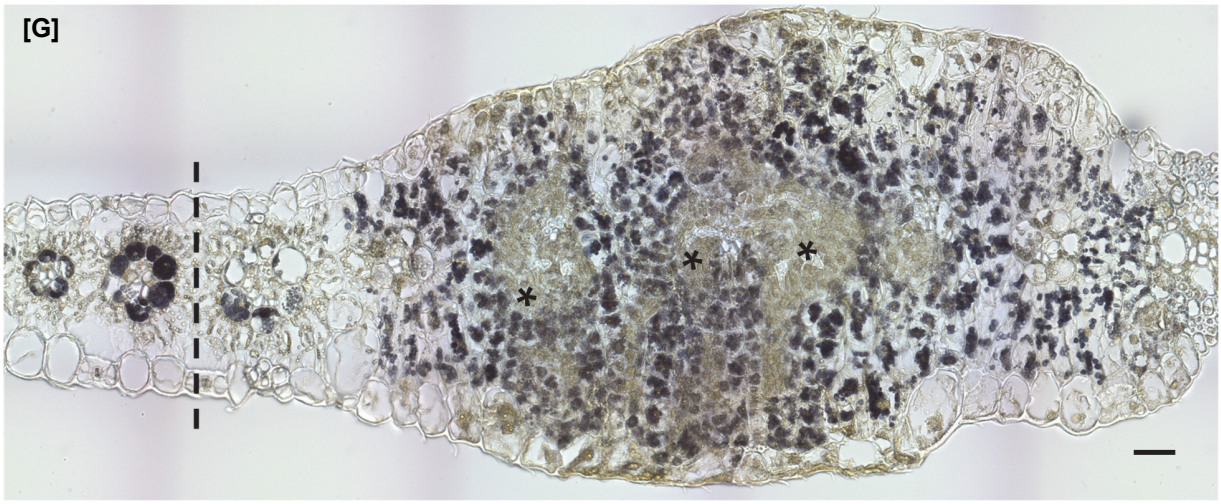

Figure 19: Iodine staining for identification of starch allocation and change of chloroplast dimorphism in leaf tissue sections upon disease progression and tumor formation
[A] Mock treated leaf section 2 dpi; **[B]** SG200 infected leaf section 2 dpi; **[C]** Mock treated leaf section 4 dpi **[D]** SG200 infected leaf section 4 dpi showing first changes in starch allocation; **[E]** Mock treated leaf section 6 dpi; **[F]** SG200 infected leaf section 6 dpi showing change of chloroplast dimorphism; **[G]** full overview of an SG200 infected leaf section 6 dpi; dashed line indicates local effect of chloroplast dimorphism change. Scale bars = 50 µm; arrowheads indicate SG200 hyphae; asterisks indicate hyperplasic tumor cells.

2.4.4 Influence of *U. maydis* infection on the cellular organization of the leaf and modulation of cell morphology during tumor formation

Many cytological studies have adressed the cellular changes that occur upon *U. maydis* infection in both leaves and anthers (Callow and Ling, 1973; Gao et al., 2013). Those studies described several *U. maydis*-induced changes of tissue structure in tumors. However, detailed information on how the fungus changes leaf tissue on the cellular level during tumor formation and concise information about the cellular origin of tumor cells was lacking to date. Therefore, a timeline of infected tissue sections was analyzed to elucidate the exact events that occur during cellular reorganization of leaf tissue during *U. maydis* infection. Cell sizes and cell number of mock treated and SG200 infected maize leaf sections were quantified from 36 hours post infection (hpi) to 13 dpi (Figure 20). The cell types tracked during tumor formation included epidermal cells, bundle sheath cells and mesophyll cells as well as the newly emerging tumor cells in infected tissue. Representative pictures of the developing tumor stages and the main cellular changes observed during tumor development are shown in Figure 20 (A-D). The respective cell types analyzed during tumor development and quantified in this analysis are color coded.

For each area of measurement during tumor formation, the maximum cell diameter was determined as representatively indicated by arrows in Figure 20 A-D. For each time point and treatment, three individual transversal leaf blade sections were analyzed. The area of interest in leaf sections was defined between two primary veins (Figure 12, area indicated between dashed boxes).

Epidermal cells in mock treated leaf sections showed a continuous increase in average longitudinal diameter from 18 µm to 35 µm which peaks at 4 dpi. The size of epidermal cells interestingly decreased back to 18 µm upon maturation of the leaf (Figure 20 E). In contrast, cell sizes of *U. maydis* infected epidermal cells continued to increase and reached their maximum of about 40 µm diameter at 8 dpi (Figure 20 E). However, the average number of epidermal cells in assessed leaf areas did not significantly change over time, neither in mock treated tissue sections nor in SG200 infected sections (Figure 20 F). A prominent morphological cell change during tumor development occurred in **mesophyll cells** (Figure 20 A-D, highlighted in light green). The average cell diameter of mesophyll cells in infected leaf areas was found to tremendously increase after 6 dpi from 20 µm to 65 µm in a fully developed tumor at 13 dpi (Figure 20 E). Despite that no increase in average cell number of mesophyll cells was observed in infected leaf areas compared to mock treated leaf areas throughout tumor development (Figure 20 F). When assessing the size of **bundle sheath cells** during *U. maydis* infection (Figure 20 A, B, highlighted in dark green) it became evident that tumor formation had no significant effect on the size of bundle sheath cells (Figure 20 E). Remarkably, the number of bundle sheath cells in *U. maydis* infected leaf sections dropped significantly already 4 dpi compared to mock treated sections (Figure 20 F). At the same time bundle sheath cells in infected leaf areas started internal cell divisions which were reflected in the appearance of newly formed cell walls inside these cells (Figure 20 B, C, bundle sheath highlighted in orange, newly emerging cells highlighted in purple). In areas where bundle sheath cells started an internal cell division, cells of a new type, the **hyperplasic tumor cells**, were formed (Figure 20 B-C, highlighted in purple). Those tumor cells increased in size during the maturation of the tumor between 6 dpi and 8 dpi and reached an average final size of 15 – 20 µm (Figure 20 E). Furthermore, the hyperplasic tumor cells started to continuously

spread around the vasculature and dramatically increased in cell number during maturation of the tumor by reaching an average of up to 600 cells between the area of two primary veins in infected tumorous tissue (Figure 20 C, D, F). After 6 dpi bundle sheath cells completely disappeared in infected leaf tissue while the number of bundle sheath cells in mock treated leaf sections remained stable throughout maturation of the leaf (Figure 20 F).

In summary three major cellular rearrangements were observed during tumor development via histological analysis. Bundle sheath cells started an internal cell division at around 4 dpi and get completely transformed into hyperplasic tissue in infected leaf areas (Figure 20). A new form of cell type, the hyperplasic tumor cells replaced the bundle sheath cells (Figure 20). This cell type was tremendously increasing in number and therefore defined a hyperplasic tissue around the vasculature of secondary veins inside a developing tumor (Figure 20). The third cellular rearrangement occurred in the mesophyll tissue. Mesophyll cells started to strongly increase in size via hypertrophic cell growth without cell division (Figure 20). Growth of *U. maydis*-induced leaf tumors is therefore defined by two different tumor cell types resulting from hyperplasia of bundle sheath cells and hypertrophy of mesophyll cells.

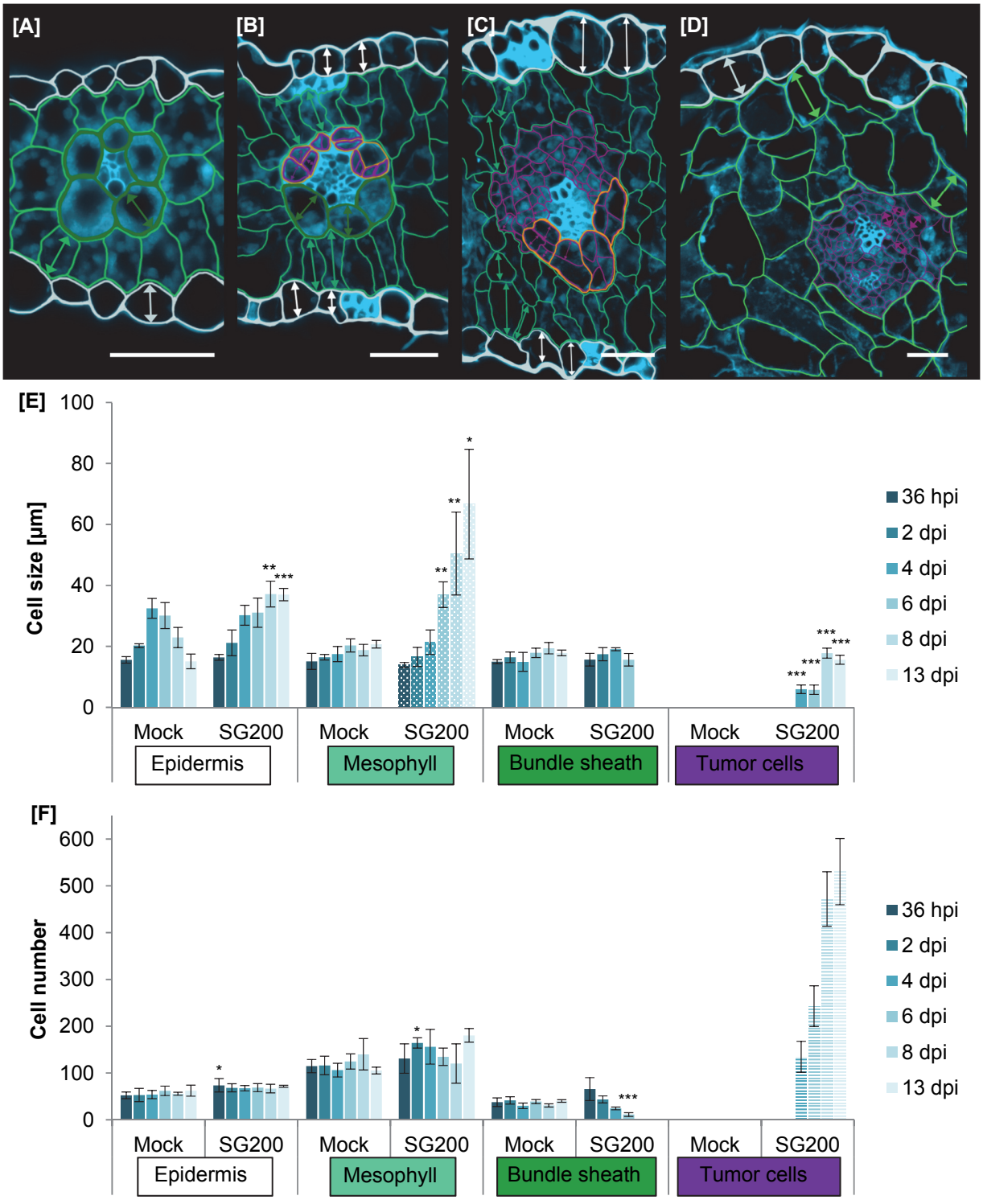

Figure 20: Overview of the most prominent morphological cell rearrangements with cell size measurements and cell counting upon *U. maydis*-induced leaf tumor formation

[A-D] Pictures show leaf tissue sections taken with a filter for cell wall autofluorescence. Cell types of interest are color coded. White: epidermis; light green: mesophyll / hypertrophic tumor cells; dark green: bundle sheath cells; orange: bundle sheath cells with internal cell division; purple: hyperplasic tumor cells; scale bars = 50 µm; Arrows indicate areas of cell diameter measurements; **[A]** Representative picture of a mock treated leaf section, 4dpi; **[B]** SG200 infected leaf section 4 dpi showing induction of hyperplasic cell division (purple); **[C]** SG200 infected leaf section 6 dpi showing hyperplasic tissue expansion (purple) **[D]** SG200 infected leaf section 8 dpi showing swelling mesophyll tissue / induction of hypertrophy (light green); **[E]** Cell size measurement and **[F]** cell counting in leaf sections from 36 hpi – 13 dpi for epidermis, mesophyll, bundle sheath cells and tumor cells. Results represent the mean ± SD from three independent biological replicates of infection experiments with SG200. Asterisks indicate data sets significantly different between SG200infected compared to mock treated tissue of the same time point. P-values were calculated using the unpaired student's t-test; *: p≤ 0.05, **: p≤ 0.01, ***: p≤ 0.001.

2.4.5 Activation of DNA synthesis induces cell division in bundle sheath cells via See1

Upon leaf tumor induction *U. maydis* reactivates the cell cycle for induction of cell division that leads to tumor formation (see chapter 2. 4. 4). Reactivation of the cell cycle and induction of hyperplasic cell division around the vasculature in this young but nonetheless determined and non-dividing tissue furthermore involves the activation of host DNA synthesis (Redkar et al., 2015a). Histological analysis revealed that hyperplasic tumor cells originate from bundle sheath cells (see chapter 2. 4. 4). In order to locate the site of hyperplasic tumor cell induction on the molecular level, DNA synthesis was monitored *in planta* via the 5-ethynyl-2-deoxyuridine (EdU) staining method. With this method, a thymidine analog can be imaged via Click-It chemistry (Kotogany et al., 2010). A previously established EdU protocol (Redkar and Doehlemann, 2016a) was adapted and combined with paraplast embeddings after EdU incorporation *in vivo* for 5 hours. Subsequent histological propidium iodide (PI) co-staining for visualization of the nuclei was then applied in combination with EdU. Mock treated and *U. maydis* infected maize leaves were treated with EdU during the stages of hyperplasic tumor cell induction at 3 dpi and 4 dpi. Also, a 5 dpi time point was included for the monitoring of hypertrophic tumor cell induction. In the EdU/PI stained leaf tissue sections cell borders were visualized by cell wall autofluorescence.

Mock treated leaf samples did not show any DNA synthesis events and nuclei in those sections were therefore only stained by PI (red) and no EdU staining (green) was detected (Figure 21 A). In contrast, EdU staining which is indicative for active DNA synthesis was observed in *U. maydis* infected bundle sheath cells already at 3 dpi (Figure 21 B). This

confirms the bundle sheath cells to be undergoing internal cell division and to be the origin of the resulting hyperplasic tumor cells (Figure 21 B).

In order to investigate if induction of tumor cell development is induced by cell type-specific effectors, the leaf-specific *U. maydis* effector knockout strain SG200Δsee1 was included in this study. See1 was previously found to interact with maize SGT1 and to be required for the induction of a DNA synthesis boost in infected host tissue detected by EdU staining at 4 dpi (Redkar et al., 2015a). Macroscopically, *U. maydis* SG200Δsee1-induced tumors are smaller compared to SG200-induced tumors but do not show any other morphological differences (Schilling et al., 2014). The leaf tumor cell anatomy as well as DNA synthesis events were studied upon infection with this effector knockout mutant in histological EdU-stained paraplast sections from 3 to 6 dpi (Figure 21 C). In contrast to *U. maydis* SG200-induced tumors (Figure 21 B), the SG200Δsee1-induced tumors mainly lacked hyperplasic tumor cell division around the vasculature in most of the tissue sections which was reflected by lack of EdU staining in bundle sheath cells even at 6 dpi (Figure 21 C). In contrast, SG200Δsee1 infected tissue showed active DNA synthesis in mesophyll cells already at 3 dpi (Figure 21 B). However, these DNA synthesis events were not linked to cell division in mesophyll tissue. The DNA synthesis events in SG200Δsee1 infected tissue led to early hypertrophy in mesophyll cells. Those hypertrophic mesophyll cells constitute the overall anatomy of SG200Δsee1-induced tumors which significantly differed from the SG200 situation (Figure 21 B).

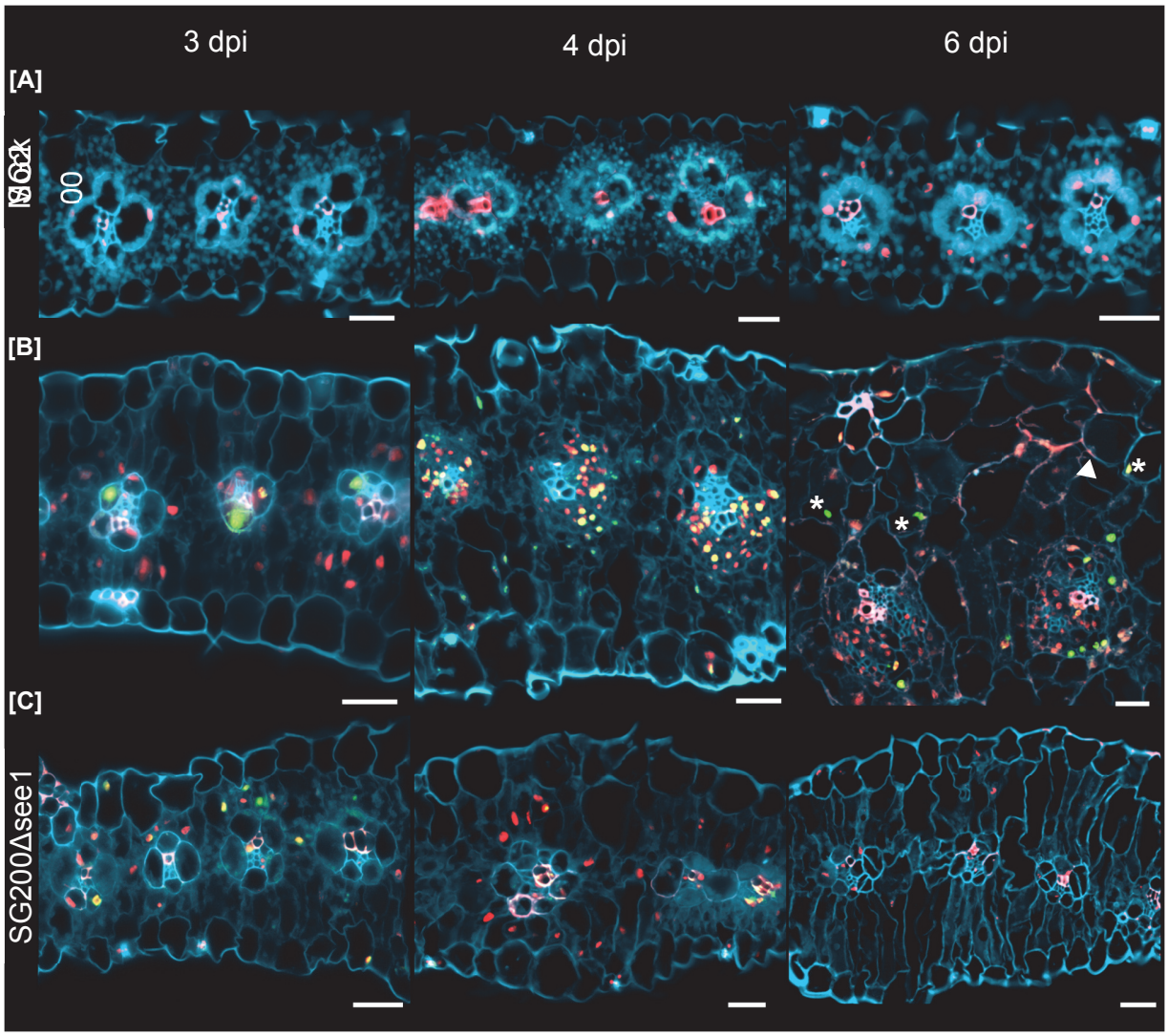

Figure 21: *In vivo* EdU incorporation and subsequent EdU visualization with Propidium iodide (PI) co-staining
[A-C] Pictures were taken with a filter for cell wall autofluorescence (425 250 nm) for visualization of cell walls overlayed with pictures taken with a green filter for visualization of AF488/EdU (455-490 nm) and a red filter for visualization of co-staining with PI (540-580 nm). **[A]** Mock treated leaf sections 3 dpi to 6 dpi; **[B]** SG200 infected leaf sections 3 dpi to 6 dpi, arrowheads indicate hypertrophic cell nuclei; **[C]** SG200Δsee1infected leaf sections 3 dpi to 6 dpi; scale bars = 50 µm; arrowhead indicates hypertrophic tumor cells. The experiment was repeated three times. Images show representative examples.

DNA synthesis events were also observed in hypertrophic SG200-induced tumor cells that originate from mesophyll tissue at later timepoints (Figure 21 B, asterisk). This is in line with hypertrophy of mesophyll cells that were observed to enlarge upon tumor maturation after 6 dpi (Figure 20 B).

2.4.6 Hypertrophy of mesophyll cells is linked to endoreduplication

The process of endoreduplication can be proportionately related to an increase in nuclear size (Chandran et al., 2010; Chandran et al., 2013). A doubling in nuclear size was defined to reflect one round of nuclear endoreduplication in maize cells (Barlow, 1985). Callow (1975) associated the *U. maydis*-induced hyperplasic maize tumor cells to endoreduplication due to an increase in nuclear size. However, the events of endoreduplication and hypertrophy had not been assigned to any specific cell type. In order to test if the early DNA synthesis observed in the mesophyll of SG200Δsee1 infected tissue (Figure 21 C) is linked to endoreduplication, nuclear size measurements were carried out in PI stained tissue sections (Figure 22). In line with the early development of hypertrophic mesophyll cells in SG200Δsee1 infected tissue at 4 dpi (Figure 21 C) nuclear sizes of mesophyll cells were increased compared to nuclei of mock treated and SG200 infected tissue sections (Figure 22). Hypertrophic mesophyll cells in SG200 infected tissue were developed at 6 dpi which coincided with an increase in nuclear size in mesophyll tissue compared to mock treated tissue at this time point (Figure 22). Bundle sheath cells and the resulting hyperplasic tumor cells did not show hypertrophy and concomitantly their nuclear sizes stayed unchanged in both SG200Δsee1 as well as SG200 infected tissue compared to mock treated tissue (Figure 22).

Together, nuclear size measurements confirmed that hypertrophy in mesophyll cells is linked to endoreduplication. Moreover, it points towards a function of See1 as a cell type-specific *U. maydis* effector that is required for the induction of hyperplasia in bundle sheath cells but dispensable for hypertrophy and endoreduplication in mesophyll cells.

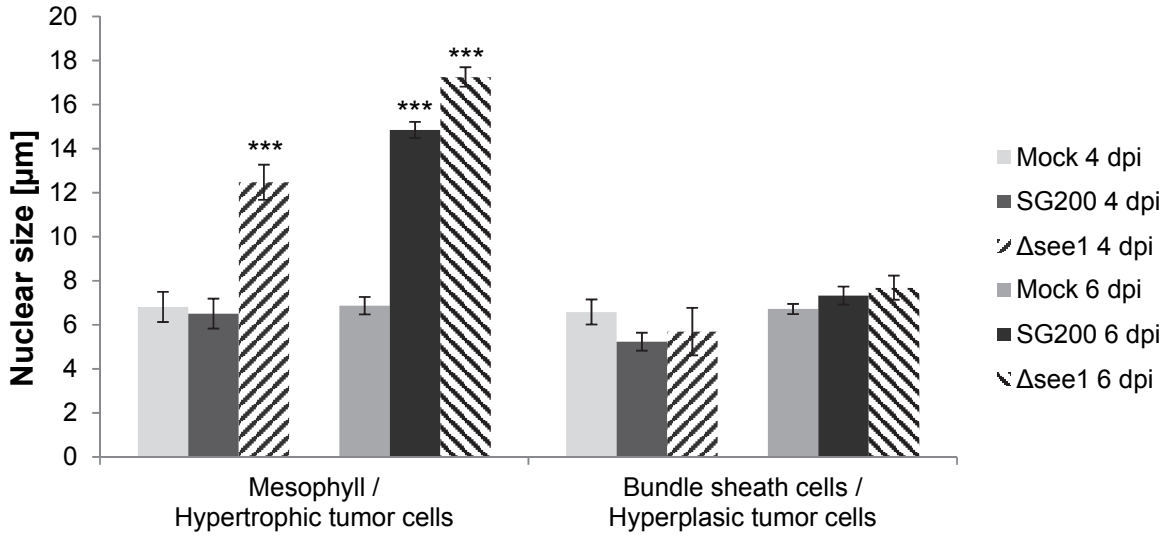

Figure 22: Cell type-specific nuclear size measurements in propidium iodide (PI) stained leaf tissue sections at major tumor development stages
Data shows nuclear size measurements 4 dpi and 6 dpi in mock treated, SG200 infected and SG200Δsee1 infected PI stained leaf tissue sections. Analyzed cell types included Mesophyll and resulting hypertrophic tumor cells, as well as bundle sheath cells and resulting hyperplasic tumor cells. A minimum of 70 nuclei was measured per tissue type. Results represent the mean ± SD from three independent leaf sections per biological replicate. Two independent biological experiments were performed. Asterisks indicate statistical significance of nuclear size compared to mock treated tissue of the same age. P-values were calculated using the unpaired student's t-test; ***: p≤ 0.001.

As stated in chapter 2. 2, the virulence defects of all organ-specific effector deletion mutants investigated in this study including SG200Δsee1 were rather mild (Table 2). Reduction in virulence was reflected by the formation of smaller tumors compared to SG200 (see chapter 2. 2, Figure 7). To investigate whether the SG200Δsee1 tumor morphology (showing a strong decrease in hyperplasic tumor cells) is See1-dependent or a general effect related to virulence reduction, SG200Δsee1-induced tumor morphology was compared to the SG200Δsts1-induced tumor morphology (Figure 23). Tumor morphology of both organ-specific mutants was compared to the morphology of SG200-induced tumors at 8 dpi when the tumor was established (Figure 23). Despite the reduced virulence of the SG200Δsts1 mutant, tumor morphology was found to be similar to SG200-induced tumors. Hypertrophic as well as hyperplasic tumor cell areas were found in both SG200 as well as SG200Δsts1-induced leaf tumors. Overall, this further substantiates the cell type-specific function of See1.

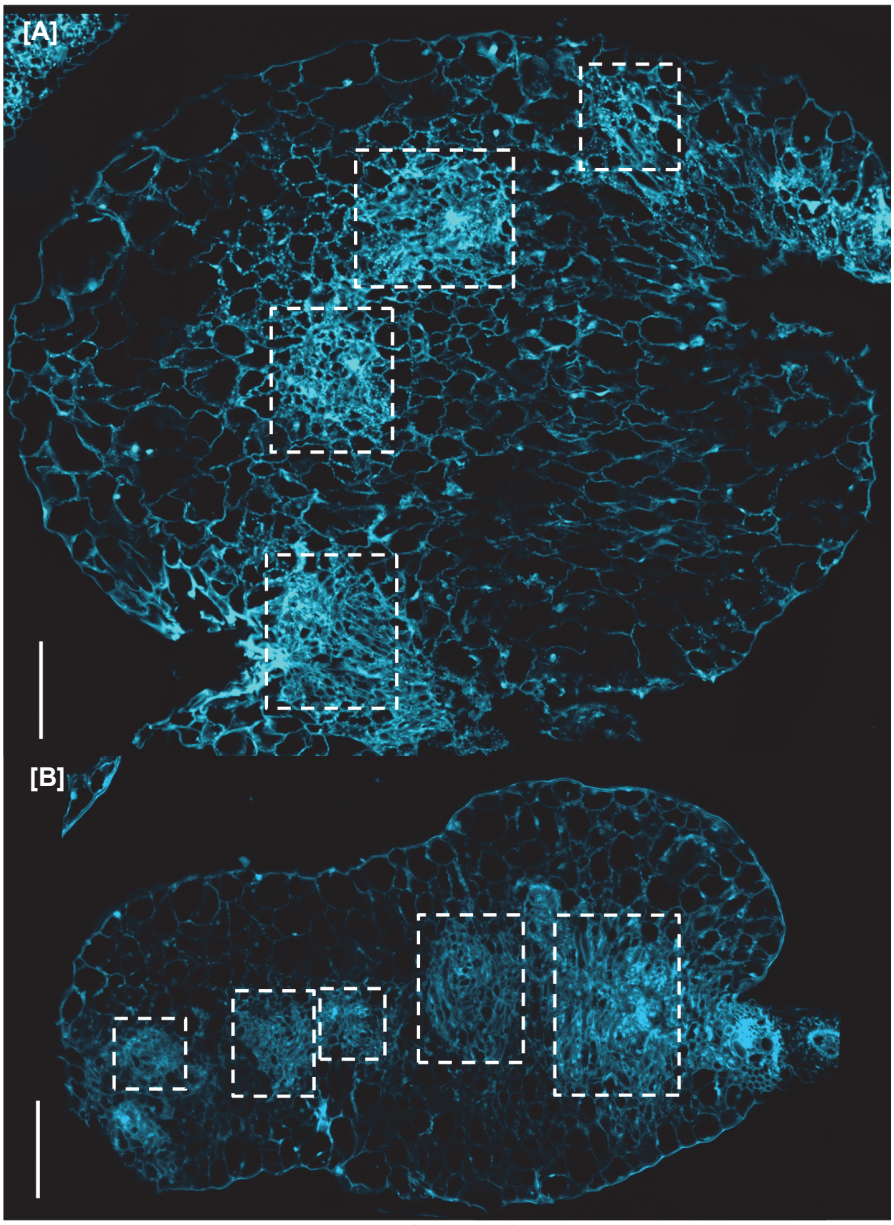

Figure 23: *U. maydis*-induced leaf tumor formation on the cellular level in SG200 and Sts1 infected tissue

Pictures show leaf tissue sections taken 8 dpi in which hyperplasic tumor cells are marked by dash-lined squares. Tissue sections were made from three independent biological replicates of infection experiments; **[A]** *U. maydis* SG200 infected leaf section 8 dpi; **[B]** *U. maydis* SG200Δsts1 infected leaf section 8 dpi; scale bars = 200 µm.

2.5 Investigation of cell type-specific effector genes by laser capture microdissection

In order to elucidate if the cell type-specific processes are reflected by differential expression of *U. maydis* effectors a transcriptomics approach was done. For isolation of different types of tumor cells, laser capture microdissection was applied. Samples were prepared at 4 dpi, because this time point was identified as the start of hyperplasic tumor cell development and morphological reorganization of infected leaf tissue (see chapter 2.4.4., Figure 20). Hypertrophy in mesophyll derived tumor cells in SG200 infected tissue was not yet established at this timepoint. The chosen tissue types of interest were mesophyll cells and bundle sheath cells for mock treated leaf tissue (Figure 24 A, B). From SG200 infected leaf sections, mesophyll (tumor-) cells that reside in infected areas (Figure 24 C) as well as bundle sheath-derived hyperplasic tumor cells were selected (Figure 24 D). Furthermore, hypertrophic mesophyll tumor tissue from SG200Δsee1 infected leaf sections was selected. For laser capture microdissection, leaf tissue of third maize leaves was cryofixed and embedded in compound for frozen sections. After preparation of cryomicrotome sections, tissue sections were dehydrated in methanol. Laser microdissection of around 2000 selected spots/cells per tissue type (Figure 24) was done, followed by RNA extraction and subsequent RNAseq analysis. Each one plant was fixed per sample and therefore three individual plants were used per treatment for the dissection of tissue types and RNA extraction.

RNAseq analysis of the dissected samples revealed the expression pattern of *U. maydis* genes in the three different cell samples. Analyses have been performed with DESeq (Anders and Huber, 2010). The *U. maydis* genome encodes 6776 annotated genes (Kämper et al., 2006) out of which 1315 were found to be expressed in SG200 infected hyperplasic tumor cells bearing a p adj value <0.1 compared to samples from uninfected tissue while 2927 genes were found to be expressed in SG200 infected mesophyll tumor cells at 4 dpi. 1520 of all *U. maydis* genes were expressed in SG200Δsee1 infected mesophyll cells. The overall transcript abundance of all read counts in RNAseq data revealed that the dissected samples contained different amounts of fungal transcripts with an average of 0.5 % fungal reads in SG200 infected hyperplasic tumor cells, and 2.7 %

fungal reads in SG200 infected mesophyll tumor cells. Fungal transcript abundance in SG200Δsee1 infected hypertrophic tumor cells was 1 %.

In a next step, all previously identified organ-specific effector genes and their corresponding average reads per kilo base of mapped reads were summarized (Table 4). Out of the leaf-specific effector genes that were previously identified (Schilling et al., 2014) *um02239* (See1) and *um05318* were exclusively expressed in SG200 infected mesophyll tumor cells but no transcript abundance was detected in hyperplasic tumor cells 4 dpi (Table 4). Furthermore transcript abundance of *um02239* (See1) was very low in SG200 infected mesophyll tumor cells and not present in SG200 infected hyperplasic tumor cells. *Um06127*, *um12313*, *um12217, um11060* and *um01690* transcript abundance was cell type specifically induced in SG200 infected mesophyll cells, while *um11030*, *um05306*, *um05495*, *um06222*, *um01829* and *um05223* did not show any cell type-specific difference in transcript abundance between SG200 infected mesophyll or hyperplasic tumor cells at 4 dpi (Table 4, Annexure Figure 31).

Surprisingly, the leaf-specific effector *um05311,* which was identified to contribute to tumor formation in leaves (Schilling et al., 2014), was not detected to be transcribed, neither in SG200 infected hyperplasic, nor in mesophyll tumor cells (Table 4). In contrast, *um03046* which was found to be required for tassel tumors (Schilling et al., 2014) was transcriptionally induced in mesophyll cells 4 dpi compared to hyperplasic tumor cells, while its transcription was reduced in SG200Δsee1 infected hypertrophic tumor cells (Table 4). *Um03650* which was also identified to contribute to virulence in tassel (Schilling et al., 2014) was interestingly found to be exclusively expressed in mesophyll tumor cells but not in hyperplasic tumor cells 4 dpi (Table 4). The tassel-specific effector gene *um05439* was not detected in any leaf cell type, confirming its prior classification as a tassel exclusive gene (Table 4).

Interestingly, transcript abundance of the previously identified leaf-specific effectors in SG200Δsee1 infected hypertrophic tumor cells strongly differed from SG200 infected mesophyll tumor cells (Table 4, Annexure Figure 31). Interestingly, SG200Δsee1 transcriptional induction of effector genes in SG200Δsee1 infected hypertrophic tumor

cells showed a very individual pattern that was completely different from SG200 infected mesophyll tumor cells and SG200 infected hyperplasic tumor cells.

The previously characterized *U. maydis* effector genes including Pit2, Pep1, Tin2 and Cmu1 (Djamei et al., 2011; Hemetsberger et al., 2012; Mueller et al., 2013; Tanaka et al., 2014) were commonly expressed in both hyperplasic and hypertrophic *U. maydis* SG200 infected tumor cells (Table 4). However, Pep1, Tin2 as well as Cmu1 showed a stronger expression in SG200Δsee1 infected hypertrophic tumor cells (Table 4).

Cell type-specific gene expression pattern between SG200 infected hyperplasic and mesophyll tumor cells was observed to occur for further individual effector genes randomly spread among all 546 *U. maydis* genes that are predicted to encode for candidate secreted effector proteins (Figure 25; Dutheil et al., 2016). Out of all 156 *U. maydis* effector genes that are organized in clusters (Kämper et al., 2006; Dutheil et al., 2016), SG200 effector gene expression pattern between hyperplasic tumor cells and mesophyll tumor cells also revealed a cell type-specific expression for individual effector genes (Annexure Figure 32). However, this did not correlate with any specific gene cluster (Annexure Figure 32).

All in all, this transcriptome analysis has shown that *U. maydis* deploys core effector genes which are constantly expressed independent of the leaf cell type during tumor induction, while a second set of effector genes exists that is differentially regulated depending on the leaf cell type. The SG200Δsee1 strain on the other hand does furthermore express a completely different set of effector genes compared to mesophyll cells infected by its progenitor strain SG200 at the same timepoint.

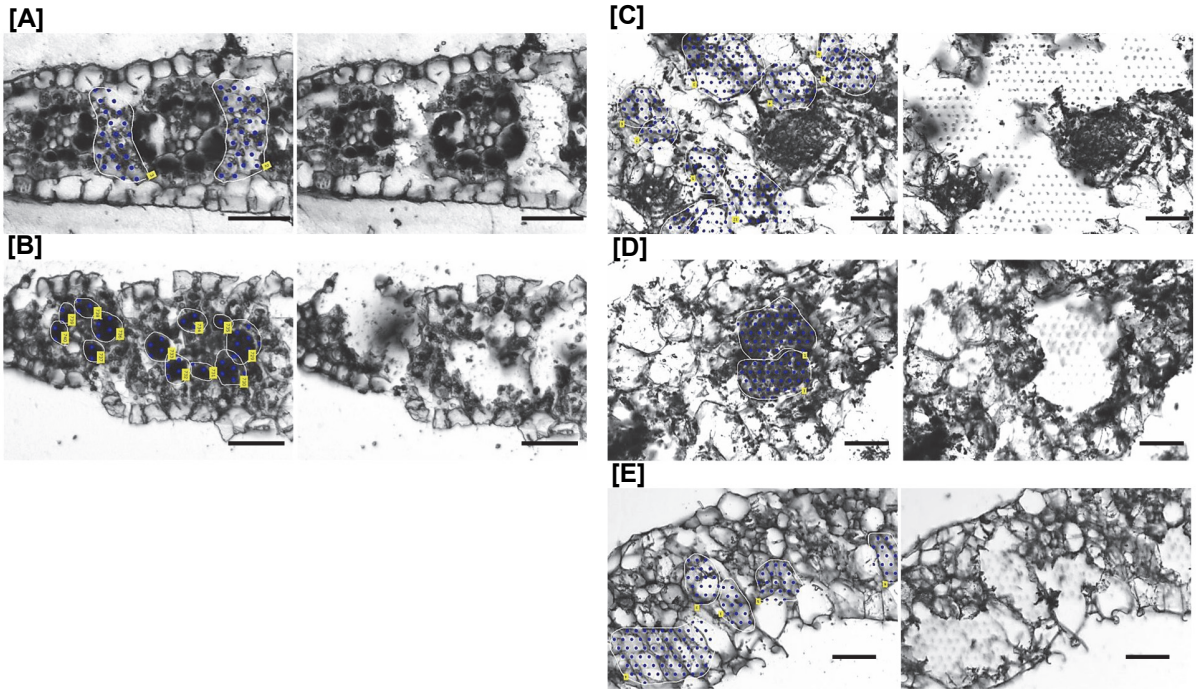

Figure 24: Selected tissue types 4 dpi for laser capture microdissection
Representative pictures for each tissue type are shown. The third leaf of one plant was fixed per sample and three individual plants were used per treatment for the dissection of tissue types. For each sample ~2000 selected spots were dissected. **[A]** Selected mesophyll spots before and after microdissection in mock treated samples; **[B]** selected bundle sheath cell spots before and after microdissection in mock treated samples; **[C]** selected mesophyll spots before and after microdissection in SG200 treated samples; **[D]** selected tumor cell spots before and after microdissection in SG200 treated samples; **[E]** selected spots of hypertrophic tumor cells before and after microdissection in SG200Δsee1 treated samples. Scale bars = 50 µm. **[F]** Venn diagram showing numbers of *U. maydis* effector gene transcripts 4 dpi bearing a coverage of ≥ 1 reads per kilobase of mapped reads in SG200 infected mesophyll seedling leaf cells (green), SG200 infected hyperplasic tumor seedling leaf cells (purple) and SG200Δsee1 infected hypertrophic seedling leaf cells (grey).

Table 4: List of organ-specific and previously characterized effector genes (core effectors) and their cell type-specific reads per kilo base of mapped reads in infected, dissected maize tissue types (4 dpi) including the respective p adjust values relative to uninfected leaf cells.

	Reads per kilo base of mapped reads 4 dpi and respective p adj values

	U. maydis gene number	Annotation	SG200 infected hyperplasic tumor cells	p adj	SG200 infected mesophyll cells	p adj	SG200 Δsee1 infected hypertrophic mesophyll cells	p adj
Leaf -specific effectors	UMAG_05318	hypothetical protein	0	0.3196	23.4282	0.0398	788.796	0.0004
	UMAG_02239	See1	0	NA	5.04945	NA	0	NA
	UMAG_06127	hypothetical protein	16.671	0.4844	141.35	0.0001	1821.64	1.26E-07
	UMAG_12313	hypothetical protein	238.586	0.0027	441.899	5.55E-05	1388.69	5,51E-06
	UMAG_12217	hypothetical protein	397.145	1.71E-09	721.291	3.55E-12	575.685	9.85E-08
	UMAG_11060	hypothetical protein	102.708	0.0511	198.449	0.0002	104.519	0.0386
	UMAG_01690	Sts1	434.583	8.32E-05	563.48	1.65E-08	4264.7	1.18E-11
	UMAG_01130	hypothetical protein	529.138	7.29E-05	512.573	4.51E-07	919.42	5.12E-06
	UMAG_05306	hypothetical protein	2152.47	3.13E-07	2491.19	3.47E-07	2042.49	4.00E-07
	UMAG_05495	hypothetical protein	1773.52	9.40E-11	1949.81	1.86E-19	15.6644	8.81E-07
	UMAG_06222	hypothetical protein	238.561	0.0319	292.171	0.0002	748.268	1.70E-05
	UMAG_01829	alpha-L-arabinofuranosidase	2226.6	8.80E-16	2305.52	2.16E-24	6787.78	1.06E-16
	UMAG_05223	related to beta-1,6-glucanase	318.184	0.0002	313.83	0.000002	2115.32	2.04E-11
	UMAG_10553	hypothetical protein	108.921	NA	80.5765	0.00494	228.127	0.00927
	UMAG_11763	related to acetylxylan esterase	4.4204	NA	3.57892	NA	0.000291767	2.69E-05
	UMAG_06223	hypothetical protein	156.643	0.6145	22.266	0.0902	4050.83	9.93E-09
	UMAG_05311	hypothetical protein	-	0.208	-	0.00424	-	0.07
Tassel	UMAG_03046	hypothetical protein	7739.25	3.21E-27	9944.7	7.74E-54	316.049	0.0104

	UMAG_03650	hypothetical protein	0	0.1118	12.8521	0.0006	0	NA
	UMAG_05439	related to chitin binding protein	-	8.59E-06	-	0.000001369	-	NA
Core effectors	UMAG_05302	Tin2	396.987	NA	356.935	9.43E-05	2484.27	3.38E-07
	UMAG_01375	Pit2	3202.81	1.21E-08	2657.78	6.65E-12	2652.08	1.14E-07
	UMAG_01987	Pep1	365.718	0.0081	547.237	0.0000155	896.204	0.000101
	UMAG_05731	Cmu1	27944.3	8.44E-29	22073.3	9.30E-43	45342.8	4.09E-20

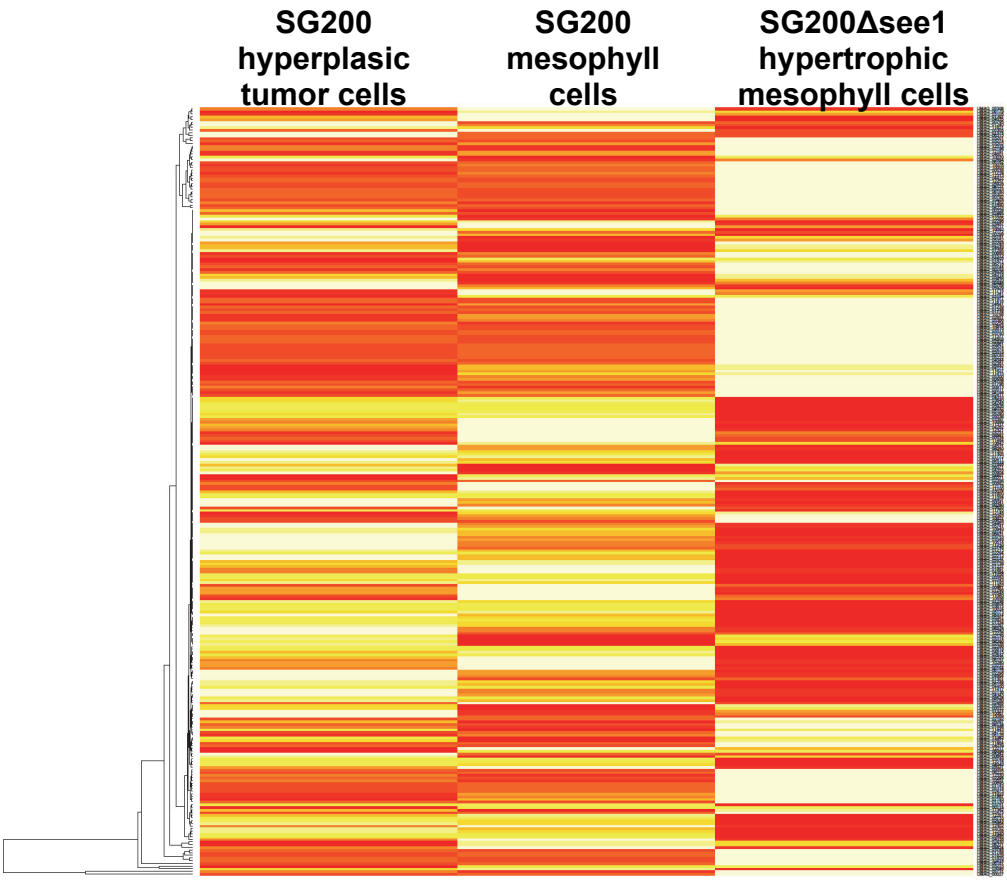

Figure 25: Heatmap representing gene expression of all *U. maydis* effector genes (Dutheil et al., 2016) in dissected maize leaf cells 4 dpi with an adjusted p value <0.05 resulting from DESeq analysis (Anders and Huber, 2010).

3 Discussion

3.1 Organ specificity in the *U. maydis* – maize interaction

In this work, *U. maydis* effectors were identified that showed an organ-specific contribution to virulence. It is shown that *U. maydis* deploys individual effectors for colonization of different organs while seven effector genes that are required for full virulence in seedling and two tassel-specific effector genes were identified (Schilling et al., 2014). This correlates with previous microarray transcriptome data which showed that more effector genes were specifically expressed in seedling compared to tassel tissue (Skibbe et al., 2010). In order to form tumorous tissue, the fungus needs to promote cell proliferation which is thought to be achieved by secretion of effector proteins. Interestingly, the fungus deploys less tassel-specific effector genes than leaf-specific effector genes which might be due to the fact that the flower tissue is actively proliferating tissue in contrast to leaf tissue (Schilling et al., 2014; Skibbe et al., 2010).

Deletion of two seedling-specifically expressed genes *um06223* and *um12217* caused virulence reduction in both organs (Table 1). However, deletion of *um06223* led to a growth defect of *U. maydis* in axenic culture (Figure 8). The general reduction in fitness likely explains the virulence defects of this strain. Although *um12217* is significantly higher expressed in seedling and was therefore selected as an organ-specifically expressed gene, it is also expressed in tassels, 3 dpi (Figure 6). Deletion of *um12217* did not cause a general fitness reduction in contrast to *um06223*. *Um12217* therefore encodes an effector protein that contributes to general virulence with no organ-specific role.

The diversity of plant cell wall fine structures has led to a diversification of secreted fungal glycosyl hydrolases (Annis and Goodwin, 1997). It is to state that most of the functionally predictable leaf-specific candidate genes encode proteins that are predicted to contribute to cell wall degradation. Cell wall degrading enzymes are known to be secreted during penetration of the plant surface and described to enable *U. maydis* to enter the leaf surface as this fungus does not build out melanized appressoria that penetrate via pressure (Schirawski et al., 2005). Furthermore, Lanver et al. (2014) have described a

transcriptional upregulation of cell wall degrading enzymes including *um01829* during early stages of *U. maydis* disease progression. However, only the deletion of the leaf-induced gene *um01829* led to a reduction in virulence implicating that most of the cell wall degrading enzymes might be redundant and their loss would therefore not impair fungal virulence (Schilling et al., 2014). *Um01829* encodes an α-L arabinofuranosidase and is a xylane-degrading enzyme that cleaves arabinose residues (Schilling, 2015; Schilling et al., 2014). Arabinoxylan is enriched in grass cell walls and described to function in linking the cellulose microfibril network and thereby providing rigidity to plant cell walls (Carpita, 1996; Carpita et al., 2001). Interestingly the arabinoxylan-cellulose interaction in grass cell walls is reported to be the likeliest target for cell wall loosening (Sampedro et al., 2015) implicating a similar function for Um01829 in cell enlargement during tumor formation. However, it is not yet investigated why Um01829 functions in an organ-specific manner and why other cell wall degrading enzymes are transcriptionally upregulated in leaves but not in tassel. This would require the tissue-specific comparison of cell wall composition between leaves and anthers in order to investigate a specific requirement of cell wall degrading enzymes.

Except *um01829*, all effector genes that showed a contribution to organ-specific virulence encode proteins without predictable functional domains (Table 1). All organ-specific mutants exhibited a quantitative virulence reduction with tumors that are reduced in size and number but not absent (Figure 7). Previously described *U. maydis* effector knockout mutants that fail to induce tumors were found to target essential plant immune system components as they fail to efficiently colonize leaves (Hemetsberger et al., 2012; Mueller et al., 2013). Effector proteins in the biotrophic pathogen *U. maydis* can therefore broadly be grouped into two major groups. The first group consists of core effectors that are essential for the establishment of the biotrophic interaction and function in the suppression of the plant's innate immune system (Doehlemann et al., 2008a). The fungus furthermore needs to acquire nutrients for growth and the successful completion of its life cycle. This nutrient acquisition and following spore maturation is known to be accompanied by tumor formation in all aerial organs. Tumor formation requires extensive cell division. In order to promote cell division for tumor induction in diverse tissues,

U. maydis deploys the here identified organ-specific effectors (Schilling et al., 2014) including See1 which was previously described to perturb host cell cycle control in order to reinitiate cell cycle progression in leaves (Redkar et al., 2015a). Upon progression throughout the tissue, the fungus encounters different cell types depending on the colonized organ which can bear diverse physiological and nutritional stages (Gao et al., 2013; Walbot and Skibbe, 2010). This implicates that the more adapted a pathogen is towards diverse organs and tissue types, the more flexible it has to be in terms of its effector weaponry. With See1 being involved in the re-initiation of cell division (Redkar et al., 2015a) and Um01829 being involved in cell wall degradation (Schilling, 2015), Sts1 was the third organ-specific effector chosen for functional characterization.

3.2 *U. maydis* Sts1 interaction with *Zea mays* carboxypeptidase II (CBPII)

Yeast II hybrid (Y2H) screening has identified the splicing variants of maize glutamate carboxypeptidase II (CBPII) T01 and T02 as potential interactors for Sts1. However, in re-transformation experiments with full length CBPII T01/ T02 and Sts1, growth of yeast strains was only observed on medium stringency selection plates but not on high stringency selection plates. A loss of interaction on high stringency media with a potential host factor fished via Y2H screening was independently also observed by A. Redkar when performing the Y2H screening for See1. Interaction of See1 with maize SGT1 was not reproducible with full length maize SGT1 in yeast (Redkar, 2014). A possible reason might be wrong posttranslational processing of plant proteins in yeast that lead to misfolding of the protein and therefore hamper correct interaction and growth of the auxotrophic yeast strain on selection media.

CBPII is a yet uncharacterized protein in maize. However, a second glutamate carboxypeptidase has been identified, maize VIVIPAROUS8 (VP8), which regulates the development of shoot apical meristem (SAM) contributing to embryo and endosperm development (Suzuki et al., 2008). The maize VP8 protein is localized to the endoplasmic reticulum (ER) and furthermore required for maize internode elongation thereby controlling plant height by promoting cell proliferation (Lv et al., 2014). *A. thaliana AMP1* (*A*ltered *m*eristem *p*rogram*1*) is an *Arabidopsis thaliana* orthologue of *VP8* (Suzuki et al.,

2008). The Arabidopsis *AMP1* gene encodes for a glutamate carboxypeptidase which is described to regulate small signaling molecule levels that control plant development (Helliwell et al., 2001). Developmental SAM defects in *AMP1* orthologs of maize (*VP8*), rice (*Oryza sativa*) and *Lotus japonicus* are very similar pointing towards a conserved function of this carboxypeptidase in plants (Kawakatsu et al., 2009; Suzaki et al., 2013; Suzuki et al., 2008).

Together with the maize glutamate carboxypeptidase II, maize VP8 and AMP1 are members of the M28B family of carboxypeptidases (MEROPS ID: M28.007 for VP8 and AMP1; MEROPS ID: M28.010 for CBPII; Poretska et al., 2016). Those family members consist of metalloproteases that share several protein motifs: N-terminal transmembrane domain (lacking in CBPII T02), a protease-associated domain and a transferrin receptor dimerization domain (MEROPS database, http://merops.sanger.ac.uk, Rawlings et al., 2016). The transmembrane domain leads to ER associated localization and might be a reason for failed reproduction of growth on Y2H high stringency medium with the full length protein. A biochemical understanding of the function of these domains in planta is still lacking. Shorter fragments of the carboxypeptidase lacking the transmembrane domain might be able to interact with Sts1 in yeast. The above named three protein domains including the protease associated domain, the peptidase domain as well as the TFR dimer would therefore need to be separately cloned and tested in yeast II hybrid experiments.

Co-IP experiments with transiently expressed Sts1-cMyc with CBPII-HA T01/T02 in *N. benthamiana* supports an *in planta* interaction of Sts1 and maize carboxypeptidase. However, when trying to corroborate this finding via BiFC assays, expression of mCherry-tagged CBPII T01/T02 was in both cases very low and hardly detectable with confocal microscopy although expression was driven by the cauliflower mosaic virus 35S promoter (Odell et al., 1985). This could indicate that overexpression of this protein is toxic to plant cells and therefore CBPII is not produced in a high amount in *N. benthamiana*. Overexpression of CBPII T01/T02 in *N. benthamiana* points towards an ER-associated localization of the maize carboxypeptidase as predicted by the MEROPS database.

However, the BiFC method is not applicable for an interaction test because Sts1 expression together with the empty SPYCE vector led to an autoactivated YFP signal.

Preliminary data from co-expression experiments of fluorescently labeled CBPII T01/T02-mCherry with STS1-GFP might suggest a stabilization of CBPII by STS1 (Annexure Figure 29). However, this was only seen in heterologous expression experiments in tobacco and might have resulted from fluorescence spectra overlaps between the fluorescently labeled proteins. Influence of Sts1 on protein stability of CBPII T01/T02 would therefore have to be verified via Western blot experiments.

Both Sts1 as well as CBPII T01/T02 can be heterologously expressed in *E. coli* (Annexure Figure 30). This would allow *in vitro* stability experiments for CBPII. It would be very interesting to test if Sts1 has an influence on CBPII T01/T02 stability or whether it inhibits CBPII T01/T02 enzymatic function. It was previously described that *Arabidopsis* AMP1 exhibits similar predicted peptidic hydrolase activity as its human homolog Glutamate carboxypeptidase II (HsGCPII) which shares 28 % amino acid sequence identity with AMP1 (Poretska et al., 2016). The biochemical functions that are described for HsGCPII were not found to apply for *Arabidopsis* AMP1 (Huang et al., 2015). HsGCPII is described to exert several enzymatic atcivities depending on the tissues and it is interestingly strongly upregulated in prostate cancer cells while its exact function for tumor development are still unknown (Barinka et al., 2012). It might be that maize CBPII has a higher functional redundancy towards HsGCPII than *Arabidopsis* AMP1 which would enable the use of previously developed enzymatical assays for the investigation of maize CBPII. *E. coli* expressed CBPII T01/T02 could be used for testing catalytic activity against the HsGCPII substrates NAAG and poly-y-L-glutamic acids (Pangalos et al., 1999). Furthermore, known inhibitors of HsGCPII that were previously identified (Zhou et al., 2005) could be tested for their function on maize CBPII.

Deletion of AMP1 in *Arabidopsis thaliana* led to hypertrophy in meristematic zones (Vidaurre et al., 2007). It would therefore be interesting to investigate whether Sts1 acts on maize CBPII during tumor development in a tissue-specific manner to support hypertrophic tumor cell formation.

3.3 Physiological changes in *U. maydis* infected leaf tissue upon tumor formation

3.3.1 The influence of *U. maydis*-induced tumor formation on cell wall lignification

The observation of *U. maydis*-induced leaf tumors being morphologically restricted in their expansion by primary leaf veins has pointed towards a function of lignin as a preformed barrier in tumor restriction. Primary leaf veins contain vascular elements that function in water transport and their cell wall composition is known to comprise enhanced lignin content for morphological stability under negative water pressure (Jones et al., 2001; Piquemal et al., 1998). Lignin which is usually required for the reinforcement of vascular tissue is furthermore deposited in cell walls as a response to pathogen attack (Haegi et al., 2008; Sattler and Funnell-Harris, 2013). The observation of enhanced autofluorescence in primary veins upon *U. maydis*-induced tumor formation could therefore be linked to the accumulation of defense lignin. *U. maydis*-induced lignification of primary veins was substantiated by histochemical Safranin-O staining. The expansion of tumor formation throughout primary veins in the *brown midrip2* (*bm2*) lignin deficient line suggests that the lack of lignin as a preformed barrier leads to enhanced tumor spreading.

The maize *bm* mutants have long been described to bear reduced lignin contents (Jorgenson, 1931). The *Bm2* gene encodes for a 4-coumarate coenzyme A ligase (4CL), an enzyme involved in monolignol biosynthesis (Tang et al., 2014). Interestingly, *bm* mutant lines are in general described not to be more susceptible towards pathogens which might be due to an accumulation of lignin precursors and phenolic compounds that act toxic towards pathogens (Sattler and Funnell-Harris, 2013; Tesso and Ejeta, 2011). A similar symptom development of SG200 infected *bm2* mutant plants compared to the progenitor inbred line A619 was previously observed for *U. maydis* infection (Tanaka et al., 2014). It might therefore be that the defect of the *bm2* line in morphological tumor restriction initially results from a preformed barrier but this process seems to be independent of general resistance towards *U. maydis*. It is therefore likely that tumor size

does not directly correlate with fungal spreading and growth. In such scenario, tumor growth would then spread in the *bm2* leaves while fungal biomass might simultaneously be restricted by toxic lignin precursors. In order to investigate this, fungal biomass would have to be quantified in *bm2* infected plants and compared to fungal biomass in control lines. This would furthermore shed light on the aspect whether the cues for tumor induction might be regulated by an *U. maydis*-induced plant signal that is spreading independently of fungal growth.

The *U. maydis* effector Tin2 was found to suppress lignification of infected leaf veins by stabilizing the maize protein kinase ZmTTK1 which leads to inhibition of lignification and enhanced anthocyanin biosynthesis in infected tissue (Tanaka et al., 2014). Lignin and anthocyanin biosynthesis pathways are described to share a competitive interconnection (Fornalé et al., 2010; Ring et al., 2013). The increase of primary vein autofluorescence in *U. maydis* infected tissue coincides with a clogging of primary veins that surround the established tumors. Interestingly the anthocyanin overexpressing maize *bronze* (*bz*) mutant lines (purple maize) were described to accumulate anthocyanin in vacuoles leading to a clogging of veins by the oxidized pigment (McLaughlin and Walbot, 1987; V. Walbot, personal communication; Rhoades, 1952). Vessel clogging by plant cell wall components is since long described to be a plant response to fungal cell wall degradation (VanderMolen et al., 1983). Over-accumulation of anthocyanins might result from a suppression of lignification and therefore lead to the clogging of primary veins that was observed upon *U. maydis*-induced tumor formation.

At late stages of SG200 infection, formation of metaxylem was observed in tumorous leaf tissue. This phenomenon might physiologically be explained by a strong requirement for water supply inside tumorous tissue. The formation of metaxylem might compensate for impaired water transport due to primary vein clogging and helping the plant to resist *U. maydis*-induced drought stress conditions which result during tumor growth. In line with that, the fungal plant pathogen *Verticilium longisporum* was found to induce a tissue-specific transdifferenciation of *A. thaliana* bundle sheath cells into xylem elements for the restoration of water supply as vessels are clogged by fungal biomass (Reusche et al., 2012). A pathogen-induced reformation of host vascular tissue was previously also

described to occur in *Fusarium oxysporum* infected plants (Baayen, 1986). Interestingly, cells underlying the infection sites of *Golovinomyces orontii* showed an upregulation of genes involved in drought stress response pointing towards a higher demand for water supply in infected tissue (Chandran et al., 2010). Arabidopsis AMP1 was furthermore found to mediate abiotic stress responces to drought and regulate several hormone pathway signaling processes including abscisic acid (ABA) and auxin (Vidaurre et al., 2007) pointing towards a potential role of the above-discussed maize CBPII in metaxylem formation.

Lignin is an endproduct of the phenylpropanoid pathway and composed of three major monolignols: guaiacyl (G), *p*-hydroxyphenyl (H) and syringyl (S) phenylpropanoid units (Boerjan et al., 2003; Bonawitz and Chapple, 2010). In a trait-specific cell wall composition analysis enriched H and S monolignols were found to be linked to resistance against *Fusarium graminearum* in wheat (Lionetti et al., 2015). The previously described defense lignin was shown to comprise elevated levels of H monolignols (Doster and Bostock, 1988; Lange et al., 1995). The monolignol composition analysis performed in this work revealed a significant decrease in H lignin composition in chlorotic tissue indicating that defense lignin formation is suppressed upon *U. maydis* infection. However, tumorous tissue did not show changes in H lignin compared to mock infected tissue. This substantiates that no defense lignin is accumulating upon tumor formation. Poplar lines bearing higher syringyl lignin levels exhibit higher recalcitrance towards fungal degradation (Skyba et al., 2013). Interestingly, wheat plants were found to accumulate S lignin during the establishment of hypersensitive response reactions (Menden et al., 2007). Chlorotic tissue of *U. maydis* infected maize plants which often surrounds tumorous areas also contains areas of dead cells (Doehlemann et al., 2008a). Those chlorotic areas might therefore reflect a successful, local defense reaction against *U. maydis* leading to an enhanced S lignin level in this tissue which might restrict fungal spreading. In contrast, tumorous tissue showed lower S lignin content compared to chlorotic tissue which might indicate successful suppression of defense responses coinciding with tumor formation. However, S lignin levels in tumors still exceeded S lignin levels of mock infected tissue. Explanation for this might come from reports showing that

higher contents of S lignins result from cell wall loosening processes that need to occur upon hypertrophic tumor cell growth (Bonawitz and Chapple, 2010).

Together, lignin deposition is a very modular and local process upon pathogen attack which differs between chlorotic and tumorous tissue. Lignification seems to be implicated in the general restriction of *U. maydis*-induced tumor formation as its induction is known to be actively suppressed by *U. maydis* (Tanaka et al., 2014). However, based on the current knowledge it is not clear if lignification directly restricts fungal growth.

3.3.2 Hemicellulose composition in leaves changes upon *U. maydis* infection

Previous studies have shown a strong interconnection between cell wall composition and susceptibility in which hemicellulose and lignin composition were found to contribute to resistance against the wheat pathogen *Fusarium graminearum* (Lionetti et al., 2015). Grass cell walls mainly consist of hemicelluloses (55 %, Cosgrove, 1997) and generation of a hemicellulose content profile provided an overview of its most prominent changes upon *U. maydis* infection. Cell wall polysaccharides including hemicelluloses are thought to form a barrier against fungal invasion but the detailed role of hemicelluloses in plant defense is still under investigation (Malinovsky et al., 2014; Santiago et al., 2013). The changes in monosaccharide compositions of hemicellulose were investigated in this study in *U. maydis* infected leaf tissue. The measurement of hemicellulose composition revealed a *U. maydis*-induced increase in the monosugars arabinose and galactose while others such as xylose, fucose and rhamnose were decreasing in infected tissue.

The most abundant hemicellulose in maize is xylan (Carpita, 1996). This was also reflected in the monosaccharide composition analysis of this study with xylan being the most abundant monosaccharide in both mock treated and *U. maydis* infected tissue. Xylans can be substituted with arabinose sidechains, called arabinoxylans (AX) / glucoarabinoxylans (GAX) in case of additional substitution with glucuronic acid (Whistler and Richards, 1970). Upon *U. maydis* infection xylose content decreases while arabinose content is increasing. This might indicate a substitution of xylose sidechains with arabinose. Interestingly, glururonic acid levels do not change upon *U. maydis*

infections indicating an arabinose-specific change of AX/GAX. Influence on xylan integrity was previously described to occur upon pathogen attack as several phytopathogenic microbes secrete xylanases which are described to function in cell wall weakening for fungal cell penetration (Belien et al., 2006). The organ-specific alpha-L-arabinofuranosidase (Um01829) together with the predicted xylanase (Um11763) might function in cell wall weakening during *U. maydis* leaf infection. As *U. maydis* bears effectors that are predicted to be involved in cell wall degradation, cell wall degrading enzymes that would act in an organ-specific manner might enable *U. maydis* to respond to tissue-specific cell wall compositions. Secretion of degrading enzymes could therefore be kept to a minimum and avoid recognition by the plant's immune system if they are tissue- or even cell type-specifically regulated.

The 6 dpi timepoint was previously reported to bear a low amount of fungal biomass although tumors are already present at this stage of infection (Doehlemann et al., 2008b). A bias caused by fungal cell wall components in monosaccharide measurements was therefore mainly excluded as the fungal biomass is relatively low at this time point. Furthermore, formation of *U. maydis* mucilaginous layer has not occurred 6 dpi in SG200 infected tissue (see annexure Figure 28) and concomitantly chitin (measured as glucosamine monosaccharide in HPAE-PAD) was not present in detectable amounts in infected leaf tissue.

It is important to note that cell wall composition can vary between accession lines but also between different tissues and cell types inside a single plant (Hazen et al., 2003). The *U. maydis* effector ApB73 (Apathogenic in B73) was recently found to contribute to fungal virulence in a cultivar-specific manner indicating that effectors might not only act in an organ-specific but also cultivar-specific manner (Stirnberg and Djamei, 2016). Investigation of disease resistance in different maize cultivars including a potential relation to cell wall composition changes would help to identify and functionally characterize ApB73 and other potential cultivar-specific effectors. As cell wall composition varies between tissues and cell types, cell type-specific wall reformation processes might have been masked by cell wall composition analyses from whole tissue cell wall extracts. A cell type-specific cell wall composition analysis using the method of laser capture

microdissection of specific cell types followed by an oligosaccharide mass profiling method (OLIMP) (Guenl et al., 2010) could elucidate cell wall reformations upon *U. maydis* infection in a tissue-specific context.

3.3.3 *U. maydis* changes chloroplast dimorphism through chlorophyll degradation

Chlorophyll content in *U. maydis* infected tissue decreased already at 2 dpi. At this time point infected seedlings are 9 d old and the third leaf has just emerged and is starting to mature and turn into a source leaf (Li et al., 2010). In addition to the photosynthesis pigment decrease shown in this study Kretschmer et al. (2016) furthermore described a decrease in lutein and xanthophyll (violaxanthin, antheraxanthin or zeaxanthin) pigments in tumorous tissue. In line with the early chlorophyll decrease, *U. maydis* infected Lugol-stained leaf tissue sections show weaker starch accumulation at 2 dpi in bundle sheath cells than mock infected leaves. It is therefore possible that the early chlorophyll decrease in *U. maydis* infected tissue hinders the leaf in its maturation process from sink to source tissue resulting in impaired photosynthesis activity and resulting in reduced starch accumulation. Decrease of chlorophyll is strongest in tumorous tissue and also macroscopically visible due to its white appearance. Photosynthetically active chlorophyll with accessory pigments (carotenoids) is localized in mesophyll chloroplast membranes of C_4 plants. Inside the mesophyll of mature C_4 plants, thylakoids are organized in grana by forming stacks of several thylakoid membranes. While carbon fixing C_4 chloroplasts in bundle sheath cells only bear longitudinal thylakoid membranes, the mesophyll chloroplasts of C_4 plants do not fix carbon and bear a typical morphology of grana stacks that consist of stacked thylakoid membranes interconnected by stroma thylakoids (Kirchanski, 1975).

Interestingly, the light-harvesting chlorophyll *a/b*-protein complex was found to mediate membrane stacking of chloroplast thylakoids in mesophyll chloroplasts (Ryrif et al., 1980). The observed early decrease of photosynthesis pigments might be required for breaking the interconnection of thylakoid/grana stacks mediated by the light-harvesting chlorophyll *a/b*-protein complexes to enable starch accumulation inside mesophyll chloroplasts. Experiments in this study have shown that starch is mainly accumulating in chloroplasts

of mesophyll cells of tumorous areas. Starch accumulation in mesophyll chloroplasts is very untypical for grass leaves as their chloroplasts exert a dimorphism with mesophyll and bundle sheath cells executing different physiological functions and morphological structures (Kirchanski, 1975).

Starch accumulation in chloroplasts of infected tissue before the onset of tumor formation was already described in early *U. maydis* studies but was not assigned to any cell type (Callow and Ling, 1973). The same study reported a decrease of chloroplasts upon maturation of the tumor. However, Lugol staining and TEM microscopy showed that mesophyll chloroplasts are retained in tumorous tissue as they accumulate starch while bundle sheath cells (and their chloroplasts) disappear upon tumor development. It was recently reported that cell expansion processes correlate with internal sugar levels (Van Dingenen et al., 2016). Induction of hypertrophy might therefore be achieved through starch accumulation in mesophyll chloroplasts.

Interestingly, starch accumulation in tumorous mesophyll chloroplasts is a very local effect. In non-tumorous, adjacent tissue the typical distribution of C_4 starch localization is retained again. This might explain why tumorous tissue does only show a tendency but no significant increase in measured starch levels of *U. maydis* infeced compared to mock tissue of the same age. The high deviation of starch levels between samples might have occurred because of photosynthetic activity and nutrient shuffeling processes during daytime. In a repeated set, plants could be incubated for more than 20 h in the dark to eliminate variation in starch levels between samples due to different photosynthetic activities.

Chloroplasts are described to play a central role in plant defense as they are the site of synthesis for the defense hormone salicylic acid which can be suppressed via the action of effectors (Jelenska et al., 2007). They furthermore contribute to the biosynthesis of other hormones like JA and ABA and are implicated in cell wall fortification processes and defence-induced ROS production (Grant and Jones, 2009; Serrano et al., 2016). The *U. maydis* effector chorismate mutase (Cmu1) might be a potential chloroplast-associated effector as it is described to promote chorismate export from the chloroplast to lower

internal chorismate levels for SA biosynthesis (Djamei et al., 2011). Interestingly, several *Pseudomonas syringae* effectors were found to target chloroplasts and lead to the destabilization of the photosystem II (PSII) complex and consequently to the inhibition of photosynthesis (Torres Zabala et al., 2015). Also effector proteins of the rust pathogen *Melampsora larici-populina* were identified to target chloroplasts but also other subcellular plant compartments (Petre et al., 2016; Petre et al., 2015). This targeting of organelles can either be achieved via direct localization of the effector to organelles or via targeting of nuclear encoded genes that encode organelle-targeted factors (Torres Zabala et al., 2015). Identification of potential *U. maydis* effectors that either target chloroplasts or their nuclear encoded genes to induce chloroplast dimorphism change will be an important and interesting aspect in the field of cell type-specific effector characterization.

Pathogen infection sites are described to transform source tissue into sink tissue (Chandran et al., 2010). In line with that, also *U. maydis* tumor induction is linked to a sink tissue induction in infected leaf areas as photosynthesis reactions are down regulated (Doehlemann et al., 2008a; Horst et al., 2008; Kretschmer et al., 2016) and photosynthesis pigments are degraded. Sink tissue is defined to bear an upregulation in glucose transporters leading to enriched hexose content which is imported into plastids for starch storage (Turgeon, 1989). Sugar levels also act as signaling platforms for the integration of environmental and developmental signals in plant growth (Häusler et al., 2014; Smeekens and Hellmann, 2014). They are directly linked to photosynthesis regulation as high intracellular sugar levels induce the repression of photosynthesis genes like *CHLOROPHYLL A/B BINDING PROTEIN* and the small subunit of Rubisco (Krapp et al., 1993). Starch storage in chloroplasts might therefore result from an induction of developmental cues for sink tissue establishment and thereby indirectly nurture the fungus.

The induction of a sink tissue and concomitant sugar level increase might be directly induced by *U. maydis* in order to mediate nutrient supply (Doehlemann et al., 2008a; Horst et al., 2008). A well-studied class of sugar efflux transporters are the plant SUGAR WILL EVENTUALLY BE EXPORTED TRANSPORTERs (SWEETs) (Chandran, 2015). Those transporters were found to be transcriptionally upregulated by the *Xanthomonas*

oryzae pv. oryzae transcription-activator like (TAL) effectors for the induction of specific *SWEET* gene expression in order to obtain host sugars for nutrition (Chen et al., 2010; Liu et al., 2011; Yu et al., 2011). Sugar and nutrients are required at the sites of fungal growth but at the same time they need to be kept low to avoid induction of immune responses (Morkunas and Ratajczak, 2014). This fine tuning of sugar levels might be obtained by an exact regulation of SWEET transporters by the invading pathogen (Chandran, 2015).

3.4 *U. maydis*-induced cell type-specific reprogramming of leaf cells towards tumorous cells via hyperplasia and hypertrohpy

In order to understand a potential cell type-specific action of *U. maydis* upon leaf tumor induction, cell type-specific disease progression was studied in this work. Three major cell morphological rearrangements in maize leaves were identified during *U. maydis* tumor formation. In order to build out a fully developed tumor, (1) epidermal cells increase in diameter but not in number, (2) bundle sheath cells show an internal cell division and are reprogrammed towards hyperplasic tumor cells while (3) mesophyll cells enlarge and form out hypertrophic tumor cells. A fungal staining with the lectin wheat germ agglutinin, Alexa Fluor499 conjugate (WGA-AF488) for visualization of fungal biomass in infected tissue was not successful in paraplast embedded tissue sections due to technical limitations. The process of induction of cell division in maize leaves is very interesting as this organ is developmentally defined and determined and therefore lacking meristematic centers. Monocot leaves can be subdivided into three cell fate areas bearing mature cells at the tip, followed by determined but expanding tissue areas and a developing area of dividing cells at the base (Fournier et al., 2005). The developing maize leaf area can be sub-classified into three developmental stages including undifferentiated cells at the base, a zone of varying cell size and shape where cells are starting to differentiate and a zone containing post-mitotic, expanding cells that are differentiated (Facette et al., 2013). *U. maydis* leaf infection rate and tumor formation is therefore most effective when the inoculum hits the young, developing leaf that is growing in the middle of the whorl, hidden by the older leaves (Figure 26A; Nelissen et al., 2016; Wenzler and Meins, 1987).

Initiation of internal cell division in bundle sheath cells resulting in hyperplasic tumor tissue was observed as one of the first histological cell rearrangements (Figure 26 B). Induction of cell division was histochemically located to occur only in bundle sheath cells at the early time point of 3 dpi via EdU staining which defines the bundle sheath cells as the origin of hyperplasic cell division. The process of internal cell division can be described as a transdifferentiation of bundle sheath cells. Transdifferentiation is defined as the conversion of one cell type to another (Okada, 1991; Tosh and Slack, 2002). It does not require dedifferentiation of cells to totipotent stem cells (Sugimoto et al., 2011; Sugimoto et al., 2010). The first induced hyperplasic tumor cells are still surrounded by the original isodiametric cell shape of bundle sheath cells indicating that no dedifferentiation process happened. The hyperplasic tumor cells constitute a newly emerging cell type. These cells are unique in size and shape and they do not bear lugol-stained chloroplasts in contrast to undifferentiated bundle sheath cells. The process of transdifferentiation of bundle sheath cells into de-novo xylem cells was observed in *A. thaliana* leaves infected by *Verticilium longisporum* (Reusche et al., 2012). De-novo xylem / metaxylem formation was also observed to be induced around the vasculature of tumorous secondary veins. However, their cellular origin was not identified.

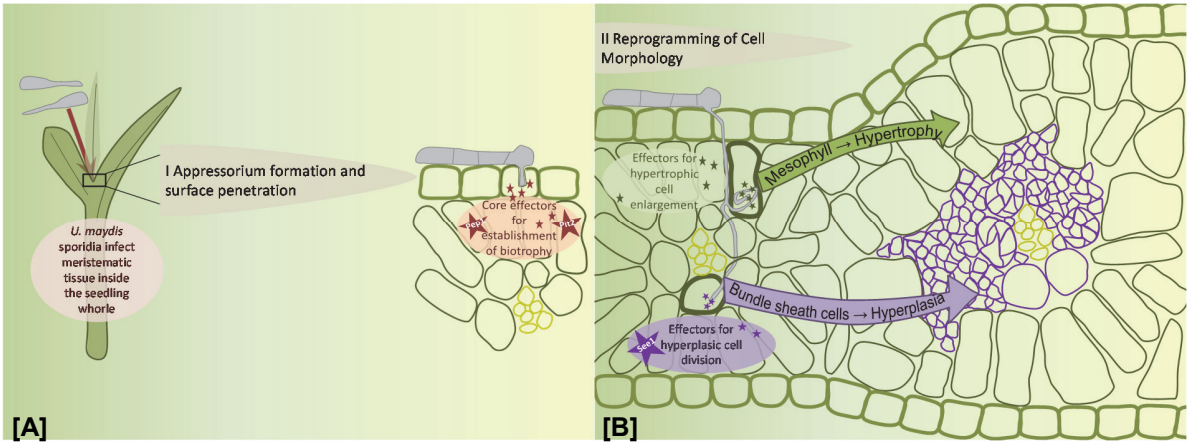

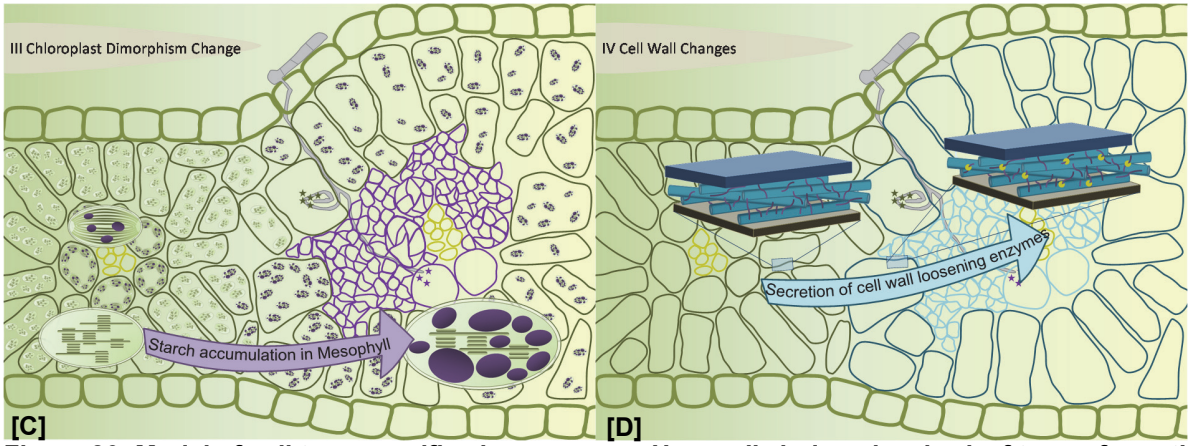

Figure 26: Model of cell type-specific changes upon *U. maydis*-induced maize leaf tumor formation **[A]** Fungal sporidia induce leaf tumors when the inoculum consisting of infective sporidia hits young, developing leaf tissue growing in the middle of the whorl. *U. maydis* secretes core effectors for the establishment of biotrophy. **[B]** Cell morphology gets reprogrammed towards the formation of hypertrophy and hyperplasia. **[C]** Chloroplast dimorphism is changed towards an accumulation of starch in mesophyll chloroplasts in *U. maydis*-induced tumors. **[D]** Model of cell wall reformation processes that involve loosening of plant cell walls for the formation of hypertrophic tumor cells. *U. maydis* effectors are depicted as stars, secreted endoglucanases [D] are depicted as yellow circular dots.

Hyperplasic cell division leads to a strong increase in cell number and is known to occur in diverse plant-pathogenic interactions including fungal pathogens, root-knot nematodes and bacteria (Depuydt et al., 2009; Jammes et al., 2005; Ji et al., 2013; Talboys, 1958). Cell fate in plants is defined to clonally propagate unless positional information changes that can induce a re-specification of cells (Costa, 2016). The resulting question is whether the *U. maydis*-induced hyperplasic tumor tissue is a pluripotent meristematic tissue that is continuously dividing or a defined, newly induced tissue type. The factors that regulate the balance of proliferation and differentiation are not fully understood. It is to be noted here, that the previously discussed AMP1 carboxypeptidase in *A. thaliana*, is involved in the regulation of meristem size (Vidaurre et al., 2007). The processes of cell division and cell growth are described to antagonize each other (Beemster et al., 2003) which is why it is interesting to investigate if the local distribution of tumor cells is influenced by cues coming from surrounding plant cells or fungal hyphae. The signals that lead to the propagation of this newly emerging tissue and its spreading would need to be elucidated. Future analysis of the obtained RNAseq data from laser microdissected *U. maydis* infected plant tissue will give support in answering open questions about the transcriptional regulation during plant tumor tissue development.

The second tumor cell type that was identified to emerge from mesophyll cells was the hypertrophic tumor tissue resulting from mesophyll cells (Figure 26 B). Mesophyll cells did not significantly increase in number upon tumor maturation but strongly increased in size and transformed into hypertrophic tumor cells. The formation of hypertrophic cells during pathogenic attack is well known from other tumor/gall inducing plant pathogens such as root knot nematodes, root cyst nematodes, arbuscular mycorrhizal fungi, endosymbiotic rhizobia and powdery mildews (Caillaud et al., 2008; Chandran et al., 2010; Genre et al., 2008; Ji et al., 2013; Kondorosi and Kondorosi, 2004).

In this context it should be noted that general processes of cell expansion or cell proliferation are controlled and regulated via internal sugar levels and chloroplast starch levels (Li et al., 2006; Van Dingenen et al., 2016). This implies a linkage between *U. maydis*-induced starch accumulation in mesophyll cell chloroplasts and hypertrophic cell enlargement. A low intracellular sucrose level with starch stored inside chloroplasts might lead to cell expansion while higher intracellular sucrose levels stimulate cell proliferation as it is observed in hyperplasic tumor tissue lacking starch staining (Van Dingenen et al., 2016).

3.4.1 Endoreduplication is a mesophyll-specific process during tumor formation and linked to hypertrophy

In biotrophic plant-microbe interactions, endoreduplication of host cells is described to play an important role in the development of hypertrophic cells at the sites of pathogenic growth including powdery mildew and nematode infections (Wildermuth, 2010). Endoreduplication might support the pathogen-induced nutrient demand by a rise of metabolic activity (Chandran et al., 2010; Gheysen and Mitchum, 2009). DNA content as well as the condensation structure of nuclei in physiologically active cells is described to be related to active gene expression leading to a directly proportional link of nuclear size and ploidy levels (Chandran et al., 2013).

SG200 infected mesophyll cells showed a doubling of nuclear size at 6 dpi which is described to correspond to one round of endoreduplication (Barlow, 1985). This coincided with the onset of cell size increase in SG200 infected mesophyll cells at 6 dpi. In contrast,

bundle sheath cells or resulting hyperplasic tumor cells in SG200 infected tissue did not show a significant nuclear size increase indicating that endoreduplication is a cell type-specific process upon leaf tumor formation. A similar observation was previously made in cells underlying the fungal feeding sites of *Golovinomyces orontii* infected *A. thaliana* mesophyll cells (Chandran et al., 2013). In summary, endoreduplication of host cells is a commonly observed feature of compatible biotrophic interactions (Wildermuth, 2010). In the *U. maydis* - maize interaction endoreduplication is specifically linked to hypertrophy in mesophyll cells.

3.4.2 See1 is a cell type-specific *U. maydis* effector required for hyperplasia

Histological analysis of *U. maydis* SG200Δsee1-induced tumor formation in transversal leaf sections revealed a cell type-specific action of the See1 effector. See1 is therefore the first *U. maydis* effector showing cell type-specific activity. SG200Δsee1-induced tumors mainly lacked hyperplasic tumor cells while hypertrophic tumor cells were retained demonstrating that this effector is involved in the induction of transdifferentiation of bundle sheath cells into hyperplasic tumor cells. This effect was specific to See1 as SG200Δsts1-induced tumors showed the same tumor tissue structure as SG200-induced tumors consisting of hyperplasic and hypertrophic tumor cells. However, it cannot be ruled out that SG200Δsts1-induced tumors have an altered cell morphological distribution as the areas of hyperplasic tumor cells seem to be more prominent compared to SG200 tumors. The investigation of a detailled cell type-specific influence on tumor morphology of STS1 would require further investigation such as tumor cell size measurements and quantification.

See1 was recently characterized as a leaf-specific effector and described to be required for the reactivation of tumor-induced DNA synthesis in leaf tumor formation (Redkar et al., 2015a). This conclusion was drawn from whole mount EdU microscopy experiments that mainly addressed the 4 dpi and 5 dpi time points. However, investigation of DNA synthesis events at 3 dpi in SG200Δsee1 infected leaf sections with EdU stainings revealed that active DNA synthesis is occurring in SG200Δsee1 infected mesophyll cells. The DNA synthesis induction in mesophyll cells of SG200Δsee1 infected leaf sections

leads to hypertrophy which was also reflected by nuclear size increase in mesophyll cells. While hyperplasia was hardly observed in SG200Δsee1 infected leaf sections compared to SG200 infected leaf sections, the development of hypertrophic tumor cells was not affected. This was in line with a mesophyll-specific increase in nuclear size. It therefore seems that hypertrophic cell enlargement is a See1-independent process which might be orchestrated by other (potentially cell type-specific) effectors while See1 seems to be cell type-specifically involved in hyperplasic cell division.

Concluding from these results, hyperplasia that is induced in *U. maydis* leaf tumor formation is a cell type-specific effect restricted to bundle sheath cells. Interestingly, the process of hyperplasic cell division seems to be driven by several factors in addition to See1 as SG200Δsee1-induced tumors showed starting of internal cell division in some bundle sheath cells.

The findings of the present study lead to an additional attribution of the See1 effector function as defined previously by Redkar et al. (2015a). See1 is required for reactivation of DNA synthesis in bundle sheath cells but not in mesophyll cells. See1 was previously identified to interact with *Zea mays* SGT1 by inhibiting nuclear localization of ZmSGT1 through inhibition of its phosphorylation (Redkar et al., 2015a). Microarray analysis revealed a prominent change in cell cycle associated genes in SG200 infected leaf tissue compared to SG200Δsee1 infected tissue (Redkar et al., 2015a). The most prominent changes were observed in cell cycle associated transcripts. Among these, DNA histone H3 which is described to be associated to DNA metabolism and cell cycle regulation was strongly induced (Gurtley et al., 1975; Redkar et al., 2015a). Histone H3 phosphorylation was shown to be required and increases during mitosis up to late G2 cell cycle phase for the initiation of chromatin condensation (Gurtley et al., 1975; Houben et al., 1999). Since SG200Δsee1-induced tumors hardly show hyperplasic tumor cells, the lack of histones might impair mitosis while endoreduplication is still possible as this process does not require chromosome condensation.

A second interesting process that is transcriptionally affected by See1 is the expression of maize *Skp1* (S phase kinase associated protein 1) gene which encodes for a protein

that is a part of the SCF type E3 ubiquitin ligase (Bai et al., 1996; Bloom and Cross, 2007). Interestingly, yeast skp1 mutants are arrested in either G1 cell cycle phase (leading to an arrest of cell cycle before onset of DNA synthesis) or in G2 cell cycle phase (following synthesis phase but stopping before mitosis phase) (Bai et al., 1996). The fact that SG200Δsee1 infected tissue sections show active DNA synthesis points towards a potential influence of See1 via skp1 at the point of G1 cell cycle phase leading to an impairment of mitosis induction. However, the process of DNA synthesis induction and subsequent cell division might be more complex. A plethora of factors influences the accessibility of a nucleus to being stimulated for DNA synthesis and subsequent cell division. Several aspects such as chromatin density and accessibility of DNA through modifications of histones play crucial roles in these processes (Bradbury, 1992).

3.4.3 *U. maydis* deploys cell type specific effector genes for leaf tumor induction

The physiological and histological insights in *U. maydis*-induced leaf tumor formation drive the main question how tumor cell types are orchestrated in their distribution and expansion. From the results obtained in this study, it seems that the fungus induces a constantly dividing meristematic sink tissue through actively dividing hyperplasic tumor tissue areas resulting from transdifferentiation of bundle sheath cells. This tissue type is opposing the non-dividing hypertrophic mesophyll tissue that is undergoing endoreduplication.

The overall transcript abundance in dissected cells from RNAseq analysis has revealed that the dissected samples had different amounts of fungal transcripts with 16 % of fungal reads in SG200 infected hyperplasic tumor cells compared to SG200 infected mesophyll tumor cells that had the highest amount of fungal transcript abundance. This reveals a difference in colonization abundance of the fungus showing that more mycelia is present in hypertrophic cell areas compared to hyperplasic areas. Transcript abundance of SG200Δsee1 in infected hypertrophic tumor cells was about 66 % reduced compared to the same tissue type infected by the SG200 progenitor strain which might hint towards less colonization by the SG200Δsee1 knockout strain in the same tissue.

RNAseq analysis has revealed that *U. maydis* deploys two different sets of effectors. Core effectors like Pep1, Pit2, Cmu1 and Tin2 (Djamei et al., 2011; Hemetsberger et al., 2012; Mueller et al., 2013; Tanaka et al., 2014) were constantly expressed independent of cell types in all three analysed sample types. Furthermore, some of the previously identified leaf specific effector genes were found to be cell type specifically higher expressed in SG200 infected hyperplasic tumor cells or SG200 infected mesophyll cells at 4 dpi pointing towards an implication in cell type specific tissue reprogrammation. Interestingly, *um06127* and *um12313,* which do not contribute to organ specific virulence as well as *um06223* and *um12217* that contribute to virulence in both leaves and tassel (Schilling et al., 2014) showed a cell type specific expression pattern. Among all cell type specifically expressed effector genes *um05318* and *um02239* (*see1*) were exclusively transcribed in SG200 infected mesophyll cells. Both effector genes were previously found to contribute to leaf specific virulence (Schilling et al., 2014). Interestingly, the effector gene *um03650* that was found to be a tassel specific *U. maydis* effector (Schilling et al., 2014) showed cell type specific expression pattern in leaves.

The See1 effector (*um02239*) was found to be transcribed only in SG200 infected mesophyll tumor cells but not in hyperplasic tumor cells and beared low transcript abundance at 4 dpi. This is rather unexpected as 4 dpi was identified to be the timepoint of hyperplasic cell division induction. However, it correlates with the previously described *see1* leaf expression pattern that is lowest at 4 dpi (Redkar et al., 2015a). Expression of *see1* in bundle sheath cells/hyperplasic tumor cells might therefore still occur at other infection timepoints. The first expression peak of *see1* occurs at 2 dpi (Redkar et al., 2015a) and might point towards an early induction of hyperplasic tumor cell division cues as this correlates with early EdU stainings in bundle sheath cells at 3 dpi. Potentially, *see1* might act already at 2 dpi to trigger cell division by interaction with SGT1 which results in onset of hyperplasia 4 dpi. Future analysis of the plant transcripts from the obtained RNAseq data will elucidate if this correlates with SGT1 transcription pattern (See1 plant target; Redkar et al., 2015a).

Interestingly, many of the above named core effectors showed higher transcript abundance in SG200Δsee1 tumor cells. Surprisingly the SG200Δsee1 strain differs in its

general expression pattern of effector genes in hyperplasic tumor cells compared to SG200 mesophyll tumor cells at the same timepoint (4 dpi). This might be due to the early induction of hypertrophy in SG200Δsee1 infected mesophyll cells. The SG200Δsee1 tumor phenotype in leaves might result from a general perturbation of effector gene expression. A lack of *see1* might hereby lead to a transcriptional overcompensation by other effectors which in the end results in an early development of hypertrophic mesophyll cells. Those strongly upregulated effector genes might therefore serve as future candidates to investigate effector-induced hypertrophy.

3.5 Conclusions and Outlook

Considering the results obtained from the investigation of the *U. maydis* effector STS1, the next objective of this part of the work would be a distinct proof of its interaction with *Zea mays* CBPII as well as a biochemical characterization of both interaction partners. For that, further Y2H experiments to investigate interaction of STS1 with CBPII subdomains could be done. This might furthermore point towards the biochemical interaction site of both proteins. Biochemical assays and subsequent western blot analysis with heterologously expressed CBPII and STS1 proteins could help to elucidate if STS1 has a stabilizing function on CBPII protein stability. For that, previously identified inhibitors of carboxypeptidases could be included as a control (Zhou et al., 2005). To obtain an *in vivo* proof of STS1 and CBPII interaction, heterologously expressed STS1-HA protein could be infiltrated into maize plants and pulldown experiments including subsequent mass spectrometry analysis for the identification of CBPII could be performed. Obtaining structural information of both, CBPII as well as STS1 via protein crystallization would help in understanding the function of both proteins. The elucidation of the protein structures would add information concerning their molecular function and a co-crystalization would furthermore hint towards the potential effect of STS1 on CBPII.

To identify potential effectors that are involved in the change of chloroplast dimorphism, paraplast sections of leaf tissue infected with cell type-specific effector knockout strains could be screened for a lack of or change in lugol-staining of tumors compared to SG200 infected tumor tissue. A further point of investigation might be the subcellular organelle targeting sites of effectors such as chloroplasts or other cell organelles either for the

degradation of chlorophyll or for organelle reprogramming towards starch accumulation. The subcellular localization of effectors potentially involved in starch accumulation could be identified via immuno-gold labeling techniques and subsequent electron microscopy. By the identification of subcellularly acting effectors, the concept of cell type specificity would be deepened towards organelle specificity of plant-pathogen interactions as it was previously observed for effectors from other pathogens (Figure 26 C; Petre et al., 2016; Petre et al., 2015).

It would additionally be interesting to test leaf- and cell type-specifically expressed *U. maydis* effector knockout mutant-induced tumors for cell type-specific changes in tumor formation as it was observed for SG200Δsee1. With the help of the obtained RNAseq data, cell type-specifically expressed *U. maydis* effector candidate genes can be chosen for further studies and characterization to understand the induction of hyperplasia and hypertrophy of plant tumor cells. Cell type-specific effector gene expression patterns obtained from RNAseq analysis could be proven by *in situ* hybridization of paraplast embedded tissue sections as described in (Javelle and Timmermans, 2012).

Fiber composition strongly influences disease resistance due to diverse physical properties and concomitantly also has an influence on nutritional properties/recalcitrance of plant tissue (Santiago et al., 2013). Testing the relation of fiber composition linked to disease susceptibility towards *U. maydis* in different maize varieties could lead to the elucidation of trait-specific compatibility factors. In order to identify local cell wall biochemical changes linked to *U. maydis* infection, cell wall composition analyses would have to be carried out in a tissue or tumor cell type specific context (Figure 26 D). Cell type specific changes in monolignol or hemicellulose composition as well as potential cellulose content changes could be analyzed by laser microdissection of the respective tissue types. Also, *U. maydis* effector knockout mutants that might be involved in cell wall degradation such as SG200Δum01829, SG200Δum11763 and others could be included into this study to screen for potential leaf-specific cell wall degradation.

The physiological investigation of *U. maydis*-induced plant leaf tumor formation will constitute an important part in the understanding of this close biotrophic interaction.

Analysis of the plant transcripts obtained from the laser microdissected tumor tissue will give an insight into transcriptional changes that are differentially regulated between mesophyll and hypertrophic cells as well as bundle sheath and hyperplasic cells. It will be of further interest to investigate if specific SWEET transporters (Chen et al., 2010; Lalonde et al., 1999) or hormone signaling pathways are differentially regulated between hypertrophic and hyperplasic cells. This analysis might potentially elucidate the function of those two different tumor cell types. In a preliminary model a sink signal is induced in hyperplasic tumor cells by continuous cell division and induction of a meristem-like tissue. On the one hand hypertrophic tumor cells might have a sugar exporting function by shuffling nutrients that arrive through the sink signal induction towards fungal nutrition. Analyzing the plant transcriptomes of hyperplasic and hypertrophic tumor cells will therefore help in the understanding of the physiological status of those two types of tumor cells.

From the observations made in this study including the light microscopy study for starch staining, it seems that fungal hyphae are not directly present in all areas where tumor tissue induction occurs. The question remains whether transdifferentiation of bundle sheath cells is directly induced via locally acting effector proteins that induce cell division or via a local change in plant hormone homeostasis leading to a hormonal mimic of meristematic tissue in infected leaf areas. A further point of investigation would be the identification of signals that induce bundle sheath cell transdifferentiation. It would be interesting to investigate if effectors directly mimic this signal or if they induce a plant-derived signal that is mobile and could reach neighboring bundle sheath collars to start hyperplasic cell division without the direct presence of hyphae. Whole mount tissue microscopy for a three dimensional visualization of hyphal distribution in areas of tumor induction could help to investigate how far fungal cues secreted by fungal hyphae can reach to induce leaf cell differentiation processes.

Cytoplasmic growth and metabolism in plant cells is regulated by the central master regulator Target of Rapamycin (TOR) Serine/Threonine kinase (Kalve et al., 2014). In the orchestration of tumor tissue development TOR might be a central hub that could be targeted by *U. maydis*. TOR controls a plethora of cellular processes including cell

expansion and cell proliferation (Sablowski and Carnier Dornelas, 2014). In line with that cell wall rebuilding processes are also regulated by TOR via its influence on cellulose synthase and expansins (Moreau et al., 2012). The TOR signaling pathway is furthermore directly connected to E2F transcription factor activation pathway (Kalve et al., 2014). During progression through the cell cycle E2Fa and E2Fb are involved in the S-phase initiation and overexpression of these transcription factors leads to enhanced cell division processes (Sozzani et al., 2006). E2Fa is a direct TOR kinase substrate that was found to be activated upon glucose signaling in *A. thaliana* showing the influence of nutrient supply on meristem regulation (Xiong et al., 2013). The induction of sink tissue signals by *U. maydis* and concomitant nutrient flow arising from the phloem might thereby contribute to the local induction of hyperplasic tumor cells around the vasculature. Detailled analysis of the plant transcriptome from this laser microdissection RNAseq experiment will therefore elucidate the cell type specific host factors upon *U. maydis* infection that are transcriptionally regulated upon tumor induction and therefore add towards the understanding of developmental cues that are involved in tumor formation.

4 Materials and methods

4.1 Materials and source of supply

4.1.1 Chemicals

All chemicals used in this study were purchased from Biozym (Hessisch Oldendorf, Germany), Difco (Augsburg, Germany), GE Healthcare (Munich, Germany), Invitrogen (Darmstadt, Germany), Merck (Darmstadt, Germany), Roche Diagnostics (Mannheim Germany), Roth (Karlsruhe, Germany), and Sigma-Aldrich (Deisenhofen, Germany) unless otherwise stated.

4.1.2 Buffers and solutions

Buffers and solutions were prepared according to Ausubel et al. (2002); Sambrook et al. (1989) if not otherwise stated in the respective method description. Sterilization of buffers and solutions was done at 121 °C, 5 min or via a sterile filter, if solution was heat sensitive (Pore size 0.2 µm, Merck, Darmstadt, Germany).

4.1.3 Enzymes and antibodies

The restriction enzymes used in this study were purchased from New England Biolabs (NEB, Frankfurt/Main, Germany), or Thermo (Thermo Fisher Scientific Inc., Bonn, Germany). DNA polymerases used in this study were Phusion® Hot Start High-Fidelity DNA-Polymerase (Thermo Fisher Scientific Inc., Bonn, Germany), KOD Xtreme™ Hot Start DNA Polymerase (Novagen®/Merck Millipore, Darmstadt, Germany), or Taq-polymerase included in RedMix (Bioline, Luckenwalde, Germany). Ligation of DNA molecules was done with T4 DNA ligase (NEB, Frankfurt/Main, Germany). The enzymatic degradation of RNA was done with RNaseA (Serva, Heidelberg, Germany) and enzymatic degradation of DNA was done with the TURBO DNA-free™ Kit (Ambion®/ Thermo Fisher Scientific Inc., Bonn, Germany). For the enzymatic degradation of fungal cell walls Novozyme234 (Novo Nodisk, Copenhagen, Denmark) was used.

Antibodies were obtained from Cell Signaling Technology (Danver, US), Thermo Fisher Scientific (Bonn, Germany) or Sigma-Aldrich (Deisenhofen, Germany). For further information concerning antibodies used in this study see Table 11.

4.1.4. Commercial kits

Plasmid DNA extraction was done using the QIAprep® Mini Plasmid Kit (Qiagen, Hilden, Germany). The DIG High Prime Kit (Roche, Mannheim, Germany) was used for the digoxigenin labeling of PCR products and for the cleanup of PCR products, the Wizard® SV Gel and PCR Clean-Up System (Promega, Mannheim, Germany) was used. Direct cloning of PCR products was done with the TOPO® TA Cloning Kit (Invitrogen, Karlsruhe, Germany). Additional kits are listed in the respective methods section.

4.2 Media and cell cultivation conditions for microorganisms

4.2.1 Media

The recipes for cultivation of microorganisms used in this study are listed in Table 5. The media was autoclaved at 121 °C for 5 min before use, unless otherwise stated.

Table 5: Media for cultivation of microorganisms

Name	Composition	Remarks
CM medium (Holliday, 1974)	0.6 % (w/v) NH_4NO_3 1 % (w/v) Casaminoacids 0.1 % (w/v) herring sperm DNA 2 % (w/v) Yeast extract 2 % (v/v) Vitamin solution	in $H_2O_{bid.}$ addition of 2 % (v/v) sterile filtered glucose after autoclaving
Vitamin solution (Holliday, 1974)	0.1 ‰ (w/v) Thiamin 0.05 ‰ (w/v) Riboflavin 0.05 ‰ (w/v) Pyridoxine 0.2 ‰ (w/v) Calcium pantothenate 0.05 ‰ (w/v) Para-aminobenzoic acid 0.2 ‰ (w/v) Nicacin 0.2 ‰ (w/v) Choline chloride 1.0 ‰ (w/v) Myo-inositol	in $H_2O_{bid.}$, sterile filtered
dYT (-Agar) (Sambrook et al., 1989)	1.6 % (w/v) Tryptone 1.0 % (w/v) Yeast extract 0.5 % (w/v) NaCl 1.5 % (w/v) Bacto Agar	in $H_2O_{bid.}$
dYT Glycerol medium	1.6 % (w/v) Tryptone 1.0 % (w/v) Yeast extract 0.5 % (w/v) NaCl 87 % glycerol	in $H_2O_{bid.}$
$YEPS_{light}$	1 % (w/v) Yeast extract	in $H_2O_{bid.}$

	1 % (w/v) Peptone 1 % (w/v) Saccharose	
Potato-Dextrose-Agar (PD)	2.4 % (w/v) Potato-Dextrose Broth 2 % (w/v) Bacto Agar	in $H_2O_{bid.}$
PD-Charcoal-Agar	addition of 1.0% (w/v) activated charcoal to the PD-Agar media	in $H_2O_{bid.}$
Regeneration Agar (Schulz et al., 1990)	1 % (w/v) Agar 1M Sorbitol In $YEPS_{light}$ (described above)	in $H_2O_{bid.}$
NSY-Glyceol	0.8% (w/v) Nutrient Broth 0.1% (w/v) Yeast extract 0.5% (w/v) Sucrose 69.6% (v/v) Glycerol	in $H_2O_{bid.}$
YPDA (-Agar)	2% (w/v) Peptone 1 % (w/v) Yeast extract 0.003% (w/v) Adenine-Hemisulfate 2% (w/v) Bacto Agar	in $H_2O_{bid.}$ pH 6.5 addition of 2 % (v/v) sterile filtered glucose after autoclaving
SD (-Agar)	0.67% (w/v) Yeast nitrogen base without amino acids 0.06% (w/v) Dropout Solution [(-Ade, -His, -Leu, -Trp) or (-His, -Leu, -Trp, -Ura)] 2% (w/v) Bacto Agar	in $H_2O_{bid.}$ pH 5.8 addition of 2 % (v/v) sterile filtered glucose after autoclaving

4.2.2 Cultivation of *A. tumefaciens*

A. tumefaciens bacteria were grown in in dYT liquid medium (Table 5 and Sambrook et al., 1989) at 28 °C with shaking at 200 rpm containing the respective antibiotics needed for selection. Glycerolstocks for long term storage of cultures were done by adding 50 % (v/v) dYT glycerol medium (Table 5) to a thickly grown overnight culture in a total volume of 2 mL and stored in a screw cap vial at -80 °C. For reuse of the long term cultures, strains were streaked out on dYT agar medium containing the respective antibiotics for selection. Antibiotics and their respective final concentration are listed in Table 6.

Table 6: **Antibiotics and working concentration used for *A. tumefaciens* cultivation**

Antibiotic	**Working concentration[µg/mL]**
Ampicillin (Amp)	100
Carbenicillin (Carb)	100
Gentamycin (Gent)	50
Kanamycin (Kan)	50
Rifampicin (Rif)	40
Tetracyclin (Tet)	25

4.2.3 Cultivation of *E. coli*

E. coli bacteria were grown in in dYT liquid medium (Table 5 and Sambrook et al., 1989) at 37 °C with shaking at 200 rpm containing the respective antibiotics needed for selection. Glycerolstocks for long term storage of cultures were done by adding 50 % (v/v) dYT glycerol medium (Table 5) to a thickly grown overnight culture in a total volume of 2 mL and stored in a screw cap vial at -80 °C. For reuse of the longterm cultures, strains were streaked out on dYT agar medium containing the respective antibiotics for selection. Antibiotics and their respective final concentration are listed in Table 7.

Table 7: Antibiotics and working concentration used for *E. coli* cultivation

Antibiotic	Working concentration[µg/mL]
Ampicillin (Amp)	100
Carbenicillin (Carb)	100
Chloramphenicol (Clm)	35
Kanamycin (Kan)	50
Spectinomycin (Spec)	100

4.2.4 Cultivation of *S. cerevisiae*

The wild type *S. cerevisiae* strain (AH109) used in this study was grown in YPDA medium (Table 5). Transformed *S. cerevisiae* strains were grown in SD medium (Table 5) supplemented with adenine, histidine, leucine and/or tryptophane, depending on the auxotrophic selection marker encoded by the plasmid used for transformation. Glycerolstocks for long term storage of cultures were done by adding 25 % (v/v) glycerol to a thickly grown overnight culture in a total volume of 2 mL and stored in a screw cap vial at -80 °C. For reuse of the long term cultures, strains were streaked out on YPD/SD agar medium containing the respective amino acids for selection. Amino acids were prepared as 10X dropout supplements, autoclaved and stored for up to 1 year at 4 °C. The respective amounts can be found in Table 8.

Table 8: 10X Dropout solutions for supplementation of SD media

Nutrient	10X Concentration	Sigma Cat. No
L-Adenine hemisulfate salt	200 mg/L	A-9126
L-Histidine HCl monohydrate	200 mg/L	H-8125
L-Leucine	1000 mg/L	L-8000
L-Tryptophan	200 mg/L	T-0254

4.2.5 Cultivation of *U. maydis*

U. maydis was grown in in $YEPS_{light}$ liquid medium (Table 5) at 28 °C with shaking at 200 rpm. Glycerolstocks for long term storage of cultures were done by adding 50 % (v/v) NSY-glycerol (Table 5) to a thickly grown overnight culture in a total volume of 2 mL and stored in a screw cap vial at -80 °C. For reuse of the longterm cultures, strains were streaked out on potato-dextrose agar medium. For selection after transformation of *U. maydis*, regeneration Agar (Table 5 and Schulz et al., 1990) was used, containing either 2 µg/mL carboxin (Cbx) (Sigma-Aldrich, Deisenhofen, Germany) or 400 µg/mL hygromycin B (Roche, Mannheim, Germany) depending on the selection marker used.

4.2.6 Determination of cell density

The cell density was determined by measuring the absorption at 600 nm (OD_{600}) in a Novaspec II photometer (Pharmacia Biotech/GE lifesciences, Munich, Germany) or a Genesis 10S VIS spectrophotometer (Thermo Fisher Scientific Inc., Bonn, Germany) and taking the corresponding culture medium as reference value. To ensure a linear dependence of the measurements, cultures were diluted to absorption values below 0.8. For *U. maydis* and *S. cerevisiae,* an absorption of 1 at OD_{600} accounts for ~1.5 $x10^7$ cells. For *A. tumefaciens* and *E. coli,* an absorption of 1 at OD_{600} accounts for ~1 $x10^9$ cells.

4.3 Microbial strains, oligonucleotides and vectors

4.3.1 *A. tumefaciens* strain

The strain used in this study for *A. tumefaciens*-mediated transformation of *N. benthamiana* was GV3101 (Koncz and Schell, 1986). This strain bears a chromosomal rifampicin resistance, the Ti-plasmid pMP90 with *vir*-genes and a gentamycin resistance as well as a Ti-helperplasmid bearing a tetracycline resistance. All plasmids generated for transformation of this strain are listed in chapter 4.3.6.6.

4.3.2 *E. Coli* strains

For plasmid amplification during normal cloning procedures, *E. coli* K-12 Top10/DH10β [F- mcrA Δ (mrr-hsd RMS-mcrBC) Φ80lacZΔM15 ΔlacO74 recA1 araΔ139 Δ (ara-leu) 7697 galU galK rpsL (StrR) endA1 nupG] (Grant et al., 1990; Invitrogen, Karlsruhe,

Germany) and *E. coli* K-12 DH5α [F- Φ80d lacZ ΔM15 Δ (lacZYA-argF) U169 deoR recA1 endA1 hsdR17 (rK-, mK+) phoA supE44 λ- thi-lgyr A96 relA1] were used (Hanahan, 1983; GibcoBRL, Eggenstein, Germany). For the heterologous expression of proteins *E. coli* BL21 (DE3) pLys [F- ompT gal dcm lon hsdSB(rB -mB -) A (DE3) pLysS (cmR)] (Novagen/Merck, Darmstadt, Germany) was used. All plasmids generated for transformation of BL21 (DE3) pLys are listed in chapter 4.3.6.3.

4.3.3 *S. cerevisiae* strain

The *S. cerevisiae* AH109 strain (Clontech, Saint-Germain-en-Laye, France) was used for all yeast two-hybrid interaction studies. This strain is auxotrophic for tryptophan, alanine, histidine and leucine. All plasmids generated for transformation of this strain are listed in chapter 4.3.6.5.

4.3.4 *U. maydis* strains

The *U. maydis* SG200 strain (Kämper et al., 2006) was used for all *U. maydis* experiments. All plasmids generated for transformation of this strain as well as the plasmids used for transformation of the knockout strains derived from this initial strain are listed in chapter 4.3.6.2. As a summary, all *U. maydis* strains produced in this study are listed in Table 17 in the annexure of this work.

4.3.5 Oligonucleotides

All oligonucleotides used in this study were purchased from Sigma-Aldrich (Deisenhofen, Germany). A list of the oligonucleotides can be found in Table 18 in the annexure of this work.

4.3.6 Plasmids

All plasmids used in this study were tested via restriction enzyme digest. In case of insertion of plasmid parts that were generated via PCR, the newly generated sequence was verified via sequencing.

4.3.6.1 Plasmid for transfer of PCR products into further plasmids

pCRII-TOPO (Invitrogen, Karlsruhe, Germany)

This plasmid was used for the intermediate cloning steps during the generation of *U. maydis* knockout constructs, especially for subcloning of left and right borders. This plasmid contains an ampicillin resistance.

4.3.6.2 Plasmids for the transformation *U. maydis*

pBS-hhn (Kämper, 2004)

This plasmid contains a hygromycin resistance cassette (*hph* gene) of 1884 bp which was used for the generation of *U. maydis* single deletion strains. The *hph* gene is controlled by the *hsp70* promoter and a *nos* terminator and was excised via SfiI.

pCRII-TOPO_Δum01130 (Schilling et al., 2014)

This plasmid consists of a pCRII-TOPO backbone which contains the hygromycin resistance cassette flanked by a 1000 bp 5' (left border) or 3' (right border) end of *um01130*. Primers used for left border: OZA43 + OZA44. Primers used for right border: OZA45 + OZA46. For the deletion of *um01130* in *U. maydis* SG200, the insert was excised via *Spe*I and *Eco*RV.

pCRII-TOPO_Δum06222 (Schilling et al., 2014)

This plasmid consists of a pCRII-TOPO backbone which contains the hygromycin resistance cassette flanked by a 1000 bp 5' (left border) or 3' (right border) end of *um06222*. Primers used for left border: Olex85 + Olex86. Primers used for right border: Olex87 + Olex88. For the deletion of *um06222* in *U. maydis* SG200, the insert was excised via *Spe*I and *Eco*RV.

pCRII-TOPO_Δum12217 (Schilling et al., 2014)

This plasmid consists of a pCRII-TOPO backbone which contains the hygromycin resistance cassette flanked by a 1000 bp 5' (left border) or 3' (right border) end of *um12217*. Primers used for left border: OAli59 + OAli60. Primers used for right border: OAli61 + OAli62. For the deletion of *um12217* in *U. maydis* SG200, the insert was excised via *Spe*I and *Eco*RV.

pCRII-TOPO_Δum06223 (Schilling et al., 2014)

This plasmid consists of a pCRII-TOPO backbone which contains the hygromycin resistance cassette flanked by a 1000 bp 5' (left border) or 3' (right border) end of *um06223*. Primers used for left border: OZA13 + OZA14. Primers used for right border: OZA15 + OZA16. For the deletion of *um06223* in *U. maydis* SG200, the insert was excised via *Spe*I and *Eco*RV.

pCRII-TOPO_Δum12313 (Schilling et al., 2014)

This plasmid consists of a pCRII-TOPO backbone which contains the hygromycin resistance cassette flanked by a 1000 bp 5' (left border) or 3' (right border) end of *um12313*. Primers used for left border: OAli63 + OAli64. Primers used for right border: OAli65 + OAli66. For the deletion of *um12313* in *U. maydis* SG200, the insert was excised via *Spe*I and *Eco*RV.

pCRII-TOPO_Δum11763 (Schilling et al., 2014)

This plasmid consists of a pCRII-TOPO backbone which contains the hygromycin resistance cassette flanked by a 1000 bp 5' (left border) or 3' (right border) end of *um11736*. Primers used for left border: OZA31 + OZA32. Primers used for right border: OZA33 + OZA34. For the deletion of *um11763* in *U. maydis* SG200, the insert was excised via *Spe*I and *Xba*I.

pCRII-TOPO_Δum10553 (Schilling et al., 2014)

This plasmid consists of a pCRII-TOPO backbone which contains the hygromycin resistance cassette flanked by a 1000 bp 5' (left border) or 3' (right border) end of *um10553*. Primers used for left border: OAli51 + OAli52. Primers used for right border: OAli53 + OAli54. For the deletion of *um10553* in *U. maydis* SG200, the insert was excised via *Spe*I and *Eco*RV.

pCRII-TOPO_Δum05306 (Schilling et al., 2014)

This plasmid consists of a pCRII-TOPO backbone which contains the hygromycin resistance cassette flanked by a 1000 bp 5' (left border) or 3' (right border) end of

um05306. Primers used for left border: OZA25 + OZA26. Primers used for right border: OZA27 + OZA28. For the deletion of *um05306* in *U. maydis* SG200, the insert was excised via *Spe*I and *Xba*I.

pCRII-TOPO_Δum06127 (Schilling et al., 2014)

This plasmid consists of a pCRII-TOPO backbone which contains the hygromycin resistance cassette flanked by a 1000 bp 5' (left border) or 3' (right border) end of *um06127*. Primers used for left border: OAli47 + OAli48. Primers used for right border: OAli49 + OAli50. For the deletion of *um06127* in *U. maydis* SG200, the insert was excised via *Spe*I and *Eco*RV.

pCRII-TOPO_Δum05311 (Schilling et al., 2014)

This plasmid consists of a pCRII-TOPO backbone which contains the hygromycin resistance cassette flanked by a 1000 bp 5' (left border) or 3' (right border) end of *um05311*. Primers used for left border: OAli43 + OAli44. Primers used for right border: OAli45 + OAli46. For the deletion of *um05311* in *U. maydis* SG200, the insert was excised via *Spe*I and *Xba*I.

pCRII-TOPO_Δum11060 (Schilling et al., 2014)

This plasmid consists of a pCRII-TOPO backbone which contains the hygromycin resistance cassette flanked by a 1000 bp 5' (left border) or 3' (right border) end of *um11060*. Primers used for left border: OAli55 + OAli56. Primers used for right border: OAli57 + OAli58. For the deletion of *um11060* in *U. maydis* SG200, the insert was excised via *Spe*I and *Eco*RV.

pCRII-TOPO_Δum05495 (Schilling et al., 2014)

This plasmid consists of a pCRII-TOPO backbone which contains the hygromycin resistance cassette flanked by a 1000 bp 5' (left border) or 3' (right border) end of *um05495*. Primers used for left border: O09 + O10. Primers used for right border: O11 + O12. For the deletion of *um05495* in *U. maydis* SG200, the insert was excised via *Spe*I and *Eco*RV.

pCRII-TOPO_Δum02239 (Schilling et al., 2014)

This plasmid consists of a pCRII-TOPO backbone which contains the hygromycin resistance cassette flanked by a 1000 bp 5' (left border) or 3' (right border) end of *um02239*. Primers used for left border: OZA7 + OZA8. Primers used for right border: OZA9 + OZA10. For the deletion of *um02239* in *U. maydis* SG200, the insert was excised via *Spe*I and *Eco*RV.

pCRII-TOPO_Δum01690 (Schilling et al., 2014)

This plasmid consists of a pCRII-TOPO backbone which contains the hygromycin resistance cassette flanked by a 1000 bp 5' (left border) or 3' (right border) end of *um01690*. Primers used for left border: O01 + O02. Primers used for right border: O03 + O04. For the deletion of *um01690* in *U. maydis* SG200, the insert was excised via *Bam*HI and *Eco*RV.

pCRII-TOPO_Δum01829 (Schilling et al., 2014)

This plasmid consists of a pCRII-TOPO backbone which contains the hygromycin resistance cassette flanked by a 1000 bp 5' (left border) or 3' (right border) end of *um01829*. Primers used for left border: OZA49 + OZA50. Primers used for right border: OZA51 + OZA52. For the deletion of *um01829* in *U. maydis* SG200, the insert was excised via *Spe*I and *Eco*RV.

pCRII-TOPO_Δum05223 (Schilling et al., 2014)

This plasmid consists of a pCRII-TOPO backbone which contains the hygromycin resistance cassette flanked by a 1000 bp 5' (left border) or 3' (right border) end of *um05223*. Primers used for left border: OZA19 + OZA20. Primers used for right border: OZA21 + OZA22. For the deletion of *um05223* in *U. maydis* SG200, the insert was excised via *Spe*I and *Eco*RV.

pCRII-TOPO_Δum03650 (Schilling et al., 2014)

This plasmid consists of a pCRII-TOPO backbone which contains the hygromycin resistance cassette flanked by a 1000 bp 5' (left border) or 3' (right border) end of

um03650. Primers used for left border: ODA51 + ODA52. Primers used for right border: ODA53 + ODA54. For the deletion of *um03650* in *U. maydis* SG200, the insert was excised via *Spe*I and *Eco*RV.

pCRII-TOPO_Δum05439 (Schilling et al., 2014)

This plasmid consists of a pCRII-TOPO backbone which contains the hygromycin resistance cassette flanked by a 1000 bp 5' (left border) or 3' (right border) end of *um05439*. Primers used for left border: O05 + O06. Primers used for right border: O07 + O08. For the deletion of *um05439* in *U. maydis* SG200, the insert was excised via SpeI and EcoRV.

p123 (Aichinger et al., 2003)

This plasmid harbors an ampicillin resistance and was used for the generation of complementation constructs of *U. maydis* knockouts. In addition, it contians the *gfp* gene controlled by the *otef* promoter and a *nos* terminator. This plasmid backbone was used for the cloning of all complementation constructs generated in this study. For transformation of *U. maydis* knockout strains, the plasmid was beforehand linearized via *Ssp*I or *Age*I in the *cbx* locus to enable integration into the *U. maydis ip* locus via homologous recombination.

P123-p12217-*um12217* (Schilling et al., 2014)

This plasmid contains *um12217* under control of its native promoter (1kb) that was amplified using the primers OAli99 + OAli100 and cloned via *Not*I and *Nde*I into the p123 vector. This plasmid was used for complementation of *U. maydis* SG200Δ12217 by linearization of the *cbx* locus and integration into the *ip* locus via homologous recombination.

p123-p05306-*um05306* (Schilling et al., 2014)

This plasmid contains *um05306* under control of its native promoter (1kb) that was amplified using the primers OAli113 + OAli114 and cloned via *Not*I and *Nde*I into the p123 vector. This plasmid was used for complementation of *U. maydis* SG200Δ05306 by

linearization of the *cbx* locus and integration into the *ip* locus via homologous recombination.

p123-p05311-*um05311* (Schilling et al., 2014)

This plasmid contains *um05311* under control of its native promoter (1kb) that was amplified using the primers OAli117 + OAli118 and cloned via *Not*I and *Nde*I into the p123 vector. This plasmid was used for complementation of *U. maydis* SG200Δ05311 by linearization of the *cbx* locus and integration into the *ip* locus via homologous recombination.

p123-p05318-*um05318* (Schilling et al., 2014)

This plasmid contains *um05318* under control of its native promoter (1kb) that was amplified using the primers OAli119 + OAli120 and cloned via *Nde*I and *Xba*I into the p123 vector. This plasmid was used for complementation of *U. maydis* SG200Δ05318 by linearization of the *cbx* locus and integration into the *ip* locus via homologous recombination.

p123-p11060-*um11060* (Schilling et al., 2014)

This plasmid contains *um11060* under control of its native promoter (1kb) that was amplified using the primers OAli109 + OAli110 and cloned via *Not*I and *Nde*I into the p123 vector. This plasmid was used for complementation of *U. maydis* SG200Δ11060 by linearization of the *cbx* locus and integration into the *ip* locus via homologous recombination.

p123-p02239-*um02239* (Schilling et al., 2014)

This plasmid contains *um02239* under control of its native promoter (1kb) that was amplified using the primers OAR01 + OAR02 and cloned via *Not*I and *Sbf*I into the p123 vector. This plasmid was used for complementation of *U. maydis* SG200Δ02239 by linearization of the *cbx* locus and integration into the *ip* locus via homologous recombination.

p123-p01690-*um01690* (Schilling et al., 2014)

This plasmid contains *um01690* (*sts1*) under control of its native promoter (1kb) that was amplified using the primers OAli97 + OAli98 and cloned via *Not*I and *Nde*I into the p123 vector. This plasmid was used for complementation of *U. maydis* SG200Δ01690 by linearization of the *cbx* locus and integration into the *ip* locus via homologous recombination.

p123-p01829-*um01829* (Schilling et al., 2014)

This plasmid contains *um01829* under control of its native promoter (1kb) that was amplified using the primers OLS122 + OLS123 and cloned into the p123 vector. This plasmid was used for complementation of *U. maydis* SG200Δ01829 by linearization of the *cbx* locus and integration into the *ip* locus via homologous recombination.

p123-p03650-*um03650* (Schilling et al., 2014)

This plasmid contains *um03650* under control of its native promoter (1kb) that was amplified using the primers OLS137 + OLS138 and cloned into the p123 vector. This plasmid was used for complementation of *U. maydis* SG200Δ03650 by linearization of the *cbx* locus and integration into the *ip* locus via homologous recombination.

p123-p05439-*um05439* (Schilling et al., 2014)

This plasmid contains *um05439* under control of its native promoter (1kb) that was amplified using the primers OLS135 + OLS136 and cloned into the p123 vector. This plasmid was used for complementation of *U. maydis* SG200Δ05439 by linearization of the *cbx* locus and integration into the *ip* locus via homologous recombination.

4.3.6.3 Plasmids for the expression of recombinant proteins in *E. coli*

pRSET-GST-PP (Schreiner et al., 2008)

The original pRSET plasmid obtained from Invitrogen (Karlsruhe, Germany) was modified by replacement of a 6x-histidine tag fused to a GST (glutathione-S-transferase) tag at the 3' end. The GST gene was followed by a region encoding a PreScission™ protease recognition sequence, which enables the removal of the GST-tag after protein purification.

This plasmid contains an ampicillin resistance and was used for cloning of Sts1 and CBPT01/T02 pRSET expression vector.

pRSET-GST-PP- ***um01690*** **(*sts1*)**

This plasmid contains the *um01690* gene (*sts1*) without signal peptide. The gene was amplified with primers OAli2619 + OAli2620 and cloned via *Bam*HI and *Eco*RI into the pRSET-GST-PP backbone.

pRSET-GST-PP-*GRMZM2G159171_T01* (*CBPII T01*)

This plasmid contains the *GRMZM2G159171_T01* gene (*CBPII T01*) without transmembrane domain. The gene was amplified with primers OAli2950 + OAli2951 and cloned via *Sac*I and *Eco*RI into the pRSET-GST-PP backbone.

pRSET-GST-PP-*GRMZM2G159171_T02* (*CBPII T02*)

This plasmid contains the *GRMZM2G159171_T02* gene (*CBPII T02*). The gene was amplified with primers OAli2952 + OAli2951 and cloned via *Sac*I and *Eco*RI into the pRSET-GST-PP backbone.

4.3.6.4 Plasmids for the preparation of multiple gene constructs for the Modular Cloning (MoClo) System in *E. coli*

pAGM1311 (Weber et al., 2011)

This plasmid contains a kanamycin resistance and was used as a level -1 (L-1) universal acceptor plasmid for the domestication of internal type II restriction enzyme sites.

pAGM1287 (Weber et al., 2011)

This plasmid contains a spectinomycin resistance and was used as a level 0 (L0) acceptor plasmid for cloning of coding sequences (CDS) without stop module.

pICH47732 (Weber et al., 2011)

This plasmid contains an ampicillin resistance and was used as level 1 (L1) acceptor plasmid for assembly of L0 parts into transcriptional units. This L1 acceptor was used for orientation of transcriptional units in level 2 (L2) position 1 forward orientation.

pICH47742 (Weber et al., 2011)

This plasmid contains an ampicillin resistance and was used as L1 acceptor plasmid for assembly of L0 parts into transcriptional units. This L1 acceptor was used for orientation of transcriptional units in L2 position 2 forward orientation.

pICH47751 (Weber et al., 2011)

This plasmid contains an ampicillin resistance and was used as L1 acceptor plasmid for assembly of L0 parts into transcriptional units. This L1 acceptor was used for orientation of transcriptional units in L2 position 3 forward orientation.

pICH41766 (Weber et al., 2011)

This plasmid contains a spectinomycin resistance and was used as L2 end linker for assembly of three L1 multi gene constructs.

pAGM4673 (Weber et al., 2011)

This plasmid contains a kanamycin resistance and was used as L2 acceptor plasmid for assembly of L1 parts into multigene constructs.

pAGM1311- um01690 (sts1)

This plasmid contains a kanamycin resistance and was used as L-1 universal acceptor plasmid for the domestication of internal type II restriction enzyme sites of *um01690* (*sts1*) without its secretion signal. The sequences of interest were amplified with primer for mutations of internal type II restriction enzyme sites. The primers used were: OAli2986 + OAli2987, OAli2988 + OAli2989 and OAli2990 + OAli2991. The L-1 assembly reaction was performed using *Bsa*I and combining the PCR products with the L-1 cloning vector with ligase in a Golden Gate digestion ligation reaction (see chapter 4.5.2.3).

pAGM1311- *GRMZM2G159171_T01* (*CBPII T01*) .1

This plasmid contains a kanamycin resistance and was used as L-1 universal acceptor plasmid for the domestication of internal type II restriction enzyme sites of the first half of *CBPII T01* (*GRMZM2G159171_T01*). The sequences of interest were amplified with primer for the mutation of internal type II restriction enzyme sites. The primers used were: OAli2975 + OAli2976, OAli2977 + OAli2978. The L-1 assembly reaction was performed using *Bsa*I and combining the PCR products with the L-1 cloning vector with ligase in a Golden Gate digestion ligation reaction (see chapter 4.5.2.3).

pAGM1311- *GRMZM2G159171_T01* (*CBPII T01*) .2

This plasmid contains a kanamycin resistance and was used as L-1 universal acceptor plasmid for the domestication of internal type II restriction enzyme sites of the second half of *CBPII T01* (*GRMZM2G159171_T01*). The sequences of interest were amplified with primer for the mutation of internal type II restriction enzyme sites. The primers used were: OAli2979 + OAli2980 and OAli2981 + OAli2982. The L-1 assembly reaction was performed using *Bsa*I and combining the PCR products with the L-1 cloning vector with ligase in a Golden Gate digestion ligation reaction (see chapter 4.5.2.3).

pAGM1311- *GRMZM2G159171_T02* (*CBPII T02*)

This plasmid contains a kanamycin resistance and was used as L-1 universal acceptor plasmid for the domestication of internal type II restriction enzyme sites of *CBPII T02* (*GRMZM2G159171_T02*). The sequences of interest were amplified with primer for the mutation of internal type II restriction enzyme sites. The primers used were: OAli2983 + OAli2984, OAli2985 + OAli2980 and OAli2981 + OAli2982. The L-1 assembly reaction was performed using *Bsa*I and combining the PCR products with the L-1 cloning vector with ligase in a Golden Gate digestion ligation reaction (see chapter 4.5.2.3).

pAGM1287- *um01690* (*sts1*)

This plasmid contains a spectinomycin resistance and was used as a L0 acceptor plasmid for cloning of *um01690* coding sequence without stop module. The sequence of interest was assembled in this L0 vector using *Bpi*I and ligase and the pAGM1311-*um01690* (*sts1*) vector in a Golden Gate digestion-ligation reaction (see chapter 4.5.2.3).

pAGM1287- *GRMZM2G159171_T01* (*CBPII T01*)

This plasmid contains a spectinomycin resistance and was used as a L0 acceptor plasmid for cloning of the *GRMZM2G159171_T01* (*CBPII T01*) coding sequence without stop module. The sequence of interest was assembled in this L0 vector using *Bpi*I and ligase and the pAGM1311-*GRMZM2G159171_T01* (*CBPII T01*).1 as well as the pAGM1311-*GRMZM2G159171_T01* (*CBPII T01*).2 vector in a Golden Gate digestion-ligation reaction (see chapter 4.5.2.3).

pAGM1287- *GRMZM2G159171_T02* (*CBPII T02*)

This plasmid contains a spectinomycin resistance and was used as a L0 acceptor plasmid for cloning of the coding sequence of *GRMZM2G159171_T02* (*CBPII T02*) without stop module. The sequence of interest was assembled in this L0 vector using *Bpi*I and ligase and the pAGM1311-*GRMZM2G159171_T02* (*CBPII T02*) vector in a Golden Gate digestion-ligation reaction (see chapter 4.5.2.3).

4.3.6.5 Plasmids for the transformation of *S. cerevisiae* AH109 and subsequent yeast two-hybrid analysis

pGBKT7 (Clontech, Mountain View, US)

This plasmid contains a kanamycin resistance and a tryptophan (TRP) auxotrophy marker. It was used as a bait vector for yeast two hybrid analysis. The empty vector was used as a control plasmid.

pGBKT7 – UmSts1

This plasmid contains *um01690* (*sts1*) without secretion signal that was amplified using the primers OAli103 + OAli104 and cloned via *Nco*I and *Not*I into the empty pGBKT7 vector. This plasmid was used as a bait plasmid for yeast two-hybrid interaction screening against the maize cDNA library. It was also used in the confirmation study for testing the interaction with CBPII T01/T02.

pGADT7 (Clonetech, Mountain View, US)

This plasmid contains an ampicillin resistance and a leucine (LEU) auxotrophy marker. It was used as a prey vector for yeast two hybrid analysis. The empty vector was used as a control plasmid

pGADT7-CBPII T01

This plasmid contains *GRMZM2G159171_T01* (*CBPII T01*) gene without transmembrane domain that was amplified using the primers OAli2950 + OAli2951 and cloned via *Sac*I and *Eco*RI into the empty pGADT7 vector. This plasmid was used as a prey plasmid for yeast two-hybrid interaction study against Sts1.

pGADT7-CBPII T02

This plasmid contains the *GRMZM2G159171_T02* gene (*CBPII T02*) gene that was amplified using the primers OAli2952 + OAli2951 and cloned via *Sac*I and *Eco*RI into the empty pGADT7 vector. This plasmid was used as a prey plasmid for yeast two-hybrid interaction study against Sts1.

4.3.6.6 Plasmids for transient expression of proteins in *N. benthamiana* via *A. tumefaciens*-mediated transformation

Plasmids used for the transient expression of proteins in *N. benthamiana* were generated by using the MoClo cloning system and the MoClo Plant tool kit (Weber et al., 2012 and Engler et al., 2014) with the L0 constructs that are listed in 4.3.6.4. L1 and L2 constructs generated and used in this work are listed in Table 9 and Table 10. The assembly of fragments was done as described in 4.5.2.3 and afterwards transformed into *E. coli* Top 10 cells as described in 4.4.1.

Table 9: L1 constructs generated for the MoClo expression system in *N. benthamiana*

Addgene backbone	Expression construct
pICH47751	2x35S-p19
pICH47761	2x35S-GFP
pICH47732	2x35S-mCherry
pICH47742	2x35S_01690-cMYC
pICH47332	2x35S_CBPT01_HA
pICH47332	2x35S_CBPT02_HA
pICH47342	2x35S_01690-GFP
pICH47332	2x35S_CBP_T01-mCherry
pICH47332	2x35S_CBP_T02-mCherry

pICH47732	2x35S_um01690-CFP-HA-ctermYFP
pICH47742	2x35S_CBP_T01-mCherry-cMyc-N-termYFP
pICH47742	2x35S_CBP_T02-mCherry-cMyc-N-termYFP
pICH47732	2x35S_CFP-HA-ctermYFP
pICH47742	2x35S_mCherry-cMyc-N-termYFP

Table 10: L2 multigene constructs generated for the MoClo expression system in *N. benthamiana* from Level 1 transcription units

Purpose of use	Addgene backbone	Multigene units		
CoIP	pAGM4723	2x35S_CBPT01-HA	2x35S_01690-Myc	2x35S_p19
	pAGM4723	2x35S_CBPT02-HA	2x35S_01690-Myc	2x35S_p19
Overexpression	pAGM4723	2x35S_CBPT01-mCherry	2x35S_01690-eGFP	2x35S_p19
	pAGM4723	2x35S_CBPT02-mCherry	2x35S_01690-eGFP	2x35S_p19
	pAGM4723	2x35S_mCherry	2x35S_eGFP	2x35S_p19
Bimolecular fluorescence complementation	pAGM4723	2x35S_01690-CFPc-termYFP	2x35S_CBPT01-mCherryN-termYFP	2x35S_p19
	pAGM 4723	2x35S_01690-CFPc-termYFP	2x35S_CBPT02-mCherryN-termYFP	2x35S_p19
	pAGM4723	2x35S_01690-CFPc-termYFP	2x35S_mCherryN-termYFP	2x35S_p19
	pAGM4723	2x35S_CFPc-termYFP	2x35S_CBPT01-mCherryN-termYFP	2x35S_p19
	pAGM4723	2x35S_CFPc-termYFP	2x35S_CBPT02-mCherryN-termYFP	2x35S_p19
	pAGM4723	2x35S_CFPc-termYFP	2x35S_mCherryN-termYFP	2x35S_p19

4.4 Microbiological methods

4.4.1 Transformation of *E. coli*

The transformation of chemocompetent *E. coli* cells was done via the rubidium chloride-mediated transformation (Cohen et al., 1972). For the production of chemocompetent bacterial cells, 100 mL dYT medium supplemented with 10 mM $MgCl_2$ and 10 mM $MgSO_4$ was inoculated with 1 mL of a freshly grown overnight culture and incubated at 37 °C at 200 rpm until the OD_{600} value reached 0.5. The cells were pelleted by centrifugation at 1500 x*g* for 15 min at 4 °C and resuspended in 33 mL ice-cold RF1 solution. After 30 - 60 min incubation at 4 °C on ice, the cells were pelleted by centrifugation at 1500 x*g* for 15 min at 4 °C. The cell pellet was resuspended in 5 mL ice-cold RF2 solution and incubated for 15 min on ice. Afterwards, the cell suspension was stored at -80 °C after shock freezing it in 1.5 mL microcentrifuge tubes as 50 µL aliquots.

RF1-Solution	100 mM RbCl 50 mM $MnCl_2$ x 4 H_2O 30 mM K-Acetate 10 mM $CaCl_2$ x 2 H_2O 15 % (v/v) Glycerine in $H_2O_{bid.}$, pH 5.8 (Acetate), sterile filtered
RF2-Solution	10 mM MOPS 10 mMRbCl 75 mM $CaCl_2$ x 2 H_2O 15 % (v/v) Glycerine in $H_2O_{bid.}$, pH 5.8 (NaOH), sterile filtered

For the transformation of chemocompetent *E. coli* cells, one aliquot of cells was thawed on ice and 1-5 ng plasmid DNA or 1-5 µL ligation mixture were added. After incubation (30 min) on ice the mixture was heat-shocked at 42 °C for 60 seconds and then re-cooled on ice for 2 min. 200 µL of dYT liquid media was added and the tube was incubated for 1 h at 37 °C and 200 rpm. Afterwards, 200 µL of this transformation mixture was plated on YT agar medium containing the antibiotic used for selection and incubated at 37 °C overnight.

4.4.2 Blue-white screen of *E. coli* transformants

For the blunt end cloning of PCR products into the pCRII-TOPO plasmid, a blue-white selection approach was used. By insertion of the cloned PCR product into the pCRII-TOPO backbone, the lacZ gene inside the plasmid gets disrupted, leading to a lack of ß-galactosidase expression. Colonies that contain the inserted PCR fragment therefore appear white on X-Gal containing plates and are easily distinguishable from blue colonies in which ß-galactosidase expression is active. For this screening, X-Gal soluiton (2 % X-Gal, dissolved in DMSO) was added to a f.c. of 0.08 % one hour before the transformation on selective YT-agar plates.

4.4.3 Transformation of *A. tumefaciens*

The preparation of chemocompetent *A. tumefaciens* cells as well as the transformation of those cells was done as described in (Hofgen and Willmitzer, 1988). Instead of YEB media, dYT liquid and YT agar medium were used, containing the respective antibiotics for selection.

4.4.4 Transformation of *U. maydis*

The preparation of protoplasts and subsequent transformation of *U. maydis* protoplasts was done as described in Schulz et al. (1990) and Gillissen et al. (1992) with changes mentioned as follows. An overnight culture of *U. maydis* cells was started from cells grown on PD medium in 4 mL $YEPS_{light}$ medium and incubated for 8-10 hours at 28 °C, 200 rpm. After 1:3000 dilution of this culture in 50 mL $YEPS_{light}$ medium, the culture was grown until it reached an optical density of OD_{600}= 0.8. At this cell density, the cells were pelleted for 10 min at 2800 x*g* at 4 °C, resuspended in ice-cold SCS buffer and pelleted again for 10 min at 2800 x*g* at 4 °C. The resulting pellet was resuspended in 2 mL SCS buffer supplied with 2.5-5 mg Novozyme. The cell suspension was incubated for 5-10 min at room temperature. Protoplastation was monitored under the microscope. The reaction was stopped when 50 % of the cells had reached a spherical shape due to lysis of the cell wall. At this time point, 10 mL ice-cold SCS buffer was added and the protoplasts were pelleted for 10 min at 1500 x*g* at 4 °C. For removal of residual Novozyme rests, the pellet was washed three times with 10 mL ice-cold SCS buffer and centrifugation at 1500 x*g* at 4 °C. After the last centrifugation step, the pellet was resuspended in 500 µL ice-cold STC buffer. The cell suspension was stored at -80 °C after shock freezing in liquid N_2 1.5 mL microcentrifuge tubes as 50 µL aliquots.

For transformation of *U. maydis* protoplasts, an aliquot of cells was thawed on ice and 5 µg linearized plasmid DNA in a maximal volume of 10 µL and 1 µL heparin solution (1 mg/mL) were added and incubated on ice for 10 min. Afterwards, 500 µL STC/PEG solution was added and the cell suspension was again incubated on ice for 10 min. This mixture was then carefully spread on a freshly prepared regeneration agar plate consisting of a 10 mL bottom layer containing 2x selection antibiotic and a 10 mL top layer without selection antibiotic. The plates were incubated for 4-7 days at 28 °C until small colonies appeared which were afterwards singled and grown on PD agar plates containing the respective antibiotics. The resulting single colonies were used for DNA extraction (see chapter 4.5.1.2) and verified via Southern blot analysis (see chapter 4.5.3.2).

SCS solution	20 mM Na-Citrate, pH 5.8

	1 M Sorbitol in $H_2O_{bid.}$, sterile filtered
STC solution	10 mM Tris-HCl, pH 7.5 100 mM $CaCl_2$
	1 M Sorbitol in $H_2O_{bid.}$, sterile filtered
STC/PEG solution	15 mL STC 10 g PEG4000
Regeneration agar	Top: 1.5 % (w/v) Bacto agar 1 M Sorbitol in $YEPS_{light}$ Bottom: same as top agar but containing 2x antibiotic concentration

4.4.5 Test for filamentous growth of *U. maydis* and growth impairment

To check for the filamentous growth and fitness of newly generated *U. maydis* strains, the strains were grown on different media. Filament formation of *U. maydis* was induced by growing the strains on CM glucose medium supplemented with 0.01 g/mL activated charcoal. For the assessment of fitness of the strains, the different strains were grown on CM glucose medium containing either, Calcofluor (100 µg/mL), Congo Red (45 µg/mL), H_2O_2 (1 mM), NaCl (1M) or Sorbitol (1 M). For that, strains were grown in 4 mL $YEPS_{light}$ medium at 28 °C, 200 rpm to an optical density of OD_{600}=0.8. After pelleting the cells at 2500 x*g* for 5 min, the pellet was resuspended in sterile water and the OD_{600} was set to 1.0. A serial dilution was made from 10^{-1} to 10^{-4} and 5 µL of each dilution were spotted on the plates. Photographs were taken 24 h – 48 h after incubation at 28 °C in the dark.

4.4.6 Transformation of *S. cerevisiae*

For transformation of *S. cerevisiae*, the *DUALmembrane starter kit* (Dualsystems Biotech) manual was followed. For that, 5 mL YPD liquid media was inoculated with a single colony of AH109 *S. cerevisiae* strain. This culture was grown overnight at 28 °C and 200 rpm and used for starting a 50 mL culture of OD_{600}=0.2 in YPD medium. This culture was grown until it reached an optical density of OD_{600}=0.8. At this point, the cells were centrifuged for 5 min at 2500 x*g* and the resulting pellet was resuspended in 2.5 mL sterile water. Afterwards, 100 µL of this suspension were added to 300 µL PEG-LiOAc mix including 1.5 µg of the plasmid DNA to be transformed and mixed carefully. This mix was heat shocked for 45 min at 42 °C and slight shaking. The cells were then centrifuged at

700 x*g* for 10 min and resuspended in 100 µL 0.9 % NaCl. This mixture was spread on SD selective medium and incubated for 3-5 days at 28 °C.

PEG / LiOAC Mix	240 µL 50 % (w/v) PEG4000 36 µL 1M lithium acetate 25 µL single-stranded carrier DNA (boiled for 5 min prior to use)

4.4.7 Drop dilution assay for *S. cerevisiae*

For the yeast drop dilution assays, single colonies were grown on a shaker in 5 mL SD -Leu, -Trp selection medium at 28 ˚C, 200 U/min overnight and OD_{600} was adjusted to 0.2 in the next morning and cultures were regrown to OD_{600}= 0.6 – 0.8. 2 mL of the culture was then spinned down for 10 min at 3000 *xg* and the resulting pellet was washed twice with sterile H_2O. The pellet was resuspended in sterile H_2O to an OD_{600} of 1 and 5 µL of a dilution series were plated (1, 1:10, 1:100, 1:1000) on low stringency plates (SD -Leu, -Trp), medium stringency plates (SD -Leu, -Trp, -His) and high stringency plates (SD -Leu, -Trp, -Ade, -His), respectively. The plates were incubated at 28 ˚C for 4-5 days.

4.5 Molecular biological methods

4.5.1 Isolation of nucleic acids

4.5.1.1 Plasmid DNA isolation from *E. coli*

For plasmid DNA isolation the QIAprep Mini Plasmid Prep Kit (Qiagen, Hilden, Germany) was used. This kit works on the principle of alkaline lysis. For that, 2 mL of a thickly grown *E. coli* overnight culture was pelleted at 17000 *xg* for 2 min in a 2 mL microcentrifuge tube. The pellet was resuspended in 250 µL P1 buffer and for lysis, 250 µL P2 buffer were added and the suspension was mixed by repeatedly inverting the tube. After incubation at room temperature for one minute, 300 µL P3 buffer were added for neutralization of the lysed cell extract and precipitation of proteins. The precipitated proteins together with the resulting cell debris were pelleted by centrifugation at 17000 *xg* for 10 min. Afterwards 600 µL of the supernatant were transferred into a 1.5 mL microcentrifuge tube containing 600 µL isopropanol. For precipitation of plasmid DNA, the tubes were incubated at -20 °C for 30 min and afterwards centrifuged at 17000 *xg* for 10 min. After discarding the

supernatant, the resulting pellet was washed by adding 800 µL of 80 % EtOH and subsequent centrifugation for 10 min at 17000 *xg*. In the end, the supernatant was completely removed and the resulting pellet containing plasmid DNA was resuspended in 50 µL sterile water.

4.5.1.2 Isolation of genomic DNA from *U. maydis*

For the isolation of genomic DNA (gDNA) from *U. maydis*, a modified version of the protocol from (Hoffman and Winston, 1987) was used. For that, 2 mL of a thickly grown *U. maydis* overnight culture was pelleted at 17000 *xg* for 2 min in a 2 mL microcentrifuge tube. After discarding the supernatant, ~ 0.3 g glassbeads (0.4-0.6 mm), 400 µL *Ustilago* lysis buffer and 500 µL of phenol/chloroform were added to the cell pellet. The microcentrifuge tube was then incubated for 20 min on a Vibrax-VXR shaker (IKA, Staufen, Germany) at 2500 rpm for 20 min. For separation of the phases, the tube was spinned down for 15 min at 17000 *xg*. The upper phase, containing the extracted DNA, was transferred to a fresh 1.5 mL microcentrifuge tube and precipitated by addition of 1 mL 100 % EtOH and centrifugation at 17000 *xg* for 2 min. Afterwards, the supernatant was discarded and the resulting pellet was dried for 1 min at room temperature and dissolved in 50 µL TE buffer containing 20 µg/mL RNaseA by incubation in a Thermomixer (Eppendorf, Hamburg, Germany) at 55 °C, 1200 rpm, 30 min. The extracted DNA was stored at -20 °C.

Ustilago lysis buffer	50 mM Tris-HCl, pH 7.5 50 mM Na_2-EDTA 1 % (w/v) SDS in $H_2O_{bid.}$
Phenol / Chloroform	50 % (v/v) Phenol (equilibrated in TE-buffer) 50 % (v/v) Chloroform

4.5.1.3 Isolation of total RNA from infected maize tissue

For isolation of total RNA, the tissue was frozen in liquid N_2 and homogenized using mortar and pestle under constant liquid N_2 cooling. TRIzol® reagent (Invitrogen, Darmstadt, Germany*)* was used for extraction of RNA according to the manufacturer's instructions. About 400 µL of homogenized leaf tissue was filled into a 1.5 mL reaction

tube and 1 mL TRIzol® reagent was immediately added to the sample. After centrifugation at 12000 *xg* for 10 min, the supernatant was transferred to a fresh 1.5 mL reaction tube and 200 µL of chloroform was added. The sample was mixed by inversion of the tubes and after a centrifugation step at 12000 *xg* for 15 min the upper aqueous phase was transferred to a fresh 1.5 mL reaction tube containing 500 µL isopropanol and incubated at room temperature for 10 min. For precipitation of the RNA, the tube was centrifuged at 12000 *xg* for 10 min and the supernatant was discarded. After a washing step with 1 mL 75 % EtOH and centrifugation at 7500 *xg* for 5 min, the supernatant was discarded and the pellet was dissolved in 35 µL RNase fee H_2O at 55 °C for 10 min.

4.5.1.3 DNase-digest after RNA extraction

For removal of residual DNA inside extracted RNA samples, the Ambion®TURBO DNA-free™ Kit (Thermo Fisher Scientific Inc., Bonn, Germany) was used according to the manufacturer's instructions. For that, 4 µL 10x DNase buffer and 1 µL DNase were added to the extracted RNA and the sample was incubated at 37 °C for 30 min. Afterwards, 4 µL inactivation beads were added and the sample was incubated for 5 min at room temperature. Finally, the sample was centrifuged at 7500 *xg* for 2 min and 35 µL were transferred to a fresh 1.5 mL reaction tube. The amount of RNA was assessed by photometric measurement on a NanoDrop ND_1000 spectrophotometer (Thermo Fisher Scientific Inc., Bonn, Germany) and quality was afterwards assessed by loading 1 µg of RNA on a 1 % TBE gel (see chapter 4.5.3.1).

4.5.1.5 Isolation of total RNA from infected maize cells after laser capture microdissection

RNA from dissected maize cells was extracted by using the PicoPure™ RNA Isolation Kit *(*Thermo Fisher Scientific Inc., Bonn, Germany) according to the manufacturer's instructions. DNase treatment in this protocol was done with the Ambion®TURBO DNA-free™ Kit (Thermo Fisher Scientific Inc., Bonn, Germany). DNAse treatment was done by adding 39 µL DNase buffer and 0.5 µL DNase after step C.2.e of the PicoPure™ RNA Isolation protocol and incubation at 37 °C for 20 min and a following centrifugation step at 8000 x*g* for 15 seconds for removal of DNase.

4. 5. 1. 6 Purification of DNA

Plasmid DNA and PCR fragments of restriction digest mixtures were purified using the Wizard SV Gel and PCR purification System (Promega, Mannheim, Germany) either directly or via gel extraction. The purification was done according to the manufacturer's instructions.

4.5.2 *In vitro* modification of nucleic acids

4.5.2.1 Restriction of DNA

The restriction of DNA was done via *type II restriction* endonucleases (NEB, Frankfurt/Main, Germany). The amount of digested DNA ranged from 1 – 5 µg. The restriction reaction was set up according to the manufacturer's instructions. A common digestion reaction was composed as follows:

1 – 5 µg DNA (plasmid or cleaned-up PCR product)
2 µL 10xNEB buffer (P1-4)
2 µL 10xBSA
0.5 U restriction enzyme
Ad 20 µL $H_2O_{bid.}$

4.5.2.2 Ligation of DNA fragments

For the ligation of DNA fragments the T4 DNA ligase (Thermo scientific, Bonn, Germany) was used according to the manufacturer's instructions. For the ligation of a desired insert with a corresponding vector backbone, a molar ratio of 3:1 – 10:1 was used to ensure a higher abundance of insert. A standard ligation mixture was set up as follows:

50 ng vector DNA
Insert DNA in a 3 – 10 times higher molar abundance
2 µL 10x T4 DNA ligasebuffer
1 µL T4 DNA ligase
Ad 20 µL $H_2O_{bid.}$

The ligation reaction was incubated at 4 °C overnight.

4.5.2.3 Assembly of fragments in the MoClo system (Weber et al., 2011)

For the assembly of fragments in L0 and L2 acceptors, *Bpi*I was used in a digestion-ligation reaction. Reactions were set up as follows:

50-100 ng of acceptor plasmid
Plasmid containing each module to be inserted in a 2:1 molar ratio of insert:acceptor
5 U *Bpi*I FD
1 µL FastDigest buffer (Thermo Fisher Scientific, Bonn, Germany)
200 U T4 DNA Ligase (NEB, Frankfurt/Main, Germany)
1 µL 10 mM ATP
Ad 10 µL $H_2O_{bid.}$
Reaction was afterwards incubated as follows:
1. 37 °C – 10 min
2. 16 °C – 10 min
3. Repeat 1. and 2. five times
4. 37 °C – 10 min
5. 65 °C – 20 min
6. 4 °C – ∞

For the assembly of fragments in L-1 and L1 acceptors, *Bsa*I was used in a digestion-ligation reaction. Reactions were set up as follows:

50-100 ng of acceptor plasmid
Plasmid containing each module to be inserted in a 2:1 molar ratio of insert:acceptor
10 U *Bsa*I
1 µL CutSmart buffer (NEB, Frankfurt/Main, Germany)
200 U T4 DNA Ligase (NEB, Frankfurt/Main, Germany)
1 µL 10 mM ATP
Ad 20 µL $H_2O_{bid.}$
Reaction was afterwards incubated as follows:
1. 40 °C – 10 min
2. 16 °C – 10 min
3. Repeat 1. and 2. five times
4. 50 °C – 10 min
5. 80 °C – 20 min
6. 4 °C – ∞

4.5.2.4 Polymerase chain reaction (PCR)

For the amplification of DNA fragments via polymerase chain reaction (PCR) different polymerases were used depending on the purpose of the experiment. For common cloning processes of genes from all organisms used in this study, except *Zea mays*, the Phusion® *Hot Start High Fidelity* DNA-Polymerase (Finnzymes/Thermo Scientific, Bonn, Germany) was used. For the cloning of genes from *Zea mays*, KOD Xtreme™ Hot Start DNA Polymerase (Merck Millipore, Darmstadt, Germany) was used. General analytical tests like colony PCR and all other PCRs that were not used for further cloning processes,

were done with the Taq-Polymerase containing RedMix (Bioline, Luckenwalde, Germany). Every PCR reaction was set up in a 20 µL or 50 µL reaction volume depending on its purpose of use. PCR reactions were set up according to the manufacturer's instructions.

4.5.2.5 cDNA synthesis

After isolation of RNA and DNase treatment (4.5.1.3 - 4.5.1.4), cDNA was synthesized using the First strand cDNA Synthesis Kit (Thermo Scientific, Bonn, Germany) according to the manufacturer's instructions. For one reaction, 0.5 µg total RNA was transcribed into cDNA using oligo$(dt)_{18}$ primer in a total reaction volume of 5.5 µL (1/2 reaction volume).

4.5.2.6 Quantitative real-time PCR

As a template for quantitative real-time PCR (qRT-PCR), cDNA (4.5.2.5) synthesized from freshly isolated RNA was used. The qRT PCR reactions were set up using the IQ SYBR® Green Supermix (Biorad, Munich, Germany) according to the manufacturer's instructions in a total volume of 25 µL. For one reaction, 1 µL cDNA was used. All qRT-PCR analyses were performed in an iCycler system (Bio-Rad, Munich, Germany) with the following program: 95 ˚C / 2 min – (95 ˚C / 30 s – 62 ˚C / 30 s – 72 ˚C / 30 s) x 45 cycles. Relative gene expression values were calculated with the Gene Expression Macro program (Bio-Rad, Munich, Germany) and relative expression was afterwards calculated manually (Pfaffl et al., 2002).

4.5.2.7 Sequencing of nucleic acids

Sequencing reactions were done by MWG (Martinsried, Germany) or GATC (Cologne, Germany). For sequencing of Plasmids, plasmid isolation was done with QiaPrepPlasmid Prep kit (Qiagen, Hilden, Germany) as described in 4.5.1.1. PCR products were cleaned up with the Wizard SV Gel and PCR purification System (Promega, Mannheim, Germany) as described in 4.5.1.6 prior to sequencing. DNA sequencing results were analyzed using Clone Manager 9 software (SciEd, Denver, US).

4.5.2.8 RNAseq

For pre-amplification of RNA the Ovation® RNA-Seq System V2 (NuGen Technologies.Inc, San Carlos, US) was used. First strand cDNA synthesis was done using poly(T) and random primers with a total amount of 90 ng RNA, followed by a second strand synthesis and isothermal strand-displacement amplification. The Illumina Nextera® XT DNA sample preparation protocol (Illumina, San Diego, US) Part #15031942 Rev. C was used with 1 ng cDNA input amount. Validation and quantification of cDNA was done with the Agilent 2200 TapeStation (Agilent Technologies, Santa Clara, US) and the Qubit System (Invitrogen, Karlsruhe, Germany). Pooled libraries were quantified using the Peqlab KAPA Library Quantification Kit (Peqlab, Erlangen, Germany) and the PRISM® 7900HT sequence Detection System (Applied Biosystems, Foster City, US). A paired-end read of 2x75 bp per lane resulted in 22,6-28,4 Mreads/sample (3.4-4.3 Gb) and a ratio of bases > Q30 of 96 %.

4.5.3 Separation and detection of nucleic acids

4.5.3.1 Agarose gel electrophoresis

Agarose gel electrophoresis was performed for the separation and estimation of size of nucleic acids. Agarose gels of 0.8 – 2 % Agarose concentration were prepared in 1x TAE or 0.5x TBE buffer depending on the need, by boiling in a microwave. After the buffer had cooled to ~60 °C, ethidium bromide (f.c. 0.25 µg/mL) was added. After solidification of the gel, the samples containing 1x DNA-loading dye were loaded for separation into the pockets of the gel and were run in a chamber containing 1x TAE/0.5x TBE buffer. Separation of DNA was then done at constant voltage of 80-120 V depending on the size and percentage of the gel in parallel to a DNA marker of defined size. DNA bands were visualized by UV radiation at 365 nm using a gel documentation unit (VILBER LOURMAT, Peqlab, Erlangen, Germany).

5x TBE buffer	440 mM Tris-Base 440 nM Boric acid 10 mM EDTA, pH 8.0
50x TAE-buffer	2 M Tris-Base 2 M Acetic acid

6x DNA loading dye	50 mM EDTA pH 8.0 50 % Sucrose 0.1 % (v/v) Bromophenol blue In TE-Buffer

4.5.3.2 Southern Blot analysis

After transformation of *U. maydis* (see chapter 4. 4. 4), transformants were singled and DNA was isolated (see chapter 4.5.1.2) and subject to Southern blot analysis (Southern, 2006) to check for the right integration into the *U. maydis* genome. For that, 5 µg of the isolated DNA was fragmented via restriction enzyme digest. The restriction enzyme was selected in order to lead to fragment sizes of the locus that define a distinguishable size difference between transformed locus of interests and corresponding wild type locus. The restriction enzyme digest was done in a volume of 200 µL and incubated overnight. The fragmented DNA was afterwards precipitated by adding 15 µL 3 M potassium acetate and 1 mL 100 % ethanol and incubation of the samples at -20 °C for 30 min followed by centrifugation for 15 min at 17000 *xg*. The samples were then washed with 750 µL 80 % ethanol and afterwards again centrifuged for 5 min at 17000 *xg*. After centrifugation for 5 min at 17000 *xg*, the supernatant was removed and the pellet was resuspended in 20 µL 1xDNA loading dye. The samples were separated via agarose gel electrophoresis (see chapter 4.5.3.1) in a 0.8 % agarose gel in 1x TAE buffer. Separation of the fragment was documented using a gel documentation unit (VILBER LOURMAT, Peqlab, Erlangen, Germany) and depurination of large fragments was done by incubation of the gel in 0.25 N HCl for 15 min and subsequent neutralization in 0.4 N NaOH for 15 min to facilitate the transfer of big DNA fragments during the blotting process. Transfer of nucleic acids was done in 0.4 N NaOH transfer solution via capillary forces to a Hybond-N^+ nylon membrane (GE, Munich, Germany) following the protocol by Southern (1975). For that, the transfer buffer was sucked overnight into paper towels through the gel and DNA fragments onto the nylon membrane lying on top of the gel. The DNA fragments on the nylon membrane were afterwards fixed by UV cross-linking using an ultraviolet crosslinker (Amersham Life Science, Amersham, UK). The membrane was then immediately pre-hybridized for 1 h at 65° C in 20 mL hybridization buffer in a hybridization oven (UVP HB-1000 Hybridizer Cambride, UK).

Detection of nucleic acids was done using dioxigenin (DIG)-labeled DNA probes. Probes were synthesized using the PCR DIG Labeling Mix kit (Roche, Mannheim, Germany) following the manufacturer's instructions. DIG-labeled PCR products were added to 20 mL of hybridization buffer and heated for 10 min to 100° C for denaturation. The pre-hybridization buffer was exchanged with probe-containing buffer and hybridization was performed at 65 °C in the hybridization oven overnight. The membrane was then washed twice with southern wash buffer for 15 min at 65° C in the hybridization oven followed by two 5 min washing steps with DIG wash buffer at room temperature and 30 min incubation in DIG buffer 2. Afterwards, the membrane Antibody solution was incubated in antibody solution for 30 min followed by two washing steps in DIG wash buffer for 15 min each. After incubation in DIG buffer 3 for 5 min, 3 mL CDP-Star solution was added. The blot was put into an autoclaving bag and exposed to a light-sensitive film (Kodak XAR-5 X-OMAZ, Kodak, Rochester, New York, U.S.) for 1-45 min depending on signal intensity. Films were developed using an X-ray film developer machine (QX-60, Konica, Munich, Germany).

1 M sodium phosphate buffer	Solution 1: 1 M Na2HPO4 Solution 2: 1M NaH2PO4 * H2O Solution 2 is added to solution 1 as long as the pH reaches 7.0
Southern hybridization buffer	500 mM Sodium phosphate buffer, pH 7.0 7 % (w /v) SDS
Southern wash buffer	0.1 M Sodium phosphate buffer, pH 7.0 1 % (w /v) SDS
DIG buffer 1	0.1 M Maleic acid, pH 7.5 0.15 M NaCl
DIG buffer 2	0.1 M Maleic acid, pH 7.5 0.15 M NaCl 1 % (w /v) Milk powder
DIG buffer 3	0.1 M Maleic acid, pH 9.5 0.1 M NaCl 0.05 M $MgCl_2$
DIG wash buffer	0.1 M Maleic acid, pH 7.5 0.15 M NaCl 0.3 % (v /v) Tween-20
CDP-Star solution	100 µl CDP-Star (Roche, Mannheim, Germany) in 10 ml DIG buffer 3

4.6. Biochemical methods

4.6.1 Separation of proteins via SDS-PAGE

Separation of proteins was done according to (Laemmli, 1970) by Sodium dodecyl sulfate polyacrylamide gel electrophoresis (SDS-PAGE). Denatured proteins are hereby separated according to their molecular size in an electric field. For that, protein samples were completely denatured by use of 1X SDS gel loading buffer supplied with 100 mM DTT and boiling for 5 min at 99˚ C. The proteins hereby get negatively charged and can migrate along an electric field. PAGE gels composed of stacking and separating gel were casted using the Mini Protean System (BioRad, Munich, Germany). Samples were loaded into the precasted gel pockets and gels were run in 1 X SDS running buffer in a gel chamber at a voltage of 120-160 V for 1 h. For later estimation of the molecular mass, the prestained protein marker 10-170 kDa (Fermentas, St. Leon-Rot, Germany) was used. After concentration of the sample inside the stacking gel due to its coarse porosity, proteins get separated according to their size in the separating gel while smaller proteins run faster through the gel than larger proteins.

6x SDS-gel loading buffer	4M Tris-HCl, pH 6.8 6 % (w /v) SDS 0.15 % (w /v) Bromophenol blue 60 % (v /v) Glycerol
SDS running buffer	25 mM Tris-HCl, pH 8.3 192 mM Glycine 4 mM SDS
Stacking gel	5 % (v/v) Acrylamide 0.1 % (w/v) SDS in 125 mM Tris-HCl, pH 6.8 0.1 % (w/v) Ammonium persulfate 0.05 % (v/v) Tetramethylethylene diamine (TEMED)
Separating gel	12-17 % (v/v) Acrylamide 0.1 % (w/v) SDS in 375 mM Tris-HCl, pH 8.8 0.1 % (w/v) Ammonium persulphate 0.05 % (v/v) TEMED

4.6.2 Staining of SDS-PAGE gels

SDS-PAGE gels were stained overnight with Page Blue Protein color solution (Fermentas, St Leon-Roth, Germany) according to the manufacturer's instructions and afterwards washed in H_20.

4.6.3 Immunological detection of proteins via chemoluminescence (Western blot)

After separation of protein samples by SDS PAGE, the proteins were transferred to a nitrocellulose membrane by a semi-dry transfer system (BioRad, Munich, Germany). For that, the SDS gel was put on a nitrocellulose membrane with an outside layer of 3 mm whatman paper on each side wetted in transfer buffer. Transfer of proteins onto the nitrocellulose membrane was performed for 1 h at 100 mA and 25 V per gel. Afterwards, immunological detection of proteins that were transferred onto the nitrocellulose membrane was done. The membrane was therefore incubated for 1 h at room temperature with TBS-T solution containing 5 % milk powder that was subsequently replaced by a 0.5 % TBS-T solution containing the primary antibody and incubated for 16 h at 4 ˚C. This was followed by three washing steps with TBS-T buffer for 15 min each and an incubation with TBS-T buffer containing the secondary antibody for 1 h at room temperature. All antibodies used in this study are listed in Table 11. After another three washing steps for 15 min each in TBS-T buffer, the membranes were incubated with ECL Plus western blotting detection reagent (GE Healthcare, Munich, Germany) and sealed in a plastic bag prior to film exposure (Kodak XAR-5 X-OMAZ, Kodak, Rochester, New York, U.S.) for 1-60 min depending on signal intensity. Films were developed with a developer machine (QX-60, Konica, Munich, Germany).

Western transfer buffer	25 mM Tris-HCl, pH 10.4 192 mM glycine 15 % (v/v) methanol
TBS-T buffer	50 mM Tris-HCl, pH 7.5 150 mM NaCl 0.1 % (v/v) Tween 20

Table 11: Antibodies used in this study

Antibody Target	Organism	Dilution	Supplier
HA	Mouse	1:30000	Sigma-Aldrich (Deisenhofen, Germany)
cMyc	Mouse	1:5000	Sigma-Aldrich (Deisenhofen, Germany)
Myc-HRP	Mouse	1:1500	Thermo Fisher Scientific (Bonn, Germany)
GST	Rabbit	1:4000	Sigma-Aldrich (Deisenhofen, Germany)
Anti-mouse-HRP	Horse	1:3000	Cell Signaling Technology (Danver, US)

4.6.4 Protein quantification according to Bradford

The quantification method by Bradford (1976) was used for quantification of protein amounts in protein extracts for Co-Immunoprecipitation experiments (see chapter 4.6.6). Calibration curves were made with bovine serum albumin (BSA) as a standard. Roti®-Quant protein quantification reagent (Carl Roth, Karlsruhe, Germany) was used for this assay.

4.6.5 Protein extractions from *S. cerevisiae* for Western blot analysis

In order to check for protein expression of the *S. cerevisiae* strains used for yeast two hybrid analysis, western blot analysis was performed. For that *S. cerevisiae* was grown overnight in a 5 mL culture and cells were harvested by centrifugation for 5 min at 17000 *xg*. The cell pellet was disrupted by addition of 0.3 g glass beads together with 50 µL SDS-gel loading buffer supplied with 100 mM DTT. Samples were afterwards heated for 5 min at 99 ˚C and shaken for 15 min on a Vibrax-VXR shaker (IKA, Staufen, Germany) followed by a subsequent heating step at 99 ˚C for 15 min. After centrifugation at 17000 *xg* for 2 min, 15 µL of sample was loaded on an SDS-PAGE gel for western blot analysis (see chapter 4.6.1 and 4.6.3).

4.6.6 Protein extraction from *N. benthamiana* for Co-Immunoprecipitation and subsequent Western blot analysis

For testing of the interaction of *U. maydis* Sts1 with *Zea mays* CBPI/CBPII splicing variants, the respective constructs bearing Sts1-Myc and CBPI-HA or CBPII-HA were transiently expressed in *N. benthamiana* and tested for interaction via *in planta* Co-immunoprecipitation. For expression control, the constructs were separately expressed. The *A. tumefaciens* strain GV3101 was used for these experiments (see chapter 4.3.1). By following the protocol of Sparkes et al. (2006), *A. tumefaciens* was infiltrated into 4

weeks old *N. benthamiana* leaves and leaves were harvested 3 dai and frozen liquid N_2. After grinding of the leaf material in liquid N_2, the powder was mixed with protein extraction buffer (50 mM Tris-HCl, 150 mM NaCl, pH 7.0). 2 mL of the protein extract was subsequently centrifuged at 3000 *xg* at 4 ˚C for 15 min to remove cell debris. Protein concentration was adjusted to an equal level in all samples by measuring protein concentrations as described in 4.6.4. 40 µL anti-HA Affinity Matrix (Roche Diagnostics, Mannheim, Germany) was added to 1 mL of leaf extract containing 2 mg/mL protein and incubated for 45 min on a rotation wheel at 4 ˚C. The samples containing the HA-affinity matrix were spinned through Pierce SpinColumns (Thermo Scientific, Rockford, US) and washed with 2 mL protein extraction buffer. Proteins bound to the HA-affinity matrix were eluted by incubating the samples in 70 µL 2XSDS loading buffer containing 100 mM DTT for 5 min at 99 ˚C. 30 µL were loaded and separated on a SDS-PAGE gel and afterwards analyzed by Western blot analysis (see chapter 4.6.1 and 4.6.3).

4.6.7 Heterologous testexpression of recombinant proteins in *E. coli*

For heterologous protein production the *E. coli* strain BL21 (DE3) pLysS was used. This strain was transformed with either pRSET-GST-PP- um01690 (sts1), pRSET-GST-PP-*GRMZM2G159171_T02* (*CBPII T02*) or pRSET-GST-PP-*GRMZM2G159171_T02* (*CBPII T02*). For testexpression of the recombinant proteins, a dYT liquid culture was inoculated with the respective *E. coli* strains and incubated overnight at 37 ˚C, 220 rpm. The next morning, this culture was diluted 1:100 in 30 mL dYT liquid medium supplemented with the respective antibiotics and regrown to OD_{600}=0.6-0.8 at 37 ˚C, 220 rpm. When the cultures reached OD_{600}=0.6, 400 µM IPTG was added for induction of the genome-encoded T7 RNA polymerase and starting of protein production. Cultures were then shifted to 28 ˚*C, 220 rpm.* Samples (2 mL) were taken every hour after induction to determine the optimal time point for protein expression. Culture samples were centrifuged at 16000 *xg* for 5 min and pellets were stored at -20 ˚C. For analysis of protein solubility cell pellets were treated as described in the QIAexpressionist protocol 6 for determination of target protein solubility (Qiagen, Hilden, Germany). SDS loading dye was added to the total cell extracts and soluble protein extracts, respectively and samples were boiled at

99 ˚C for 10 min and separated via SDS-PAGE (see chapter 4.6.1). Gels were subsequently stained with Page Blue Protein color solution (see chapter 4.6.2).

4.6.8 Hemicellulose composition analysis of infected maize tissue via high-performance anion-exchange chromatography with pulsed amperometric detection (HPAE-PAD)

Maize *cv.* Early Golden Bantam leaf areas from mock treated as well as *U. maydis* infected chlorotic and tumorous tissue were harvested 6 dpi (6 g per tissue type) in three independent biological experiments. Harvested material was immediately frozen in liquid N_2 and lyophilized. Dried tissue material was ground at 30 Hz for 5 min using a ball mill and 2-4 mg was used for further extraction. Samples were extracted in three repetitions with 1 ml 70 % EtOH followed by three extractions with 1 ml 1:1 (v/v) chloroform:methanol. After drying of samples, 10 U alpha-amylase and 1 U amyloglucosidase was used for enzymatic starch removal from the insoluble residue at 37 °C for 16 h in 200 mM sodium acetate buffer (pH 5. 5). Samples were afterwards dried and cell wall matrix polysaccharides were hydrolyzed with 2 M TFA at 121 °C for 90 min. Monosaccharides were quantified via HPAE-PAD as described in Voiniciuc et al. (2015). To test for fungal material, glucosamine was measured but not detected in quantifiable amounts.

4.6.9 Lignocellulosic composition analysis of infected maize tissue via pyrolysis-gas chromatography-mass spectrometry (Py-GC-MS) analysis

Lyophilized tissue (see chapter 4.6.8) was filled into self-made tubes (0.9 cm length, 1.8 mm diameter) made from ferromagnetic metal foil (0.9 x 0.67 cm, Japan Analytical Industry, T_c = 590 °C). Powdered biomass (1-2 mg) was used for analysis. Solutions of 0.2 mg/µL acetone were prepared in case of high-viscous Organocat lignin solutions. 5 µL of these solutions were added to the self-made metal tubes filled with diatomaceous earth. The metal tubes were inserted into a glass liner and placed into a Curie point pyrolyzer (Pilodist, Bonn, Germany) for pyrolysis. Pyrolysis was carried out at 590 °C for 10 s. Pyrolysis products were afterwards separated by an Optima-5-HT column (60 m x 0.25 mm, 0.25 µm filmthickness, Macherey-Nagel, Düren, Germany). A constant He gas

flow (1.0 mL/min) was applied. Samples were heated from 80 °C to 340 °C (temperature was hold for 20 min) at a rate of 5 °C/min. Injector temperature (280 °C) was kept constant. Mass spectrometer was used in the electron impact (EI, 70 eV) mode and scanned over the range *m*/*z* 30 – 650 with an acquisition rate of 3 microscans. Transfer line and ion source were kept constantly at 280 °C. An alkane mixture solution (C8-C24) was analysed for a better assignment of the peaks in the pyrolysis chromatograms by calculation of Kovat's indices. Data was processed with the XCalibur 2.0.7 software (Thermo Fisher Scientific Inc., Bonn, Germany). Pyrolysis products were identified by comparison of mass spectra with the NIST and Wileymass spectral libraries by comparison with compounds reporded by (Ralph and Hatfield, 1991).

4.6.10 Chlorophyll measurements

Photosynthesis pigments were quantified by spectralphotometric measurements following the protocol of Lichtenthaler and Wellburn (1983). For extraction of pigments 500 mg mock treated as well as *U. maydis* infected chlorotic or tumorous leaf material was ground in 4 mL acetone and extinction a 1:10 dilution was measured in acetone at 662 nm (for chlorophyll a), 645 nm (for chlorophyll b) and 470 nm (for carotenoids). Concentration of pigments was afterwards calculated using the coextinction coefficients determined by Lichtenthaler and Wellburn (1983).

4.6.11 Starch measurement

3-5 mg of alcohol insoluble residue (AIR) from 4.6.8 was incubated for 20 min at 100 °C in 500 µl 200 mM sodium acetate buffer (pH 5.5). After samples reached room temperature 1.4 U amyloglucosidase (Roche Diagnostics, Mannheim Germany) and 10 U alpha-amylase (Roche Diagnostics, Mannheim Germany) were added and samples were incubated overnight at 37 °C. Released glucose was determined with the D-Glucose Assay Kit (GOPOD Format; Megazyme, Wicklow, Ireland). Measurements were carried out according to the manufacturer's instructions. The assay was hereby adapted to 96-well microtiter plates. Therefore, volumes of samples and all reagents were scaled down to 1/10th and a glucose standard curve was prepared to ensure linearity of the assay.

4.7 Plant methods

4.7.1 Maize (*Zea mays* sp.) varieties

For seedling and tassel infection with *U. maydis* and subsequent disease symptom scoring the maize variety *Zea mays* cv. Early Golden Bantam (Old Seeds, Madison, WI, US) was used. For histological analyses including transmission electron microscopy *Zea mays* cv. Early Golden Bantam was used, unless otherwise stated. The lignin mutant lines *Z. mays* chalcone synthase mutant M541J (A1 A2 C1 c2 R1-nj) and cognate control strain M142V (A1 A2 C1 C2 R1-nj) were obtained from the Maize Genetics Stock Center, University of Illinois, IL, US. The brown midrib mutant (*bm2*) was obtained from the Walbot lab, Stanford University, CA, US.

4.7.2 Cultivation of maize

Maize plants were grown in controlled conditions with a day phase at 28 ˚C, up to 90,000 LUX and 40 % humidity for 15 h and a night phase of 9 h at 20 ˚C and 60 % humidity. The daytime phase included a ramping set in which sunrise was simulated for 2.5 h and sunset was simulated for 2.5 h. Maize plants were cultivated in soil type “Frühstorfer Erde Typ T” and watered on a daily basis.

4.7.3 Infection of maize with *U. maydis*

U. maydis strains were grown overnight (28 ˚C, 200 rpm) in $YEPS_{light}$ liquid medium, rediluted to OD_{600}= 0.2 in the morning and regrown to OD_{600}=0.6-0.8. Cells were pelleted for 5 min, 2400 *xg* and adjusted with sterile H_2O to OD_{600}= 1 for disease symptom scoring or OD_{600}= 3 for microscopy. Seedlings were syringe infected by injection of the inoculum into the whorl of the 7 d old plants at the base of the plant above the meristematic center as described in Redkar and Doehlemann, 2016. For tassel infections 5-6 weeks old plant whorls were syringe infected with 1-2 mL inoculum at the height of the plant where thickening due to tassel formation occurred as described in Redkar and Doehlemann, 2016.

4.7.4 *U. maydis* disease rating and symptom quantification

Disease symptoms on maize seedlings infected by *U. maydis* were scored after 6 dpi and after 12 dpi while disease symptoms on maize tassels were scored after 14 dpi. For that, the scoring scheme developed by Kämper et al. (2006) and Schilling et al. (2014) was applied. For seedling and tassel infections about 40 plants per biological replicate were scored for each *U. maydis* strain that was assessed in its virulence. Disease symptom classification for seedling and tassel symptoms are listed in Table 12 and Table 13, respectively.

Table 12: Classification of disease symptoms in infected maize seedlings

Disease symptom	Description of symptom
No symptoms	The leaf does not show any disease symptoms or sign of infection
Chlorosis	The leaf has chlorotic areas around the infection site on the infected leaf and younger leaves
Small tumors	Tumors around the infection area are ≤ 1 mm on the infected leaf and younger leaves
Normal tumors	Tumors around the infection area are ≥ 1 mm on the infected leaf and younger leaves
Big tumors	Very big tumors are formed on the infected leaf or younger leaves including the plant stem that lead to an overall bending of the plant
Dead plant	Plant has died due to *U. maydis* infection

Table 13: Classification of disease symptoms in infected maize tassels

Symptom classification	Description of symptom
Small tumors 1	≤ 50 % of the male flower bears small tumors (1-4 mm)
Small tumors 2	≥ 50 % of the male flower bears small tumors (1-4 mm)
Big tumors 1	≤ 50 % of the male flower bears big tumors (≥ 4 mm)
Big tumors 2	≥ 50 % of the male flower bears big tumors (≥ 4 mm)
No development of the male flower	The male flower stays undeveloped and stunted

4.7.5 Cultivation of *N. benthamiana*

N. benthamiana seeds were sown on soil type “Frühstorfer Pikiererde Typ T“ and transplanted into single pots 7 days after germination. The plants were grown under controlled conditions with a day phase at 21 ˚C with a 16 h light and 8 h night period. About 4-5 weeks old plants were used for infiltration experiments.

4.7.6 Infiltration of *N. benthamiana* leaves for *Agrobacterium* mediated transformation

For transient overexpression experiments *N. benthamiana* leaves were syringe-infiltrated with *A. tumefaciens* strains that bear the respective overexpression constructs (see chapter 4.3.6.6). Cultivation of *A. tumefaciens* was done as described in chapter 4.3.1. Syringe-infiltrated *N. benthamiana* leaves were harvested 3 dai for the respective experiments. Pictures from leaves that were transiently overexpressing fluorescently labeled proteins were taken with a ChemiDoc™ XRS+ System (Biorad, Munich, Germany).

4.7.7 Bimolecular fluorescence complementation (BiFC) in *N. benthamiana*

BiFC experiments were done via transient overexpression in *N. benthamiana* leaves. The previously generated BiFC parts each contain one half of the nucleotide sequence encoding for the YFP chromophore together with the nucleotide sequence for either mCherry or CFP for expression control. The BiFC expression set thereby consists of two parts, a mCherry-tag fused to the N-terminal part of YFP (pSPYNE_N) and a CFP-tag fused to the C-terminal part of YFP (pSPYCE_C). Direct interaction of the tagged proteins of interest would bring both proteins into close proximity and thereby lead to an interaction of the two YFP fragments. This interaction is possible due to spatial proximity would then allow the formation of a functional chromophore and lead to YFP fluorescence (Waadt and Kudla, 2008). The constructs used for BiFC were previously generated by C. Hemetsberger (MPI Marburg, Germany). Their coding sequence was cloned into the MoClo vector system plant toolkit for *A. tumefaciens* mediated transformation (see chapter 4.3.6.6). *N. benthamiana* leaves expressing the respective constructs were investigated by confocal microscopy (4.8.3).

4.8 Tissue fixation, staining and microscopy

4.8.1 Tissue embedding and sectioning for laser capture microdissection (LCM)

For LCM of maize leaf tissue, the third leaf of infected or mock infected plants was harvested for tissue fixation. One infected leaf was embedded per sample. Plant tissue was vacuum infiltrated with cold calcium-magnesium-free PBS (pH 7.2) containing 0.4% paraformaldehyde and 10 % sucrose. During infiltration samples were kept on ice. Vacuum infiltration was done with 250 mbar for 5 min, followed by ATM for 5 min. This step was repeated three times. Samples were afterwards embedded in embedding compound (Surgipath® Cryo-Gel™, Leica, Nussloch, Germany) and arranged in tissue Tissue-Tek®Cryomold intermediate vinyl specimen molds 15mmx15mmx5mm (Sakura Finetek, VWR, Darmstadt, Germany). Molds were allowed to slowly freeze by incubation on a plastic petri dish, floating on liquid N_2. Frozen tissue molds were stored at -80 °C until required for LCM. Transverse sections of embedded plant material were cut at -20 °C using a cryostat (CM1900, Leica, Nussloch, Germany) to a thickness of 14 µm and mounted on normal microscopy slides. Tissue sections were immediately immersed in 50 % methanol for 1 min, further dehydrated by immersion in a methanol dehydration series (70 %, 1 min, 80 %, 1 min, 90 %, 1 min, 100 % methanol, 1 min), followed by 5 min immersion in xylene. Tissue sections were afterwards air-dried and subsequently used for LCM analysis.

4.8.2 Tissue embedding and sectioning for transmission electron microscopy (TEM)

Tissue fixation for TEM was done by cutting leaf tissue to small size (0.25 cm x 0.5 cm) and subsequent infiltration in fixing solution (2.5 % paraformaldehyde, 0.5 % glutaraldehyde, 0.06 M Sørensen phosphate buffer, pH 7.2) followed by incubation at room temperature overnight. Vacuum infiltration was done with 250 mbar for 5 min, followed by ATM for 5 min. This step was repeated three times. Samples were afterwards washed with 0.06 M Sørensen phosphate buffer (pH 7.2) for 4 times and then dehydrated using an acetone dehydration gradient (50 %, 2 h, 70 %, 2 h, 90 %, 2 h) at room

temperature. Samples were afterwards infiltrated with LR-White resin (London Resin Company Ltd., Berkshire, UK) using a gradient (30 %, 12 h, 60 %, 12 h, 90 %, 12 h) mixed with 90 % acetone. Samples were embedded in 100 % LR-White resin in gelatin capsules and polymerized at 50 °C for 24 h under anaerobic conditions. Transversal ultrathin leaf sections with a thickness of 60 nm were cut with a Reichert Ultracut S ultramicrotome (Leica Microsystems, Nussloch, Germany).

4.8.3 Paraplast embedding of maize leaf tissue

Paraplast embedding was done as described in Jackson (1991). Leaf tissue for paraplast fixations was harvested at indicated time points and infiltrated with fixing solution (50 % EtOH, 3.7 % formaldehyde, 5 % glacial acetic acid, 0.5 % Triton X-100, 1 % DMSO, 39,8 % H_2O). Vacuum infiltration was done with 250 mbar for 5 min, followed by ATM for 5 min. This step was repeated three times. Samples were incubated on a shaker overnight at 4 °C. The next day, half of the volume of fixing solution was removed and replaced with cold (4 °C) 95 % EtOH. Samples were incubated with gentle agitation at 4 °C. This step was repeated twice with a minimum of 2 h between changes. All remaining solution was replaced with cold 95 % EtOH and samples were incubated with gentle agitation for at least 2 h. At the end of the day, all solution was replaced with 100 % EtOH and incubated overnight at 4 °C with gentle agitation. The following day, EtOH was replaced with fresh, cold 100 % EtOH and placed on a shaker at room temperature. When samples had reached room temperature, gradual Histoclear infiltration with a timeframe of 2 h per incubation step was done with Histoclear (Roti-Histol, Roth, Karlsruhe, Germany). EtOH was removed and replaced with a 1:3 Histoclear:EtOH solution followed by a 1:1 Histoclear:EtOH solution. Half of the volume was afterwards replaced twice with 100 % Histoclear. At the end of the day all liquid was replaced with 100% Histoclear and incubated on a shaker overnight at room temperature. The following day, paraffin infiltration was done by addition of ¼ volume of paraplast (Surgipath®Paraplast®, Leica Biosystems, Richmond, IL, US). Samples were incubated on a shaker for at least 3 h until the paraplast chips had partially dissolved. At the end of the day, another ¼ volume of Paraplast was added and incubated on a shaker overnight at room temperature. The next morning, samples were transferred to 42 °C until all paraplast had melted and then

transferred to 65 °C. All following additions were done with previously melted paraplast chips that had been incubated at 65 °C. Half volume of melted paraplast was added and incubated at 65 °C for 3 h. At the end of the day all liquid was changed for 100 % melted paraplast. This step was repeated twice every 12 h. Embedded tissue was arranged in molds for embedding (Tissue-Tek®Cryomold Sakura Finetek, VWR, Darmstadt, Germany). Tissue samples were afterwards transversely sectioned with a thickness of 12 µm using a Leica RM2235 manual rotary microtome. Tissue sections were mounted on a droplet of water on microscopy slides that had been heated on a slide heater at 45 °C. Slides were kept on the slide heater for at least 2 h until all water evaporated.

Tissue sections were de-waxed before microscopy by incubation in fresh 100 % Histoclear for 20 min at room temperature followed by an EtOH hydration gradient. For that, slides were incubated in EtOH gradient solution for 2 min in each solution (2x 100 % EtOH, 95 % EtOH, 90 % EtOH, 80 % EtOH, 70 % EtOH, 50 % EtOH, 30 % EtOH, 2x H_2O).

4.8.4 EdU-based DNA synthesis assay in tissue sections

DNA synthesis in planta was monitored on the cellular level by an *in vivo* incorporation of 5-ethynyl-2-deoxyuridine (EdU) protocol followed by paraplast embedded transversal leaf sections. For that, *U. maydis* SG200-infected, SG200Δsee1-infected and mock treated seedling leaves were infiltrated with 10 µM EdU (Invitrogen, Karlsruhe, Germany) and afterwards incubated in a growth chamber for 5 h after 3 dpi, 4 dpi and 6 dpi as described in Redkar and Doehlemann (2016a). Afterwards, the respective leaf samples were fixed in 100 % (v/v) ethanol followed by a paraplast embedding (see chapter 4.8.3). 12 µm tissue sections were rehydrated in 1xPBS (pH 7.4) as described in chapter 4.8.3 and the EdU protocol after Redkar and Doehlemann (2016a) was applied. For that, microscopy slides were washed twice in 1xPBS (pH 7.4) + 2 % BSA for 5 min each followed by an incubation in permeabilization solution consisting of 1xPBS (pH 7.4) + 1 % Triton X-100 for 20 min while shaking. Slides were afterwards washed twice in 1xPBS (pH 7.4) + 2 % BSA for 5 min each followed by an incubation (30 min at room temperature) with EdU Click-IT cocktail supplied with 20 µg/mL PI (Propidium iodide, Molecular Probes, Eugene, Oregon, U. S.) for detection. Microscopy slides were washed twice in 1xPBS (pH 7.4) +

2 % BSA for 5 min each and washed with 1xPBS (pH 7.4) before imaging with a Nikon Eclipse Ti inverted microscope using the filter set indicated in chapter 4.8.9. The following filters were used: CFP-2432C (for cell wall autofluorescence) exciter: 425-250 nm and emitter: 475-500 nm; HC-Filterset mCherry (for PI detection) extiter: 540-580 nm and emitter: 600 nm – 690 nm; EGFP HC Filter Set (for EdU detection) exciter: 455 nm-490 nm and emitter: 500 nm-540 nm.

4.8.5 Fuchsin staining of paraplast-embedded tissue

Rehydrated paraplast tissue sections (see chapter 4.8.3) were immersed for 30 min in a Methylene Blue solution and rinsed in H_2O. Afterwards, slides were incubated for 30 seconds in a Basic Fuchsin solution. Slides were rinsed in H_2O before mounting.

Methylene Blue solution	0.26 % (w/v) Methylene Blue 0.04 % (w/v) Azur II 20 % (v/v) Glycerol 20 % (v/v) Methanol 0.12 M Na_2HPO_4 0.06 M KH_2PO_4 in $H_2O_{bid.}$, pH 6.9
Basic Fuchsin solution	1 % (w/v) Basic Fuchsin 20 % (v/v) EtOH in $H_2O_{bid.}$

4.8.6 Starch staining according to Lugol

Rehydrated paraplast tissue sections (see chapter 4. 8. 3) were immersed for 5 min in Iodine-potassium iodide solution according to Lugol (Roth, Karlsruhe, Germany). Slides were rinsed in H_2O before mounting.

4.8.7 Safranine-O staining

For staining of Lignin, rehydrated paraplast tissue sections (see chapter 4. 8. 3) were immersed for 5 min in 1 % Safranine-O in H_2O (Merck, Darmstadt, Germany). Slides were rinsed in H_2O before mounting.

4.8.8 Confocal microscopy

Confocal microscopy was performed using a Leica TCS SP8 confocal laser scanning microscope (Leica, Wetzlar, Germany). For confocal imaging a high-resolution CCD camera (C4742, Hamamatsu) was used. Laser channels used for confocal microscopic analysis are listed in Table 14. Image data was processed using the Leica Application Suite software (Leica, Wetzlar, Germany).

Table 14: Lasers used for confocal microscopy with their respective excitation and detection wavelength

Laser	Excitation wavelength	Detection wavelength	Purpose of use
405 Diode	405 nm	435-480 nm	Cell wall autofluorescence
Argon	458 nm	470-490 nm	CFP
Argon	488 nm	500-520 nm	GFP
Argon	514 nm	520-540 nm	YFP
561 DPSS	561 nm	590-630 nm	mCherry

4.8.9 Fluorescence microscopy

Imaging was done with a Nikon Eclipse Ti inverted microscope (Nikon Instruments Microscopes and Digital Imaging Systems, Alzenau, Germany) using the filter set indicated in Table 15. Digital images of a high resolution were recorded using a Hamamatsu C11440 ORCA-flash4.0LT camera (Hamamatsu Photonics, Herrsching am Ammersee, Germany) for fluorescence microscopy and a Jenoptic ProgRes CT5 camera (Jenoptic Optical Systems GmbH, Jena, Germany) for light microscopy staining.

Table 15: Filters used for fluorescence microscopy with their respective spectra

Filter	Excitation spectra	Detection spectra	Purpose of use
CFP-2432C	425-450 nm	475-500 nm	Cell wall autofluorescence
mCherry HC Filterset	540-580 nm	600 nm-690 nm	PI detection, chlorophyll autofluorescence
EGFP HC Filterset	455 nm-490 nm	500 nm-540 nm	EdU detection

4.8.10 Laser capture microdissection microscopy

Approximately 1800-2000 cells/selected tissue spots were captured using the PALM MicroBeam system (Zeiss, Jena, Germany) onto a single adhesive cap (AdhesiveCap 200 opaque, Zeiss, Göttingen, Germany). After dissection 10 µL extraction buffer from Arcturus® PicoPure® RNA isolation kit were added and samples were incubated at 42 °C

as stated in the Arcturus® PicoPure® RNA isolation kit. Samples were afterwards kept at -80 °C before proceeding with RNA extraction (see chapter 4.5.1.5)

4.8.11 Transmission electron microscopy (TEM)

After washing of ultrathin sections in H_2O (2x, 5 min), grids containing microsections were post-stained with uranyl-acetate (2 % dissolved in H_2O) for 15 s and then investigated with a Philips CM10 transmission electron microscope. Micrographs were taken with a Gatan ORIUS CCD camera (Model 830.P07W44, Gatan Inc, Pleasanton, US).

4.8.12 Image processing and measurement

Leaf sections were analyzed and measured using the Nikon Instruments NIS-Elements (Nikon Instruments Microscopes and Digital Imaging Systems, Alzenau, Germany) software for imaging and cell size measurements, Leica Application Suite software (Leica, Wetzlar, Germany) and Photoshop CS6 (Adobe Systems Engineering GmbH, Hamburg, Germany).

4.9 Bioinformatic methods

4.9.1 RNAseq analysis

RNAseq data was provided by the Cologne Center for Genomics, Cologne, Germany. Reads from RNAseq data were mapped with Bowtie v2.2.9 (Langmead and Salzberg, 2012) and TopHat v2.1.1 (Kim et al., 2013) against the reference genomes of *Zea mays* B73 RefGen v3 and *Ustilago maydis* 521 v2.0 obtained from the NCBI Genome Server (ftp://ftp.ncbi.nih.gov/genomes/) on October 17th, 2016 under consideration of the corresponding annotations. Differentially expressed genes were determined following the protocol described in Trapnell et al. (2012). Fragments per kilobase per million fragments mapped (FPKM) were determined with Cufflinks v2.2.1 (Trapnell et al., 2013).

4.9.2 Further bioinformatic analysis tools

For planning of cloning strategies, amino acid and nucleotide sequence comparisons for cloning the program Clone Manager 9.0 (Sci-Ed-Software) was used. Nucleotide sequences of interest were obtained from the National Center for Biotechnology Information (NCBI; www.ncbi.nlm.nih.gov/; Altschul et al., 1997), the MIPS PEDANT3

U. maydis database (http://mips.helmholtz-muenchen.de/genre/proj/ustilago/; Walter et al., 2009) and the Gramene database (http://www.gramene.org; Tello-Ruiz et al., 2016). Protein domains were analyzed using the SMART (Simple Modular Architecture Research Tool) online tool (smart.embl-heidelberg.de; Letunic et al., 2015) and the SignalP 4.0 online tool (www.cbs.dtu.dk/services/SignalP/; Bendtsen et al., 2004). A Pfam database scan (Pfam; http://www.ebi.ac.uk/Tools/pfa/pfamscan/help/; Mistry et al., 2007) was done for prediction of functional protein domains.

5 Bibliography

Aichinger, C., Hansson, K., Eichhorn, H., Lessing, F., Mannhaupt, G., Mewes, W., and Kahmann, R. (2003). Identification of plant-regulated genes in *Ustilago maydis* by enhancer-trapping mutagenesis. Mol Genet Genomics *270*, 303-314.
Alexandratos, N., and Bruinsma, J. (2012). World Agriculture towards 2030/2050: The 2012 Revision. ESA Working Paper *12*.
Altschul, S.F., Madden, T.L., Schäffer, A.A., Zhang, J.H., Zhang, Z., Miller, W., and Lipman, D.J. (1997). Gapped Blast and Psi-Blast - a New Generation of Protein Database Search Programs. Nucleic Acids Res *25*, 3389-3402.
Anders, S., and Huber, W. (2010). Differential expression analysis for sequence count data. Genome Biol *11*.
Annis, S.L., and Goodwin, P.H. (1997). Recent advances in the molecular genetics of plant cell wall-degrading enzymes produced by plant pathogenic fungi. Eur J Plant Pathol *103*, 1-14.
Aspinall, G.O. (1959). Structural chemistry of the hemicelluloses. Adv Carbohydr Chem *14*.
Ausubel, F.M., Brent, R., Kingston, R.E., Moore, D.D., Seidman, J.G., Smith, J.A., and Struhl, K. (2002). Short protocols in molecular biology: a compendium of methods from current protocols in molecular biology. Wiley
Baayen, R.P. (1986). Regeneration of vascular tissues in relation to Fusarium-wilt resistance of carnation. Eur J Plant Pathol *92*, 273-285.
Bai, C., Sen, P., Hofmann, K., Ma, L., Goebl, M., Harper, J.W., and Elledge, S.J. (1996). SKP1 connects cell cycle regulators to the ubiquitin proteolysis machinery through a novel motif, the F box. Cell *86*, 263-274.
Banuett, F., and Herskowitz, I. (1996). Discrete developmental stages during teliospore formation in the corn smut fungus, Ustilago maydis. Development *122*, 2965-2976.
Barinka, C., Rojas, C., Slusher, B., and Pomper, M. (2012). Glutamate carboxypeptidase II in diagnosis and treatment of neurologic disorders and prostate cancer. Curr Med Chem *19*, 856-870.
Barlow, P.W. (1985). Nuclear Chromatin Structure in Relation to Cell Differentiation and Cell Activation in the Cap and Quiescent Centre of *Zea mays* L. J Exp Bot *36*, 1492-1503.
Barros, J., Serk, H., Granlund, I., and Pesquet, E. (2015). The cell biology of lignification in higher plants. Ann Bot *115*, 1053-1074.
Basse, C.W. (2005). Dissecting defense-related and developmental transcriptional responses of maize during *Ustilago maydis* infection and subsequent tumor formation. Plant physiology *138*, 1774-1784.
Beemster, G.T., Fiorani, F., and Inzé, D. (2003). Cell cycle: the key to plant growth control? Trends in plant science *8*, 154-158.
Begerow, D., Stoll, M., and Bauer, R. (2006). A phylogenetic hypothesis of Ustilaginomycotina based on multiple gene analyses and morphological data. Mycologia *98*, 906-916.

Belien, T., Van Campenhout, S., Robben, J., and Volckaert, G. (2006). Microbial endoxylanases: effective weapons to breach the plant cell-wall barrier or, rather, triggers of plant defense systems? Molecular plant-microbe interactions : MPMI *19*, 1072-1081.
Bellincampi, D., Cervone, F., and Lionetti, V. (2014). Plant cell wall dynamics and wall-related susceptibility in plant-pathogen interactions. Front Plant Sci *5*.
Bendtsen, D.J., Nielsen, H., von Heijne, G., and Brunak, S. (2004). Improved prediction of signal peptides: SignalP 3.0. Journal of molecular biology *340*, 783-795.
Blinks, L.R. (1954). The Photosynthetic Function of Pigments Other Than Chlorophyll. Annu Rev Plant Physiol *5*, 93-114.
Bloom, J., and Cross, F.R. (2007). Multiple levels of cyclin specificity in cell-cycle control. Nature reviews Molecular cell biology *8*, 149-160.
Boerjan, W., Ralph, J., and Baucher, M. (2003). Lignin Biosynthesis. Annu Rev Plant Biol *54*, 519-546.
Boller, T. (1995). Chemoperception of microbial signals in plant cells. Annu Rev Plant Physiolo Plant Mol Biol *46*, 189-214.
Boller, T., and Felix, G. (2009). A renaissance of elicitors: Perception of microbe-associated molecular patterns and danger signals by pattern-recognition receptors. Annual Rev Plant Biol *60*, 379-406.
Boller, T., and He, S.Y. (2009). Innate immunity in plants: an arms race between pattern recognition receptors in plants and effectors in microbial pathogens. Science *324*, 742–744.
Bonawitz, N.D., and Chapple, C. (2010). The genetics of lignin biosynthesis: Connecting genotype to phenotype. Annual review of genetics *44*, 337-363.
Bradbury, E.M. (1992). Reversible histone modification and the chromosome cell cycle. Bio Essays *14*, 9-16.
Bradford, M.M. (1976). A rapid and sensitive method for the quantitation of microgram quantities of protein utilizing the principle of protein-dye binding. Anal Biochem *72*, 248-254.
Brefort, T., Doehlemann, G., Mendoza-Mendoza, A., Reissmann, S., Djamei, A., and Kahmann, R. (2009). Ustilago maydis as a Pathogen. Annual review of phytopathology *47*, 423-445.
Brutus, A., Sicilia, F., Macone, A., Cervone, F., and Lorenzo, G. (2010). A domain swap approach reveals a role of the plant wall-associated kinase 1 (WAK1) as a receptor of oligogalacturonides. Proc Natl Acad Sci *107*, 9452–9457.
Caillaud, M.C., Dubreuil, G., Quentin, M., Perfus-Barbeoch, L., Lecomte, P., de Almeida-Engler, J., Rosso, M.N., and Favery, B. (2008). Root-knot nematodes manipulate plant cell functions during a compatible interaction. Journal of plant physiology *165*, 104-113.
Callow, J.A. (1975). Endopolyploidy in Maize Smut Neoplasms Induced by the Maize Smut Fungus, Ustilago Maydis. The New phytologist *75*, 253-257.
Callow, J.A., and Ling, I.T. (1973). Histology of neoplasms and chlorotic lesions in maize seedlings following the injection of sporidia of Ustilago maydis (DC) Corda. Physiol Plant Pathol *3*, 489-494.
Carpita, N.C. (1996). Structure and Biogenesis of the Cell Walls of Grasses. Annual review of plant physiology and plant molecular biology *47*, 445-476.

Carpita, N.C., Defernez, M., Findlay, K., Wells, B., Shoue, D.A., Catchpole, G., Wilson, R.H., and McCann, M.C. (2001). Cell wall architecture of the elongating maize coleoptile. Plant physiology *127*, 551-565.
Carpita, N.C., and Gibeaut, D.M. (1993). Structural models of primary cell walls in flowering plants: consistency of molecular structure with the physical properties of the walls during growth. Plant J *3*, 1-30.
Cesari, S., Bernoux, M., Moncuquet, P., Kroj, T., and Dodds, P.N. (2014). A novel conserved mechanism for plant NLR protein pairs: the "integrated decoy" hypothesis Front Plant Sci *5*.
Chandran, D. (2015). Co-option of developmentally regulated plant SWEET transporters for pathogen nutrition and abiotic stress tolerance. Iubmb Life *67*, 461-471.
Chandran, D., Inada, N., Hather, G., Kleindt, C.K., and Wildermuth, M.C. (2010). Laser microdissection of Arabidopsis cells at the powdery mildew infection site reveals site-specific processes and regulators. Proc Natl Acad Sci *107*, 460-465.
Chandran, D., Rickert, J., Cherk, C., Dotson, B.R., and Wildermuth, M.C. (2013). Host cell ploidy underlying the fungal feeding site is a determinant of powdery mildew growth and reproduction. Molecular plant-microbe interactions : MPMI *26*, 537 - 545.
Chaudhury, A., Letham, S., Craig, S., and S., D.E. (1993). *amp1* - a mutant with high cytokinin levels and altered embryonic pattern, faster vegetative growth, constitutive photomorphogenesis and precocious flowering. The Plant Journal *4*, 907-916.
Chen, L.Q., Hou, B.H., Lalonde, S., Takanaga, H., Hartung, M.L., Qu, X.Q., Guo, W.J., Kim, J.G., Underwood, W., Chaudhury, B.*, et al.* (2010). Sugar transporters for intercellular exchange and nutrition of pathogens. Nature *468*, 527-532.
Chevalier, C. (2007). Cell cycle control and fruit development. Cell Cycle Control and Plant Development; Annual Plant Reviews *32*, 294-310.
Chisholm, S.T., Coaker, G., Day, B., and Staskawicz, B.J. (2006). Host-microbe interactions: Shaping the evolution of the plant immune response. Cell *124*, 803-814.
Chowdhury, J., Henderson, M., Schweizer, P., Burton, R.A., Fincher, G.B., and Little, A. (2014). Differential accumulation of callose, arabinoxylan and cellulose in nonpenetrated versus penetrated papillae on leaves of barley infected with Blumeria graminis f. sp. hordei. The New phytologist *204*, 650-660.
Christensen, J.J. (1963). Corn smut caused by *Ustilago maydis*. Am Phytopathol Soc Monogr *2*, 1-41.
Cohen, S.N., Chang, A.C., and Hsu, L. (1972). Nonchromosomal antibiotic resistance in bacteria: genetic transformation of *Echerichia coli* by R-factor DNA. Proc Natl Acad Sci *69*, 2110-2114.
Conrath, U., Beckers, G.J., Langenbach, C.J., and Jaskiewicz, M. (2015). Priming for enhanced defense. Annual review of phytopathology *53*, 97-119.
Cosgrove, D.J. (1997). Assembly and enlargement of the primary cell wall in plants. Annual review of cell and developmental biology *13*, 171-201.
Costa, S. (2016). Cell identity: a matter of lineage and neighbours. The New phytologist *210*, 1155-1158.
Couto, D., and Zipfel, C. (2016). Regulation of pattern recognition receptor signalling in plants. Nat Rev Immunol *16*, 537-552.
Cui, H., Tsuda, K., and Parker, J.E. (2015). Effector-triggered immunity: from pathogen perception to reobust defense. Annu Rev Plant Biol *66*, 487-511.

Dangl, J.L., and Jones, J.D. (2001). Plant pathogens and integrated defence responses to infection. Nature *411*, 826-833.
Dangl, J.L., M., H.D., and Staskawicz, B.J. (2013). Pivoting the plant immune system from dissection to deployment. Science *341*, 746-751.
De Bary, A. (1853). Untersuchungen über die Brandpilze und die durch sie verursachten Krankheiten der Pflanzen mit Rücksicht auf das Getreide und andere Nutzpflanzen. Berlin, W W F Müller.
de Wit, P.J., Mehrabi, R., Van den Burg, H.A., and Stergiopoulos, I. (2009). Fungal effector proteins: past, present and future. Molecular plant pathology *10*, 735-747.
Depuydt, S., Trenkamp, S., Fernie, A.R., Elftieh, S., Renou, J.P., Vuylsteke, M., Holsters, M., and Vereecke, D. (2009). An integrated genomics approach to define niche establishment by Rhodococcus fascians. Plant physiology *149*.
Djamei, A., and Kahmann, R. (2012). *Ustilago maydis*: Dissecting the Molecular Interface between Pathogen and Plant. PLoS pathogens *8*, e1002955.
Djamei, A., Schipper, K., Rabe, F., Ghosh, A., Vincon, V., Kahnt, J., Osorio, S., Tohge, T., Fernie, A.R., Feussner, I.*, et al.* (2011). Metabolic priming by a secreted fungal effector. Nature *478*, 395-398.
Dodds, P.N., and Rathjen, J.P. (2010). Plant immunity: towards an integrated view of plant-pathogen interactions. Nat Rev Genet *11*, 539-548.
Doehlemann, G., Reissmann, S., Assmann, D., Fleckenstein, M., and Kahmann, R. (2011). Two linked genes encoding a secreted effector and a membrane protein are essential for Ustilago maydis-induced tumour formation. Molecular microbiology *81*, 751-766.
Doehlemann, G., van der Linde, K., Assmann, D., Schwammbach, D., Hof, A., Mohanty, A., Jackson, D., and Kahmann, R. (2009). Pep1, a secreted effector protein of *Ustilago maydis*, is required for successful invasion of plant cells. PLoS pathogens *5*, e1000290.
Doehlemann, G., Wahl, R., Horst, R.J., Voll, L.M., Usadel, B., Poree, F., Stitt, M., Pons-Kuhnemann, J., Sonnewald, U., Kahmann, R.*, et al.* (2008a). Reprogramming a maize plant: transcriptional and metabolic changes induced by the fungal biotroph Ustilago maydis. Plant J *56*, 181-195.
Doehlemann, G., Wahl, R., Vranes, M., de Vries, R.P., Kämper, J., and Kahmann, R. (2008b). Establishment of compatibility in the *Ustilago maydis*/maize pathosystem. Plant physiology *168*, 29-40.
Dong, X. (1998). SA, JA, ethylene, and disease resistance in plants. Curr Opin Plant Biol *1*, 316-323.
Doster, M.A., and Bostock, R.M. (1988). Quantification of lignin formation in almond bark in response to wounding and infection by Phytophthora species. Phytopathology *78*, 473-477.
Douchkov, D., Lueck, S., Hensel, G., Kumlehn, J., Rajaraman, J., Johrde, A., Doblin, M.S., Beahan, C.T., Kopischke, M., Fuchs, R.*, et al.* (2016). The barley (Hordeum vulgare) cellulose synthase-like D2 gene (HvCslD2) mediates penetration resistance to host-adapted and nonhost isolates of the powdery mildew fungus. The New phytologist *212*, 421-433.

Dubacq, C., Guerois, R., Courbeyrette, R., Kitagawa, K., and Mann, C. (2002). Sgt1p contributes to cyclic AMP pathway activity and physically interacts with the adenylyl cyclase Cyr1p/Cdc35p in budding yeast. Eukaryot Cell *1*, 568-582.

Dutheil, J.Y., Mannhaupt, G., Schweizer, G., Sieber, C.M.K., Münsterkötter, M., Güldener, U., Schirawski, J., and Kahmann, R. (2016). A tale of genome compartmentalization: the evolution of virulence clusters in smut fungi Genome Biol Evol *8*, 681-704.

Engler, C., Youles, M., Gruetzner, R., Ehnert, T.M., Werner, S., Jones, J.D.G., Patron, N.J., and Marillonnet, S. (2014). A Golden Gate Modular Cloning Toolbox for Plants. ACS Synth Biol *3*, 839-843.

Facette, M., Shen, Z., Björnsdottir, F.R., Briggs, S.P., and Smith, L.G. (2013). Parallel Proteomic and Phosphoproteomic Analyses of Successive Stages of Maize Leaf Development. The Plant cell *25*, 2798-2812.

Felix, G., Duran, J.D., Volko, S., and Boller, T. (1999). Plants have a sensitive perception system for the most conserved domain of bacterial flagellin. The Plant Journal *18*, 265 - 276.

Ferrari, S., Savatin, D.V., Sicilia, F., Gramegna, G., Cervone, F., and Lorenzo, G.D. (2013). Oligogalacturonides: plant damage-associated molecular patterns and regulators of growth and development. Front Plant Sci *4*.

Fornalé, S., Shi, X., Chai, C., Encina, A., Irar, S., Capellades, M., Fuguet, E., Torres, J.L., Rovira, P., Puigdomènech, P.*, et al.* (2010). ZmMYB31 directly represses maize lignin genes and redirects the phenylpropanoid metabolic flux. Plant J *64*, 633-644.

Fournier, C., Durand, J.L., Ljutovac, S., Schäufele, R., Gastal, F., and Andrieu, B. (2005). A functional-structural model of elongation of the grass leaf and its relationships with the phyllochron. The New phytologist *166*, 881-894.

Fu, Z.Q., and Dong, X. (2013). Systemic acquired resistance: turning local infection into global defense. Annu Rev Plant Biol *64*, 839-863.

Gao, L., Kelliher, T., Nguyen, L., and Walbot, V. (2013). Ustilago maydis reprograms cell proliferation in maize anthers. Plant J *75*, 903-914.

Genre, A., Chabaud, M., Faccio, A., Barker, D.G., and Bonfante, P. (2008). Prepenetration apparatus assembly precedes and predicts the colonization patterns of arbuscular mycorrhizal fungi within the root cortex of both *Medicago truncatula* and *Daucus carota*. The Plant cell *20*, 1407-1420.

Gheysen, G., and Mitchum, M.G. (2009). Molecular insights in the susceptible plant response to nematode infection. Cell Biology of Plant Nematode Parasitism *Vol 15*.

Gillissen, B., Bergemann, J., Sandmann, C., Schröer, B., Bölker, M., and Kahmann, R. (1992). A two-component regulatory system for self/non-self recognition in *Ustilago maydis*. Cell *68*, 647-657.

Gimenez-Ibanez, S., Boter, M., Fernandez-Barbero, G., Chini, A., Rathjen, J.P., and Solano, R. (2014). The bacterial effector HopX1 targets JAZ transcriptional repressors to activate jasmonate signaling and promote infection in Arabidopsis. PLoS Biol *12*.

Glazebrook, J. (2005). Contrasting mechanisms of defense against biotrophic and necrotrophic pathogens. Annual review of phytopathology *43*, 205-227.

Göhre, V., and Robatzek, S. (2008). Breaking the barriers: microbial effector molecules subvert plant immunity. Annual review of phytopathology *46*, 189-215.

Gomez-Gomez, L., and Boller, T. (2000). FLS2: an LRR receptor-like kinase involved in the perception of the bacterial elicitor flagellin in Arabidopsis. Mol Cell *5*, 1003-1011.
Grant, M.R., and Jones, J.D. (2009). Hormone (dis)harmony moulds plant health and disease. Science *324*, 750-752.
Grant, S.G., Jessee, J., Bloom, F.R., and Hanahan, D. (1990). Differential plasmid rescue from transgenic mouse DNAs into Escherichia coli methylation-restriction mutants. Proc Natl Acad Sci U S A *87*, 4645-4649.
Green, P.B. (1976). Growth and Cell Pattern Formation on an Axis: Critique of Concepts, Terminology, and Modes of Study. Botanical Gazette *137*, 187-202.
Guenl, M., Gille, S., and Pauly, M. (2010). Oligo mass profiling (OLIMP) of extracellular polysaccharides. Journal of Visualized Experiments *40*.
Gurtley, L.R., Walters, R.A., and Tobey, R.A. (1975). Sequential phosphorylation of histone subfractions in the Chinese hamster cell cycle. J Biol Chem *250*, 3936-3944.
Haegi, A., Bonardi, V., Dall'Aglio, E., Gilissant, D., Tumino, G., Collins, N.C., Bulgarelli, D., Infantino, A., Stanca, A.M., Delledonne, M.*, et al.* (2008). Histological and molecular analysis of Rdg2a barley resistance to leaf stripe. Molecular plant pathology *9*, 463-478.
Hanahan, D. (1983). Studies on transformation of Escherichia coli with plasmids. Journal of molecular biology *166*, 557-580.
Hann, D.R., Dominguez-Ferreras, A., Motyka, V., Dobrev, P.I., Schornack, S., Jehle, A., Felix, G., Chinchilla, D., Rathjen, J.P., and Boller, T. (2014). The Pseudomonas type III effector HopQ1 activates cytokinin signaling and interferes with plant innate immunity. The New phytologist *201*, 585-598.
Hann, D.R., Gimenez-Ibanez, S., and Rathjen, J.P. (2010). Bacterial virulence effectors and their activities. Curr Opin Plant Biol *13*, 388-393.
Hanna, W.F. (1929). Studies in the physiology and cytology of Ustilago zeae and Sorosporium reilianum. Phytopathology *19*, 415-422.
Hartley, R.D. (1972). p-Coumaric and ferulic acid components of cell walls of ryegrass and their relationships with lignin and digestibility. Science of Food and Agriculture *23*, 1347-1354.
Häusler, R.E., Heinrichs, L., Schmitz, J., and Flügge, U.I. (2014). How sugars might coordinate chloroplast and nuclear gene expression during acclimation to high light intensities. Molecular plant *7*, 1121-1137.
Hazen, S.P., Hawley, R.M., Davis, G.L., Henrissat, B., and Walton, J.D. (2003). Quantitative trait loci and comparative genomics of cereal cell wall composition. Plant physiology *132*, 263-271.
Heath, M. (2000). Hypersensitive response-related death. Plant Mol Biol *44*, 321-334.
Helliwell, C., Chin-Atkins, A.N., Wilson, I.W., Chapple, R., Dennis, E.S., and Chaudhury, A. (2001). The Arabidopsis *AMP1* Gene Encodes a Putative Glutamate Carboxypeptidase. The Plant cell *13*, 2115-2125.
Hematy, K., Cherk, C., and Somerville, S. (2009). Host-pathogen warfare at the plant cell wall. Curr Opin Plant Biol *12*, 406-413.
Hemetsberger, C., Herrberger, C., Zechmann, B., Hillmer, M., and Doehlemann, G. (2012). The Ustilago maydis effector Pep1 suppresses plant immunity by inhibition of host peroxidase activity. PLoS pathogens *8*, e1002684.

Hemetsberger, C., Mueller, A.N., Matei, A., Herrberger, C., Hensel, G., Kumlehn, J., Mishra, B., Sharma, R., Thines, M., Huckelhoven, R.*, et al.* (2015). The fungal core effector Pep1 is conserved across smuts of dicots and monocots. The New phytologist *206*, 1116-1126.
Hoffman, C.S., and Winston, F. (1987). A ten-minute DNA preparation from yeast efficiently releases autonomous plasmids for transformation of *Escherichia coli*. Gene *57*, 267-272.
Hofgen, R., and Willmitzer, L. (1988). Storage of competent cells for Agrobacterium transformation. Nucleic Acids Res *16*, 9877.
Holliday, A.R. (1974). Molecular aspects of genetic exchange and gene conversion. Genetics *78*, 273-287.
Hongkun, L.V., Zheng, J., Tianyu, W., Fu, J., Huai, J., Min, H., Zhang, X., Tian, B., Shi, Y., and Wang, G. (2014). The maize *d2003*, a novel allele of *VP8*, is required for maize internode elongation. Plant Mol Biol *84*, 243-257.
Horbach, R., Navarro-Quesada, A.R., Knogge, W., and Deising, H.B. (2011). When and how to kill a plant cell: infection strategies of plant pathogenic fungi. Journal of plant physiology *168*, 51-62.
Horst, R.J., Engelsdorf, T., Sonnewald, U., and Voll, L.M. (2008). Infection of maize leaves with *Ustilago maydi*s prevents establishment of C_4 photosynthesis. Journal of plant physiology *165*, 19-28.
Houben, A., Wako, T., Furushima-Shimogawara, R., Presting, G.G., Kunzel, G., Schubert, I., and Fukui, K. (1999). The cell cycle dependent phosphorylation of histone H3 is correlated with the condensation of plant mitotic chromosomes. The Plant Journal *18*, 675-679.
Huang, W., Pitorre, D., Poretska, O., Marizzi, C., Winter, N., Poppenberger, B., and Sieberer, T. (2015). ALTERED MERISTEM PROGRAM1 suppresses ectopic stem cell niche formation in the shoot apical meristem in a largely cytokinin-independent manner Plant physiology *167*, 1471-1486.
Hülskamp, M., Misra, S., and Jürgens, G. (1994). Genetic dissection of trichome cell development in arabidopsis. Cell *76*, 555-566.
Inzé, D., Gutiérrez, C., and Chua, N.H. (1999). Trends in plant cell cycle research. The Plant cell *11*, 991-994.
Jackson, D. (1991). In-situ hybridisation in plants. Molecular Plant Pathology: A Practical Approach. Oxford University Press.
Jacob, F., Vernaldi, S., and Maekawa, T. (2013). Evolution and Conservation of Plant NLR Functions. Front Immunol *4*.
Jammes, F., Lecomte, P., de Almeida-Engler, J., Bitton, F., Martin-Magniette, M.L., Renou, J.P., Abad, P., and Favery, B. (2005). Genome-wide expression profiling of the host response to root-knot nematode infection in Arabidopsis. Plant J *44*, 447-458.
Javelle, M., and Timmermans, M.C. (2012). In situ localization of small RNAs in plants by using LNA probes. Nat Protoc *7*, 533-541.
Jelenska, J., Yao, N., Vinatzer, B.A., Wright, C.M., Brodsky, J.L., and Greenberg, J.T. (2007). A J domain virulence effector of pseudomonsas syringae remodels host chloroplasts and suppresses defenses. Curr Biol *17*, 499-508.
Ji, H., Gheysen, G., Denil, S., Lindsey, K., Topping, J.F., Nahar, K., Haegeman, A., De Vos, W.H., Trooskens, G., Van Criekinge, W.*, et al.* (2013). Transcriptional analysis

through RNA sequencing of giant cells induced by Meloidogyne graminicola in rice roots Journal of experimental botany *64*, 3885-3898.
Jones, J.D., and Dangl, J.L. (2006). The plant immune system. Nature *444*, 323-329.
Jones, J.D.G., Vance, R.E., and Dangl, J.L. (2016). Intracellular innate immune surveillance devices in plants and animals. Science *354*.
Jones, L., Ennos, A.R., and Turner, S.R. (2001). Cloning and characterization of irregular xzlem4 (irx4): a severely lignin/deficient mutant of Arabidopsis. Plant J *26*, 205-216.
Jorgenson, L.R. (1931). Brown midrip in maize and its lignage relations. J Am Soc Agron *23*, 549-557.
Kahmann, R., Romeis, T., Bolker, M., and Kamper, J. (1995). Control of mating and development in Ustilago maydis. Curr Opin Genet Dev *5*, 559-564.
Kalve, S., De Vos, D., and Beemster, G.T. (2014). Leaf development: a cellular perspective. Front Plant Sci *5*.
Kämper, J. (2004). A PCR-based system for highly efficient generation of gene replacement mutants in Ustilago maydis. Mol Genet Genomics *271*, 103-110.
Kämper, J., Kahmann, R., Bölker, M., Ma, L.J., Brefort, T., Saville, B.J., Banuett, F., Kronstad, J.W., Gold, S.E., Müller, O.*, et al.* (2006). Insights from the genome of the biotrophic fungal plant pathogen *Ustilago maydis*. Nature *444*, 97-101.
Kawakatsu, T., Taramio, G., Itoh, J., Allen, J., Sato, Y., Hong, S.K., Yule, R., Nagasawa, N., Kojima, M., Kusaba, M.*, et al.* (2009). PLASTOCHRON3/GOLIATH encodes a glutamate carboxypeptidase required for proper development in rice. Plant J *58*, 1028-1040.
Kazan, K., and Lyons, R. (2014). Intervention of Phytohormone Pathways by Pathogen Effectors. The Plant cell *26*, 2285-2309.
Kim, D., Pertea, G., Trapnell, C., Pimentel, H., Kelley, R., and Salzberg, S.L. (2013). TopHat2: accurate alignment of transcriptomes in the presence of insertions, deletions and gene fusions. Genome Biol *14*.
Kirchanski, S.J. (1975). The Ultrastructural Development of the Dimorphic Plastids of Zea mays L. . Am J Bot *62*, 695-705.
Koncz, C., and Schell, J. (1986). The promoter of TL-DNA gene 5 controls the tissue-specific expression of chimaeric genes carried by a novel type of Agrobacterium binary vector. Molec Gen Genet *204*, 383-396.
Kondorosi, E., and Kondorosi, A. (2004). Endoreduplication and activation of the anaphase-promoting complex during symbiotic cell development. FEBS letters *567*, 152-157.
Kotogany, E., Dudits, D., Horvath, G.V., and Ayaydin, F. (2010). A rapid and robust assay for detection of S-phase cell cycle progression in plant cells and tissues by using ethynyl deoxyuridine. Plant Methods *6*.
Krapp, A., Hofmann, B., Schäfer, C., and Stitt, M. (1993). Regulation of the expression of rbcS and other photosynthetic genes by carbohydrates: a mechanism for the 'sink regulation' of photosynthesis? The Plant Journal *3*, 817-828.
Kretschmer, M., Croll, D., and Kronstad, J.W. (2016). Chloroplast-associated metabolic functions influence the susceptibility of maize to Ustilago maydis. Molecular plant pathology *[Epub ahead of print]*.

Krol, E., Mentzel, T., Chinchilla, D., Boller, T., Felix, G., Kemmerling, B., Postel, S., Arents, M., Jeworutzki, E., Al-Rasheid, K.A.*, et al.* (2010). Perception of the *Arabidopsis* danger signal peptide 1 involves the pattern recognition receptor *At*PEPR1 and its close homologue *At*PEPR2. The Journal of biological chemistry *285*, 13471-13479.

Laemmli, U.K. (1970). Cleavage of structural proteins during the assembly of the head of bacteriophage T4. Nature *227*, 680-685.

Lalonde, S., Boles, E., Hellmann, H., Barker, L., Patrick, J.W., Frommer, W.B., and Ward, J.M. (1999). The Dual Function of Sugar Carriers: Transport and Sugar Sensing. The Plant cell *11*, 707-726.

Lange, B.M., Lapierre, C., and Sandermann Jnr, H. (1995). Elicitor-induced spruce stress lignin. Structural similarity to early developmental lignins. Plant physiology *108*, 1277-1287.

Langmead, B., and Salzberg, S.L. (2012). Fast gapped-read alignment with Bowtie 2. Nature Methods *9*, 357-359.

Lanver, D., Berndt, P., Tollot, M., Naik, V., Vranes, M., Warmann, T., Münch, K., Rössel, N., and Kahmann, R. (2014). Plant Surface Cues Prime *Ustilago maydis* for Biotrophic Development. PLoS pathogens *10*, e1004272.

Larkin, M.A., Blackshields, G., Brown, N.P., Chenna, R., McGettigan, P.A., McWilliam, H., Valentin, F., Wallace, I.M., Wilm, A., Lopez, R.*, et al.* (2007). Clustal W and Clustal X version 2.0. Bioinformatics *23*, 2947-2948.

Laurie, J.D., Ali, S., Linning, R., Mannhaupt, G., Wong, P., Guldener, U., Munsterkotter, M., Moore, R., Kahmann, R., Bakkeren, G.*, et al.* (2012). Genome comparison of barley and maize smut fungi reveals targeted loss of RNA silencing components and species-specific presence of transposable elements. The Plant cell *24*, 1733-1745.

Lee, J., Eschen-Lippold, L., Lassowskat, I., Böttcher, C., and Scheel, D. (2015). Cellular reprogramming through mitogen-activated protein kinases. Front Plant Sci *6*.

Leech, R.M., Rumsby, M.G., and Thomson, W.W. (1973). Plastid differentiation, acyl lipid, and Fatty Acid changes in developing green maize leaves. Plant physiology *52*, 240-245.

Letunic, I., Doerks, T., and Bork, P. (2015). SMART: recent updates, new developments and status in 2015. Nucleic Acids Res *43*, D257-D260.

Li, P., Ponnala, L., Gandotra, N., Wang, L., Si, Y., Tausta, S.L., Kebrom, T.H., Provart, N., Patel, R., Myers, C.R.*, et al.* (2010). The developmental dynamics of the maize leaf transcriptome. Nat Genet *42*, 1060-1067.

Li, Y., Lee, K.K., Walsh, S., Smith, C., Hadingham, S., Sorefan, K., Cawley, G., and Bevan, M.W. (2006). Establishing glucose- and ABA-regulated transcription networks in Arabidopsis by microarray analysis and promoter classification using a Relevance Vector Machine. Genome Res *16*, 414-427.

Lichtenthaler, H.K., and Wellburn, A.R. (1983). Determination of the total carotinoids and chlorophylls a and *b* of leaf extracts in different solvents. Biochem Soc Transactions *603*, 591-593.

Lionetti, V., Giancaspro, A., Fabri, E., Giove, S.L., Reem, N., Zabotina, O.A., Blanco, A., Gadaleta, A., and Bellincampi, D. (2015). Cell wall traits as potential resources to

improve resistance of durum wheat against Fusarium graminearum. BMC plant biology *15*.
Lipka, U., Fuchs, R., and Lipka, V. (2008). Arabidopsis non-host resistance to powdery mildews. Curr Opin Plant Biol *11*, 404 - 411.
Liu, Q., Yuan, M., Zhou, Y., Li, X., Xiao, J., and Wang, S. (2011). A paralog of the MtN3/saliva family recessively confers race-specific resistance to Xanthomonas oryzae in rice. Plant Cell Environ *34*, 1958-1969.
Lo Presti, L., Lanver, D., Schweizer, G., Tanaka, S., Liang, L., Tollot, M., Zuccaro, A., Reissmann, S., and Kahmann, R. (2015). Fungal effectors and plant susceptibility. Annu Rev Plant Biol *66*, 513-545.
Lv, H., Zheng, J., Wang, T., Fu, J., Huai, J., Min, H., Zhang, X., Tian, B., Shi, Y., and Wang, G. (2014). The maize d2003, a novel allele of VP8, is required for maize internode elongation. Plant Mol Biol *84*, 243-257.
Mackey, D., Belkhadir, Y., Alonso, J.M., Ecker, J.R., and Dangl, J.L. (2003). Arabidopsis RIN4 Is a Target of the Type III Virulence Effector AvrRpt2 and Modulates RPS2-Mediated Resistance. Cell *112*, 379-389.
Malinovsky, F.G., Fangel, J.U., and Willats, W.G. (2014). The role of the cell wall in plant immunity. Front Plant Sci *5*.
Martinez-Espinoza, A.D., Garcia-Pedrajas, M.D., and Gold, S.E. (2002). The Ustilaginales as plant pests and model systems. Fungal genetics and biology : FG & B *35*, 1-20.
Matei, A., and Doehlemann, G. (2016). Cell biology of corn smut disease-*Ustilago maydis* as a model for biotrophic interactions. Current opinion in microbiology *34*, 60 - 66.
McLaughlin, M., and Walbot, V. (1987). Cloning of a mutable *bz2* allele of maize by transposon tagging and differential hybridization. Genetics *117*, 771-776.
Menden, B., Kohlhoff, M., and Moerschbacher, B.M. (2007). Wheat cells accumulate a syringyl-rich lignin during the hypersensitive resistance response. Phytochemistry *68*, 513-520.
Menke, W. (1962). Structure and chemistry of plastids. Annu Rev Plant Physiol *13*, 27-44.
Mistry, J., Bateman, A., and Finn, R.D. (2007). Predicting active site residue annotations in the Pfam database. BMC Bioinformatics *8*.
Miya, A., Albert, P., Shinya, T., Desaki, Y., Ichimura, K., Shirasu, K., Narusaka, Y., Kawakami, N., Kaku, H., and Shibuya, N. (2007). CERK1, a LysM receptor kinase, is essential for chitin elicitor signaling in Arabidopsis. Proc Natl Acad Sci *104*, 19613-19618.
Monaco, M.K., Sen, T.Z., Dharmawardhana, P.D., Ren, L., Schaeffer, M., Naithani, S., Amarasinghe, V., Thomason, J., Harper, L., Gardiner, J.*, et al.* (2013). Maize Metabolic Network Construction and Transcriptome Analysis. The Plant Genome *6*.
Monaghan, J., and Zipfel, C. (2012). Plant pattern recognition receptor complexes at the plasma membrane. Curr Opin Plant Biol *15*, 349-357.
Moreau, M., Azzopardi, M., Clement, G., Dobrenel, T., Marchive, C., Renne, C., Martin-Magniette, M.L., Taconnat, L., Renou, J.P., Robaglia, C.*, et al.* (2012). Mutations in the Arabidopsis homolog of LST8/GβL, a partner of the target of Rapamycin kinase, impair plant growth, flowering, and metabolic adaptation to long days. The Plant cell *24*, 463-481.

Morel, J.B., and Dangl, J.L. (1997). The hypersensitive response and the induction of cell death in plants. Cell death and differentiation *4*, 671-683.
Morkunas, I., and Ratajczak, L. (2014). The role of sugar signaling in plant defense responses against fungal pathogens. Acta Physiol Plant *36*, 1607-1619.
Mueller, A.N., Ziemann, S., Treitschke, S., Assmann, D., and Doehlemann, G. (2013). Compatibility in the *Ustilago maydis*-maize interaction requires inhibition of host cysteine proteases by the fungal effector Pit2. PLoS pathogens *9*, e1003177.
Mueller, O., Kahmann, R., Aguilar, G., Trejo-Aguilar, B., Wu, A., and de Vries, R.P. (2008a). The secretome of the maize pathogen *Ustilago maydis*. Fungal genetics and biology : FG & B *45 Suppl 1*, S63-70.
Mueller, O., Schreier, P.H., and Uhrig, J.F. (2008b). Identification and characterization of secreted and pathogenesis-related proteins in Ustilago maydis. Mol Genet Genomics *279*, 27-39.
Muthamilarasan, M., and Prasad, M. (2013). Plant innate immunity: An updated insight into defense mechanism. J Biosci *38*, 433-449.
Nagl, W. (1976). DNA endoreduplication and polyteny understood as evolutionary strategies. Nature *261*, 614-615.
Navarro, L., Bari, R., Achard, P., Lison, P., Nemri, A., Harberd, N.P., and Jones, J.D. (2008). DELLAs control plant immune responses by modulating the balance of jasmonic acid and salicylic acid signaling. Curr Biol *18*, 650-655.
Nelissen, H., Gonzalez, N., and Inzé, D. (2016). Leaf growth in dicots and monocots: so different yet so alike. Curr Opin Plant Biol *33*, 72-76.
Noel, L.D., Cagna, G., Stuttmann, J., Wirthmüller, L., Betsuyaku, S., Witte, C.P., Bhat, R., Pochon, N., Colby, T., and Parker, J.E. (2007). Interaction between SGT1 and cytosolic/nuclear HSC70 chaperones regulates Arabidopsis immune responses. The Plant cell *19*, 4061-4076.
Nuernberger, T., Brunner, F., Kemmerling, B., and Piater, L. (2004). Innate immunity in plants and animals: striking similarities and obvious differences. Immunological reviews *198*, 249-266.
Nuhse, T.S. (2012). Cell wall integrity signaling and innate immunity in plants. Front Plant Sci *3*, 280.
Odell, J.T., Nagy, F., and Chua, N.H. (1985). Identification of DNA sequences required for activity of the cauliflower mosaic virus 35S promoter. Nature *313*, 810-812.
Oerke, E.C. (2006). Crop losses to pests. J Agric Sci *144*, 31-43.
Okada, T.S. (1991). Transdifferentiation: Flexibility in Cell Differentiation. Oxford University Press.
Okmen, B., and Doehlemann, G. (2014). Inside plant: biotrophic strategies to modulate host immunity and metabolism. Curr Opin Plant Biol *20*, 19-25.
Pangalos, M.N., Neefs, J.M., Somers, M., Verhasselt, P., Bekkers, M., van der Helm, L., Fraiponts, E., Ashton, D., and Gordon, R.D. (1999). Isolation and expression of novel human glutamate carboxypeptidases with N-acelylated alpha-linked acidic dipeptidase and dipeptidyl peptidase IV activity. J Biol Chem *274*, 8470-8483.
Panstruga, R., and Dodds, P.N. (2009). Terrific protein traffic: the mystery of effector protein delivery by filamentous plant pathogens. Science *324*, 748-750.
Pauly, M., Gille, S., Liu, L., Mansoori, N., de Souza, A., Schultink, A., and Xiong, G. (2013). Hemicellulose biosynthesis. Planta *238*, 627-642.

Pauly, M., and Keegstra, K. (2010). Plant cell wall polymers as precursors for biofuels. Curr Opin Plant Biol *13*, 305-312.
Petre, B., Lorrain, C., Saunders, D.G., Win, J., Sklenar, J., Duplessis, S., and Kamoun, S. (2016). Rust fungal effectors mimic host transit peptides to translocate into chloroplasts. Cellular microbiology *18*, 453-465.
Petre, B., Saunders, D.G., Sklenar, J., Lorrain, C., Win, J., Duplessis, S., and Kamoun, S. (2015). Candidate Effector Proteins of the Rust Pathogen Melampsora larici-populina Target Diverse Plant Cell Compartments. Molecular plant-microbe interactions : MPMI *28*, 689-700.
Pfaffl, M.W., Horgan, G.W., and Dempfle, L. (2002). Relative expression software tool (REST (c)) for group-wise comparison and statistical analysis of relative expression results in real-time PCR. Nucleic Acids Res *30*.
Piquemal, J., Lapierre, C., Myton, K., O'Connell, A., Schuch, W., Grima-Pettenati, J., and Boudet, A.M. (1998). Down-regulation of Cinnamoyl-CoA Reductase induces significant changes of lignin profiles in transgenic tobacco plants. The Plant Journal *13*, 71-83.
Poretska, O., Yang, S., Pitorre, D., Rozhon, W., Zwerger, K., Uribe, M.C., May, S., McCourt, P., Poppenberger, B., and Sieberer, T. (2016). The Small Molecule Hyperphyllin Enhances Leaf Formation Rate and Mimics Shoot Meristem Integrity Defects Associated with AMP1 Deficiency. Plant physiology *17*, 1277-1290.
Ralph, J., and Hatfield, R.D. (1991). Pyrolysis-GC-MS characterization of forage materials. J Agric Food Chem *39*, 1426-1437.
Randolph, L.F. (1922). Cytology of Chlorophyll Types of Maize. Botanical Gazette *73*, 337-375.
Rawlings, N.D., Barrett, A.J., and Finn, R.D. (2016). Twenty years of teh MEROPS database of proteolztic enzymes, their substrates and inhibitors. nucleic Acids Res *44*.
Redkar, A. (2014). Functional Characterization of an Organ Specific Effector See1 of Ustilago maydis. Dissertation *Philipps-Universität, Marburg, Germany*.
Redkar, A., and Doehlemann, G. (2016a). EdU Based DNA Synthesis and Cell Proliferation Assay in Maize Infected by the Smut Fungus *Ustilago maydis*. bio-protocol *6*.
Redkar, A., and Doehlemann, G. (2016b). Ustilago maydis Virulence Assays in Maize. Bio-protocol *6*, e1760.
Redkar, A., Hoser, R., Schilling, L., Zechmann, B., Krzymowska, M., Walbot, V., and Doehlemann, G. (2015a). A Secreted Effector Protein of Ustilago maydis Guides Maize Leaf Cells to Form Tumors. The Plant cell *27*, 1332-1351.
Redkar, A., Villajuana-Bonequi, M., and Doehlemann, G. (2015b). Conservation of the Ustilago maydis Effector See1 in related smuts. Plant signaling & behavior, 0.
Reusche, M., Thole, K., Janz, D., Truskina, J., Rindfleisch, S., Drübert, C., Polle, A., Lipka, V., and Teichmann, T. (2012). Verticillium infection triggers VASCULAR-RELATED NAC DOMAIN7-dependent de novo xylem formation and enhances drought tolerance in Arabidopsis. The Plant cell *24*, 3823-3837.
Rhoades, M.M. (1952). The Effect of the Bronze Locus on Anthocyanin Formation in Maize. The American Naturalist *86*, 105-108.
Ring, L., Yeh, S.Y., Hüchering, S., Hoffmann, T., Blanco-Portales, R., Fouche, M., Villatoro, C., Denoyes, B., Monfort, A., Caballero, J.L.*, et al.* (2013). Metabolic

interaction between anthocyanin and lignin biosynthesis is associated with peroxidase FaPRX27 in strawberry fruit. Plant physiology *163*, 43-60.
Ryrif, I.J., Anderson, J.M., and Goodchild, D.J. (1980). The Role of the Light-Harvesting Chlorophyll *a/b* -Protein Complex in Chloroplast Membrane Stacking. FEBS Journal *107*, 345-354.
Sabelli, P.A., Liu, Y., Dante, R.A., Lizarraga, L.E., Nguyen, H.N., Brown, S.W., Klingler, J.P., Yu, J., LaBrant, E., Layton, T.M.*, et al.* (2013). Control of cell proliferation, endoreduplication, cell size, and cell death by the retinoblastoma-related pathway in maize endosperm. Proc Natl Acad Sci *110*, 1827-1836.
Sablowski, R., and Carnier Dornelas, M. (2014). Interplay between cell growth and cell cycle in plants. Journal of experimental botany *65*, 2703-2714.
Sambrook, J., Fritsch, E.F., and Maniatis, T. (1989). Molecular cloning: a laboratory manual. Cold Spring Harbor Laboratory, Cold Spring Harbor, New York.
Sampedro, J., Guttman, M., Li, L.C., and Cosgrove, D.J. (2015). Evolutionary divergence of ß-expansin structure and function in grasses parallels emergence of distinctive primary cell wall traits. Plant J *81*, 108-120.
Sanchez-Vallet, A., Saleem-Batcha, R., Kombrink, A., Hansen, G., Valkenburg, D.J., Thomma, B.P., and Mesters, J.R. (2013). Fungal effector Ecp6 outcompetes host immune receptor for chitin binding through intrachain LysM dimerization. eLife *2:e00790*.
Santiago, R., Barros-Rios, J., and Malvar, R.A. (2013). Impact of Cell Wall Composition on Maize Resistance to Pests and Diseases. Int J Mol Sci *14*, 6960-6980.
Sattler, S.E., and Funnell-Harris, D.L. (2013). Modifying lignin to improve bioenergy feedstocks: strengthening the barrier against pathogens? Front Plant Sci *4*.
Scheller, H.V., and Ulvskov, P. (2010). Hemicelluloses. Annu Rev Plant Biol *61*, 263-289.
Schilling, L. (2015). Identifizierung und Charakterisierung organspezifischer *Ustilago maydis* Effektoren. Dissertation *Philipps-Universität, Marburg, Germany*.
Schilling, L., Matei, A., Redkar, A., Walbot, V., and Doehlemann, G. (2014). Virulence of the maize smut Ustilago maydis is shaped by organ-specific effectors. Molecular plant pathology *15*, 780-789.
Schirawski, J., Böhnert, H.U., Steinberg, G., Snetselaar, K., Adamikowa, L., and Kahmann, R. (2005). Endoplasmic reticulum glucosidase II is required for pathogenicity of *Ustilago maydis*. The Plant cell *17*, 3532-3543.
Schirawski, J., Mannhaupt, G., Munch, K., Brefort, T., Schipper, K., Doehlemann, G., Di Stasio, M., Rossel, N., Mendoza-Mendoza, A., Pester, D.*, et al.* (2010). Pathogenicity determinants in smut fungi revealed by genome comparison. Science *330*, 1546-1548.
Schreiner, P., Chen, X., Husnjak, K., Randles, L., Zhang, N.X., Elsasser, S., Finley, D., Dikic, I., Walters, K.J., and Groll, M. (2008). Ubiquitin docking at the proteasome through a novel pleckstrin-homology domain interaction. Nature *453*, 548-552.
Schulz, B., Banuett, F., Dahl, M., Schlesinger, R., Schafer, W., Martin, T., Herskowitz, I., and Kahmann, R. (1990). The *b* alleles of *U. maydis*, whose combinations program pathogenic development, code for polypeptides containing a homeodomain-related motif. Cell *60*, 295-306.

Selin, C., de Kievit, T.R., Belmonte, M.F., and Fernando, W.G. (2016). Elucidating the Role of Effectors in Plant-Fungal Interactions: Progress and Challenges. Front Microbiol *7*.
Serrano, I., Audran, C., and Rivas, S. (2016). Chloroplasts at work during plant innate immunity. J Exp Biol *67*, 3845-3854.
Shirasu, K. (2009). The HSP90-SGT1 chaperone complex for NLR immune sensors. Annu Rev Plant Biol *60*, 139-164.
Shirasu, K., and Schulze-Lefert, P. (2003). Complex formation, promiscuity, and multi-functionality: protein interactions in disease resistance pathways. Trends in plant science *8*.
Skibbe, D.S., Doehlemann, G., Fernandes, J., and Walbot, V. (2010). Maize tumors caused by *Ustilago maydis* require organ-specific genes in host and pathogen. Science *328*, 89-92.
Skyba, O., Douglas, C.J., and Mansfield, S.D. (2013). Syringyl-rich lignin renders poplars more resistant to degradation by wood decay fungi. Appl and Environ Microbiology *79*, 2560-2571.
Smeekens, S., and Hellmann, H.A. (2014). Sugar sensing and signaling in plants. Front Plant Sci *5*.
Snetselaar, K.M. (1994). Light and electron microscopy of Ustilago maydis hyphae in maize. Mycol Res *98*, 347-355.
Snetselaar, K.M., and Mims, C.W. (1992). Sporidial Fusion and Infection of Maize Seedlings by the Smut Fungus Ustilago-Maydis. Mycologia *84*, 193-203.
Snetselaar, K.M., and Mims, C.W. (1993). Infection of Maize Stigmas by Ustilago-Maydis - Light and Electron-Microscopy. Phytopathology *83*, 843-850.
Snetselaar, K.M., and Mims, C.W. (1994). Light and Electron-Microscopy of Ustilago-Maydis Hyphae in Maize. Mycol Res *98*, 347-355.
Somerville, C.R., Bauer, S., Brinistool, G., Facette, M., Hamann, T., Milne, J., Osborne, E., Paredez, A., Persson, S., Raab, T.*, et al.* (2004). Toward a systems approach to understanding plant cell walls. Science *306*, 2206-2211.
Southern, E. (2006). Southern blotting. Nat Protoc *1*, 518-525.
Sozzani, R., Maggio, C., Varotto, S., Canova, S., Bergounioux, C., Albani, D., and Cella, R. (2006). Interplay between Arabidopsis activating factors E2Fb and E2Fa in cell cycle progression and development. Plant physiology *140*, 1355-1366.
Sparkes, I.A., Runions, J., Kearns, A., and Hawes, C. (2006). Rapid, transient expression of fluorescent fusion proteins in tobacco plants and generation of stably transformed plants. Nature protocols *1*, 2019-2025.
Srebotnik, E., and Messner, K. (1994). A Simple Method That Uses Differential Staining and Light Microscopy To Assess the Selectivity of Wood Delignification by White Rot Fungi. Appl and Environ Microbiology *60*, 1383-1386.
Steensgard, P., Garre, M., Muradore, I., Transidico, P., Nigg, E.A., Kitagawa, K., Earnshaw, W.C., Faretta, M., and Musacchio, A. (2004). Sgt1 is required for human kinetochore assembly. EMBO Rep *5*, 626-631.
Stergiopoulos, I., and de Wit, P.J. (2009). Fungal effector proteins. Annual review of phytopathology *47*, 233-263.

Stirnberg, A., and Djamei, A. (2016). Characterization of ApB73, a virulence factor important for colonization of Zea mays by the smut Ustilago maydis. Molecular plant pathology *17*, 1467-1479.
Sugimoto, K., Gordon, S.P., and Meyerowitz, E.M. (2011). Regeneration in plants and animals: Dedifferentiation, transdifferentiation, or just differentiation? . Trends in cell biology *21*, 212-218.
Sugimoto, K., Jiao, Y., and Meyerowitz, E.M. (2010). Arabidopsis regeneration from multiple tissues occurs via a root development pathway. Dev Cell *18*, 463-471.
Suzaki, T., Kim, C.S., Takeda, N., Szczyglowski, K., and Kawaguchi, M. (2013). TRICOT encodes an AMP1-related carboxypeptidase that regulates root nodule development and shoot apical meristem maintenance in Lotus japonicus. Development *140*, 353-361.
Suzuki, M., Latshaw, S., Sato, Y., Settles, A.M., Koch, K.E., Hannah, L.C., Kojima, M., Sakakibara, H., and McCarthy, D.R. (2008). The Maize Viviparous8 locus, encoding a putative ALTERED MERISTEM PROGRAM1-like peptidase, regulates abscisic acid accumulation and coordinates embryo and endosperm development. Plant physiology *146*, 1193-1206.
Talboys, P.W. (1958). Association of tylosis and hyperplasia of the xylem with vascular association of the hop by Verticillium albo-atrum. Trans Br Mycol Soc *41*, 249-260.
Tanaka, S., Brefort, T., Neidig, N., Djamei, A., Kahnt, J., Vermerris, W., Koenig, S., Feussner, K., Feussner, I., and Kahmann, R. (2014). A secreted Ustilago maydis effector promotes virulence by targeting anthocyanin biosynthesis in maize. eLife *3*, e01355.
Tang, H.M., Liu, S., Hill-Skinner, S., Wu, W., Reed, D., Yeh, C.T., Nettleton, D., and Schnable, P.S. (2014). The maize *brown midrib2* (*bm2*) gene encodes a methylenetetrahydrofolate reductase that contributes to lignin accumulation. The Plant Journal *77*, 380-391.
Tello-Ruiz, M.K., Stein, J., Wei, S., Preece, J., Olson, A., Naithani, S., Amarasinghe, V., Dharmawardhana, P., Jiao, Y., Mulvaney, J.*, et al.* (2016). Gramene 2016: comparative plant genomics and pathway resources. Nucleic Acids Res *44*, 1133-1140.
Tesso, T., and Ejeta, G. (2011). Stalk strength and reaction to infection by *Macrophomina phaseolina* of brown midrib maize (*Zea mays*) and sorghum (*Sorghum bicolor*). Fields Crops Research *120*, 271-275.
Thordal-Christensen, H. (2003). Fresh insights into processes of nonhost resistance. Curr Opin Plant Biol *6*, 351 - 357.
Tollot, M., Assmann, D., Becker, C., Altmüller, J., dutheil, J.Y., Wegner, C.E., and Kahmann, R. (2016). The WOPR Protein Ros1 Is a Master Regulator of Sporogenesis and Late Effector Gene Expression in the Maize Pathogen Ustilago maydis. PLoS pathogens *12*.
Torres Zabala, M., Littlejohn, G., Jayaraman, S., Studholme, D., Bailey, T., Lawson, T., Tillich, M., Licht, D., Bölter, B., Delfino, L.*, et al.* (2015). Chloroplasts play a central role in plant defence and are targeted by pathogen effectors. Nat Plants *1*.
Tosh, D., and Slack, J.M.W. (2002). How cells change their phenotype. Nature reviews Molecular cell biology *3*, 187-194.

Trapnell, C., Hendrickson, D.G., Sauvageau, M., Goff, L., Rinn, J.L., and Pachter, L. (2013). Differential analysis of gene regulation at transcript resolution with RNA-seq. Nature biotechnology *31*, 46-53.
Trapnell, C., Roberts, A., Goff, L., Pertea, G., Daehwan, K., Kelley, D.R., Pimentel, H., Salzberg, S.L., Rinn, J.L., and Pachter, L. (2012). Differential gene and transcript expression analysis of RNA-seq experiments with TopHat and Cufflinks. Nature protocols *7*, 562-578.
Turgeon, R. (1989). The Sink-Source Transition in Leaves. Annu Rev Plant Physiol *40*, 119-138.
Turner, J.G., Ellis, C., and Devoto, A. (2002). The jasmonate signal pathway. The Plant cell *14*, S153 - S164.
Van Dingenen, J., De Milde, L., Vermeersch, M., Maleux, K., De Rycke, R., De Bruyne, M., Storme, V., Gonzalez, N., Dhondt, S., and Inze, D. (2016). Chloroplasts Are Central Players in Sugar-Induced Leaf Growth. Plant physiology *171*, 590-605.
VanderMolen, G.E., Labavitch, J.M., Strand, L.L., and DeVay, J.E. (1983). Pathogen-induced vascular gels: ethylene as a host intermediate. Physiol Pathol *59*, 573-580.
Vanholme, R., Demedts, B., Morreel, K., Ralph, J., and Boerjan, W. (2010). Lignin biosynthesis and structure. Plant physiology *153*, 895-905.
Vidaurre, D.P., Ploense, S., Krogan, N.T., and Berleth, T. (2007). *AMP1* and *MP* antagonistically regulate embryo and meristem development in *Arabidopsis*. Development *134*.
Voiniciuc, C., Schmidt, M.H., Berger, A., Yang, B., Ebert, B., Scheller, H.V., North, H.M., Usadel, B., and Günl, M. (2015). MUCILAGE-RELATED10 Produces Galactoglucomannan That Maintains Pectin and Cellulose Architecture in Arabidopsis Seed Mucilage. Plant physiology *169*, 403-420.
Waadt, R., and Kudla, J. (2008). In planta visualization of protein interactions using bimolecular fluorescence complementation (BiFC). CSH Protoc *2008*, pdb prot4995.
Walbot, V., and Skibbe, D.S. (2010). Maize host requirements for *Ustilago maydis* tumor induction. Sex Plant Reprod *23*, 1-13.
Walter, M.C., Rattei, T., Arnold, R., Güldener, U., Münsterkötter, M., Nenova, K., Kastenmüller, G., Tischler, P., Wölfing, A., Volz, A.*, et al.* (2009). PEDANT covers all complete RefSeq genomes. Nucleic Acids Res, D408-411.
Walton, J.D. (1994). Deconstructing the Cell Wall. Plant physiology *104*, 1113-1118.
Wawra, S., Djamei, A., Albert, I., Nürnberger, T., Kahmann, R., and Van West, P. (2013). In vitro translocation experiments with RxLR-reporter fusion proteins of Avr1b from Phytophthora sojae and AVR3a from Phytophthora infestans fail to demonstrate specific autonomous uptake in plant and animal cells. Molecular plant-microbe interactions : MPMI *26*, 528 - 536.
Weber, E., Engler, C., Gruetzner, R., Werner, S., and Marillonnet, S. (2011). A modular cloning system for standardized assembly of multigene constructs. PloS one *6*, e16765.
Wenzler, H., and Meins, F.J. (1987). Persistent changes in the proliferative capacity of maize leaf tissues induced by Ustilago infection. Phys and Mol Plant Pathol *30*, 309-319.
Whisson, S.C., Boevink, P.C., Moleleki, L., Avrova, A.O., Morales, J.G., Gilroy, E.M., Armstrong, M.R., Grouffaud, S., van West, P., Chapman, S.*, et al.* (2007). A translocation signal for delivery of oomycete effector proteins into host plant cells. Nature *450*, 115-118.

Whistler, R.L., and Richards, E.L. (1970). Hemicelluloses. The Carbohydrates, Pigman, W, Horton, D, Eds; Academic Press: New York, NY, USA *2a*, 447-469.
Wildermuth, M.C. (2010). Modulation of host nuclear ploidy: a common plant biotroph mechanism. Curr Opin Plant Biol *13*, 449-458.
Winter, D., Vinegar, B., Nahal, H., Ammar, R., Wilson, G.V., and Provart, N.J. (2007). An "Electronic Fluorescent Pictograph" Browser for Exploring and Analyzing Large-Scale Biological Data Sets. PloS one *2*.
Wu, C.H., Krasileva, K.V., Banfield, M.J., Terauchi, R., and Kamoun, S. (2015). The "sensor domains" of plant NLR proteins: more than decoys? Front Plant Sci *6*.
Xiang, T., Zong, N., Zou, Y., Wu, Y., Zhang, J., Xing, W., Li, Y., Tang, X., Zhu, L., Chai, J.*, et al.* (2008). *Pseudomonas syringae* effector AvrPto blocks innate immunity by targeting receptor kinases. Curr Biol *18*, 74-80.
Xiong, Y., McCormack, M., Li, L., Hall, Q., Xiang, C., and Sheen, J. (2013). Glucose-TOR signalling reprograms the transcriptome and activates meristems. Nature *496*, 181-186.
Yamaguchi, Y., and Huffaker, A. (2011). Endogenous peptide elicitors in higher plants. Curr Opin Plant Biol *14*, 351-357.
Yamaguchi, Y., Pearce, G., and Ryan, C.A. (2006). The cell surface leucine-rich repeat receptor for *At*Pep1, an endogenous peptide elicitor in *Arabidopsis*, is functional in transgenic tobacco cells. Proc Natl Acad Sci USA *103*, 10104-10109.
Yu, Y., Streubel, J., Balzergue, S., Champion, A., Boch, J., Koebnik, R., Feng, J., Verdier, V., and Szurek, B. (2011). Colonization of rice leaf blades by an African strain of Xanthomonas oryzae pv. oryzae depends on a new TAL effector that induces the rice nodulin-3 Os11N3 gene. Molecular plant-microbe interactions : MPMI *24*, 1102-1113.
Zhao, Q. (2016). Lignification: Flexibility, Biosynthesis and Regulation. Trends in plant science *21*, 713-721.
Zhou, J., Neale, J.H., Pomper, M.G., and Kozikowski, A.P. (2005). NAAG peptidase inhibitors and their potential for diagnosis and therapy. Nat Rev Drug Discov *4*, 1015-1026.
Zipfel, C., Kunze, G., Chinchilla, D., Caniard, A., Jones, J.D., Boller, T., and Felix, G. (2006). Perception of the bacterial PAMP EF-Tu by the receptor EFR restricts Agrobacterium-mediated transformation. Cell *125*, 749-760.

6 Annexure

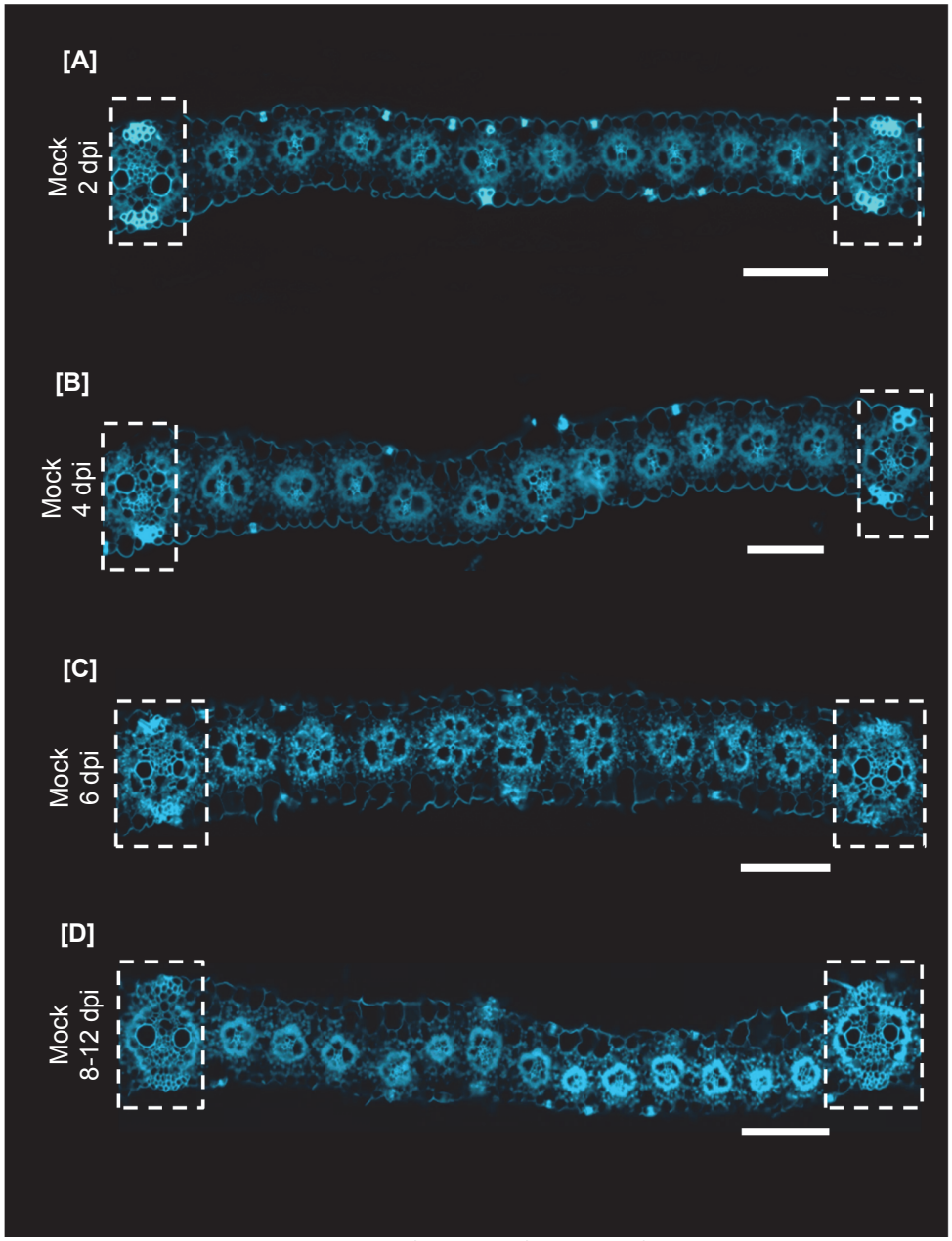

Figure 27: Histological sections of mock infected leaf tissue
Images show mock treated leaf sections taken with a filter for cell wall autofluorescence (425-450 nm). Dash-lined boxes indicate primary veins. **[A]** Representative picture of a mock treated leaf section 2 dpi, **[B]** 4 dpi, **[C]** 6 dpi, **[D]** 8-12 dpi. Tissue from four independent biological replicates of infection experiments was embedded and sectioned. Scale bars = 100 µm.

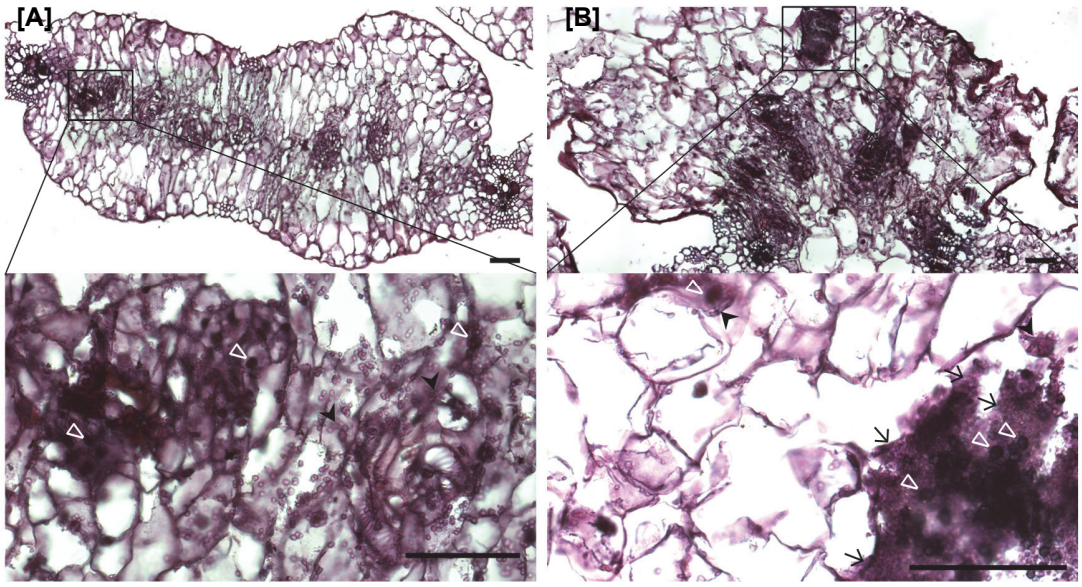

Figure 28: Histological sections of fuchsin stained tumors for mucilage layer staining
Images show SG200 infected, tumorous leaf sections **[A]** 6 dpi and **[B]** 8 dpi. Spores are indicated by white arrwoheads, black arrwoheads indicate fungal hyphae and mucilage layer is indicated by black arrows. Scale bars = 100 µm.

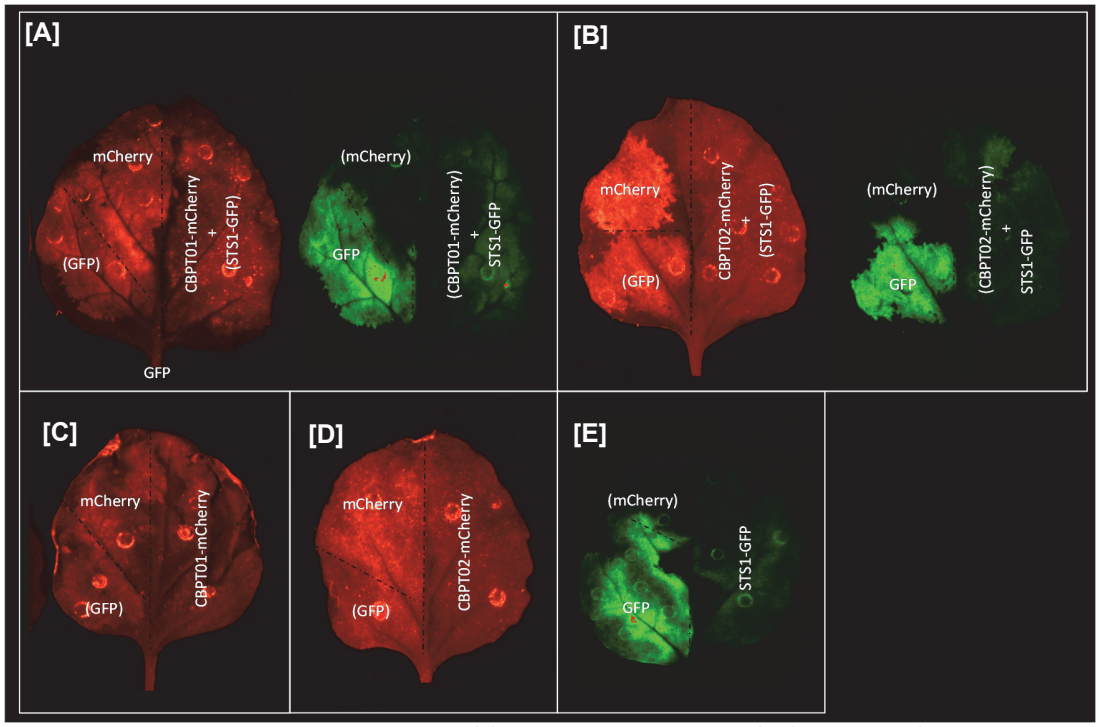

Figure 29: Heterologuos expression of fluorescently labeled STS1 and/or CBPII in *N. benthamiana*
Images show *N. benthamiana* leaves 3 dai. Expression of transiently overexpressed constructs driven by the CMV 35S promoter was investigated under fluorescent light with a filter for mCherry and GFP, respectively.GFP and mCherry were transiently co-expressed in each leaf as a transformation control **[A]** CBPII T01-mCherry and STS1-GFP were co-expressed and investigated for fluorescence light. **[B]** CBPII

T02-mCherry and STS1-GFP were co-expressed and investigated for fluorescence. **[C]** Single expression of CBPII T01-mCherry, **[D]** CBPII T02-mCherry and **[E]** STS1-GFP with the respective mCherry and GFP expression controls and investigated for fluorescence.

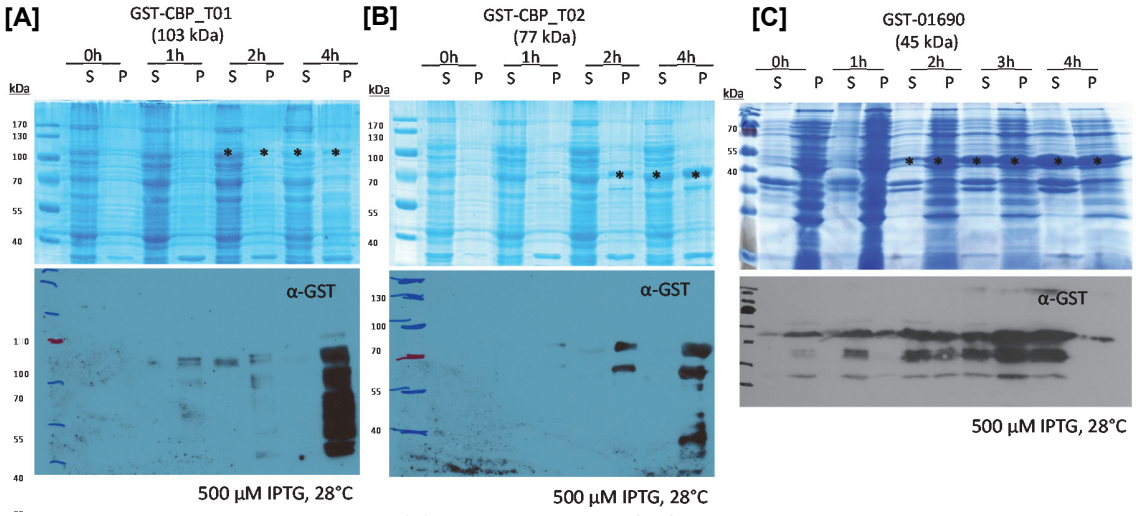

Figure 30: Heterolgous expression of CBPII T01/T02 or STS1 in *E. coli*
Coomassie stained SDS PAGE gel from soluble (S) and insoluble (P) *E. coli* protein extracts after induction with 500 µM IPTG. Samples from heterologously expressing cultures were taken 0, 1, 2 and 4 hours after induction of protein expression. Expression of the protein of interest was tested for each expression construct via western blot. Testexpression of **[A]** GST-CBP_T01, **[B]** GST-CBP_T02 and **[C]** GST-STS1 revealed best expression results at 28 °C with 500 µM IPTG. Bands showing the size of the respective protein of interest are highlighted by asterisks.

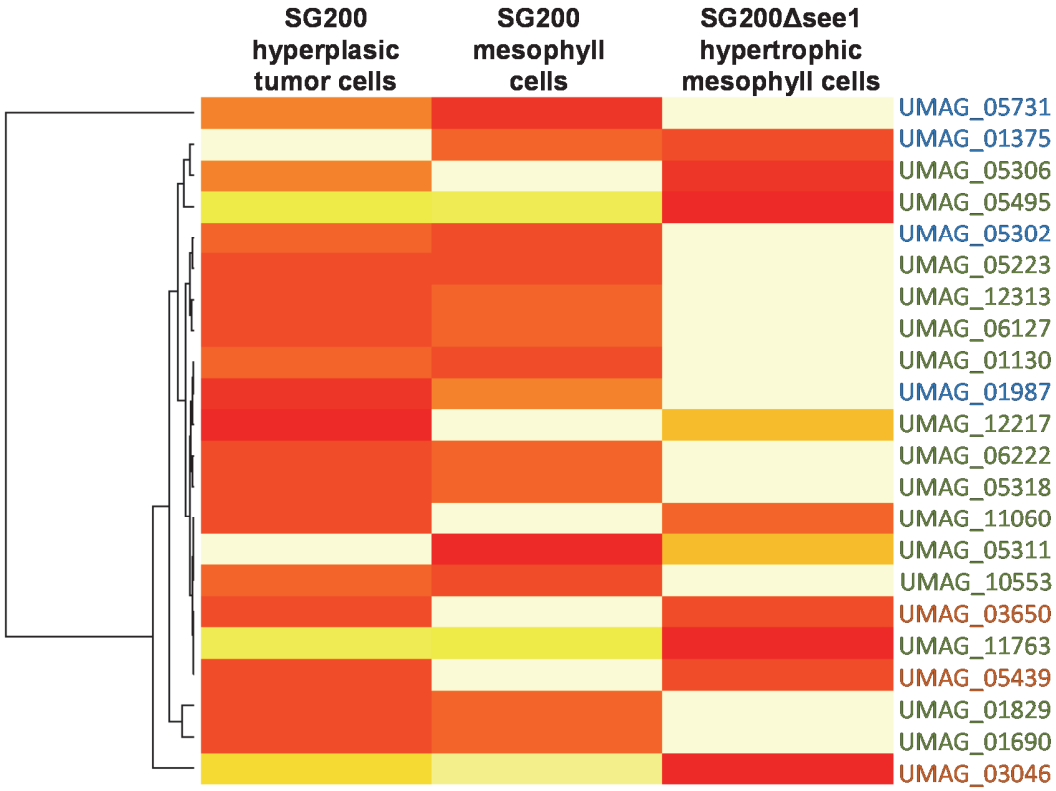

Figure 31: Heatmap representing gene expression of the *U. maydis* organ-specific and core effector genes summarized in Table 4 in dissected maize leaf cells 4 dpi with an adjusted p value <0.05 resulting from DESeq analysis (Anders and Huber, 2010).

Figure 32: Heatmap representing gene expression of the *U. maydis* effector genes that are organized in gene clusters defined by Kämper et al., 2006 in dissected maize leaf cells 4 dpi with an adjusted p value <0.05 resulting from DESeq analysis (Anders and Huber, 2010).

Table 17: *U. maydis* strains used in this study

Name	Genotype	Resistance	Reference
SG200	*a1 mfa2 bE1 bW2*	Phleo	Kämper *et al.*, 2006
SG200Δum01130	*a1 mfa2 bE1 bW2 Δum01130*	Phleo, Hyg	Schilling *et al.*, 2014
SG200Δum01690	*a1 mfa2 bE1 bW2 Δum01690*	Phleo, Hyg	Schilling *et al.*, 2014
SG200Δum01690-um01690	*a1 mfa2 bE1 bW2 Δum01690::hph ipr[Pwt-um01690]ips*	Phleo, Hyg, Cbx	Schilling *et al.*, 2014
SG200Δum01829	*a1 mfa2 bE1 bW2 Δum01829*	Phleo, Hyg	Schilling *et al.*, 2014
SG200Δum01829-um01829	*a1 mfa2 bE1 bW2 Δum01829::hph ipr[Pwt-um01829]ips*	Phleo, Hyg, Cbx	Schilling *et al.*, 2014
SG200Δum02239	*a1 mfa2 bE1 bW2 Δum02239*	Phleo, Hyg	Schilling *et al.*, 2014
SG200Δum02239-um02239	*a1 mfa2 bE1 bW2 Δum02239::hph ipr[Pwt-um02239]ips*	Phleo, Hyg, Cbx	Schilling *et al.*, 2014
SG200Δum03046	*a1 mfa2 bE1 bW2 Δum03046*	Phleo, Hyg	Schilling et al., 2014
SG200Δum03650	*a1 mfa2 bE1 bW2 Δum03650*	Phleo, Hyg	Schilling et al., 2014
SG200Δum03650-um03650	*a1 mfa2 bE1 bW2 Δum03650::hph ipr[Pwt-um03650]ips*	Phleo, Hyg, Cbx	Schilling et al., 2014
SG200Δum05223	*a1 mfa2 bE1 bW2 Δum05223*	Phleo, Hyg	Schilling et al., 2014
SG200Δum05306	*a1 mfa2 bE1 bW2 Δum05306*	Phleo, Hyg	Schilling et al., 2014
SG200Δum05306-um05306	*a1 mfa2 bE1 bW2 Δum05306::hph ipr[Pwt-um05306]ips*	Phleo, Hyg, Cbx	Schilling et al., 2014
SG200Δum05311	*a1 mfa2 bE1 bW2 Δum05311*	Phleo, Hyg	Schilling et al., 2014
SG200Δum05311-um05311	*a1 mfa2 bE1 bW2 Δum05311::hph ipr[Pwt-um05311]ips*	Phleo, Hyg, Cbx	Schilling et al., 2014

SG200Δum05318	*a1 mfa2 bE1 bW2 Δum05318*	Phleo, Hyg	Schilling et al., 2014
SG200Δum05318-um05318	*a1 mfa2 bE1 bW2 Δum05318::hph ipr[Pwt-um05318]ips*	Phleo, Hyg, Cbx	Schilling et al., 2014
SG200Δum05439	*a1 mfa2 bE1 bW2 Δum05439*	Phleo, Hyg	Schilling et al., 2014
SG200Δum05439-um05439	*a1 mfa2 bE1 bW2 Δum05439::hph ipr[Pwt-um05439]ips*	Phleo, Hyg, Cbx	Schilling et al., 2014
SG200Δum05495	*a1 mfa2 bE1 bW2 Δum05495*	Phleo, Hyg	Schilling et al., 2014
SG200Δum06127	*a1 mfa2 bE1 bW2 Δum06127*	Phleo, Hyg	Schilling et al., 2014
SG200Δum06222	*a1 mfa2 bE1 bW2 Δum06222*	Phleo, Hyg	Schilling et al., 2014
SG200Δum06223	*a1 mfa2 bE1 bW2 Δum06223*	Phleo, Hyg	Schilling et al., 2014
SG200Δum10553	*a1 mfa2 bE1 bW2 Δum10553*	Phleo, Hyg	Schilling et al., 2014
SG200Δum11060	*a1 mfa2 bE1 bW2 Δum11060*	Phleo, Hyg	Schilling et al., 2014
SG200Δum11060-um11060	*a1 mfa2 bE1 bW2 Δum11060::hph ipr[Pwt-um11060]ips*	Phleo, Hyg, Cbx	Schilling et al., 2014
SG200Δum11763	*a1 mfa2 bE1 bW2 Δum11763*	Phleo, Hyg	Schilling et al., 2014
SG200Δum12217	*a1 mfa2 bE1 bW2 Δum12217*	Phleo, Hyg	Schilling et al., 2014
SG200Δum12217-um12217	*a1 mfa2 bE1 bW2 Δum12217::hph ipr[Pwt-um12217]ips*	Phleo, Hyg, Cbx	Schilling et al., 2014
SG200Δum12313	*a1 mfa2 bE1 bW2 Δum12313*	Phleo, Hyg	Schilling et al., 2014

Table 18: Oligonucleotides used in this study

Name	Description	Sequence	Purpose of use
KL318	ppi RT fw	ACATCGTCAAGGCTATCG	qRT-PCR *ppi*
KL319	ppi RT rv	AAAGAACACCGGACTTGG	qRT-PCR ppi
O01	01690lb_fw	TTCAGATACGAGAAGAAGCGAACAGC	KO um01690
O02	01690b_rv	CACGGCCTGAGTGGCCCACGACACGG CTCAGATTCATCAC	KO um01690
O03	01690rb_fw	GTGGGCCATCTAGGCCGTCCTGACAG GGAAGCTCCTCTCG	KO um01690
O04	01690rb_rv	TCACCAACTACAACCTCGGTAAATCC	KO um01690
O05	05439lb_fw	GAGCTCGATCGCTGTCTTTG	KO um05439
O06	05439lb_rv	TTCGGCCATCTAGGCCTGCAGACTGGA TCTGCTTGAAC	KO um05439
O07	05439rb_fw	CACGGCCTGAGTGGCCATGGTTGCGA GGGAGAACAAGAG	KO um05439
O08	05439rb_rv	TGCGCTATGCCCAAGTCTATACG	KO um05439
O09	05495lb_fw	GGCGTGGTTGCAAGATACGG	KO um05495
O10	05495lb_rv	TTCGGCCATCTAGGCCGACAAGGGCG TCTTGGATGG	KO um05495
O11	05495rb_fw	CACGGCCTGAGTGGCCAAACGCACGA AGCGGAAGAAGTAG	KO um05495
O12	05495rb_rv	AGTGACGAGAACAAGGAAGTTCAG	KO um05495
OAli03	um12313 RT fw	CGTGCTCAAGCTCAACG	qRT-PCR *um12313*
OAli04	um12313 RT rv	TGCGACCAGATGCGATG	qRT-PCR *um12313*
OAli05	um06127 RT fw	ACGACGTAGAGTATGGTCAC	qRT-PCR *um06127*
OAli06	um06127 RT rv	GGCAGAAGAGAACCACTTTG	qRT-PCR *um06127*
OAli07	um10553 RT fw	TGCCCTCTTCTCTGTCTAC	qRT-PCR *um10553*
OAli08	um10553 RT rv	CGACTCTGGGTGGAAATG	qRT-PCR *um10553*
OAli100	compl. KO12217_rv	CATATGGATGATGAAAGGATGCCG	Komplementation KO *um12217*
OAli103	01690_pGBKT7fwd_NcoI	TACTACCCATGGTGTACATTGCAGTGC CCCAAC	For cloning of um01690 (sts1) in pGBKT7
OAli104	01690_pGBKT7rev_NotI	AATATAGCGGCCGCTATTCAGGCGTCC GGCTT	For cloning of um01690 (sts1) in pGBKT7
OAli109	compl. KO11060_fwI	CATATGCGCCGGGTGGCCTTGC	Komplementation KO *um11060*

OAli110	compl. KO11060_rv	AGGCGGCCGCTCAGGCCTTGTAGTTC CTG	Komplementation KO *um11060*
OAli113	compl. KO05306_fwI	CATATGCCTGCACATCTCAACATC	Komplementation KO *um05306*
OAli114	compl. KO05306_rv	AGGCGGCCGCTCAAGTAGGCGGTCTG TAAG	Komplementation KO *um05306*
OAli117	compl. KO05311_fwI	CGCAATAAGCTTTGTATTGTGAGCCCG TGCTG	Komplementation KO *um05311*
OAli118	compl. KO05311_rv	CGCATCATGCATATCCGATGAGTCGAA CAC	Komplementation KO *um05311*
OAli119	compl. KO05318_fwI	TAGCTTGCGGCCGCACAAAAGCGTGTA CGAAG	Komplementation KO *um05318*
OAli120	compl. KO05318_rv	CTGCGGCATATGCTAGAAGTGCAAAGC AAGTG	Komplementation KO *um05318*
OAli13	um05311 RT fw	GAGCGTCGAGAATCTCAAG	qRT-PCR *um05311*
OAli14	um05311 RT rv	CGTGGACAGACTCGTAATC	qRT-PCR *um05311*
OAli17	um11060 RT fw	CAGAGCTCGTTCAGCATAC	qRT-PCR *um11060*
OAli18	um11060 RT rv	CCTGTTGCGACCATACTTC	qRT-PCR *um11060*
OAli23	um12217 RT fw	CGTATTGTCCGCCTTGC	qRT-PCR *um12217*
OAli24	um12217 RT rv	CAGACGCCTCGAGAATG	qRT-PCR *um12217*
OAli2619	01690_fwd_woSP_BamHI	ATACAGGGATCCATTGCAGTGCCCCAA CCTGA	For cloning of um01690 (sts1) in pRSET
OAli29	um06223 RT fw	TGGCACCTTTGACGATCC	qRT-PCR *um06223*
OAli2920	01690_rev_EcoRI	TATTAAGAATTCATCAGGCGTCCGGCT TGGGCTCC	For cloning of um01690 (sts1) in pRSET
OAli2950	CBT_T01_woTM_SacI_fwd	GTAGCAGAGCTCGACCTCCTCGTGCC AACCAATTC	For cloning of GRMZM2G159171 T01 in pRSET
OAli2950	CBT_T01_woTM_SacI_fwd	GTAGCAGAGCTCGACCTCCTCGTGCC AACCAATTC	For cloning of GRMZM2G159171 T01 in pGADT7
OAli2951	CBP_T01_woTM_EcoRI_rev	GAATTCCGGATCTCATGTTAGTTTACCA TCCAGG	For cloning of GRMZM2G159171 T01/T02 in pRSET
OAli2951	CBP_T01_woTM_EcoRI_rev	GAATTCCGGATCTCATGTTAGTTTACCA TCCAGG	For cloning of GRMZM2G159171 T01/T02 in pGADT7
OAli2952	CBP_T02_SacI_fwd	GTATTAGAGCTCGACAGCGAGGAGAT GCCGGGCATC	For cloning of GRMZM2G159171 T02 in pRSET
OAli2952	CBP_T02_SacI_fwd	GTATTAGAGCTCGACAGCGAGGAGAT GCCGGGCATC	For cloning of GRMZM2G159171 T02 in pGADT7
OAli2975	CBP_start_fwd_MoClo_01	TTTGGTCTCAACATAATGGCCACGTCT CGCTGC	For cloning of CBP T01 into the MoClo system
OAli2976	CBP_rev_MoClo_02	TTTGGTCTCAGGTTTCTTGCACCAAGG AGAACGG	For cloning of CBP T01 into the MoClo system
OAli2977	CBP_fwd_MoClo_03	TTTGGTCTCAAACCTACAAAGGCGACC CGTAC	For cloning of CBP T01 into the MoClo system
OAli2978	CBP_rev_MoClo_04	TTTGGTCTCAACAAGGTCACCAAACCT CTCCACCCAAA	For cloning of CBP T01 into the MoClo system
OAli2979	CBP_fwd_MoClo_05	TTTGGTCTCAACATGACCCCTTGTTCC ACAGGCATGTTGC	For cloning of CBP T01 into the MoClo system
OAli2980	CBP_rev_MoClo_06	TTTGGTCTCAGGCCTCCCGACCAGTCC TTCTCGG	For cloning of CBP T01 into the MoClo system
OAli2981	CBP_fwd_MoClo_07	TTTGGTCTCAGGCCATGGTACAAGCAT ATGAT	For cloning of CBP T01 into the MoClo system
OAli2982	CBP_rev_MoClo_08	TTTGGTCTCAACAACGAAGATGTTAGTT TACCATCCAGGAC	For cloning of CBP T01 into the MoClo system
OAli2983	CBP_T02_fwd_MoClo_09	TTTGGTCTCAACATAATGCCGGGCATC CCGGCG	For cloning of CBP T02 into the MoClo system

OAli2984	CBP_T02_rev_MoClo_10	TTTGGTCTCAGGTCACCAAACCTCTCCACCCAAA	For cloning of CBP T02 into the MoClo system
OAli2985	CBP_T02_fwd_MoClo_11	TTTGGTCTCAGACCCCTTGTTCCACAGGCATGTTGC	For cloning of CBP T02 into the MoClo system
OAli2986	01690_fwd_MoClo01	TTTGGTCTCAACATAATGTTTGTGGCCTTTGCGATC	For cloning of um01690 into the MoClo system
OAli2987	01690_rev_MoClo02	TTTGGTCTCAGAGTCCGCAACCCAAACCGACCTTC	For cloning of um01690 into the MoClo system
OAli2988	01690_fwd_MoClo03	TTTGGTCTCAACTCAACTGGGACAAGGGCCAAC	For cloning of um01690 into the MoClo system
OAli2989	01690_rev_MoClo04	TTTGGTCTCAGGTTTCACCAAAGTGAACGCCGAC	For cloning of um01690 into the MoClo system
OAli2990	01690_fwd_MoClo05	TTTGGTCTCAAACCAAGATCAACCTGAACCTG	For cloning of um01690 into the MoClo system
OAli2991	01690_rev_MoClo06	TTTGGTCTCAACAACGAAGTGGCGTCCGGCTTGGGCTCCTTG	For cloning of um01690 into the MoClo system
OAli30	um06223 RT rv	AGTGTAGTGGTCCTCCTCTC	qRT-PCR *um06223*
OAli31	um05306 RT fw	TCCACAGACGGTCGTAAC	qRT-PCR *um05306*
OAli32	um05306 RT rv	CGCACACGATGTCCATTC	qRT-PCR *um05306*
OAli33	um01690 RT fw	GGCGTTCACTTTGGTGAG	qRT-PCR *um01690*
OAli34	um01690 RT_rv	GCGGGATGGGTTTAGTTG	qRT-PCR *um01690*
OAli35	um05318 RT fw	CCTTTGGCGGAACATACG	qRT-PCR um05318
OAli36	um05318 RT rv	AGGGTGAAACGGGTAGTG	qRT-PCR um05318
OAli43	05311lb_fw	TGATCGGGTGGCTCTTAATG	KO um05311
OAli44	05311lb_rv	GGCCATCTAGGCCGTTGGTGCAAGACTCTC	KO um05311
OAli45	05311rb_fw	GGCCTGAGTGGCCAGAGCATAGTTGGTCATATC	KO um05311
OAli46	05311rb_rv	CCGAGGCTTTCTGATCAC	KO um05311
OAli47	06127lb_fw	TCTTTGGCTCTCGAAGACTC	KO um06127
OAli48	06127lb_rv	GGCCATCTAGGCCAGCGTCGAGCAAATC	KO um06127
OAli49	06127rb_fw	GGCCTGAGTGGCCTCGTGAGTACCACGCTGATG	KO um06127
OAli50	06127rb_rv	GAAACACGGACACCATCCTAC	KO um06127
OAli51	10553lb_fw	AAAGTGTGGCGTCACATC	KO um10553
OAli52	10553lb_rv	GGCCATCTAGGCCCTGCCCGTGATTGATCTTTG	KO um10553
OAli53	10553rb_fw	GGCCTGAGTGGCCCATTGTTGAAGGTTGCGATTTAG	KO um10553
OAli54	10553rb_rv	GCAGTGCAAACAGGTAATGG	KO um10553
OAli55	11060lb_fw	GGGCGACATCTGATACAAC	KO um11060
OAli56	11060lb_rv	GGCCATCTAGGCCGACAAGAGGCCAGGCTGTG	KO um11060
OAli57	11060rb_fw	GGCCTGAGTGGCCTTGTTAATTCATGGTCCTTC	KO um11060
OAli58	11060rb_rv	CGACTTTGGTCGCCAAAGATG	KO um11060
OAli59	12217lb_fw	GTTCGTCAGCTCCACACTTC	KO um12217
OAli60	12217lb_rv	GGCCATCTAGGCCTGGTCTCTTGTGACTTTC	KO um12217
OAli61	12217_rb_fw	GGCCTGAGTGGCCGCACAATGGCAGCTCGTGAT	KO um12217
OAli62	12217rb_rv	AACTGTCAGCGTCGAGCCTTGG	KO um12217
OAli63	12313lb_fw	CCGCAAGCATTGACAGATAG	KO um12313
OAli64	12313lb_rv	GGCCATCTAGGCCATACAGCGCGTGGTTTGGTG	KO um12313
OAli65	12313rb_fw	GGCCTGAGTGGCCTGCGCTTGCAAACGTGTCC	KO um12313
OAli66	12313rb_fw	AGTGGGCATTCCGTAACGAG	KO um12313

OAli97	compl. KO01690_fwl	TTAGCGGCCGCTCAGGCGTCCGGCTTGGG	Komplementation KO um01690
OAli98	compl. KO01690_rv	CATATGGTTGATGAGCTGACAGG	Komplementation KO um01690
OAli99	compl. KO12217_fwl	GGCGGCCGCTTAGTTGCTGTCTTTTGTGTC	Komplementation KO um12217
OAR01	compl. KO2239_fw	GACCTGCAGGGTGTGCACGGTGCTACTG	Komplementation KO um02239
OAR02	compl. KO2239_rv	GAGCGGCCGCCCCACTCGTGACTGCTAC	Komplementation KO um02239
OAR05	um02239 RT fw	TCAGGTGCAAGGAGAAGG	qRT-PCR um02239
OAR06	um02239 RT rv	ACAGAATACTCCGCTTCCC	qRT-PCR um02239
ODA51	03650lb_fw	CCTGCGTAGCCTCAAGAGTC	KO um03650
ODA52	03650lb_rv	TTCGGCCATCTAGGCCACCGGGAGAGGATCGGATAG	KO um03650
ODA53	03650rb_fw	CACGGCCTGAGTGGCCTCTCCGCTCTGGACTATACTACC	KO um03650
ODA54	03650rb_rv	CCAGGCTCCTCTTCTTTCTGAATC	KO um03650
Olex85	06222lb_fw	CTGCAAACTAGCGTATCGCCTCTC	KO um06222
Olex86	06222lb_rv	TTCGGCCATCTAGGCCCGCGAAACGCAATGATCGTTCC	KO um06222
Olex87	06222rb_fw	CACGGCCTGAGTGGCCGCATCTTGAACCAGTGCTCTTGTC	KO um06222
Olex88	06222rb_rv	CTGCCAAGCTCCAAGTGTATCG	KO um06222
OLS100	um05495 RT fw	TCAGCTGGAAGGGTAAGAC	qRT-PCR um05495
OLS101	um05495 RT rv	CTCGGGCTGCAATCTAAAG	qRT-PCR um05495
OLS102	um03650 RT fw	TCCACGTATCGTCGTCTG	qRT-PCR um03650
OLS103	um03650 RT rv	CATGGCTGCTTTGGGATAG	qRT-PCR um03650
OLS104	um06222 RT fw	GCCATCAGCTCCGTATTTC	qRT-PCR um06222
OLS105	um06222 RT rev	TCATCGCAGGATGTCGTAG	qRT-PCR um06222
OLS106	um05439 RT fw	GACAACAATGGAGGCTCAAG	qRT-PCR um05439
OLS107	um05439 RT rv	CGGAAGCATTGGGAGAAC	qRT-PCR um05439
OLS108	um03046 RT fw	CTTCTGCGTAGACAAAGGAC	qRT-PCR um03046
OLS109	um03046 RT rv	GAAGAACTTGCCGGTTGG	qRT-PCR um03046
OLS122	compl. KO1829_fw	GTCATATGGCAGCTCAGCTCACTTCC	Komplementation KO um01829
OLS123	compl. KO1829_rv	GATAGCGGCCGCCGCTTTCAAGCAACCTTG	Komplementation KO um01829
OLS135	compl. KO5439_fw	CGCATATGCTGCGCTATGCCCAAGTC	Komplementation KO um05439
OLS136	compl. KO5439_rv	GTATGCGGCCGCGATCTTTTGCGGACGATC	Komplementation KO um05439
OLS137	compl. KO3650_fw	CGCATATGGCAATCGATCCAAGGAGAG	Komplementation KO um03650
OLS138	compl. KO3650_rv	CTATGCGGCCGCGTTGATCAAAGAGGCATG	Komplementation KO um03650
OLS92	um11763 RT fw	GGATGCGGTCATCAACTTC	qRT-PCR um11763
OLS93	um11763 RT rv	CTTCTTGTCGGGAGTTTCG	qRT-PCR um11763
OLS96	um1130 RT fw	AGGCCATAGACGCATCAG	qRT-PCR um01130
OLS97	um1130 RT rv	TCGAACAAGCCGTAGAGG	qRT-PCR um01130
OLS98	um01829 RT fw	CCCTCGAGAAGCAGCCTATC	qRT-PCR um01829
OLS99	um01829 RT rv	CCTTGGACGCAGGAGTCTTG	qRT-PCR um01829
OZA10	02239rb_rv	CTTCGACCTTACGGCATC	KO um02239
OZA13	06223lb_rv	TTCGGCCATCTAGGCCCGGTGATGAGTCAAGAAG	KO um06223
OZA14	06223lb_fw	GCGTTTGGTGGCATTTAG	KO um06223
OZA15	06223rb_fw	CACGGCCTGAGTGGCCGTTCTCTTGGACTTCTGC	KO um06223
OZA16	06223rb_rv	AGACGCTGGCCTAGACAA	KO um06223
OZA19	05223lb_rv	TTCGGCCATCTAGGCCGAAGCGATGCGAGTTGGA	KO um05223
OZA20	05223lb_fw	ACACGAATGCACCTCATC	KO um05223
OZA21	05223rb_fw	CACGGCCTGAGTGGCCCATGGTCATACCTGTCAC	KO um05223

OZA22	05223rb_rv	CGATGAAAGGGTGCAGAT	KO um05223
OZA25	05306lb_rv	TTCGGCCATCTAGGCCCAAGTGCGTCTTGGTGTG	KO um05306
OZA26	05306lb_fw	AATTGCCACCACTTCCTC	KO um05306
OZA27	05306rb_fw	CACGGCCTGAGTGGCCCGCACTACCTTGAACAGC	KO um05306
OZA28	05306rb_rv	TGCCCTCACATTCTGCTT	KO um05306
OZA31	11763lb_rv	TTCGGCCATCTAGGCCTTCTTAGGGGGAAGGAGG	KO um11763
OZA32	11763lb_fw	CATGAAGTGGGTCAGTCG	KO um11763
OZA33	11763rb_fw	CACGGCCTGAGTGGCCATACTGTCCTTCGCTGAG	KO um11763
OZA34	11763rb_rv	AGCATCCTCACTTGCATC	KO um11763
OZA43	01130lb_rv	TTCGGCCATCTAGGCCCATACACTACGCTACCGC	KO um01130
OZA44	01130lb_fw	TTGGCAGCGCATCCGAA	KO um01130
OZA45	01130rb_fw	CACGGCCTGAGTGGCCATAGACCCGCCATGAATC	KO um01130
OZA46	01130rb_rv	GAGGAGATTGCCAAGATG	KO um01130
OZA49	01829lb_rv	TTCGGCCATCTAGGCCGATGAGGGGGAATACCTG	KO um01829
OZA50	01829lb_fw	CTGAAGCGCGAAATCTTG	KO um01829
OZA51	01829rb_fw	CACGGCCTGAGTGGCCGTATCGCATTGCATCGAC	KO um01829
OZA52	01829rb_rv	TTGCCTCGACTGAGTGAC	KO um01829
OZA7	02239lb_rv	TTCGGCCATCTAGGCCGATGTTTTGCGAGCGAAG	KO um02239
OZA8	02239lb_fw	TCGGAAACCGTTCTGAGC	KO um02239
OZA9	02239rb_fw	CACGGCCTGAGTGGCCAGTAGCAGTCACGAGTGG	KO um02239

Abgrenzung der Eigenleistung

Die in dieser Arbeit präsentierten Ergebnisse wurden von mir selbstständig und ohne andere als die hier aufgeführte Hilfe durchgeführt. Dabei erfolgte die Konzipierung der Experimente in Zusammenarbeit mit meinem Betreuer Prof. Dr. Gunther Döhlemann. Im Folgenden werden weitere, an dieser Arbeit beteiligte Personen sowie deren experimentelle Beiträge genannt:

Ziba Ajami Rashidi, Dr. Amey Redkar, Dr. Lena Schilling, Dr. Alexander Hof und Daniela Assmann
Ziba Ajami Rashidi hat die *U. maydis* Deletionsstämme für *um06223*, *um11763*, *um05495* *um02239* (*Δsee1*) erstellt. Der Komplementationsstamm für *um02239* wurde von Dr. Amey Redkar erstellt. Dr. Lena Schilling erstellte die Deletionsstämme für *um01130*, *um01829* und *um05223*, *um01829, um03650* sowie die Komplementationsstämme für *um03650* und *um05439*. Der Deletionsstamm für *um06222* wurde von Dr. Alexander Hof erstellt. Der Deletionsstamm für *um05439* wurde von Daniela Assmann erstellt. Der Deletionsstamm für *um05318* wurde von Frau Prof. Dr. Kahmann zur Verfügung gestellt, *um03046* von Herrn Prof. Dr. Kämper.

Dr Makus Günl und Dr. Björn Thiele

führten die in Kapitel 2.4 gezeigten Zellwandanalysen (Lignocellulose Kompositionsanalyse und Hemicellulose Kompositionsanalyse) mit Hilfe von Py-GC-MS und HPAEC-PAD sowie die vorhergehende Zellwandextraktionen durch.

Sebastian Wittek
hat bei der Erstellung der in Kapitel 2.4.3 gezeigten elektronenmikroskopischen Aufnahmen geholfen.

Dr. Janine Altmüller und Christoph Becker

waren an der RNAseq Analyse Sequenzierung der in Kapitel 2.5 genannten RNA aus lasermikrodissizierten Zellen beteiligt. Sie führten die Prä-amplifizierung, Zweitstrangsynthese und Probenvorbereitung zur Sequenzierung der Proben durch.

Corinna Ernst

war an der in Kapitel 2.5 gezeigten Auswertung der RNAseq Daten beteiligt. Von ihr wurde das Mapping und die Analyse der exprimierten Gene erstellt.

Danksagung

Mein erster Dank gilt Prof. Dr. Gunther Döhlemann, der mir die Möglichkeit gab, meine Arbeit in seiner Abteilung anzufertigen. Für die große Freiheit das verfolgen zu dürfen, was mich am meisten interessierte und dass Du stets ein offenes Ohr für Projektideen und ihre Verwirklichung hattest. Deine konstruktive Kritik trug damit in großem Maße zum Gelingen dieser Arbeit bei.

Ein großer Dank gilt Frau Prof. Dr. Regine Kahmann für die Übernahme des Zweitgutachtens. In allererster Linie aber dafür, dass Sie in diesem Projekt stets weiterführende und professionelle Unterstützung während der jährlichen Forschungsberichte geleistet haben. Ihre Erfahrung und Ihre Ratschläge waren eine große Hilfe bei der Umsetzung dieses Projektes.

Herzlich danken möchte ich auch Herrn Prof. Dr. Batschauer. Ihre Unterstützung vor allem von der Seite der Pflanzenphysiologie ist aus diesem Projekt nicht wegzudenken und ich danke Ihnen für Ihre positive Unterstützung während der Projektdiskussionen sowie für die Übernahme des Koreferates.

Einen besonderen Dank schulde ich Prof. Dr. Volker Lipka für die Bereitschaft meiner Prüfungskommission beizuwohnen. Volker, danke für Deine stete Unterstützung, die Einladungen zu Euren Weihnachtsfeiern, die mir stets das Gefühl gaben nie gegangen zu sein, die vielen Ratschläge und Dein offenes Ohr, vor allem auch bei der Entscheidung wie es nach dem Dr. weitergehen soll (It‘s the terror of knowing what this world is about...).

Thanks to Prof. Virginia Walbot for initiating the LCM analysis. Thanks for your active support in this project and your warm hospitality during my stay in Stanford.

Markus Günl danke ich für die Zellwandanalyse und die hilfreiche Kommunikation. Einen großen Dank schulde ich Corinna Ernst für die spontane Bereitschaft zur Auswertung der RNAseq Daten und das so schöne Wiedersehen nach dem Studium.

Bei den Mitgliedern der AG Döhlemann, AG Zuccharo und AG Kahmann möchte ich mich ebenfalls bedanken, bei einigen in ganz besonderem Maße:

Leona und Daniel, Euch danke ich für die Unterstützung, die Ihr im Rahmen Eures Studienprojektes oder als Hiwi geleistet habt. A big thank you to Amey for all the interesting discussions about organ specificity and for reading the manuscript.

André, Zippi, Robin, Basti, Elaine, und (nochmals) Daniel. Danke für die wundervollen Stunden und vielen lustigen Momente, die Marburg und Köln für mich unvergesslich haben werden lassen. Danke, Elaine für Deine stete Zuverlässigkeit und Deinen Beistand im Leid der Gewebefixierungen und dass Du einfach ein lieber Mensch bist. Danke Basti, für das Begleiten nach Hause in Marburg und dass Du uns so oft zum Lachen gebracht hast. Danke Daniel, dass Du unser letztes Jahr in der AG so bereichert hast und für jeden Unsinn zu haben bist. Danke Zippi, für die wundervolle Zeit vor allem in Köln auf der Mauer, auf dem Dach, in Deiner lieben WG oder bei mir. Die Zeit mit Dir hat Dich für mich nicht nur zu einem super Kollegen, sondern auch zu einem sehr guten Freund gemacht und vieles erleichtert. Ich hatte so viel Spaß mit Dir zusammen mit Jules, Rotter, Henne. Es war einfach wunderbar mit Euch.

Danke André – nur Du allein weißt wofür.

Ebenfalls bedanken möchte ich mich bei allen Mitgliedern aus der AG Lipka in Göttingen, die ich glücklicherweise im Rahmen der Lasermikrodissektion auch noch in der letzten Zeit sehr oft sehen durfte und die mir die Zeit dort immer wundervoll gemacht haben - mit der Erlaubnis mich wie zu Hause fühlen zu dürfen.

Danke liebe Yvi, Karin, Charlotte und auch Johanna einfach für alles. Die vielen schönen Abende, das Quatschen, das Essen, das Feiern, die Ironie und den Sarkasmus, einfach Eure tiefe Freundschaft, die Reisen, die Ratschläge, das gemeinsame Durchstehen des Studiums und auch der letzten Jahre trotz der großen Entfernung und dass Ihr immer da seid! Charlotte und Yvi, danke, dass Ihr bereit wart die Arbeit zu lesen.

Und auch Dir, Jeannine, danke ich für die stete Überbrückung der Entfernung an so vielen wundervollen Wochenenden. Sei es in London, Berlin, Marburg, Köln oder Wien. Wo auch immer Du bist, ich danke Dir für die vielen Gespräche, für London, die Shoppingtouren, die Konzerte und Musicals, all das Schöne was uns am Sparen von unserem Doktorandengehalt und an wochenendlicher Laborarbeit gehindert hat.

Von ganzem Herzen bedanke ich mich bei meiner Familie, die mir durch ihre Liebe und ihren Zuspruch immer gezeigt haben, dass ich die richtigen Ziele verfolge, die immer für mich da ist und mich in jeglicher Hinsicht stets unterstützt. Danke Mama und Papa, Oma und Opa, Inge und Silviu und Sebastian.